

THESE

Présentée en vue de l'obtention du grade de

DOCTEUR DE L'UNIVERSITE PARIS-SEINE

Spécialité: Chimie Organique – Science des matériaux

Soutenue publiquement 16 May 2019 par:

Diego A. MAGALDI-LARA

Synthesis of New Carbazole-based Hole Transport Molecules for Hybrid Perovskite Solar Cells

Devant le jury composé de :

Pr. Thierry TOUPANCE	Université de Bordeaux	Examineur
Pr. Hyacinthe RANDRIAMAHAZAKA	Université Paris Diderot	Rapporteur
Dr. Kathleen MOINEAU-CHANE CHING	CNRS Toulouse	Rapporteur
Dr. Frédéric DUMUR	Aix-Marseille Université	Examineur
Pr. Fabrice GOUBARD	Université de Cergy-Pontoise	Directeur de thèse
Dr. Thanh-Tuân BUI	Université de Cergy-Pontoise	Co-encadrant

ECOLE DOCTORALE SCIENCES ET INGENIERIE (**Université de Cergy-Pontoise**)

Unité de recherche: LPPI, Laboratoire de Physicochimie des Polymères et des Interfaces, EA2528

Glossary

ACN	acetonitrile
AFM	atomic force microscopy
bl	blocking layer
CE	counter electrode
CTA	chain transfer agent
CV	cyclic voltammetry
Cz	carbazole
D/A	donor/acceptor
DCM	dichloromethane
DFT	density functional theory
DMF	dimethylformamide
DPA	4,4'-dimethoxydiphenylamine
DSC	differential scanning calorimetry
DSSC	dye sensitized solar cell
DVB	divinylbenzene
E_{gap}	energy bandgap
E_{ox}	oxidation onset
ETL	electron transport layer
FF	fill factor
FTO	fluor-tin oxide glass
HR-MS	high-resolution mass spectroscopy
HTL	hole transport layer
HTM	hole transport material
ITO	indium-tin oxide glass
J_{sc}	short-circuit current
MAI	methylammonium iodide
MAPI	methylammonium lead triiodide (MAPbI_3)
MeOH	methanol

MO	molecular orbital
NMR	nuclear magnetic resonance
OSC	organic solar cell
PCBM	phenyl-C ₆₁ -butyric acid methyl ester
PCE	power conversion efficiency
PDOT-PSS	poly(3,4-ethylenedioxythiophene) polystyrene sulfonate
PET	polyethylene terephthalate
P _{eth}	Petroleum ether
PSC	perovskite solar cell
PV	photovoltaic
Ra	arithmetic mean roughness
Rq	root mean square roughness
sDSSC	solid-dye sensitized solar cell
SEC	size-exclusion chromatography
TGA	thermogravimetric analysis
TPA	4-bromo-N,N-bis(4-methoxyphenyl)aniline
V _{oc}	open-circuit voltage
WE	working electrode
η	photocurrent conversion efficiency
S _N 2	nucleophilic substitution

Contents

Glossary	3
Contents.....	5
Introduction	9
1. State of the art: from the solar energy to the photovoltaic devices	15
1.1 Photovoltaic Overview	16
The aim of this thesis	17
1.2 State of the Art: emergent hybrid photovoltaics	18
1.2.1 Dye-sensitized solar cells.....	18
1.2.2 Perovskite solar cell.....	20
1.3 Device Architecture and Perovskite Solar Cells (PSCs)	26
1.3.1 Perovskite Configuration	26
1.3.2 Mesoporous electron transport layer	26
1.3.3 Mesoporous insulating PSC	28
1.3.4 Planar PSC.....	29
1.3.5 HTM-free PSC.....	30
1.3.6 Inverted PSC.....	31
1.4 Device Components: Semiconductor TiO ₂ layer as dense ETL layer.....	33
1.5 Device Components: Mesoporous ETL layer and interface with Perovskite material.....	34
1.6 Device Components: Perovskite as active layer	36
1.7 Device Components: Hole transport material.....	38
1.7.1 Inorganic p-type HTM.....	39
1.7.2 Organic small molecules as Hole Transport Materials	40
1.8 Contact metallic layer	42
1.9 Carbazole as organic hole transport materials.....	43
2. Carbazole substituted Isomers derivatives as HTM for perovskite solar cells.....	51

2.1 Strategy	52
2.2 Synthesis objective	53
2.3 Synthesis of DMx and iDMX molecules.....	54
Synthetic strategy of DMx or 3,6-carbazole substituted molecules.....	54
Synthetic strategy of iDMx or 2,7-carbazole substituted molecules.....	54
2.3.1 Synthetic procedures	55
2.3.1.3 General synthesis procedure for compounds DM1 and DM2.	57
2.4 Characterization of physical properties of these carbazole species.....	64
2.4.1 Thermal properties	64
2.4.2 Optical properties	72
2.4.3 Electrochemistry measurements	75
2.4.4 General physical properties table of DMx and i-DMx series	79
2.4.5 Computational Studies	81
2.4.6 Surface morphology studies by atomic force microscopy	83
2.5 Photovoltaic measurements	88
2.5.1 Characterization of solar cells.....	90
2.5.2 Analysis and discussion	90
2.5.3 Photovoltaic performance of iDMx.....	92
2.5.4 Contact angle over MAPbI ₃ surface	93
2.5.5 Light soaking effect	96
2.6 Conclusions.....	99
3. Carbazole-based polymeric/oligomeric hole transporting materials.....	101
3.1 State of the art.....	102
3.2 Carbazole non-conjugated polymer DM1P	106
3.2.1 Material synthesis	106
3.2.3 Characterization of DM1P	112
3.2.4 General physical properties of DM1P	119

3.2.5 Photovoltaic Performances	120
3.2.6 Conclusions.....	122
3.3 Carbazole based conjugated Oligomer	123
3.3.1 Synthesis objective.....	123
3.3.2 Synthesis of PCzX series.....	124
3.3.3 Characterization.....	130
3.3.4 Conclusions.....	140
4. Bicarbazylum and 1,4-bicarbazolyl--benzene HTMs.....	141
4.1 State of the art.....	142
4.2 Carbazole oxidative coupling.....	143
4.2.1 Synthesis objective.....	143
4.2.2 Synthetic procedures	144
4.2.3 Synthesis of dimer (DM18) by oxidative coupling	148
4.2.4 Characterization.....	149
4.2.5 General properties physical properties of DM1X series	157
4.2.6 Computational Studies	159
4.2.7 Surface morphology studies by atomic force microscopy	161
4.2.8 Angle Contact.....	163
4.2.6 Conclusions.....	163
General Conclusions and Perspectives.....	164
Bibliography	167
Annex.....	180
Annex 2	186
DM1	186
DM2	188
DM1P	190
iDM1	191

iDM2	194
iDM3	197
iDM4	200
DM11	202
DM12	204
DM13	205
DM15	206
DM18	208
PCz1	210
PCz2	211
PCz3	213
PCzX precursors	214
N-(4-methoxybenzene)-carbazole	214
N-(4-methoxybenzene)-3,6-dibromo-carbazole	214
N-(4-(N,N-bis(4-methoxyphenyl)aniline)carbazole (CzTPA).....	216
N-(4-(N,N-bis(4-methoxyphenyl)aniline)-3,6-dibromocarbazole (Br ₂ CzTPA).....	217
Abstract	218
Résumé	220
Synthesized molecules.....	222

Introduction

Energy in form of electrical current is one of the basic needs of the modern human society. Electricity is produced mainly through firing vegetal material, such as wood and coal or fossil fuels. Thermal energy released by the combustion of the mentioned sources, is transformed into mechanical or kinetic energy which in turn is converted into electricity by turbine's movement or combustion motors. In this way, more than 84% of the total energy demand of all human society is produced, leaving the rest of the energy production to, nuclear (4%), hydroelectric (7%) and renewable (2%) power ¹.

On earth, at the base of the trophic level, we find that plants and/or algae and cyanobacteria are the primary source of energy for the rest of the living beings. Plants and algae, via photosynthesis transform sunlight into chemical energy that afterwards is stored in form of biomass all around the earth. Over time (60 million years), ancient biomass deposited underground at 2,000 meters was subjected to temperatures that reached over 100°C and eventually transformed in what we know as fossil fuels.

Until now, human society benefited from the energy contained in fossil fuel deposits, but never directly from the sunlight due to the lack of adequate technology that can harvest sunlight, transform it and store its energy to take advantage of its tremendous potential.

From solar radiation, the amount of energy that hits the earth over the high atmosphere is about 174 petawatts (PW, 10^{15} watts), approximately 30% is reflected and clouds, oceans and landmass absorb the rest. Within the landmass we can include the energy stored through photosynthesis in plants which corresponds to more than 3,000 exajoules (EJ, 10^{18} joules) in the form of biomass². In short, the energy that reaches the earth's surface is so vast and abundant that in one year the amount of energy is more than twice that will ever be obtained from the total of the non-renewable resources existing on earth³.

In an attempt to take advantage of this huge and inexhaustible source of energy, great innovators like Augustin Mouchot⁴, around the year 1864 developed the first model of solar concentrators to produce steam with the first designed solar steam engine. He said, *"One must not believe, despite the silence of modern writings, that the idea of using solar heat for mechanical operations is recent. On the contrary, one must recognize that this idea is very ancient*

and its slow development across the centuries it has given birth to various curious devices” ⁴ meaning that since long time ago humankind has tried to grid energy from the sun. Added to the last mentioned, this great visionary character also spoke of the disadvantages and consequences caused by the use of fossil fuels to the environment. As usually happens with those ahead of their time, nobody listened to them and the solar concentrators will not be thoroughly studied until the late 80's. In this way, the first modern time solar technology emerges.

Currently solar technology is not anymore a project supported by dreamers and radicals but is more a race to reach the most convenient and friendly way to produce energy from the widespread source around the earth, the solar power.

Solar energy is now harnessed in a number of different ways in all different grades of complexity, ranging from the most simple solar-thermal water heaters, house heating systems, solar furnaces for cooking and water-purification treatments to the more complex molten salt energy storage along with solar concentrators. The aforementioned processes are the simplest ways that thermal energy from the sun is used directly to perform a useful energy conversion. Nowadays, new high-tech options are in development, like photovoltaics, photochemical hydrogen production and electrolysis fueled by solar power, artificial photosynthesis reduction of CO₂ to produce methanol or different hydrocarbons among many other experimental technologies.

It should be noted that evolution of solar photovoltaic technology has been growing in parallel with storage methods such as batteries and capacitors, since such a high-energy production is of no valuable use if there is no means to store it adequately, so that energy can be distributed according to its demand.

Industrialized countries are concerned about the increase of CO₂ levels on the atmosphere. This contributes to the rising temperature around the planet by the well-known greenhouse effect and consequently the acceleration of the climate change. The main drive for the development and improvement of technologies with a low environmental impact is to counter such greenhouse effects and supply the energy demand for human society. During the last 10 years harvesting light from the sun, resemble like a very plausible alternative for an efficient energy production. Nevertheless the actual technologies are still quite expensive for their commercialization and difficult to implement in an already established society heavily dependent on coal, gas and oil accounting more than the 84% production of total energy consumption in the society that we are living⁵.

The International Energy Agency (IEA) supports and promotes global collaboration on energy technology creation to secure future energy supplies and mitigate their environmental impact. They established that by 2040 nearly 60% of all new power generation capacity on the main scenario (Europe and English speaking countries) must come from renewables and photovoltaics (PVs) is expected to be capable of generate between 10-25% of this total.

Historically United States was the energy production leader through photovoltaics and its capacity counted with 77 MW by 1996. Ten years later PV electricity production in Europe led by Germany and Japan and China in Asia, matched US records. Those countries continued with this tendency surpassing the US with 40 GW by 2007. Nowadays, China is the world's largest producer of photovoltaic power with more than 100 GW capacity.⁶

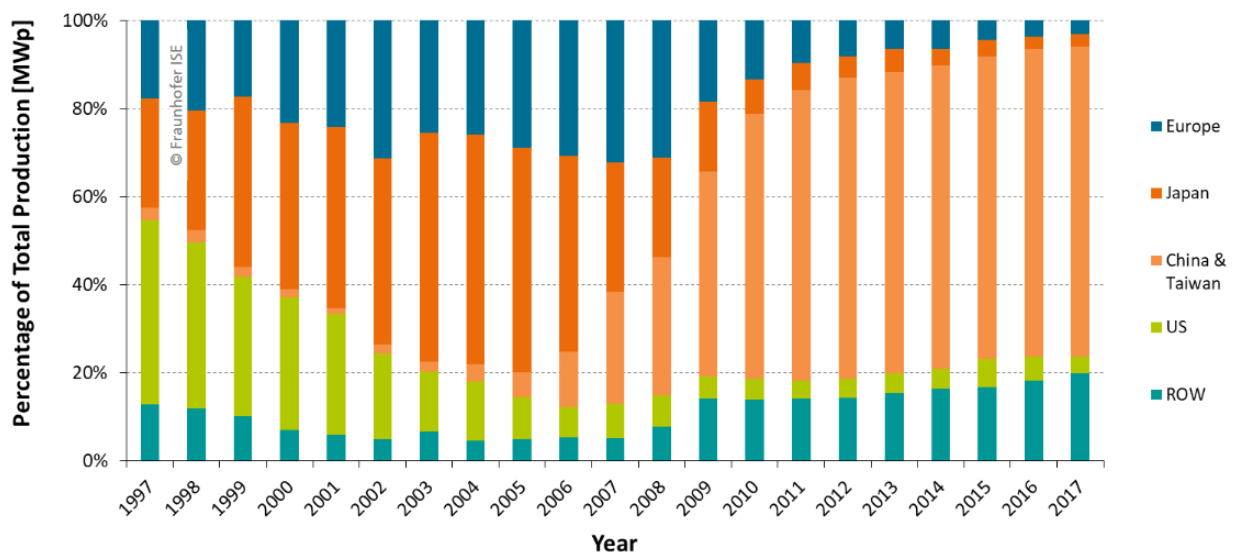


Figure 1 PV Module Production by Region 1997-2017 Percentage of Total MWp Produced

Among all the possible alternatives to face such challenge, PV technologies emerge as one of the best and promising responses to the energy demands for several reasons. The most important reason relies on the amount of energy that the sun can provide. Solar radiation reaches a unit area near the Earth's orbit at a rate of 1,366 kWh/m² (kilowatt-hour per square meter) per year, as measured upon a normal surface (at a right angle) to the Sun, this value is consider as the "solar constant". To obtain this energy value, the atmosphere had already absorbed about 19% and clouds reflected a further 35% of the total solar energy. Therefore, the solar energy received at the sea level can variate; its peak power has insolation values ranging from 800 to 950 kWh/m² in Norway to up to 2,900 kWh/m² in Australia giving a generally accepted value of 1,020-1,366

W/m² as average. With this amount of energy⁷ the theoretical potential represents more energy striking the earth's surface in one and a half hours (480 EJ) than the worldwide energy consumption in the year (2001) from all sources combined (430 EJ). This theoretical potential could be used to generate 18 TW of carbon-neutral power from 10%-efficient solar-conversion systems covering only 0.17% of the earth's surface area (Figure 2).⁸

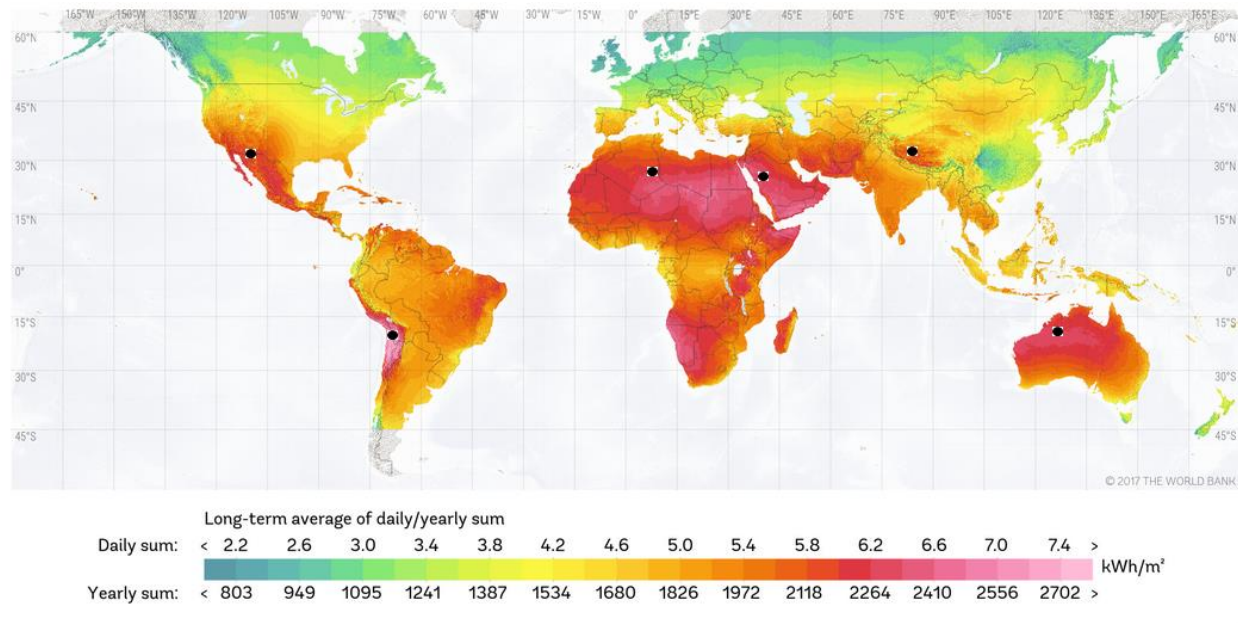


Figure 2 Average needed area to supply the world's total energy demand⁴

Nowadays the most spread and the best commercial option to produce electric energy directly from the sunlight is trough photovoltaic⁹ devices based on amorphous crystalline silicon panels whereas three companies broke the record of 25.6% efficiency or power conversion efficiency (PCE) for a silicon solar cell, being Panasonic's one the most efficient.⁴ Nevertheless, such technology is still in development phase and the cost is high for commercial purposes thus a big effort it is being done to expand the limits of PV using new materials and configurations that reduces the prices of this kind of technology having in mind a commercial expansion.

Most of commercial photovoltaics cells use crystalline silicon, making them expensive to manufacture and the process creates toxic by-products. However, an entirely different approach does exist using perovskites. Perovskites have a crystal structure of a tetrahedral arrangements of atoms and molecules, and depending of which elements are used they have different properties. Perovskite depending on their composition can be superconductive¹⁰, magnetoresistive¹¹ or photovoltaic¹².

A perovskite solar cell (PSC) is based on the crystal sensible to light called perovskite, from which they take their name. Perovskites are relatively cheap and easy to assemble and its photocurrent conversion efficiency has increased from 2-3% in 2009 to a 23.7% in 2018. The rapid progress of this technology makes of PSCs one of the most promising discoveries to help with the enormous humanity's energy demand.

Hybrid perovskite solar cells prototypes are constructed in a tandem architecture, like a sandwich disposition generally by three layers. Those layers are designed as electron transport layer (ETL), perovskite layer and hole transport layer (HTL) and the three of them are enclosed by their respective anode and cathode.

This work is focused on the design and development of materials that could stand as efficient hole transport materials (HTMs) for PSCs. A series of single molecules and oligomers/polymer based on the carbazole heterocycle are proposed as new alternative hole transport materials.

In this study, final molecules are fully characterized and the differences on the optoelectronic and thermal characteristics will be compared based on their substitution configuration between structural isomers or between monomer and the derived oligomer/polymer.

Chapter 1 is a brief resume on photovoltaics and state of the art of PSC. The introduction describes the most common composition and function of the different layers that constitute the photovoltaic device's layers. The introduction is followed by a review of several carbazole-based molecules used as HTM, in which are described and compared to lay the foundation of the present work.

Chapter 2 reports the synthesis of two series of new hole transport materials (HTMs). The presented molecules are composed by two diphenylamine(DPA) fragments linked to carbazole unit. From dibromo-carbazole as a starting material, synthesis is performed by a simple two-step synthetic procedure providing the target products in good yields. Two series of molecules designated as DMx and iDMx are obtained, positional isomers differentiated between each other by their substitution position 3,6-Cz (DMx) vs 2,7-Cz (iDMx) over the carbazole (Cz) core by the DPA groups. The molecules are examined along with thermal and optoelectronic characterization, film formation ability and further test on perovskite photovoltaic devices as well.

Chapter 3 is a detailed description of anionic and radical polymerization essays over the molecule called DM1, which bears an alkene polymerizable function. The resulted polymer DM1P, is fully

characterized and tested over PSC modules and compared with its origin monomer. The second part of Chapter 3, consist on the synthesis of a series of 3,6-carbazole linked conjugated oligomers, designated as PCzX series. With the present PCzX oligomers, we explore the possibility to use conjugated oligomers on PSC devices as an alternative to the actual small molecules. The synthetized oligomers are fully characterized and preliminary photovoltaic results are presented. Chapter 4 describes a series of bicarbazolyl (two carbazole heterocycles connected by N- atom to a benzene ring in para position) molecules (DM1X), conceived to test their oxidative coupling reactivity. This kind of coupling reaction can be potentially achievable with carbazole-based molecules under the right conditions. The present study pretends to compare the optoelectronic and thermal differences between monomers and the derived molecules.

1. State of the art: from the solar energy to the photovoltaic devices

1.1 Photovoltaic Overview

The term photovoltaic comes from conjunction “photo” which in Greek means light and “volt” the derived unit for electric potential difference named after the Italian physicist Alexandro Volta. Thus, photovoltaic defines those dispositives or technology that generates an electric potential from sunlight. Date back to 1839 when a French physicist Edmund Becquerel¹³ interested in phosphorescence and luminescence, chemical reactions caused by exposing certain substances to light, discovered in the 1840s that these reactions could generate an electric current in both, liquids and metals. Since then, many scientists seized upon the connection between light energy and chemical energy and research around this subject has led to the development of the photovoltaic cells.

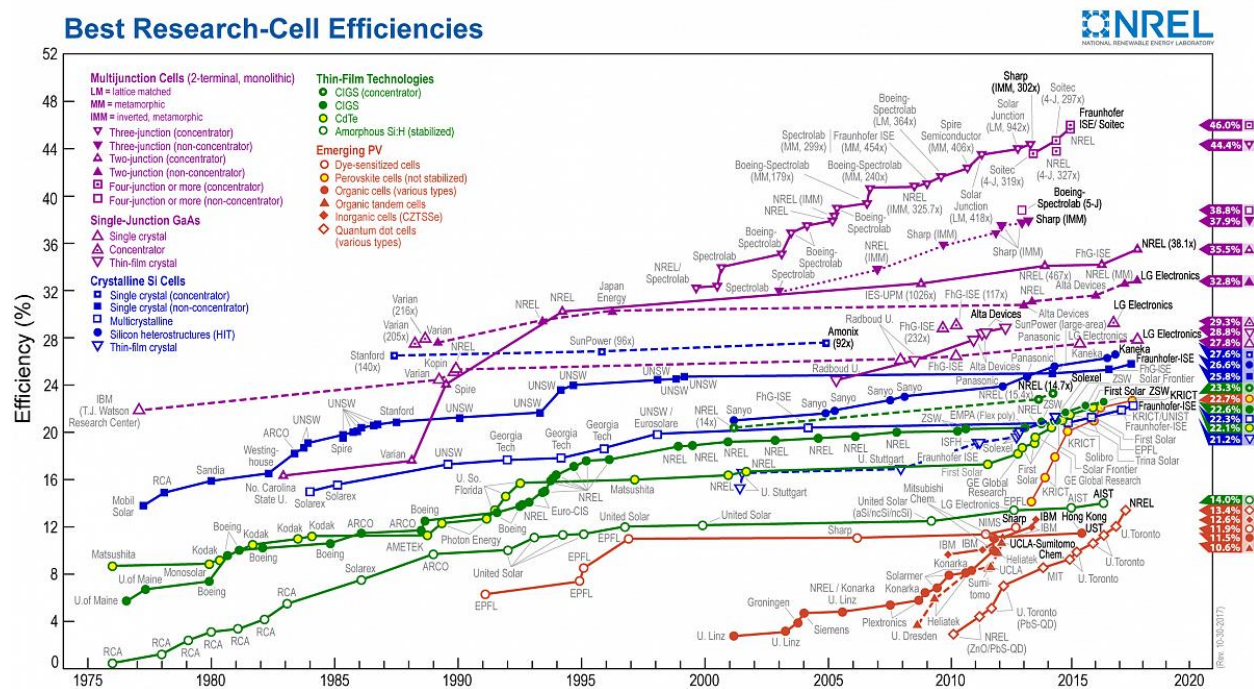


Figure 3 Efficiencies chart for photovoltaic technologies¹⁴

Solar cell efficiencies goes from 26%¹⁵ for amorphous silicon-based solar cells to 44.0% with multiple-junction concentrated photovoltaics. However, for commercial purposes energy conversion efficiencies with available photovoltaics are around 14–22%.

According to the National Renewable Energy Laboratory, which maintains a record of the progress and the best efficiencies evolution from 1976 to date (Figure 3), all PV technology is

classified in five different families depending on the semiconductor composition and junction number.

(1) Multijunction cell, (2) single-junction gallium arsenide cells, (3) crystalline silicon cells, (4) thin-film technologies and (5) emerging photovoltaics with some 26 different subcategories included in the total families.

Hybrid perovskite solar cells (PSCs) power conversion efficiency has rocketed to a greater than 20 percent in just only 4 years^{16–18}, putting PSCs in a very important place in the race for alternative energy production. Such improvement in short time encourage us to contribute on the research for better and reliable options to increase the efficiency and lifetime of PSCs.

The aim of this thesis

The great potential for PSCs and the rapid progress that has achieved the research in this field during the last eight years, positioning this technology as a reliable option for a large-scale industrial application in the a near future thanks to the combination of low cost, relatively simple manufacture and high efficiency factors. Thus, the aim of this thesis is to synthesize a new generation of organic carbazole-based hole transport materials with high mobility and conductivity that can be comparable with the standard Spiro-MeOTAD for their application on high performance PSCs. In this matter, we propose to synthesize carbazole based HTMs with polymerizable functions in order to obtain and compare the differences raising from monomer to polymer, related to its conductivity and stability. In other hand, we also study the differences of physical properties, depending on internal conjugation. Carbazole isomers bearing 3,6- and 2,7- position substitutions are synthesized and characterized to compare their final voltage output and the differences on the device's efficiency derived from internal conjugation changes. We want to understand the role of organic carbazole *p*-type HTMs and its properties based on their internal conjugation and functional moieties, in order to improve the design for the next generation of this basic component in hybrid PSC's architecture. Properties as photophysical, electrochemical, thermal and photovoltaic for these new synthesized molecules will be studied and compared.

1.2 State of the Art: emergent hybrid photovoltaics

The hybrid PV technology stands as one of the most promising alternatives to fulfill the actual global energy demand: the essential and needed requirements as a clean, low cost and sustainable energy source. Moreover, emergent PVs outlook as an environmental friendly option with sights to occupy an important place on worldwide energy production.

Unlike inorganic solar cells or silicon based photovoltaics, the use of single molecule or polymeric absorbers, carrier transports and electron acceptors is advantageous: all of them can be manufactured from low cost precursors and potentially relatively easy to synthesized. Is for this reason that emergent PVs are especially strong competitors for a commercial energy production. Nowadays, emergent hybrid photovoltaics begins to reach the same light to power efficiency (between 9 to 22% depending on the type) ^{12,19,20}. Moreover, an encouraging initial life time over 5000 hours among other different features like low cost solution processability (roll to roll manufacturing process²¹), low thermal production budget²², flexibility, allow us to consider the possibility to add them to already existing surfaces like windows and ceilings, etc. and more than anything, to open the possibility to take the process to an industrial scale for its distribution.²³ The following section is a brief summary of the history and evolution of organic photovoltaics since the beginning until what today are called hybrid perovskite solar cells.

1.2.1 Dye-sensitized solar cells

Dye-sensitized solar cells (DSSCs) can be considered as the first prototypes for a whole new generation of hybrid photovoltaic technology based on organic molecules and traditional semiconductor thin films as TiO₂. Significantly improved in 1991 by Brian O'Regan and Michael Grätzel²⁴, with a simple experiment, they settled down what would be the basic principle for all the up-coming PV technologies.

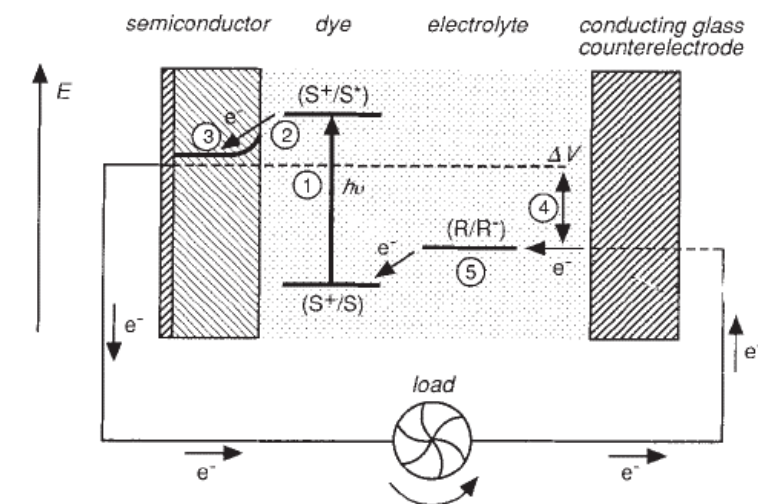


Figure 4 Representation of energy levels and functioning for the DSSC using a liquid electrolyte phase²⁴.

With a liquid redox electrolyte based on the I^-/I_3^- couple as carrier phase transport, a ruthenium bipyridine dye-sensitizer molecule as light harvesting material and porous TiO_2 semiconductor layer as n-type semiconductor. This device configuration reach both an incredible 7.1 - 7.9 % energy conversion yield and a great stability (five million turnovers without decomposition) for a two month space under simulated sunlight with AM1.5 spectral distribution. With a 10 μm thickness, this new prototype represented a great alternative for electricity generation from the existing commercial devices competing in cost, size and relatively easy manufacture. That evolution has continued progressively since then with a certified efficiency now over 14 %²⁵. Nevertheless DSSCs almost reached their theoretical limit efficiency and moreover their life-time is not long enough for nowadays market demands. Still DSSCs are a very important relative member on the development of PV family.

Regarding to its architecture, DSSC's electron transport layer usually consist in a deposited/printed TiO_2 layer over a FTO, ITO conductive glass electrode with around 10 μm thickness, depending on the used technique. Other metal oxides like ZnO , $SrTiO_3$, SnO_2 ²⁶, have been used as electron transport layer but still, the most common choice is TiO_2 due to the availability, low cost, UV light resistance, good conductivity, etc²⁷.

In relation to the sensitizers, the materials used to absorb the sunlight, the most desired features for them are the low cost manufacture, high molar absorptivity and long term stability. Improvement of prototype's stability is one of biggest challenges regarding this technology,

because due to the light induced oxidation, dye-sensitizers tend to degrade under the sunlight and consequently have short-life times. Most of them are based²⁸ in organic small molecules or organic coordination complexes with a transition metal atom center like ruthenium. The common characteristics on them are the redox reversibility, electron rich full conjugated molecules and high molar extinction coefficient.

The electrolyte is also a crucial component and at the same time the most controversial, of the DSSC²⁹, which consist in a redox couple and additives dissolved in a liquid solvent. The electrolyte assumes the task of carrier transport and dye regeneration between the working electrodes (WEs) and counter electrodes (CEs)³⁰. At the same time is the major drawback for DSSC due to its liquid nature and leaks derived from it. It is important to note that DSSC found a very important variation in a full solid-state dye sensitized solar cell (sDSSC)³¹ dispensing from the liquid electrolyte. In this way a full solid-state device, lay the foundations of what will be the future generation of hybrid perovskite solar cells.

1.2.2 Perovskite solar cell

Named after the Russian mineralogist Lev Perovski, perovskite crystal structure is identified in 1945 from X-ray diffraction giving the corresponding formula, ABX_3 where halide perovskite is described with A = monovalent cation, B = divalent cation and X = halogen anion. In 1978, a new combination of perovskite material is discovered by using an organic cation (methyammonium, etc) leading to the organic-inorganic hybrid lead halide perovskite. The newly hybrid perovskite displays a variation in coloration in function of the halogen anion chloride, bromine and iodide, going from orange to black and some coloration in the middle that indicates a change on energy gap values.³²

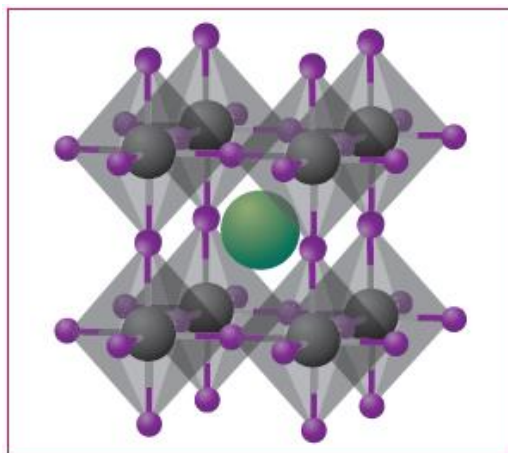


Figure 5 Representation of perovskite's crystal structure with the generic chemical formula ABX_3 . where A (green) corresponds to an organic cation, B (grey) metal dication and X (purple) the halogen.³³

It was observed that these colored materials also presented superconductivity¹⁰ and ferroelectricity³⁴ leading the attention around these materials into other areas. Methyl ammonium lead iodide perovskite has been extensively investigated due to its interesting optical and electronic properties. It is a semiconductor material with a wide absorption range that starts from visible and near infrared domain with 780 nm light absorption onset corresponding to a HOMO energy level of -5.43 eV and a band gap of 1.5 eV which makes of this material a good light absorber³⁵. The material exhibits high carrier mobilities for holes ($12.5 \text{ cm}^2 \text{ V}^{-1} \text{ s}^{-1}$ - $66 \text{ cm}^2 \text{ V}^{-1} \text{ s}^{-1}$)³⁶ and for electrons ($7.5 \text{ cm}^2 \text{ V}^{-1} \text{ s}^{-1}$)³⁷ which allows to be carried each other apart before they recombine. Therefore, despite of being a good light absorbance they didn't attract the attention for PV purposes until 2009³⁸ when Miyasaka *et al.* reported for very first time that $\text{CH}_3\text{NH}_3\text{PbX}_3$ (X = I and Br) perovskite materials showed a high light absorbance when used as sensitizers in a liquid electrolyte. In this PV cell, the bromide perovskite was deposited on nanocrystalline TiO_2 and displayed a power conversion efficiency (PCE) of 3.1%. However, this work was not cited for two years, probably due to problems reproducing the recipe and derived problems related to stability. In 2011, Park *et al.*³⁹ reported a higher PCE of 6.5% using $\text{CH}_3\text{NH}_3\text{PbI}_3$ and optimizing the coating solution concentration, the TiO_2 film thickness and electrolyte formulation. This work demonstrated the potential of organic lead halide perovskites as photovoltaic materials. Nevertheless, these photovoltaic devices were susceptible to fast degradation due to a rapid dissolution of perovskite in polar electrolyte solutions. In 2012 the

stability problem was solved by replacing the liquid electrolyte with a solid hole-transport material, leading to the first functional hybrid perovskite solar cell with an efficiency of 9.7%⁴⁰ and 12%⁴¹. These wonderful discovered properties and the solid state of the perovskite device for photovoltaic applications continue its fast rising development during the next 5 years.

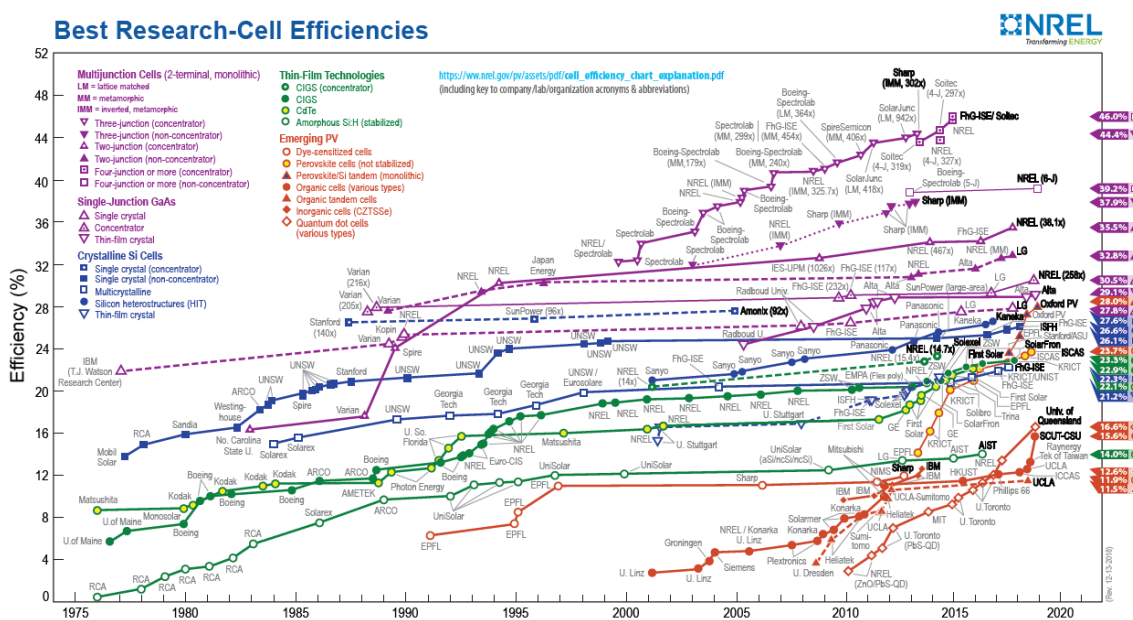


Figure 6 Progress of perovskite solar cell efficiency chart. A PCE of 3.8% in 2009 was improved to 23.7% in 2018 by Prof Park et al.⁴² The PCE highlighted with the red circle is certified by an independent accredited test center.⁴³

By the absorption of one photon at a determinate wavelength, one electron is promoted from the highest occupy molecular orbital (HOMO) into the lowest unoccupied molecular orbital (LUMO). The absence of the electron leaves behind a free space with a positive charge denominated hole.

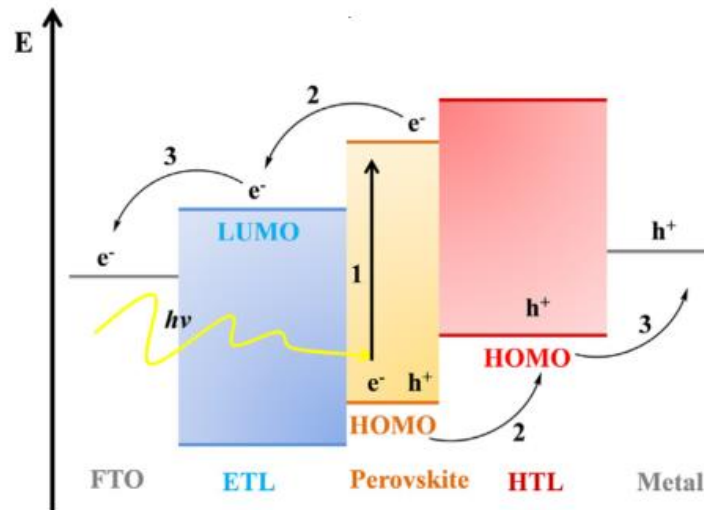


Figure 7 Band diagram and PSC: 1 Absorption of photon and free charges generation; 2 Charge transport; 3 Charge extraction.

The event of light absorption and charge separation occurs on the perovskite layer with an energy bandgap of 1.55 eV for the traditional methylammonium lead triiodide (MAPI), energy equivalent to 800 nm or near infrared wavelength. For the efficient generation of free electrons and holes, the consideration of some layer intrinsic factors are crucial.

Table 1 Main parameters for MAPI perovskite⁴⁴

Parameter	PSCs MAPbI ₃
Bandgap	1.55 eV
Exciton binding energy	<0.05 eV
Electron mobility	2-10 cm ² V ⁻¹ s ⁻¹
Hole mobility	5-12 cm ² V ⁻¹ s ⁻¹

Numerous researches have studied the perovskite layer and its performance by modifying different parameter as layer thickness⁴⁵ and morphology (planar or mesoporous)⁴⁶, grain size⁴⁷, composition and mixture of different halogens⁴⁸ and cations⁴⁹, etc.

The later studies suggest that the balance between the last mention (thickness, perovskite composition, etc.) parameters have to be optimized in order to achieve the optimal carrier diffusion and consequently the better performance.

Perovskite MAPI low charge recombination and long carrier lifetime rates⁵⁰ are one of the main keys for an efficient generation of free electrons. Give the proper conditions for a suitable charge diffusion by designing appropriate ETLs and HTLs is essential to avoid charge recombination and derived low performance. Thus MAPI provides ambipolar transport (values of electron and hole generation and carrier are quite close), ideally on layer with a thickness around 200 - 500 nm⁴⁵. However, some researches have extend the limits for both, electron diffusion length and hole diffusion length in perovskite layers exceeding 1 μm ^{51,52}. If the later can be considered as a limitation for PSCs, such thickness and carrier diffusion values are still quite superior to traditional organic solar cells (thickness = 50 - 100 nm, electron mobility $2 \times 10^{-3} \text{ cm}^2\text{V}^{-1}\text{s}^{-1}$ hole mobility = $1 \times 10^{-4} \text{ cm}^2\text{V}^{-1}\text{s}^{-1}$)⁴⁴, placing PSCs in a very important place on the race for PVs.

Nowadays long-term stability is one of the major concerns around PSC that impedes this technology's commercialization. The long-term device stability is the most pressing drawback, given the achieved 23.7% efficiency PCE^{53,54} PSCs are not a useful technology with such short-life time spans.

The perovskite light absorbing material is widely studied for being susceptible to degradation under ambient conditions like atmospheric oxygen, ultraviolet light exhaustion and environmental moisture^{19,55-58}. Hence different research groups have demonstrated that such problems can be overcome by a proper manufacture of the different interface layer stacks and adequate encapsulation. Without cell encapsulation, the stability can be up to 1000 hours of continuous operation, proving that a long term decay that leads to a durable device performance can be realistic.⁵⁴

The evolution of PSC device different structures is shown in Figure 8. Diverse architectures have been developed, ranging from the dye-sensitized TiO_2 structure to the p-i-n junction structure, consisting in a three doped regions. Like a natural evolution from dye sensitized solar cells (DSSC), the first PSC was designed under that concept, using perovskite as a dye sensitizer deposited over TiO_2 in form of nano-dots Figure 8 (a). Afterwards, due to the capacity of perovskite to transport electrons, it can be used as a bifunctional material, as light harvester and *n*-type semiconductor. In order to profit of this bifunctional perovskite capacity, the TiO_2 electron transport layer is

removed and substituted by Al_2O_3 Figure 8 (b). In a sort of insulating scaffold, Al_2O_3 is covered with thin layer of perovskite.⁵⁹ Based on this fact, the perovskite was used to completely fill the pores over the Al_2O_3 film instead of the common titanium dioxide. In this configuration, the electron carrier function was performed by the same perovskite. Even when the perovskite has the capacity to be an electron carrier, the Al_2O_3 scaffold configuration makes evident the importance of the electron transport layer. Eventually, devices manufacture lead to depositing a thin layer of perovskite directly over a mesoscopic (high surface area) layer of TiO_2 , thick enough to act as a conduction band, creating then, the most used structure known as the mesoscopic perovskite solar cell (Figure 8 (c)). The mesoscopic contact layer consist of two different layers with morphologies. The TiO_2 mesoscopic with a big surface area and in contact with the perovskite layer and a bulk thin film designated as blocking layer (bl).^{60,61} Some researches have chosen to remove the mesoscopic layer with good results in what is called the planar heterojunction⁴⁶ (Figure 8(d)). Such structure, consisted on a perovskite layer deposited between a compact TiO_2 layer as electron-acceptor and a hole transport material ⁶² what is so called the sandwich planar heterojunction configuration. Finally, the latest variation for perovskite solar cell architecture is called inverted configuration. Figure 8(e) illustrates the inverted configuration layout, similar to organic photovoltaics device. In this configuration the perovskite layer is sandwiched between the transparent conductive electrode in one part and in other part the metal electrode with an electron collecting material, commonly used as C_{60} -butyric acid methyl ester (PCBM)^{61,63,64}.

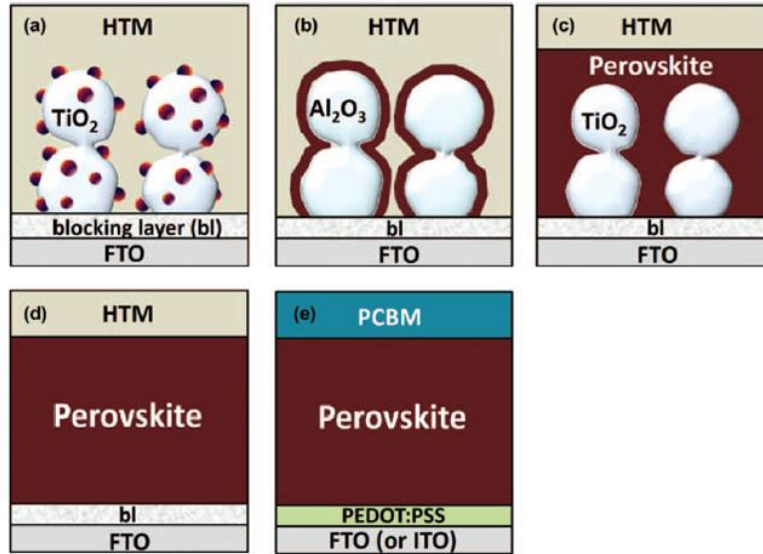


Figure 8 Different types of perovskite solar cell structures. (a) TiO_2 PV sensitized (b) Al_2O_3 PV super-structured, (c) mesoscopic TiO_2 structure with PV capping layer, (d) planar PV heterojunction and (e) inverted disposition.⁶⁵

1.3 Device Architecture and Perovskite Solar Cells (PSCs)

1.3.1 Perovskite solar cell configuration

Basically the device configuration, depends on role of the bottom and top electrodes. In section 1.2.2 five different configurations⁶⁶ are presented: mesoporous-conductive scaffold; mesoporous-insulating oxide; planar; HTM-free and inverted configurations. All configurations present different advantages and are adapted to the other components of the final device. Up to now, the most common used configuration due to easy manipulation, deposition techniques and high efficiencies are the mesoporous with a 21.6%⁶⁷ and planar with a 20.7%⁶⁸ photocurrent conversion efficiency (certified PCE). For our matter, a mesoporous configuration will be consider for this work.

1.3.2 Mesoporous electron transport layer

Mesoporous PSC, the most studied and used architecture, is a very successful option due to its simple fabrication. The use of mesoporous TiO_2 has different advantages like wide band

gap energy (3.2 eV), high chemical and thermal stabilities, photo stability, non-toxic and low cost⁶⁹.

Snaith *et al.*⁷⁰ demonstrated that a TiO₂ mesoporous electron transport layer with thickness between 260 nm and 440 nm was enough to fulfill⁷¹ the optimum balance between the maximum light absorption by the perovskite and minimum recombination caused by a long path length (Figure 9).

Afterwards, Saliba *et al.*⁴⁹, modified the composition of the perovskite material reaching good results using a quadruple cation perovskite composition (rubidium/cesium/methylammonium/formamidinium) combined with Poly-tryarilamine (PTAA) HTM (Figure 11) and mesoporous TiO₂ as conductive layer reaching a stabilized PCE of 21.6%. Moreover, the device retained 95% of its initial power conversion efficiency after a strong conditions aging protocol at 85°C for 500 h under full solar illumination. The last mentioned research demonstrated that, the stabilization of the perovskite layer by the addition of combination of different cations was enough to extend the device lifetime, by only modifying the perovskite layer and using the well-known mesoporous TiO₂ structure.

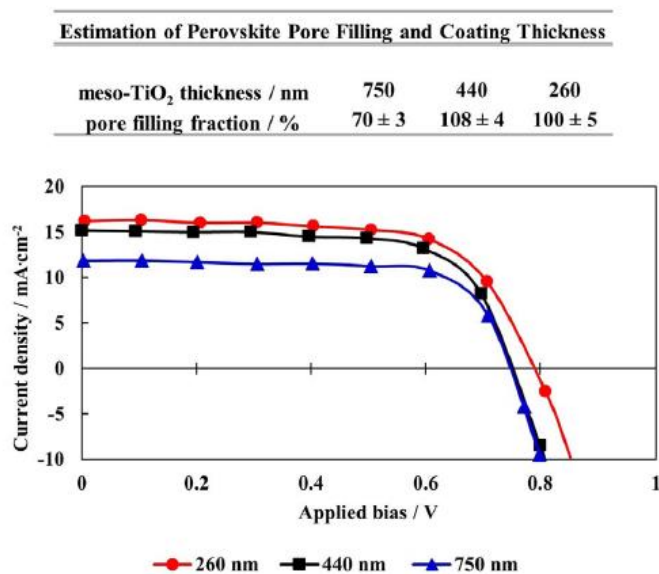


Figure 9 PSC J-V curves for different pore filling and coating thickness⁷¹.

1.3.3 Mesoporous insulating PSC

Another interesting PSC configuration based on the mesoporous structure, was discovered by replacing titanium dioxide electron transport layer by an Al_2O_3 insulating scaffold⁷². In this case, the perovskite layer, the light harvester, fulfill the double function of electron and hole transporter, represented on the Figure 10.

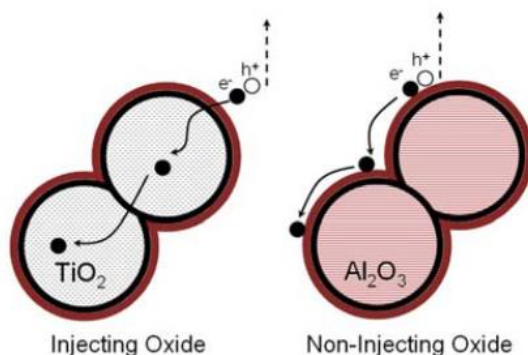


Figure 10 Electron transfer and transport in a mesoporous TiO_2 , (left) and a Al_2O_3 scaffold perovskite solar cell, (right).⁵⁹

Comparisons showed that the use of MAPbI_2Cl and TiO_2 mesoporous layer give a PCE = 8% against TiO_2 with the Al_2O_3 as insulating scaffold, the PCE is improved to 11%^{59,73}. Added to this, was discovered that Al_2O_3 was more stable, under same conditions as TiO_2 , because Al_2O_3 based devices aged slowly under UV light, due to the light-induced desorption of surface-adsorbed oxygen. Leijtens *et al.*⁷² showed stable photocurrent over 1000 h continuous exposure and operation under full spectrum simulated sunlight.

Using this configuration, with alumina layer thickness of 400 nm, PCE value was improved as high as 15.9% ($V_{oc} = 1.02$ V; $FF = 0.71$; $J_{sc} = 21.5$ mA cm^{-2})⁷⁴.

Results⁷⁵ showed that Al_2O_3 reduces the effective carrier path allowing electrons to be carried on straight injection path over the insulating Al_2O_3 scaffold, avoiding grain boundaries that create isolated charged areas that promote the hysteretic behavior (different values in reverse/forward scans) in TiO_2 mesoporous layers.

Generally, research has demonstrated that different synthetic routes for the mesoporous TiO_2 layer lead to substantial differences in the solar-to-energy conversion efficiency for this PSCs. Thus, even when the electron transfer process at some point was considered less efficient with

mesoporous TiO_2 , due to the high current achieved with Al_2O_3 scaffold.⁷⁶ The last mentioned studies helped to understand and improve the TiO_2 mesoporous configuration leaving the use of Al_2O_3 practically in disuse to give place for the mesoporous use of TiO_2 .

1.3.4 Planar PSC

This architecture type is the simplest among the different PSC configurations and was specially used to understand the mechanism on charge separation and transport between layers due to the large heterogeneous phase contact and avoiding the mesoporous infiltration problems⁷⁷. Another advantage for this method is that no high temperature treatment is needed like those required to form mesoporous TiO_2 and consequently allowing the use of flexible substrates with low temperature solution processed planar-structure perovskite solar cells. Concerning their performances, in the beginning, power conversions for planar PSC were lower than their high temperature process mesoporous counterparts. Nowadays, planar architecture PSC have become a real competitor on the map. Planar PSC exhibits lower efficiency but at the same time low hysteretic response. Research based on planar architecture reported a big success ($\text{PCE} = 19.9\%$)⁷⁸ in suppressing hysteresis and record efficiency for planar devices using tin oxide (SnO_2) electron-transport layer has increased since then.⁷⁹

Jiang *et al.*⁸⁰ found that a moderate residual of PbI_2 can deliver stable and high efficiency of solar cells without hysteresis, while too much residual PbI_2 will lead to serious hysteresis and poor transit stability. Solar cells with the efficiencies of 21.6% in small size (0.07 cm^2) and 20.1% in large size (1 cm^2) were obtained. The certificated efficiency for small size shows the efficiency of 20.9%, which is the highest efficiency ever recorded in planar-structure perovskite solar cells until 2016.

By using ZnO nanoparticles Kelly *et al.*⁸¹ made improvements on device performance for cells prepared on rigid substrates. Then the process was migrated to a flexible substrate Polyethylene terephthalate (PET). Based on this architecture ($\text{ITO}/\text{ZnO}/\text{CH}_3\text{NH}_3\text{PbI}_3/\text{Spiro-OMeTAD}/\text{Ag}$) power efficiencies as high as 15.7% were obtained which makes them some of the highest-performing perovskite solar cells of this type reported to date with a total thickness of around $1 \mu\text{m}$ without considering the PET substrate.

Planar PSCs represents the possibility to produce a flexible devices at large scale thanks to its potential for roll-to-roll manufacture that can allow their commercialization.⁸¹

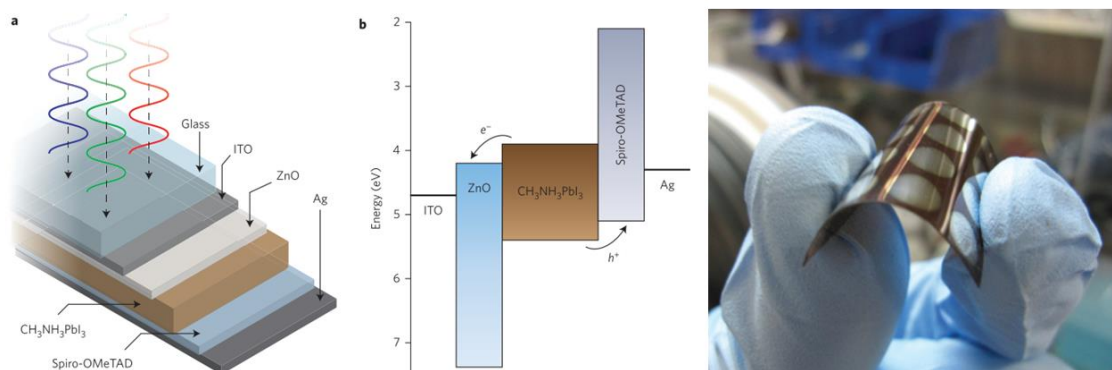


Figure 11 Architecture and energy levels of planar structure PSC and its flexible prototype⁸¹

1.3.5 HTM-free PSC

As mentioned before, perovskite by itself can play the double role of electron-hole transporter. Aiming to simplify the PSC structure some researchers essayed to dispense of the HTM layer by directly depositing the back contact electrode into the perovskite layer. The first HTM-free PSC reported by Etgar *et al.*⁸² consisted of a mesoporous TiO₂ layer loaded with MAPbI₃ perovskite. The cell prototype presented a PCE of 5.5% (Figure 12)⁸².

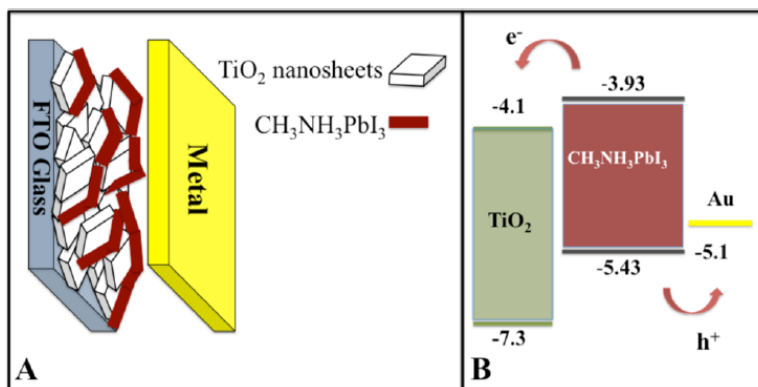


Figure 12 (A) Scheme of the HTM free PSC device structure. (B) Energy level diagram of the CH₃NH₃PbI₃/TiO₂ solar cell⁸².

Some difficulties may arise from this configuration like short-circuit between the back contact electrode and the electron transport layer. To solve this problem, May *et al.*⁸³ inserted an

insulating scaffold between the perovskite layer and the ETL, combining then what could be the mesoporous insulating and HTM-free PSCs architectures achieving a certified power conversion efficiency of 12.8%. Moreover, the obtained device was stable for >1000 hours in ambient air under full sunlight. Perovskite layer was deposited by drop-casting from a PbI_2 , methylammonium iodide (MAI) and 5-ammoniumvaleric acid (5-AVA) iodide solution through a porous carbon film, displacing the expensive Au cathode back contact. The last mention research attains to solve two different problems. Leave aside the use of the two most expensive components of PSCs, the HTM and gold cathode.

Designed and reported for the first time in 2013 by Jeng *et al.*⁸⁴, inverted PSC configuration. It was constituted over ITO substrate followed by the deposition of poly(3,4-ethylenedioxythiophene) poly(styrene-sulfonate) (PEDOT:PSS) as hole transport layer/cathode, perovskite/fullerene (C₆₀) bilayer structure as the active layer and thin bathocuproine (BCP) film as an exciton- or hole-blocking layer (EBL or HBL), and an aluminum (Al) anode. The resulting cell demonstrated very promising photovoltaic performance of 3.9% PCE after optimization (Figure 13).

Figure 13 (a) Inverted configuration architecture (b) Scheme of the energy levels of each layer in the device⁸⁴

the inorganic and the polymeric organic options. For the inorganic inverted PSC some research uses heavily p-doped $\text{Ni}_x\text{Mg}_{1-x}\text{O}$ and n-doped TiO_x contacts. Those are the most common studied materials, but other oxide metals represent a viable option like V_2O_5 or SnO_2 or CuSCN . The best power conversion efficiency for inverted configuration was reported by Zhu *et al.*⁸⁵, displaying 18.8% and retained 90% of its initial PCE after 30 days stored in a 70% relative humidity environment.

On the organic molecules side, for inverted configuration PSC, polymers emerge as a class of macromolecular conductors (like PTAA, PffBT4T-2OD) that are composed by conjugated⁸⁶ or non-conjugated polymers. Zheng *et al.*⁸⁷ develop a polymer Figure 14 with stable open-shell (unpaired electrons) chemical functionalities on the pendant groups of the polymer. The radical non-conjugated polymer put aside the use of doping agents. Moreover, radical electrons reduce interfacial charge recombination and improve the crystallization of perovskite hybrids that are casted on the top of the hole transport layer (HTL). As a result, the stable PSCs incorporated with poly(2,2,6,6-tetramethylpiperidinyloxy-4-yl methacrylate)-co-(4-benzoylphenyl methacrylate) (PTMA-BP) exhibit a 15% power conversion efficiency, which is slightly higher than the same device without PTMA-BP layer in Figure 14.

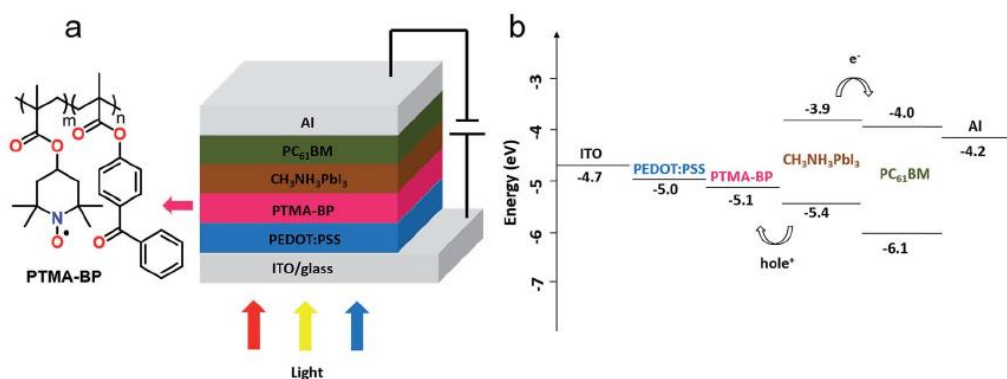


Figure 14 (a) Molecular structure of PTMA-BP and the inverted PSC configuration. (b) HOMO-LUMO of the device components⁸⁷

Another interesting solution due to its simplicity is presented by Xiao *et al.*⁸⁸ where polyaniline (PANI) with brachyplast (arm, branch) structure is synthesized and deposited by using a two-step cyclic voltammetry (CV) into the fluorinated tin oxide (FTO) glass substrate. The polymer acts as the sensitizer and HTM for the perovskite sensitized solar. The PSC based on the PANI delivers a photovoltaic conversion efficiency of 7.34%, and reduces from 7.34% to 6.71% after 1000 h,

thereby 91.42% of the energy conversion efficiency is kept, indicating a good long-term stability of the device.

Different research groups like those above mention, working on the inverted configuration have attained remarkable PCE results. Still, some challenges need to be resolved before inverted configuration before be a true competitor on the PSC scene.

1.4 Device components: Semiconductor TiO₂ layer as dense ETL layer

The semiconductor layer or electron transport layer (ETL) has the important role of accepting the promoted electrons from perovskite light collecting material.

One of the main advantages of working with TiO₂ is that can be processed at atmospheric conditions without any problem. Several different techniques are used to deposit TiO₂. The most common and efficient methods to deposit a TiO₂ layer consist on the traditional and most used spin-coating (SC-TiO₂)⁸⁹, atomic layer deposition (ALD)⁹⁰ and thermal oxidation method (TO-TiO₂)⁹¹. The above mentioned, not only represent the most efficient deposition techniques in terms of current and voltage output, but also those represent the most efficient in terms of current and voltage output. Moreover, ALD and TO methods have the potential to be scaled up, for an industrial process. Here are briefly described the different deposition method for a matter of comparison.

The traditional SC-TiO₂ method uses acidic ethanol solution of titanium(IV) isopropoxide, spin-coated at 3000 rpm for 30 s, followed by annealing at 500 °C for 2 hours. Thermal oxidation method, electro deposits a thin layer of titanium metal in order to be oxidized by thermal means in a rich oxygen atmosphere to obtain a TiO₂ compact layer (5-15nm).

ALD TiO₂ is deposited in an atomic layer deposition system using Tetra(dimethylamino) titanium and H₂O were used as precursors to react at 80 °C. After the deposition, the ALD coated films are sintered at 500 °C for 2 hours. This technique allows to form a functional mesoporous thin film (5-20 nm).

The three methods present some differences that are summarized in the Table 2. At laboratory scale, spin-coating deposition of TiO₂ layer is the best and most simple way to achieve good performance. The present revision helps to visualize the differences between the three most

common and efficient deposition methods and their efficiencies in function of the layer thickness. Thermal oxidation method has one of the best J_{sc} (22.0 mA cm^{-2}) and V_{oc} (1.09 V) compared to SC-TiO₂ J_{sc} (22.0 mA cm^{-2}) and V_{oc} (1.09 V) but is much 5 times thinner than the SC-TiO₂. In other hand, the atomic deposition layer can have smaller thickness values than SC-TiO₂ and TO-TiO₂, being one of the thinner options for layer deposition.

Table 2 Photovoltaic Parameters of PCS with different dense TiO₂ layer thickness and deposition method, Spin-coated (SC) Thermal-oxidation (TO)⁹¹ and Atomic layer deposition (ALD)⁹²

ETL thickness TiO ₂	V_{oc} (V)	J_{sc} (mA cm^{-2})	FF	PCE (%)
60 nm SC	1.09	21.16	0.58	13.47
15 nm TO	1.09	21.97	0.63	15.07
10 nm ALD	0.98	21.8	0.57	13.6

1.5 Device components: Mesoporous ETL layer and interface with Perovskite material

As it has been addressed before, the metal oxide should provide mesoporous structure for perovskite contact and suits a bandgap edge levels adjusted with respect to the MAPI energy levels. The generation of voltage mainly depends up on the appropriate match of both materials energy band levels.

The widely studied titanium dioxide has a long history as a semiconductor material in many different applications. Besides its optical and semi-conducting properties, TiO₂ material is highly abundant, easy to handle and manipulate and nontoxic for environment. Other metal oxides can also be used like ZnO⁹³, Al₂O₃⁹⁴, SnO₂⁸⁵ pure or as a scaffold. Several research groups have test them and concluded that most of the time their efficiency is low compared to TiO₂. Ascribed to the less mesoporous structure in general they present low electron mobility. In addition, an appropriate internal network structure is important to achieve high charge collection efficiency and higher electron carrier ability. The different energy levels for several ETL materials are shown in Figure 15.

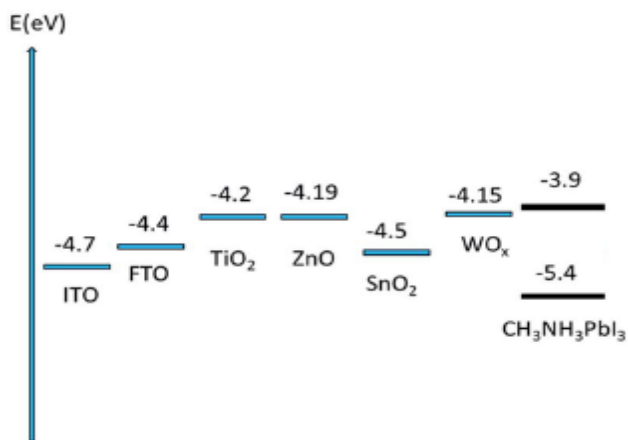


Figure 15 LUMO energy level diagram of various metallic oxide ETLs⁹⁵.

Synthesized TiO₂-based materials have distinct structural and geometrical features. Mesoporous TiO₂ represent an important part in the architecture of a PSC device in both fundamental and applied materials research. A big discussion around the TiO₂ mesoporous role on the device efficiency and performance is on the table but until now there is not a conclusive answer to this matter but the fact is that in general the mesoporous structure has better performance than a planar ETL-perovskite interface^{96,97}. The difference between mesoporous and planar PSCs are in part due to the different crystallinity of the perovskite layer when deposited on top of the porous or flat layer.⁴⁶ However, there are clear differences even when the morphology of the perovskite layer, including the grain size distribution and pinholes density, is comparable between the two architectures⁶⁸.

Hence, Snaith *et al.*⁹⁸ noted that "solar cells made with thinner TiO₂ layers completely covered by a perovskite layer benefit from an improved charge collection efficiency".

Seems to be that the perovskite coverage by the electron transport layer plays a fundamental role on electron transport in order to avoid charge recombination. Figure 16 exemplifies the above mention. Studies have found that TiO₂ thickness between 750 to 260 nm do not change the photocurrent but rather improve the charge collection.

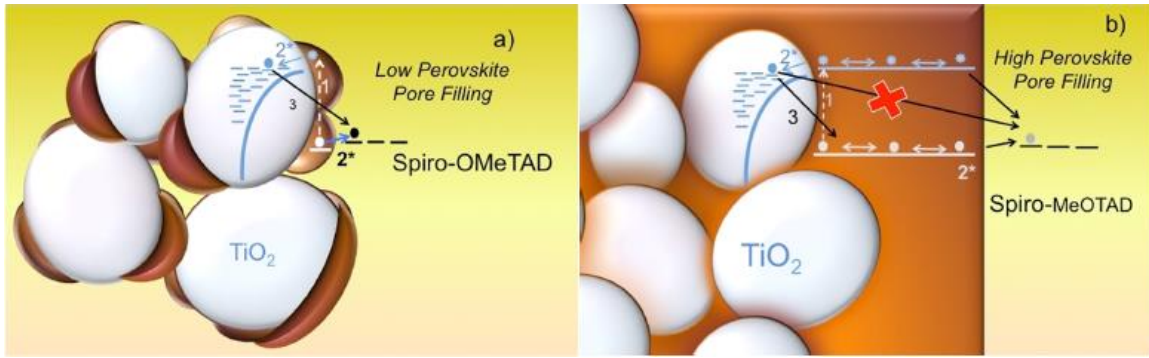


Figure 16 Leijtens et al. “Proposed Recombination Mechanism for Solar Cells with Incomplete (a) and complete (b) Perovskite Pore filling fractions. Step 1 (white arrow) stands for photo excitation of the perovskite absorber, step 2 (light blue arrow) to electron injection into TiO_2 and hole transfer to the HTM, while step 3 (black arrow) represents the recombination pathways”⁷⁰.

The improvement in device performance can be attributed to the enhanced charge collection over the large mesoporous area. Efficiency improved by charge transport in the mesoporous TiO_2 layer.⁹⁹

Carrier transport ability and photovoltaic performance of photovoltaic cells based on spin coated deposition of mesoporous TiO_2 layer are one of the best-known and laboratory-friendly techniques used so far. The photovoltaic cells used for this thesis work are based in mesoporous TiO_2 layer.

1.6 Device components: Perovskite as active layer

As it was mention before, the name perovskite solar cell derives from the crystal structure ABX_3 called perovskite, which is the main component of the photovoltaic device. Perovskite acts as light absorber and free charge generator. The most studied form of the perovskite material for photovoltaic purposes consist in a structure composed by methylamonium lead trihalide with formula $\text{CH}_3\text{NH}_3\text{PbX}_3$ ($\text{X}=\text{F}, \text{Cl}, \text{Br}, \text{I}$). Nevertheless a combination of different halide ratios including Br and Cl has being largely studied^{70,100–102}. The main conclusion based on the halide substitution is that the band gap energy values can be tuned remains on the appropriate energy values and moreover, important contributions on charge transport can be obtained by these means.

A proved essential point concerns to the perovskite deposition or fabrication: different methods have been reported variant from one-step or sequential depositions. Like drop-casting or spray coating, combined with different synthetic strategies of solvent engineering or self-induced passivation for example. The above mentioned processes can have important contributions on the size crystal modification, which consequently can improve or decrease the final modules efficiency. Several studies are devoted to kinetics of nucleation and crystal growth of perovskite^{67,103–105}. Alternately the crystallinity and the film morphology can be controlled with additives in one-step or two-step spin-coating¹⁰³ method to improve devices performances. The two-step size-controllable procedure is schematically presented in Figure 17. First, the PbI_2 solution in dimethylformamide (DMF) is spin-coated on the mesoporous TiO_2 film and this is followed by the spin-coating addition of $\text{CH}_3\text{NH}_3\text{I}$ solution in isopropanol (IPA). To conclude the substrate is 100°C heated to form the black perovskite. As the scanning electron microscopy (SEM) images show, the smaller the concentration, the bigger the crystal size. It is remarkable also that is necessary to find the proper balance between crystal size and crystal packing, this is a consequence of large crystals are not closely packed on the substrate, which can lower the final device efficiency.

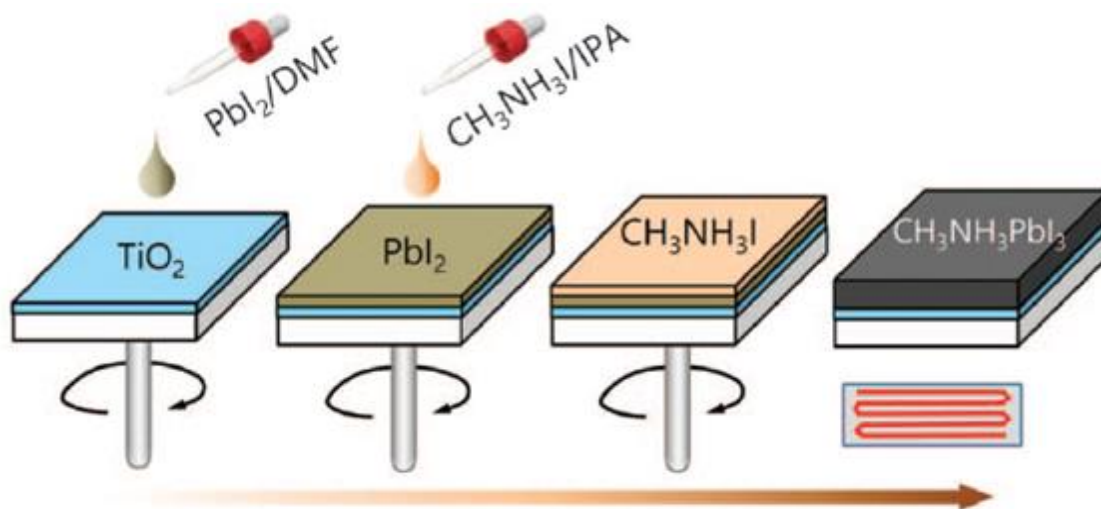


Figure 17 “ Two-step spin-coating procedure for $\text{CH}_3\text{NH}_3\text{PbI}_3$. A PbI_2 solution is spin-coated on the mesoporous TiO_2 film, dried at a temperature lower than 100°C for a few minutes, and then a $\text{CH}_3\text{NH}_3\text{I}$ solution is spin-coated. Finally, the film is heated at 100°C to form a black perovskite”¹⁰³.

One of the main argument against the use of perovskite materials in photovoltaic cells is the well-known toxic nature of lead which is potentially harmful for human environment ^{106,107}. That is why it is important to mention that significant research is done on lead-free PSC. Nevertheless, a candidate for lead substitution seems to be currently hard to find. The absorption of MAPbI₃ is notably 25 times higher than Si and yet better than GaAs^{108,109}. Moreover, this material offers a long-lived photogenerated electrons and holes, long charge diffusion length and good ambipolar transport.

Preliminary calculation studies have found that one of the potential candidates to replace lead in perovskite structure could be silicon on a mixed composition. The calculations solution gives for the perovskite mixture MACa_{0.125}Si_{0.875}I₃ an excellent absorption efficiency and suitable band gap value (1.54 eV) compared to MAPbI₃ ($E_g = 1.55$ eV)¹¹⁰.

The above mentioned studies are only one of the main currently researches done about this subject, but also elements like Cu, Ag, Au, In and Tl¹¹¹ are theoretically stable as potential metal cations. In other hand, a common element, sulfur,¹¹² as anion has been already used, the PCE of approximately 2.3%, further confirms its reliability conducted with unencapsulated cells at 85°C in air, under 40% average relative humidity in the dark. After 30-days of storage, the devices retained 91% of their initial PCEs.

It is worth to be mentioned that the immense combination with all elements from the first and second group¹¹³ on the periodic table as counter parts for the perovskite composition is possible. With some optimism is anticipated that lead containing perovskites will find a safe and environmentally friendly alternative¹¹⁴. But still this is a new research field by its own and is on developing phase through computer modeling and calculations. Thus for standardization and practical reasons during this work the use of lead perovskite MAPI will be the chosen material.

1.7 Device components: Hole transport material

The first achieved solid-state perovskite-based solar cells using Spiro-OMeTAD (2,2',7,7'-tetrakis-(N,N-di-p-methoxyphenylamine)-9,9'-bifluorene) as hole transport material (HTMs) was manufactured with mesoscopic TiO₂ and super-mesostructured Al₂O₃ support, reaching a PCE beyond 9%⁴⁰. As a progression from solid state dye-sensitized solar cells (DSSCs), the typical PSC is composed of a compact hole-blocking layer deposited on a transparent conductive oxide (TCO)

supporting layer, followed by a mesoporous metal oxide as the electron transport material (ETM). The perovskite is then filled on the mesoporous layer followed by the deposition of HTM in order to extract the holes selectively from the photoexcited perovskite layer.

Basically, the HTM can be classified in three different types depending on its composition: inorganic, organic small molecules and polymeric. The three of them present different features with advantages and disadvantages against the others.

1.7.1 Inorganic p-type HTM

Despite that the PCE records efficiencies are achieved with PSC using organic HTM as Spiro-OMeTAD or PTAA, poor stability and short life due to thermal stability, use of additives as lithium salts and *tert*-butylpyridine (*t*-BP) limits its large scale commercial application.¹¹⁵ Consequently research has leaned to application studies of inorganic HTM for perovskite solar cells. Recently, devices based mostly in Cu and Ni compounds as HTM have demonstrated to be good candidates and even delivered efficiencies close to its organic counterpart.¹¹⁶

Interest for inorganic materials like nickel oxide (NiO) is based on its availability. Inorganic HTM like some metal oxides or halogenates possess good thermal and chemical stability and a non-competitive wavelength absorption with the perovskite layer, complying with the requirements to be a good candidate. Moreover, inorganic HTM must have high hole mobility, a suitable band gap energy around -5.3 eV and a well-positioned conduction band. A material that meets all the last mention physical properties for its role as hole transport material (HTM) in a PSC device is the NiO. On the first essays using an inverted configuration and an inorganic HTL based on NiO_x nanosheets¹¹⁷ reached a PCE of 11.9 %. Nowadays inverted configuration devices based on NiO_x HTM reach efficiencies over 20%^{118,119}

Different inorganic molecules have also been tested like indium gallium selenide (IGS)¹²⁰, silicon based and copper complex, CuSCN¹²¹ (15.6% PCE) and CuI¹²² or Cu_xO¹²³ (19% PCE).

Recently, an exciting PCE of up to 20.4% was realized in regular PSCs through use of CuSCN as HTM and TiO₂ as ETM, which is comparable to 20.9% of spiro-MeOTAD HTM.¹²⁴ The addition of a conductive reduced graphene oxide spacer layer between CuSCN and gold allowed PSCs to retain >95% of their initial efficiency after aging at a maximum power point for 1000 hours under full solar intensity at 60°C.

All the latter inorganic HTMs suffer from some disadvantages related to solvent used in their deposition which partially degrades or dissolves the perovskite film compromising the device's stability ¹²⁵, nevertheless such issue can be solved by using an inverted configuration in some of the cases.

1.7.2 Organic small molecules as Hole Transport Materials

Spiro-OMeTAD (2,2',7,7'-Tetrakis[N,N-di-p-methoxyphenylamine]-9,9'-spirobifluorene), is currently the most used organic molecular HTM. However, since Spiro-OMeTAD possesses a relatively low charge carrier mobility, therefore doping is necessary to enhance the mobility. Oxygen doping using bis(trifluoromethane)sulfonimide lithium salt (LiTFSI) or chemical doping with cobalt complexes like tris(2-(1H-pyrazol-1-yl)-4-tertbutylpyridine)cobalt(III) bis(trifluoromethylsulphonyl) imide (FK209) are the most commonly used ways to increase the performance. A PCE of 20.9% was published by the group of Grätzel *et al.*¹²⁴ using Spiro-OMeTAD as hole transport, which was doped with a combination of LiTFSI and 4-*tert*-butylpyridine.

But what are the intrinsic properties that gives Spiro-OMeTAD its good performance as an HTM? Observing its structure can be noted that two N,N,N',N'-tetrakis(4-methoxyphenyl)-[1,1'-biphenyl]-4,4'-diamine groups attached by a sp³ carbon in a perpendicular way, this gives a fixed, rigid tridimensional structure which grants Spiro-OMeTAD its electrochemical properties. DFT calculations made using the hybrid (B3LYP and 6-31G) basis set in Gaussian, suggested that the bulky 3D structure resulting from the multidirectional arrangement of the MeO-DPA (methoxy diphenylamine) units, facilitates the intramolecular and intermolecular charge transport, while the π - π stacking between the molecules favors the intermolecular charge transport.¹²⁶

This was proved by Son *et al.*¹²⁷ who designed PCP-TPA (Figure 18) a 3D rigid structure that reaches the impressive PCE value of 17.8% against 15.4% for Spiro-OMeTAD. It has to be noted that this is one of the first examples of small organic molecule HTMs that found application in planar PSCs after Spiro-OMeTAD. This opens the road to understand the mechanism underplayed, not only by the internal conjugation of the molecule but for its spatial structure.

Despite of its excellent performance, one of the main drawbacks of PCP-TPA is its low synthetic yield, which only consist of two steps and has a final synthetic yield of less than 2%¹²⁸ making of it a very expensive and unlikely molecule to scale up its production.

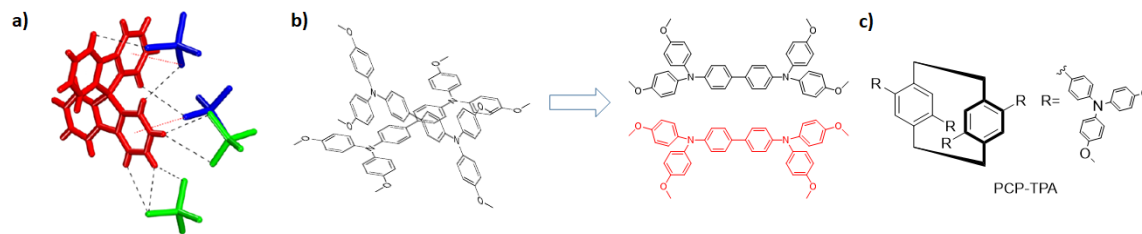


Figure 18 a) 9,9'-spirobi[9H-fluorene] X-ray structure¹²⁶ b) Schematic representation of Spiro-OMeTAD 3D structure, C) PCP-TPA structure.¹²⁷

Certainly, Spiro-OMeTAD is not the only HTM, a lot of research is being done around the development of new suitable option that can replace it. Some of the most representative and studied options bears core molecules as 3,4-ethylene-dioxythiophene (EDOT)¹²⁹, azomethine¹³⁰, thiophene¹³¹, acridine¹³², triphenylamine¹³³, azulenes¹³⁴, trizatruxenes¹³⁵, carbazole¹³⁶, etc., or the combination those. A good compilation of different HTM has been done by Grätzel et al¹³⁷ comparing the advantages of different molecules and analyzing the strategies for a better HTM design.

The basics principles to design a molecule which stands as a possible HTM are i) at least one intramolecular π -conjugated system, ii) an heterocycle that must include a N, S, O atom which works as a p-donor.

It was observed in the literature a trend to synthesize large π -conjugated molecules with cumbersome synthetic steps, failing in the demanding task for its wide scale application. Until now, most of the synthesized HTM molecules are characterized by a final coupling reaction between the core centers and two to four ending capping molecules. Usually capping molecules consist on 4,4'-methoxy-diphenylamine (DPA) or 4,4'-methoxy-triphenylamine (TPA) groups, where two, three or even four ending capping molecules are coupled to obtain the final molecule. It is well known that the higher the number of substitutions in a molecule, the lower the final yield.

High purity, UV-sensitivity, low hole mobility, and the risk of crystallization during heat stress are difficulties that make the search for a better performance HTM a holy grail that only few molecules can equal to the so called Spiro-OMeTAD standard.

A big part of this thesis is devoted to the development of organic small HTM, aiming for a reliable source of HTM. As is required for an ideal HTM molecules, the synthesized compounds must be transparent for most of the visible wavelength avoiding the screen effect and competition for the

exciton charge separation with the perovskite layer. Evidently the energy gap level must be appropriate towards the perovskite and consequently promote in this way a the hole extraction and also have good hole mobility ($>10^{-3} \text{ cm}^2\text{V}^{-1}\text{s}^{-1}$) to prevent charge recombination. Regarding to the physicochemical properties is required a relatively high temperature decomposition for an organic molecule and a glass transition temperature preferably above 100°C to avoid crystallization and finally an adequate solubility to properly fill the mesoscopic architecture.

1.8 Contact metallic layer

Concerning low cost manufacture, the use of noble metals as back contact electrodes as gold which is expensive and silver which is a little bit cheaper but not long term stable (due to iodine migration from perovskite layer to form AgI^{138}), are drawbacks for the PSC commercial use. In an effort to find a more reliable option as a back contact electrode some researchers have been given the task of mapping the behavior of different metals.

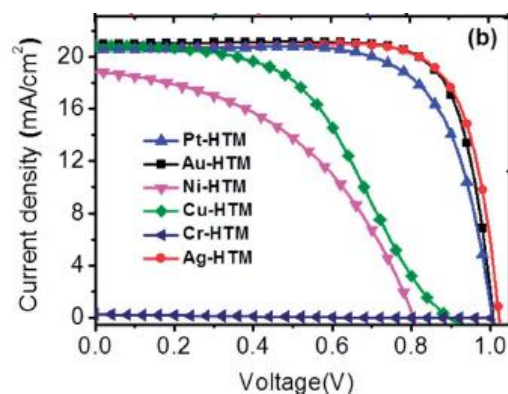


Figure 19 J-V curves of PSCs with a Spiro-OMeTAD HTM layer using different metal contact. ¹³⁸.

Figure 19 shows the comparison with the most common metals, but results Au and Ag exhibit the undeniable superiority against the other elements followed by Pt. Efficiencies of 14.3% and 16.4% were obtained for Pt- and Au-based cells with HTM. Pt and Au were chemically stable, while Cu and Ag were unstable¹³⁸.

Even though functional PSC have been fabricated using common materials as carbon¹³⁹, silicon¹⁴⁰ or aluminum¹⁴¹ back contact electrode. All of them are present very special conditions synthesis for work, but is expected that for commercial purposes in a near future, carbon, in form of

graphene¹⁴² or carbon tape¹⁴³, will be the best option to work as an electrode closing the circuit on perovskite solar cells.

For the purposes of standardization, a traditional Au vacuum deposition will be used for this work.

1.9 Carbazole as organic hole transport materials

Carbazole based small molecules

The subject molecule for this study, Carbazole (Cz), is a quite versatile molecule which has many and wide variety applications in such different domains such as pharmaceutical^{144–146} and biochemistry^{147,148}, industrial dye¹⁴⁹, as a CO and CO₂ adsorption molecules^{150–152}, thermally activated delayed fluorescence (TADF) polymer catalyzer^{153,154}, etc.

But indubitably, the more extended application for carbazole derived molecules remains on organic electronics field, where can be used as an efficient diode light emitter¹⁵⁵, switch memory device¹⁵⁶, dye sensitizer^{157,158} or co-sensitizer¹⁵⁹ in DSSC, molecular rectifier¹⁶⁰ for organic semiconductors and hole transport material for PSC, the subject for this study.

Such application diversity is a direct consequence of Cz's electron rich structure and the ability to donate them, which provides it with ideal characteristics of a suitable p-donor. Consequently Cz's derived compounds act as hole concentrator materials therefore if the conditions are adequate Cz derived compound will function as hole transport material (HTM).

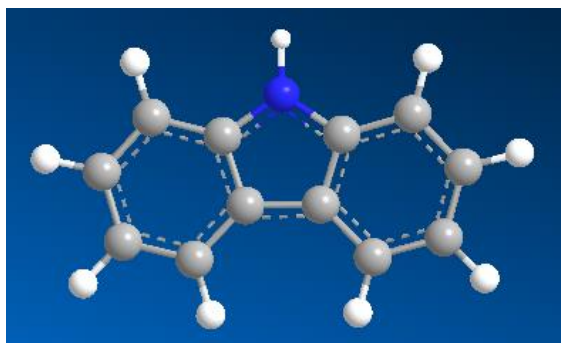


Figure 20 Carbazole tridimensional structural representation

Carbazole is an aromatic heterocyclic compound constituted by two phenyl rings fused together by two different positions, firstly by a nitrogen atom and second connected by a C-C bond giving to Cz a tricyclic configuration which enhance the conjugation between the two phenyl rings through these molecular bonds.¹⁶¹ Also by aromaticity means, a fully conjugated π orbital along the whole molecule is established and a planar structure is derived from this property.

Pointing the later, Cz is our molecule of choice for this study, to explore its reactivity and the obtainment of new Cz derived or containing molecules. One of the main reasons to work with this molecule is due to its easy use, derived from low cost fabrication, simple manipulation, relative stability, among many other advantages like the modification and ease tuning of its electrical properties by the substitution on the 2-,3-, 6-, 7- and 9H-positions. One of the first uses of Cz as HTM is the derivative, 1,3,5-tris(2-(9-ethylcarbazyl-3)-ethylene)benzene (TECEB) (Figure 21) used as a HTM in an Organic Light-Emitting Diode (OLED). Introduction of a carbazole moiety into the core molecule of TECEB¹⁶² added thermal and morphological stable thin films of organic materials having a high glass-transition temperature and improved hole transport properties.

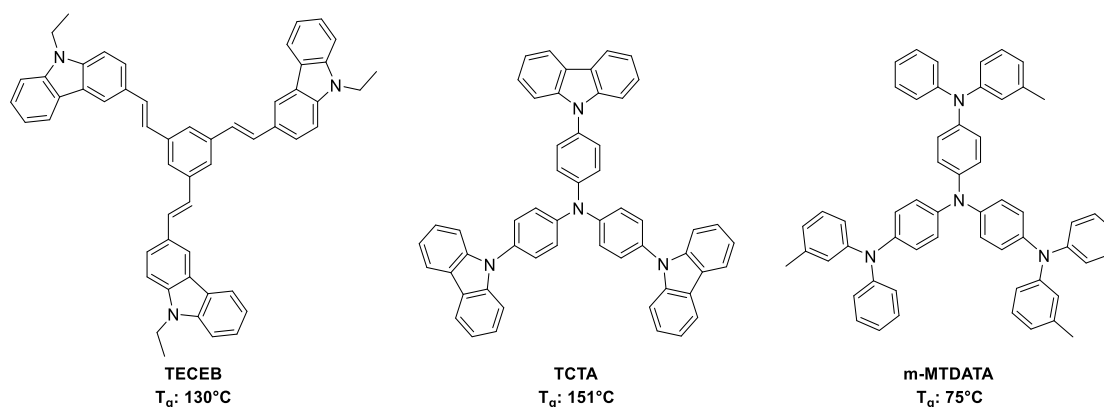


Figure 21 Structure of TECEB¹⁶², TCTA and m-MTDATA¹⁶³

Moreover, improvement of physical properties by the incorporation of a carbazole structurally rigid moiety was also demonstrated by Shiroata et al.¹⁶³ with the comparative study of 4,4',4''-tris(3-methylphenylphenylamino)-triphenylamine (m-MTDATA) and 4,4',4''-tri(N-carbazolyl)triphenylamine (TCTA) (Figure 21) where T_g is dramatically increased due to carbazole addition which exhibits better performance characteristics and a significant thermal stability. Crystallization or melting of organic amorphous materials caused by their exposure to sunlight (80°C at 150 mW/cm²)¹⁶⁴ for a photovoltaic device or Joule heat¹⁶⁵ (resistive heating), can damage the HTL layer which eventually will cause the PSC failure. Therefore, both morphologically and thermally stable amorphous organic materials must be designed in order to asset the required stability conditions.

Certainly, a useful HTM is not only characterized by a high T_g but should also have a low energy barrier for hole injection and the ability to block electron injection from the perovskite layer, which is achieved by properly tuning the energy bandgap trough the addition of electron rich

groups. For this reasons carbazole-based compounds gives to the whole molecule structure three main physical important improvements

(1) The thermal stability or glassy-state durability of organic compounds can be greatly increased upon incorporation of the carbazole moiety due to its rigidity^{163,165,166}.

(2) Carbazole is chemically stable by itself and can be easily modified at the 3, 6- or 2,7- and 9 position¹⁶⁷, for easily tune of HOMO-LUMO levels¹⁶⁸.

(3) The moderately high oxidative potential of carbazole containing compounds make them promising as HTMs.

The above mention explains why carbazole derivatives are widely used as material for electroluminescent (EL) and hole-transporting layers (HTL) for OLEDs devices. Nowadays these characteristics make of Cz compounds a suitable candidates for hole transport materials on sDSSC and more recently in PSC.

Thomas *et al.*¹⁶⁷ investigated the influence of substitution on Cz aromatic benzene rings as well as the influence of substituents on the nitrogen and the modification of the optical and electrochemical properties, its proper application of these properties with various applications (HTM and emissive layer) in OLEDs. Moreover, through the modification of the coupling position over carbazole is possible not only tune the HOMO-LUMO energy levels but also the energy bandgap and mobility properties.¹⁶⁹ It is worth to mention that isomers bearing 2,7- substitution and 3,6- substitution (Figure 22) displays different electronic properties despite of being molecular identical. Nevertheless, the bond conjugation through the benzene ring or the nitrogen¹⁷⁰ atom grants different electronic characteristics to each isomer.

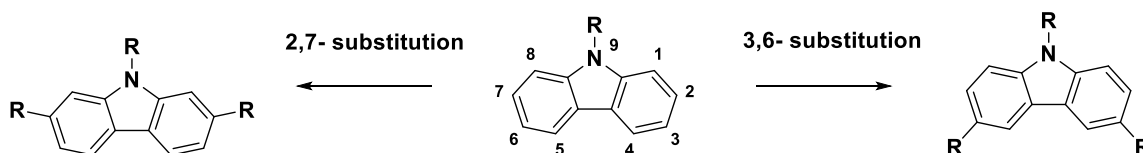
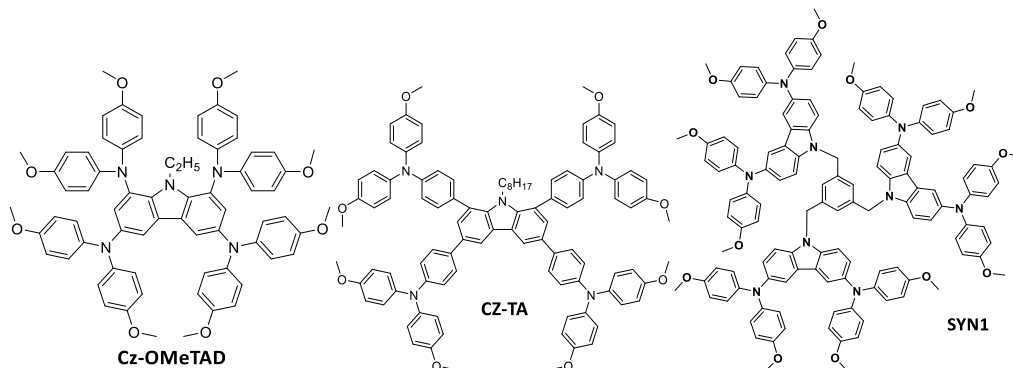
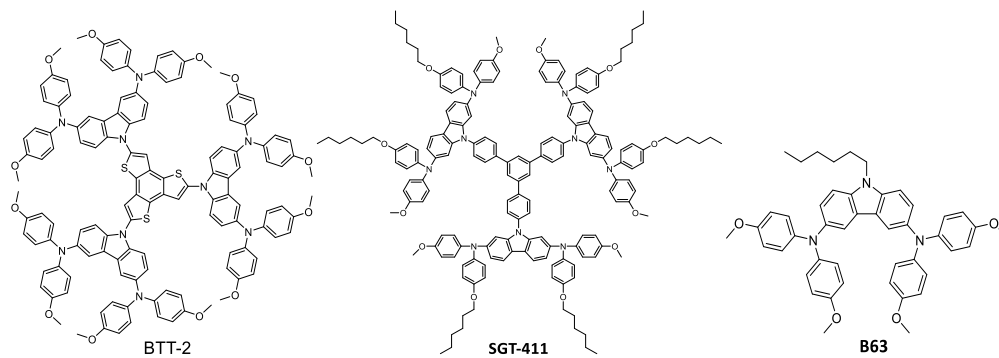
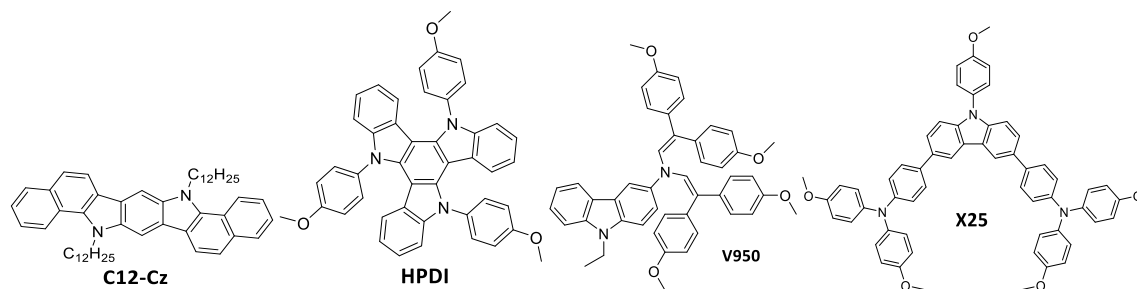
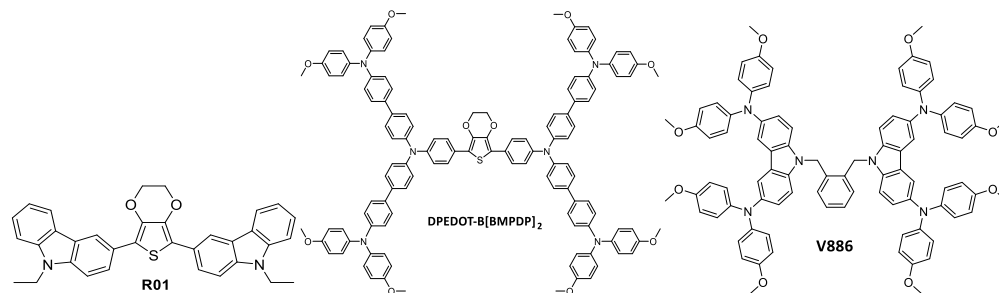
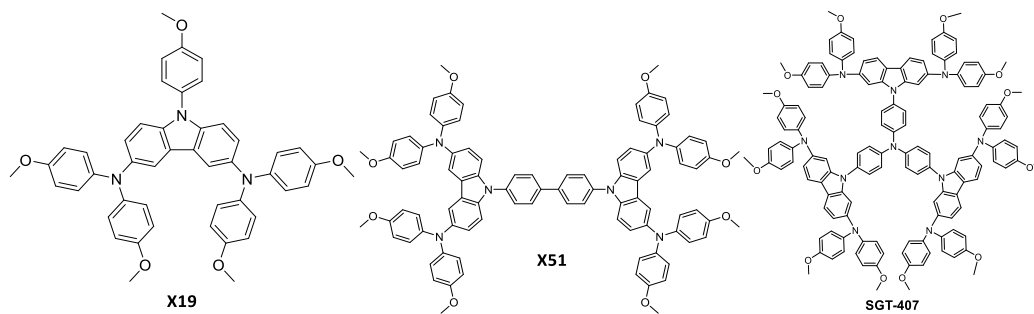


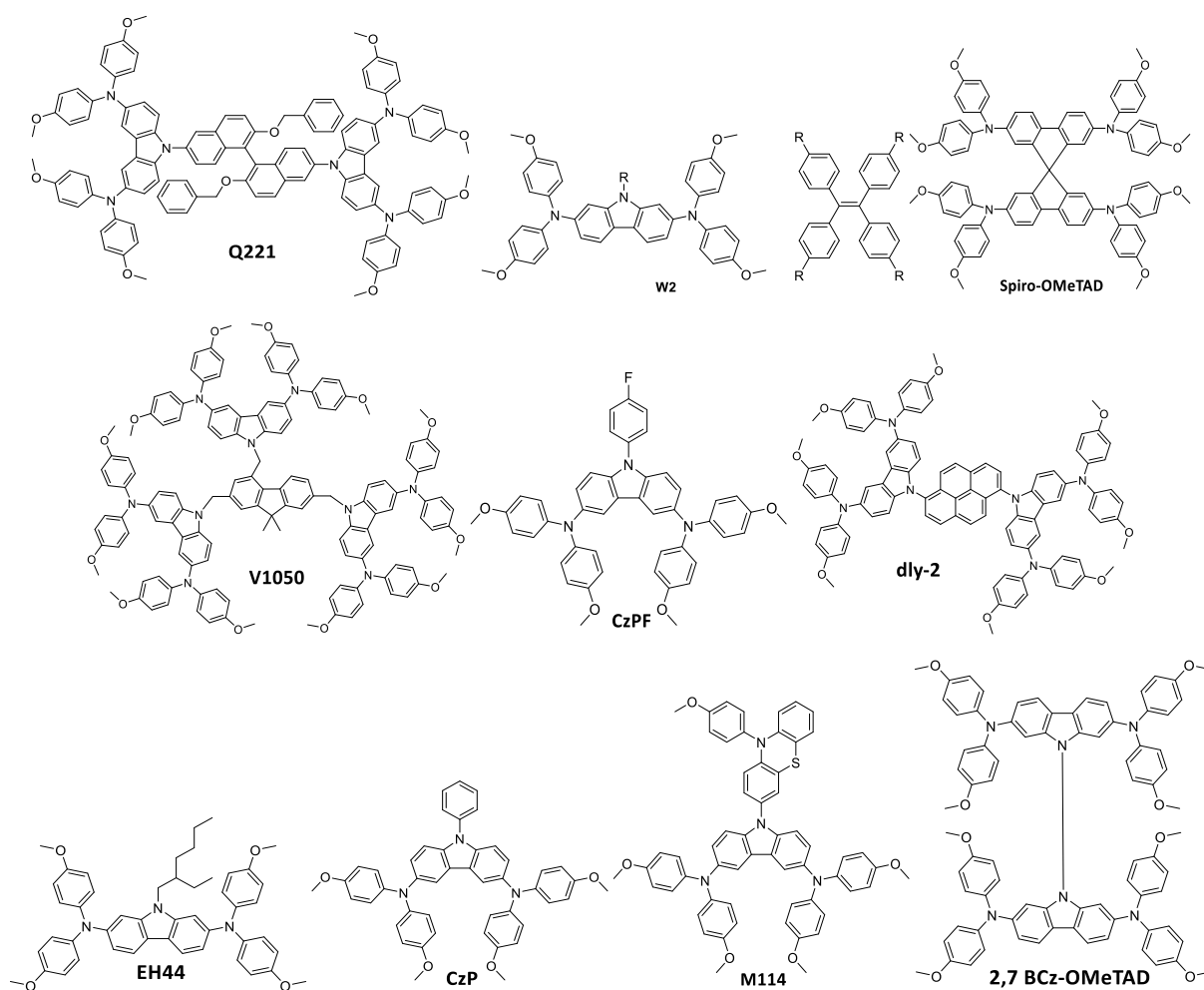
Figure 22 Schematic representation of the carbazole number substitution

Table 3 presents a compilation of carbazole-based molecules that function as a HTM for PSCs. The following molecules were selected in function of their best-reported efficiency. This table includes all the HTM based carbazole molecules articles published so far.

Table 3 HTM carbazole containing molecules

HTM	Hole Mobility (cm ² V ⁻¹ s ⁻¹)	Conductivity (Scm ⁻¹)	HOMO	LUMO	V _{oc} (V)	J _{sc} (mA cm ⁻²)	FF	PCE/Spiro PCE	Year/ Reference
X19	1.19 x 10 ⁻⁴	2.88 x 10 ⁻⁵	-5.43	0.5	0.76	17.14	0.58	7.6/10.2	2014 ¹⁷¹
X51	1.51 x 10 ⁻⁴	1.5 x 10 ⁻⁴	-5.49	0.08	0.88	16.79	0.66	9.8/10.2	2014 ¹⁷¹
SGT-407	-	-	-5.26	-2.26	0.993	20.35	0.686	13.86/15.23	2014 ¹⁷² , 2015 ¹⁷³
R01	2.05 x 10 ⁻⁴	9.36 x 10 ⁻⁵	-5.30	-2.42	0.86	16.7	0.522	7.47/7.46	2015 ¹⁷⁴
DPEDOT- B[BMPDP] ₂	8.45 x 10 ⁻⁵	-	-5.22	-2.55	0.947	21.07	0.713	14.23/14.55	2015 ¹²⁹
V886	6.4 x 10 ⁻⁴	4.2 x 10 ⁻⁵	-5.27	-	1.085	21.38	0.73	16.91/18.36	2015 ^{136,175}
C12- carbazole	5.1 x 10 ⁻²	-	-5.29	-2.32	0.86	21.13	0.62	11.26/9.62	2015 ¹⁷⁶
HPDI	-	-	-5.41	-2.15	0.976	19.16	0.576	10.82/12.93	2015 ¹⁷⁷
V950	5.2 x 10 ⁻⁴	-	-5.04	-	1.07	22.5	0.74	17.8/18.6	2016 ¹⁷⁸
X25	-	2.8 x 10 ⁻⁴	-5.16	-1.96	1.1	22.5	0.70	17.4/ND	2016 ¹⁷⁹
BTT-2	-	1.3 x 10 ⁻⁵	-5.2	-	1.092	21.29	76.7	17.0/18.1	2016 ¹⁸⁰
SGT-411	-	-	-5.28	-2.28	0.997	18.60	0.672	13.00/13.76	2015 ¹⁷³ 2017 ¹⁸¹
B63	1.77 x 10 ⁻⁷	-	-4.7	-1.93	0.87	10.86	0.52	10.8/11.2	2017 ^{182,183}
Cz- OMeTAD	1.82 x 10 ⁻³	1.2 x 10 ⁻⁴	-5.27	-2.52	1.14	22.26	0.71	17.81/18.59	2017 ¹⁸⁴
CZ-TA	1.65 x 10 ⁻⁴	-	-5.11	-2.01	1.044	21.66	0.81	18.32/18.28	2017 ¹⁸⁵
SYN1	-	-	-5.28	-2.39	1.01	19.76	0.635	13.1/12.0	2017 ¹⁸⁶
Q221	-	-	-5.41	-2.13	0.949	15.82	0.69	10.37/10.06	2017 ¹⁸⁷
W2	3.06 x 10 ⁻⁴	-	-5.20	-2.25	1.02	22.23	0.74	16.74/14.14	2017 ¹⁸⁸
Spiro- OMeTAD	1.9 x10 ⁻⁴	-	-5.22	-	1.13	22.75	0.751	19.3	2017 ¹⁸⁹
V1050	1.7 x 10 ⁻⁴	-	-5.11	-	1.05	22.0	0.795	18.3/18.9	2018 ¹⁹⁰
CzPF	5.5 x 10 ⁻⁶	-	-4.92	-2.79	1.03	17.31	0.70	12.41/13.45	2018 ¹⁹¹
dly-2	1.43 x 10 ⁻³	-	-4.88	-2.62	1.038	23.24	0.755	18.23/19.59	2018 ¹⁹²
EH44	-	-	-	-	1.091	21.71	0.779	18.5/19.6	2018 ⁵⁴
CzP	-	-	-4.95	-2.15	1.04	18.22	0.69	13.08/13.45	2018 ¹⁹¹
M114	4.63 x 10 ⁻⁵	1.6 x 10 ⁻⁶	-5.00	-1.88	1.055	22.24	0.732	17.17/18..07	2018 ¹⁹³
2,7 BCz- OMeTAD	9.5 x 10 ⁻⁵	-	-5.15	-2.25	1.089	22.38	0.725	17.6/18.5	2018 ¹⁹⁴





Most of the molecules included in this selection are derivatives of 3,6-bis(4-metoxydiphenylamine)carbazole (DPA₂Cz). Such molecule have all the necessary characteristics to work as an HTM, like good solubility, adequate HOMO-LUMO energy levels, high glass temperature and contain methoxy-diphenyl groups that are a structural part of the standard reference HTM, Spiro-OMeTAD. Is important to remark that the bigger the number of substitutions those hyper-branched molecules containing DPA₂Cz motif in their structure make their synthesis more difficult and consequently the final synthetic yields are lower. Although, if some of these molecules become more efficient than the same Spiro-OMeTAD, their difficult production and purification place them away from one of the first objectives that is the design of the molecules that are affordable and with low cost production. However, it has been seen that hyperbranched and high molecular weight is not a determining factor for a good performance. A clear example is R01 (see Table 3), a low molecular weight molecule which almost equals Spiro-

OMeTAD on final PCE and hole mobility, in a pristine form (7.47 % PCE) and 12 mol % dopant (12.03 % PCE).¹⁷⁴ This case clearly demonstrates how small a molecule, easy to synthesize, can almost match Spiro-OMeTAD standard.

The molecules can be classified on many different ways, but for practical matter, we will use two classifications, planar and tridimensional. Strictly planar molecules included on this table are C12-Cz and HDPI (see Table 3), while we can find another two with an almost planar structure V950 and R01. Planar molecules like C12-Cz and HDPI consist of carbazole-fused rings in a completely planar configuration that gives these molecules a layer aggregation. If the use of Spiro-OMeTAD tends to demonstrate that amorphous and unidirectional aggregation is necessary, the efficiency reached for planar molecules (C12-Cz and HDPI versus Spiro 11.26/9.62% and 10.82/12.93%) proposes a parallel solution to tridimensional molecules as HTM in PSC. If these molecules have a very good performance and for C12-Cz case, its performance is even better than that observed with Spiro-OMeTAD. The last mentioned molecules present a major drawback, their onerous synthesis make of them a non-economically viable option to up-scale their production.

For the second proposed category, tridimensional molecules can be classified by number of branches or their substitution number. More than three substitutions on carbazole core (hyperbranched) or more than one carbazole core in one molecule with high molecular weight or one carbazole with two substitutions (low branched) and low molecular weight. From a synthetic point of view, it is important to remark that, higher the substitution number, lower the final yields and more expensive its synthesis.

Most of the synthesized compounds presented on this compilation are substituted in the positions 3,6- on the carbazole core due to is relatively easy way to obtain them. In other hand, only three compounds are presented on the table bearing a substitution over 2,7- position on the carbazole core.

One of the 2,7- Cz substituted mention compounds, a low molecular weight carbazole molecule (EH44) and two high molecular weight (W2 and 2,7 BCz-OMeTAD). EH44 molecule, one of the latest carbazole-based HTM synthesized and published as HTM for PSCs, shows a good performance compared to its close relatives 3,6- substituted molecules, demonstrating that 2,7- substitution could be an important alternative on Cz based HTMs. In the case of W2 molecule, its final efficiency over stands Spiro-OMeTAD, but as was mention before, highly branched molecules tends to have low synthetic yields. Even though for the case of and 2,7 BCz-OMeTAD,

an hyperbranched HTM, the production cost is 1/6 compared to production cost for Spiro-OMeTAD, making of it a highly convenient option to replace the so called standard.

To summarize, a good HTM needs to present five requirements:

- 1) High hole mobility
- 2) Optimal HOMO-LUMO energy levels
- 3) Good solubility and film forming properties
- 4) Thermal stability
- 5) Low cost, at least compared with used reference standard Spiro-OMeTAD

For the latter reasons research around new hole transport materials is open to improvement by creating new molecules.

2. Carbazole substituted isomers derivatives as HTM for perovskite solar cells

2.1 Strategy

After describing the quality and required properties of materials used in photovoltaic cells focused on HTM layer and in particular on the opportunity to use carbazole derivatives as HTM like those examples depicted in Chapter 1. We synthesized six new carbazole derivatives constituted by a carbazole unit connected to a two 4,4'-dimethoxydiphenylamine groups (DPA). Chapter 2, presents the synthetic details of two carbazole series DMx and iDMx, distinguished between each other by their isomeric substitution 2,7-Cz (iDMx) or 3,6-Cz (DMx) but also on the presence of alkyl chain or phenyl group attached to the carbazole N- atom.

Our strategy is to compare the physical properties derived from isomeric substitution and carry out their optoelectronic characterization for their eventual test as HTM on perovskite photovoltaic devices. The targeted molecules DMx and iDMx are shown in *Figure 23*.

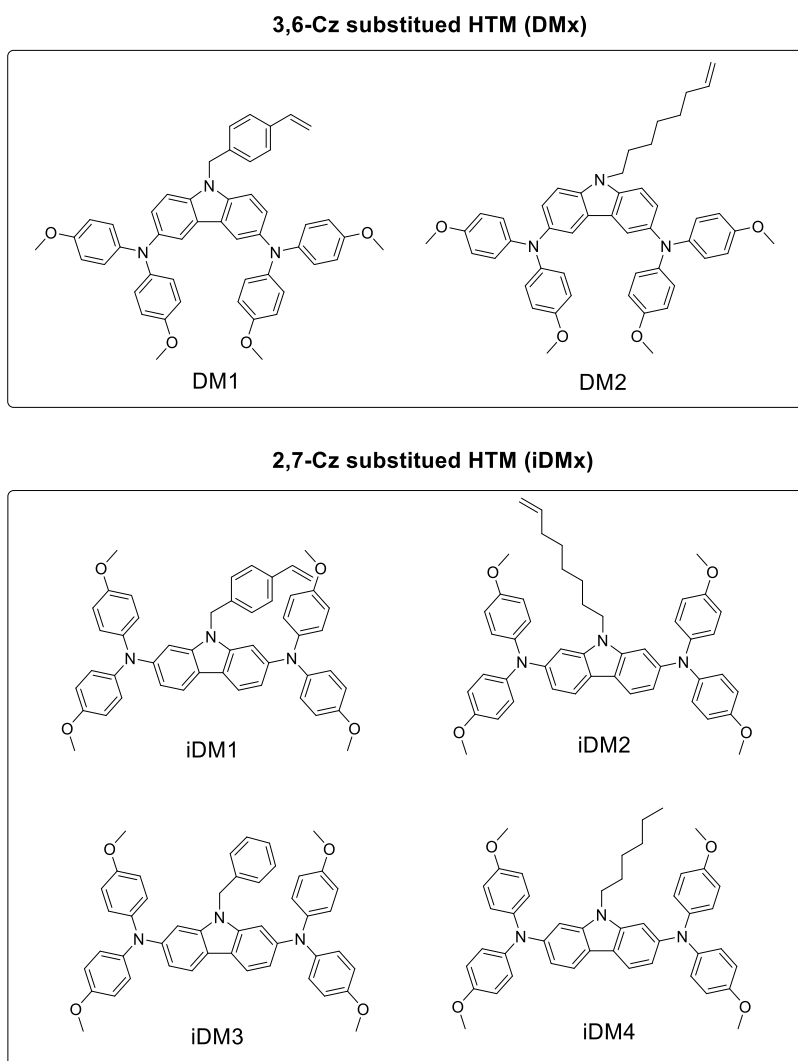
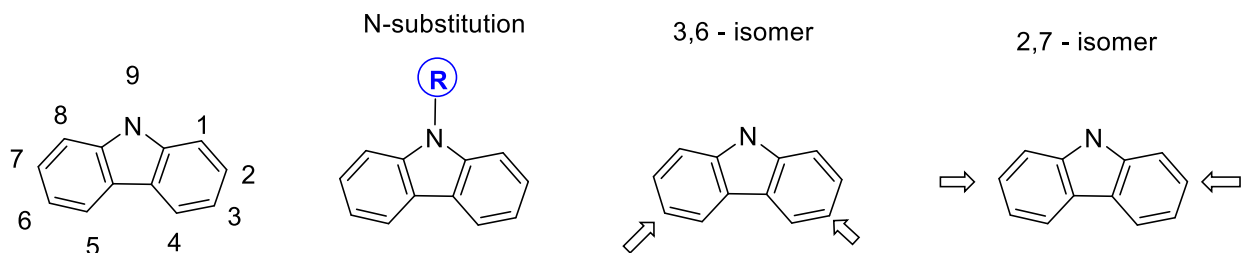


Figure 23: Design of studied HTM

DM1, iDM1 and iDM3 (Figure 23) molecules, bear an aromatic vinyl or phenyl function attached to the N- atom. DM2, iDM2 and iDM4 are N- substituted by an alkyl chain, alkene functionalized for DM2 and iDM2. The objective for those alkene functionalized compounds is to be precursor monomers for chemical polymerization. Only single molecules results are presented, polymerization results are discussed in Chapter 3. It seems important for us to compare and observe the differences between a small molecule and a polymer HTM layer for PSC application.

2.2 Synthesis objective

The general design approach of this work is illustrated in Scheme 1. The first part of this project is focused on the synthesis of a group of molecules composed with one carbazole unit as core bearing different functions attached to the N heteroatom. The first criterion is to functionalize carbazole molecule by the addition of two different kind of moieties that can be an alkyl chain or an aromatic ring. From the obtained molecules, we want to observe and compare the differences on physical, optoelectronic and film formation ability. Some of these molecules have an alkene function for a further polymerization.



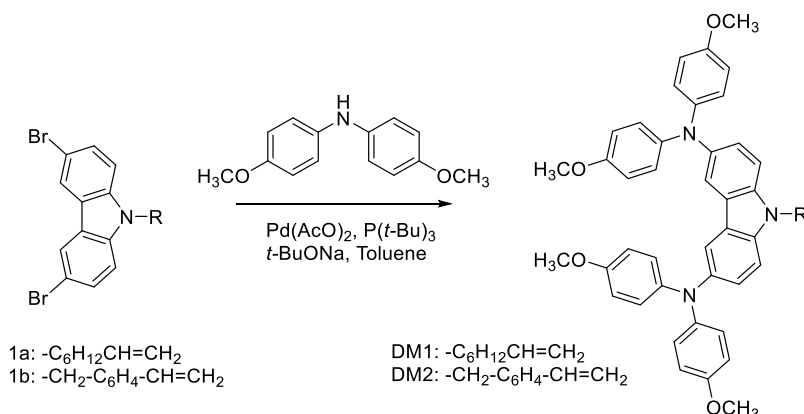
Scheme 1 Carbazole different substitutions

The second approach of this study is to observe the difference between molecules bearing different substitution configuration. Structural isomers will be compared between 2,7- and 3,6- functionalization over the carbazole core. With this study we expect to compare the electronic properties emerging from a para-position conjugation respect to the N atom (3, 6-), or para-position respect the C-C bond in the heterocycle and determinate the consequences of the internal conjugation and how this affects or improves the final performance of a whole device.

2.3 Synthesis of DMx and iDMX molecules

Synthetic strategy of DMx or 3,6-carbazole substituted molecules

From carbazole as starting material, the synthetic path will begin with a bromination. The selective bromination in position 3,6- on the carbazole ring is directed by the N atom contained in the heterocycle that stands as a para-director respect both sites (3,6-). Thus a stoichiometry controlled bromination will result in a quantitative 3,6-dibromocarbazole. Once carbazole is brominated, the following step is the functionalization of the N atom by alkyl or benzyl agent. This can be easily done by a simple S_N2 substitution carried under mild basic conditions and the respective alkylating agent. Usually this reaction gives quantitative yields. Once the N atom is functionalized and protected, in order to complete the synthetic route, it is necessary to couple the di(4-methoxyphenyl)amine with the alkyl-N-carbazole. This will be done by a Buchwald-Hartwig amination, which consist in a transmetallation coupling reaction catalyzed by a Pd agent. All final compounds were obtained in good yields.



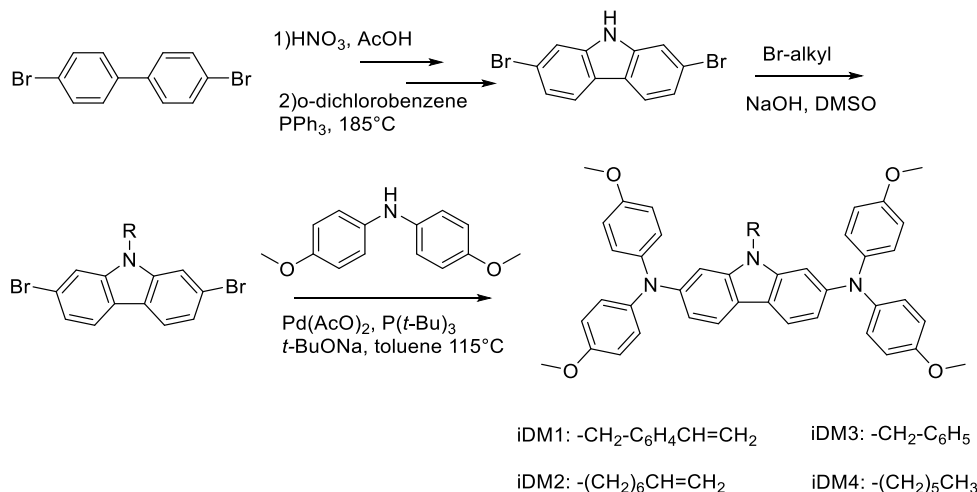
Scheme 2: Synthesis procedure of 3,6-carbazole substituted molecules (DMx)

Synthetic strategy of iDMx or 2,7-carbazole substituted molecules

The nitrogen atom in the carbazole ring is a para/ortho director, due to this fact the strategy to brominate carbazole in 2,7- position is different to 3,6- synthetic route. In this case, carbazole ring has to be synthesized with the bromide atoms already attached to its structure. To perform the synthesis of 2,7-dibromocarbazole, the best route begins from nitration of 4,4'-dibromobiphenyl. It is well known that halogens are ortho/para directors but nitration of the

biphenyl group will occur in the meta position respect the halogen atom on the first ring. This is a direct influence of the stabilized resonance structure by the bromide atom in the contiguous ring, resulting in observed nitration (Scheme 3).

The following step consist on a triphenylphosphine-mediated reductive cyclization of 2-nitro-4,4'-dibromo-biphenyl in o-dichlorobenzene to give as a result the desired 2,7-dibromocarbazole (Scheme 3). With the 2,7- substituted carbazole, it is possible to follow the same synthetic steps as the DMx series, passing by the alkylation and followed by the coupling amination.

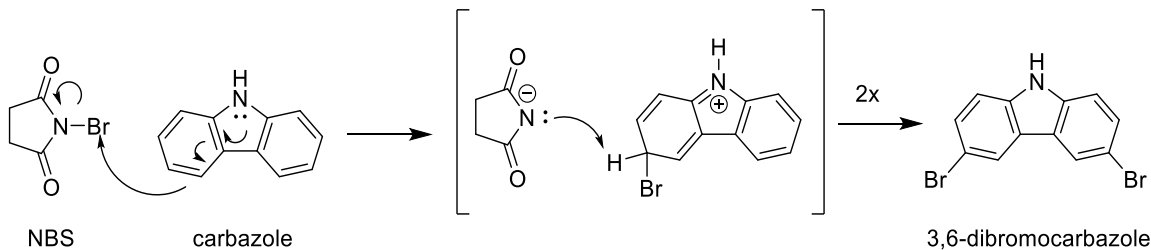


Scheme 3: Synthesis procedure of 2,7-carbazole substituted molecules (iDMx)

2.3.1 Synthetic procedures

2.3.1.1 General synthesis procedure for 3,6-Dibromocarbazole.

In a dry 100 mL round-bottom flask, carbazole (17 mmol, 1 eq) and N-Bromosuccinimide (34 mmol, 2 eq), dissolved in DMF (50 mL) were charged. Reaction conditions are at -78°C . After 2h allowed to cool at -10°C temperature. The mixture was quenched with brine (50 mL) and extracted with CH_2Cl_2 (3 x 50 mL) (Scheme 4). The organic layers were combined and washed with distilled water, dried over anhydrous MgSO_4 filtered and concentrated under vacuum. The crude product is pure enough to use on the following step without further purification after its recrystallization. This reaction yields 90% of a white solid.



Scheme 4 Synthesis procedure for 3,6-Dibromocarbazole

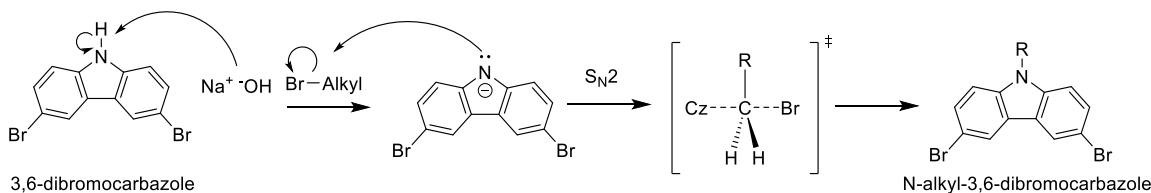
Characterization

¹H NMR 250MHz (DMSO-d₆) δ 7.57 (m, 4H), 8.45 (d, 2H), 11.67 (s, 1H).

¹³C {¹H} NMR 62,9MHz (DMSO-d₆); δ (ppm) 115, 117, 121, 122, 128, 149.21.

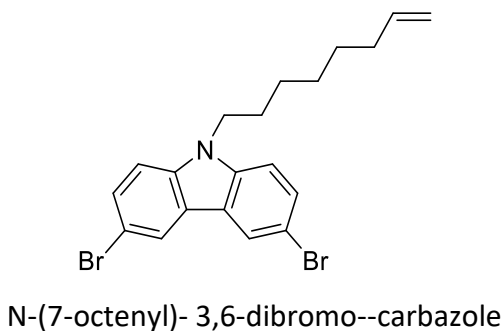
2.3.1.2 General synthesis procedure for compounds N-alkyl-3,6-dibromocarbazole

In a dry 100 mL round-bottom flask, 3,6-dibromocarbazole (0.6 mmol, 1 eq), 1-bromoalkene (0.9 mmol, 1.5 eq), NaOH (4.7 mmol, 8 eq dissolved in 1 mL of water) and DMSO (6 mL) were charged (Scheme 5). The reaction mixture is let it react at 50°C for 5 h. The reaction mixture was quenched with brine (10 mL) and extracted with CH₂Cl₂ (3 x 15 mL). The organic fractions were combined and washed with brine, dried over anhydrous MgSO₄ filtered and concentrated under vacuum. The crude product was purified by column chromatography eluting with CH₂Cl₂/petroleum ether (4/6 v/v) to yield the 85% of a with solid compound.



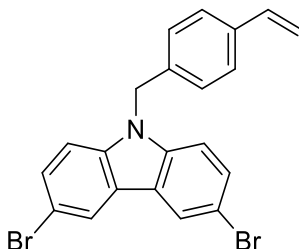
Scheme 5 synthetic procedure for N-alkyl-3,6-dibromocarbazole compounds.

Characterization



¹H NMR 250MHz (DMSO-d₆) δ 1.32 (m, 6H), 1.83 (m, 2H), 2.0 (m, 2H), 4.24 (t, 2H, *J* = 8.5 Hz), 4.9-4.95 (m, 1H_{cis}), 5.0-4.98 (m, 1H_{trans}), 5.76 (m, 1H), 7.26 (d, 2H, *J*_o = 10.5 Hz), 7.55 (dd, 2H, *J*_o = 10.5 Hz, *J*_m = 2.4 Hz), 8.42 (d, 2H, *J*_m = 2.4 Hz).

¹³C {¹H} NMR 62,9 MHz (DMSO-d₆); δ (ppm) 27, 28.6, 28.7, 28.8, 33.6, 43.3, 110.4, 111.9, 114.4, 123.3, 123.4, 129.0, 138.7, 139.3.



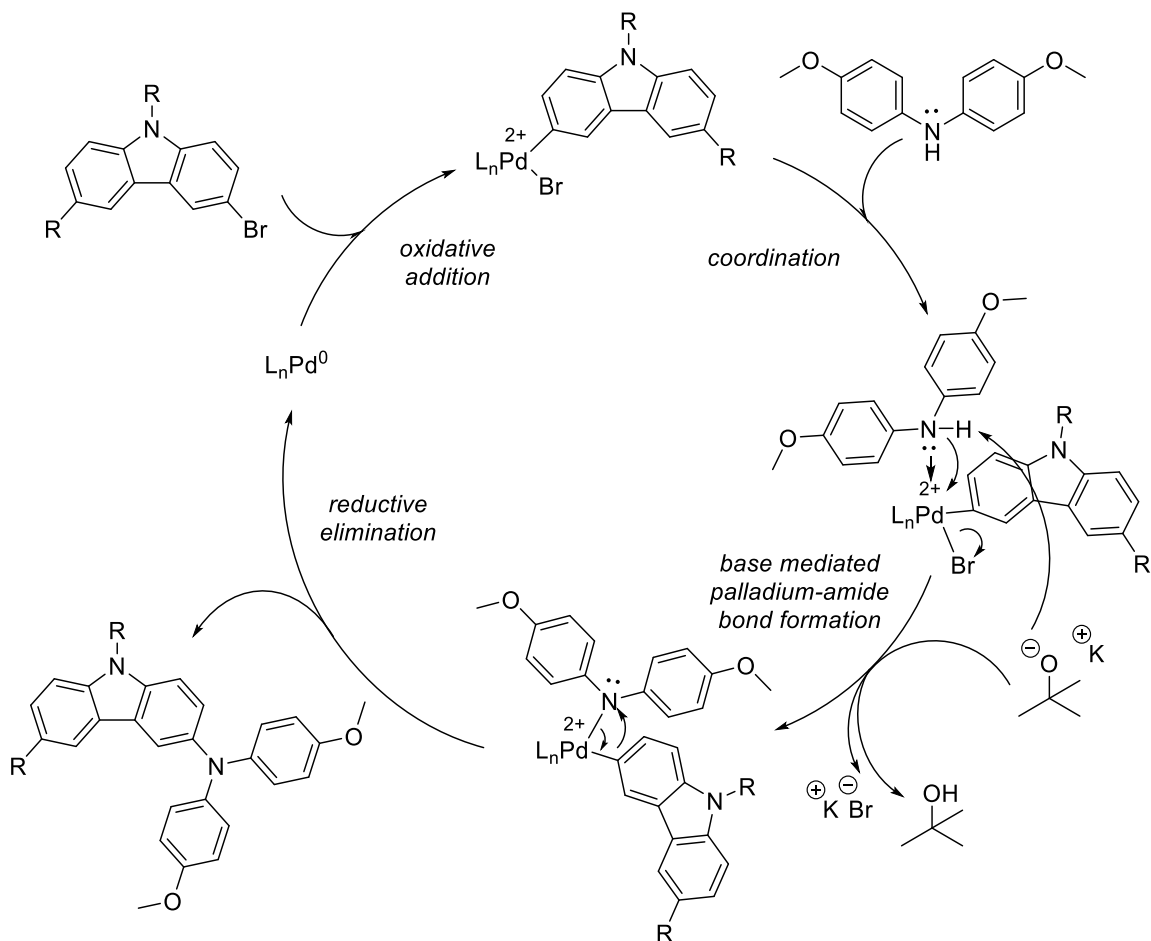
N-(4-vinylbenzyl)-3,6-dibromocarbazole

¹H NMR 250 MHz (DMSO-d₆) δ 5.2 (d, 1H_{cis}, *J* = 11Hz), 5.67 (s, 2H), 5.74 (d, 1H_{trans}, *J* = 18 Hz), 6.35 (dd, 1H, *J* = 11 and 17 Hz), 7.10 (d, 2H, *J* = 9 Hz), 7.36 (d, 2H, *J* = 8 Hz), 7.63 (m, 4H), 8.85 (m, 2H).

¹³C {¹H} NMR 62,9 MHz (DMSO-d₆); δ (ppm) 45.6, 111.7, 111.9, 114.4, 123.1, 123.6, 126.4, 126.9, 129.0, 136.1, 136.3, 136.84, 139.23.

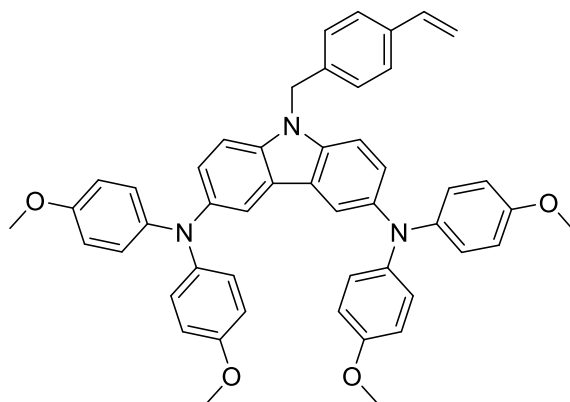
2.3.1.3 General synthesis procedure for compounds DM1 and DM2.

According to Scheme 6, a Buchwald–Hartwig amination takes place in a dry Schlenk tube. N-alkenyl-3,6-dibromocarbazole (1.0 mmol, 1 eq), bis(4-methoxyphenyl)amine (3 mmol, 3 eq), Palladium(II) acetate (0.05 mmol, 0.05 eq), sodium tert-butoxide (4.0 mmol, 4 eq), tri-tert-butylphosphine (0.1 mmol, 0.1 eq, dissolved in 1 mL of toluene) and anhydrous toluene (10 mL) were charged. The septum-sealed Schlenk was evacuated and refilled with Argon five times. The mixture was stirred under argon atmosphere at 105°C for 80 h and allowed to cool at room temperature. The mixture was diluted with AcOEt (75 mL) and washed with water (x 3) and brine (x 1), dried over anhydrous MgSO₄, filtered, and concentrated under reduced pressure to give a viscous oil (around. 2–3 mL). The crude product was purified by fast column chromatography eluting with CH₂Cl₂, solvent removed under vacuum to give an oily product that was added to methanol (200 mL) with vigorous stirring to precipitate the product. The precipitate was then filtered, rinsed with methanol several times and purified by silica gel column 4/1 hexane/AcOEt to yield a 70-75% of a yellowish amorphous solid.



Scheme 6 Coupling procedure for compounds DM1 and DM2

Characterization



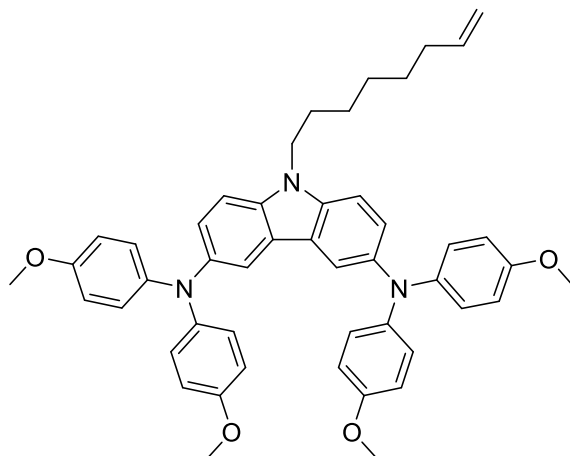
N-(4-benzyl-6-vinyl)-3,6-bis(4,4'-dimethoxydiphenylaminyl)carbazole (DM1)

C₄₉H₄₃N₃O₄, Elem. Analysis (%) Exp. C 78.35, H 5.88, N 5.4, O 8.2; Calculated C 79.76, H 5.87, N 5.69, O 8.67.

HR-MS: m/z=738.3305 [M+H]⁺

¹H NMR 250 MHz (DMSO-d₆) δ 3.72 (s, 12H), 5.25 (d, 1H, *J*_{trans} = 12.6 Hz), 5.08 (d, 1H, *J*_{cis} = 20.4 Hz), 6.71 (dd, 1H, *J*_{cis} = 22.05 Hz, *J*_{trans} = 13.5 Hz), 6.82-6.91 (m, 16H), 7.12 (dd, 2H, *J*_o = 10.3 Hz, *J*_m = 2.9 Hz), 7.25 (d, 2H, *J*_o = 9.6 Hz), 7.44 (d, 2H, *J*_o = 9.9 Hz), 7.58 (d, 2H, *J*_o = 10.5 Hz), 7.73 (d, 2H, *J*_m = 2.1 Hz).

¹³C {¹H} NMR 62,9 MHz (DMSO-d₆); δ (ppm) 55.17, 55.7, 114.65, 116.38, 116.84, 119.91, 120.89, 122.77, 123.75, 126.41, 127.2, 136.16, 132.27, 137.56, 140.29, 140.85, 142.05, 154.19.



N-(7-octene)-3,6-bis(4,4'-dimethoxydiphenylaminy)carbazole (DM2)

C₄₈H₄₉N₃O₄, Elem. Analysis (%) Exp. C 78.11, H 6.85, N 5.47, O 7.96; Calculated C 78.77, H 6.75, N 5.74, O 8.74.

HR-MS: m/z=732.3773 [M+H]⁺

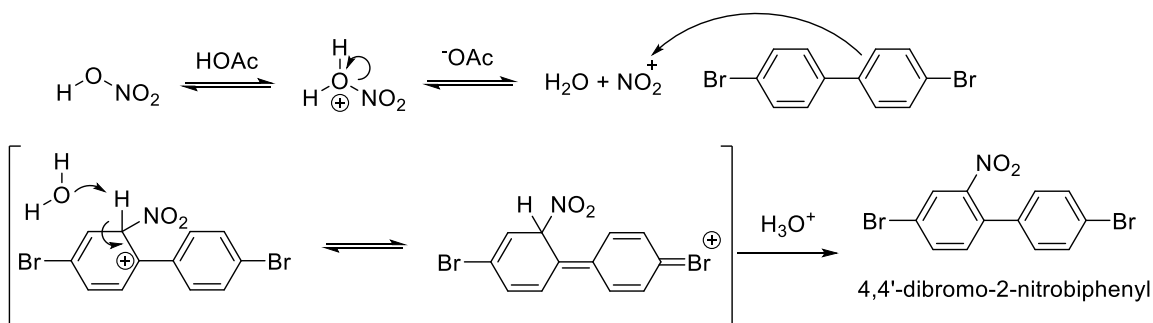
¹H NMR 250 MHz (DMSO-d₆) δ 1.28 (s, 6H), 1.53 (s, 1H), 1.73 (s, 2H), 1.93 (s, 2H), 3.67 (s, 12H), 4.28 (m, 2H), 4.87-4.91 (m, 1H_{cis}), 4.97 (m, 1H_{trans}), 5.69-5.75 (m, 1H), 6.76-6.86 (m, 16H), 7.09 (d, 2H), 7.47 (d, 2H), 7.64 (s, 2H).

¹³C {¹H} NMR 62,9 MHz (DMSO-d₆); δ (ppm) 23.61, 28.16, 28.25, 28.69, 33.05, 42.45, 55.15, 110.27, 114.59, 116.59, 122.56, 123.63, 124.38, 131.06, 137.21, 138.72, 139.87, 140.10, 154.11.

2.3.1.4 Synthesis procedure for 4,4'-dibromo-2-nitrobiphenyl.

In a dry 100 mL round-bottom flask and condenser, 4,4'-dibromobiphenyl (8 mmol) is dissolved in 42 mL of acetic acid at 100°C, followed by the addition, drop by drop of nitric acid (6 mL) in 20 min and let it react for 1 hour (Scheme 7). Then the reaction is quenched by the addition of ice water, precipitated, filtered and washed with a basic solution of sodium carbonate 3 M until is neutralized. Product is dissolved in CHCl₃, washed with brine, dried with anhydrous MgSO₄

and solvent is removed under vacuum. The solid can be purified by silica column with a solvent gradient from petroleum ether / dichloromethane (7/3 v/v) or recrystallized it from the crude product in a P_{eth} / chloroform (3/1 v/v) mixture. A pale yellow solid is obtained with a yield of 70%. ¹H NMR 250 MHz (CDCl₃) δ (ppm) 7.17-7.21 (m, 2H), 7.29 (d, 1H), 7.54-7.60 (m, 2H), 7.73-7.77 (m, 1H), 8.02 (d, 1H).

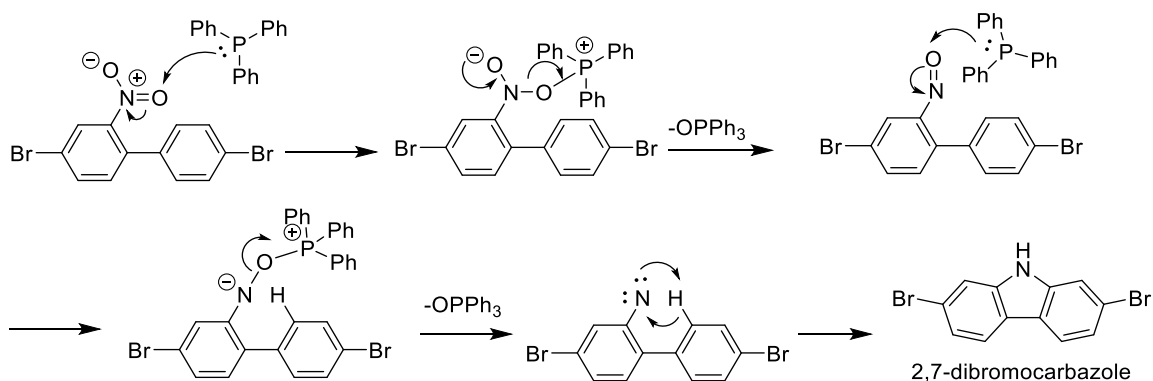


Scheme 7: Synthesis procedure for 4,4'-dibromo-2-nitrobiphenyl

2.3.1.5 Synthesis procedure for 2,7-dibromocarbazole

In a 100 mL Schlenk tube equipped with a condenser (2.7 mmol, 1 eq) of 4,4'-dibromo-2-nitrobiphenyl and (7.84 mmol, 2.6 eq) of triphenylphosphine are dissolved in 14 mL of o-Dichlorobenzene. The reaction is heated for 24 hours at 185°C under argon atmosphere (Scheme 8). After the reaction is purified directly in a flash silica column from petroleum ether/dichloromethane (8/2 v/v). A white solid is obtained with a yield of 85%.

¹H NMR 250 MHz (CDCl₃) δ 7.38 (dd, 2H, *J*=8.42, *J*=1.66 Hz), 7.89 (d, 2H, *J*=8.37 Hz), 7.90 (d, 2H, *J*=1.68 Hz), 8.18 (s, N-H).

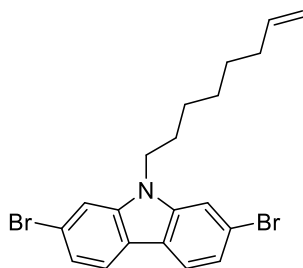


Scheme 8: Synthesis procedure for 2,7-dibromocarbazole

2.3.1.6 Synthesis procedure for N-vinylbenzyl-2,7-dibromo-carbazole and 2,7-bis(4,4'-dimethoxydiphenylaminyl)carbazole (iDM1, iDM2, iDM3, iDM4)

For the alkylation of 2,7-dibromocarbazole and following Buchwald–Hartwig amination, the same procedure of 2.3.1.2 and 2.3.1.3 are followed. Obtaining a bright yellow solid with a yield of between 45 to 75%.

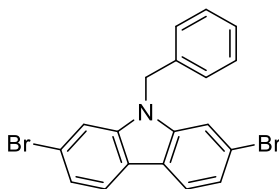
Characterization



N-(7-octenyl)-2,7-dibromocarbazole

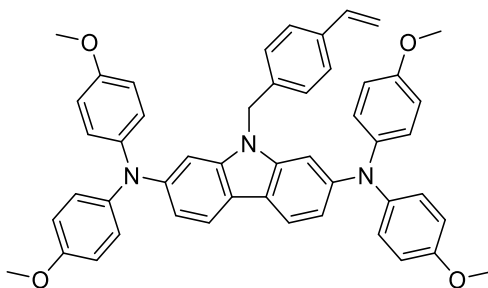
^1H NMR 250 MHz (DMSO- d_6) δ 1.26 (s, 6H), 1.69 (m, 2H), 1.95 (m, 2H), 4.37 (t, 2H), 4.91 (m, 2H), 5.74 (m, 1H), 7.37 (m, 1H), 7.35 (dd, 2H, $J = 8.37$ Hz, $J = 1.66$ Hz), 7.89 (d, 2H, $J = 8.37$ Hz), 8.11 (d, 2H, $J = 1.58$ Hz)

^{13}C { ^1H } NMR 62.9 MHz (DMSO- d_6); δ (ppm) 26.02, 28.17, 28.18, 28.27, 42.32, 112.42, 114.64, 119.16, 120.66, 122.09, 122.18, 138.70, 141.08.



N-benzyl-2,7-dibromocarbazole

^1H NMR 250 MHz (DMSO- d_6) δ (ppm) 5.71 (s, 2H), 7.11 (d, 2H, $J = 8.37$), 7.27 (m, 3H), 7.39 (d, 2H, $J = 8.21$), 7.92 (s, 2H), 8.15 (d, 2H, $J = 8.37$)



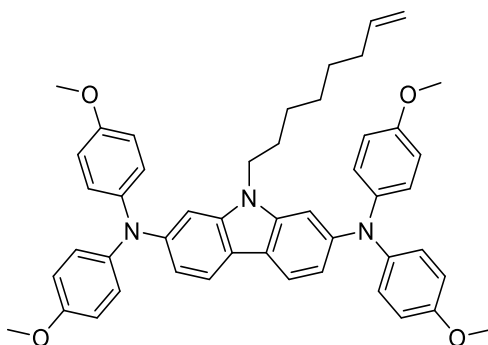
N-(benzyl-4-vinyl)-2,7-bis(4,4'-dimethoxydiphenylaminyl)carbazole (iDM1)

C₄₉H₄₃N₃O₄, Elem. Analysis (%) Exp. C 78.35, H 5.88, N 5.4, O 8.2; Calculated C 79.76, H 5.87, N 5.69, O 8.87.

HR-MS: m/z=738.3314 [M+H]⁺

¹H NMR 250 MHz (DMSO-d₆) δ 3.72 (s, 12H, 6), 5.19 (s, 2H, 7), 5.25 (d, 1H, 12, *J* = 15.64 Hz), 5.79 (d, 1H, 11, *J* = 17.69 Hz), 6.65 (d, 2H, 2, *J* = 8.37 Hz), 6.73 (m, 1H, 10), 6.84 (d, 10H, 4, 8, *J* = 9.17), 6.94 (d, 10H, 5, 9, *J* = 9.0 Hz), 7.31 (d, 2H, 1, *J* = 8.22 Hz), 7.78 (d, 2H, 3, *J* = 8.37 Hz).

¹³C {¹H} NMR 62.9 MHz (DMSO-d₆); δ (ppm) 55.64, 81.98, 102.55, 114.68, 114.78, 115.17, 117.54, 120.42, 125.25, 126.21, 127.16, 136.10, 136.21, 136.97, 141.00, 141.41, 146.01, 155.07.

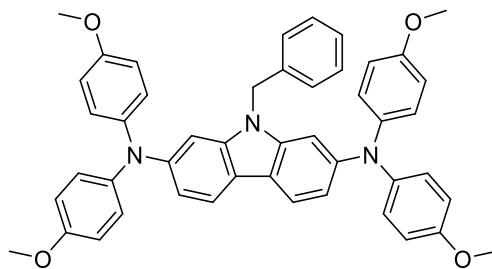


N-(7-octenyl)-2,7-bis(4,4'-dimethoxydiphenylaminyl)carbazole (iDM2)

C₄₈H₄₉N₃O₄, Elem. Analysis (%) Exp. C 78.11, H 6.85, N 5.47, O 7.96; Calculated C 78.77, H 6.75, N 5.74, O 8.74.

HR-MS: m/z=732.3781 [M+H]⁺,

¹H NMR 250 MHz (DMSO-d₆) δ (ppm) 1.07 (m, 6H), 1.48 (m, 2H), 1.87 (m, 2H), 3.71 (s, 12H), 3.90 (m, 2H), 4.91 (m, 2H), 5.71 (m, 1H), 6.65 (m, 2H), 6.84 (m, 10H), 6.97 (m, 8H), 7.76 (d, 2H).



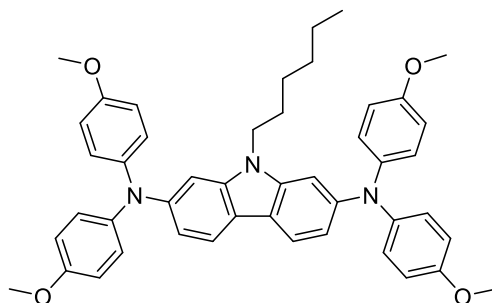
N-(benzyl)-2,7-bis(4,4'-dimethoxydiphenylaminy)carbazole (iDM3)

C₄₇H₄₁N₃O₄, Elem. Analysis (%); Calculated C 79.30, H 5.81, N 5.90, O 8.99.

HR-MS: m/z=712.3169 [M+H]⁺,

¹H 250 MHz (DMSO-d₆) δ (ppm) 3.78 (s, 12H), 5.22 (s, 2H), 6.30-8.07 (m, 27H).

¹³C {¹H} NMR 62.9 MHz (DMSO-d₆); δ (ppm) 45.37, 55.20, 102.08, 114.74, 119.99, 125.32-126.23, 126.98, 127.20, 128.42, 137.26, 141.39, 1551.11, 155.19.



N-(hexyl)-2,7-bis(4,4'-dimethoxydiphenylaminy)carbazole (iDM4)

C₄₆H₄₇N₃O₄, Elem. Analysis (%); Calculated C 78.27, H 6.71, N 5.95, O 9.07.

¹H NMR 250 MHz (DMSO-d₆) δ (ppm) 0.61-0.82 (m, 3H), 0.92- 1.16 (m, 6H), 1.33-1.51 (m, 3H), 3.69 (s, 12H), 3.76-3.86 (m, 2H), 6.64 (dd, 2H, J= 8.53Hz), 6.90 (dd, 16H, J=16.27, 8.84), 6.91-6.99 (m, 2H), 7.72 (d, 2H, J= 8.37Hz).

¹³C {¹H} NMR 62.9 MHz (DMSO-d₆); δ (ppm) 13.75, 21.86, 25.99, 27.91, 30.73, 41.61, 55.14, 101.68, 114.21, 114.51, 114.69, 116.95, 118.01, 119.92, 125.54, 125.84, 141.13, 141.35, 146.00, 155.04.

2.4 Characterization of physical properties of DMx and iDMx

2.4.1 Thermal properties

To evaluate their thermal stability, both DMx and iDMx series were analyzed by Thermal Gravimetric Analysis (TGA) in Figure 24 (for DM1 and DM2) and Figure 25 (for iDM1, iDM2, iDM3 and iDM4), show, a single stage decomposition in a range that goes from 0 to 700 °C.

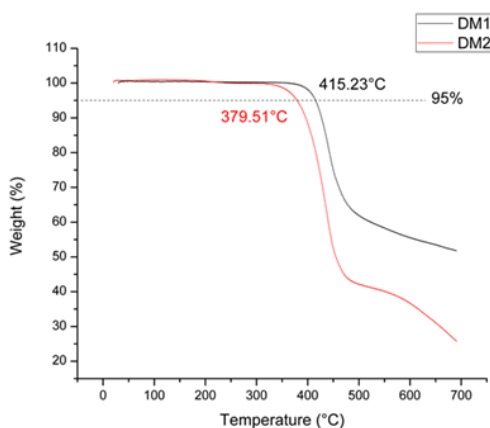


Figure 24: TGA analysis of DM1 and DM2

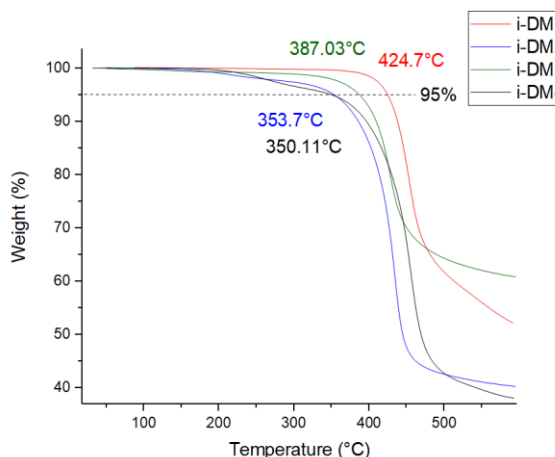


Figure 25: TGA analysis of iDM1, iDM2, iDM3 and iDM4

More specifically, a plateau that extends to around 350 °C is observed for all the compounds. The more stable compounds are DM1, DM3, iDM1 with T_d= 415, 387 and 424 °C respectively. It is worth noticing that the presence of a phenyl group linked to an amine from a carbazole unit gives more stability to the compounds, raising the decomposition temperature. It is well known that aromatic rings give extra stability compared with alkyl derivative chain molecules. Molecules with π -systems, like benzene, stabilized by resonance, confer an extra thermodynamic stability compared with alkyl chains, raised from the interaction between different π -system containing molecules and the inherent stability of resonance of π -system and stacking effect. The benzene dimer is the prototypical system for the study of π -stacking with a calculated bond energy of 8–12 kJ/mol.¹⁹⁵ Thus, to be able to degrade the DM1, iDM1 and iDM3 molecules, an extra energy contribution has to be given, which can be translated as a temperature increment for the T_d in molecules with an extra aromatic ring.

Concerning to thermal properties, all the compounds were analyzed by Differential Scanning Calorimetry (DSC). In general, two cycles were recorded from 0°C to 250 °C with a sweep increment of 20 °C/min under Argon flux.

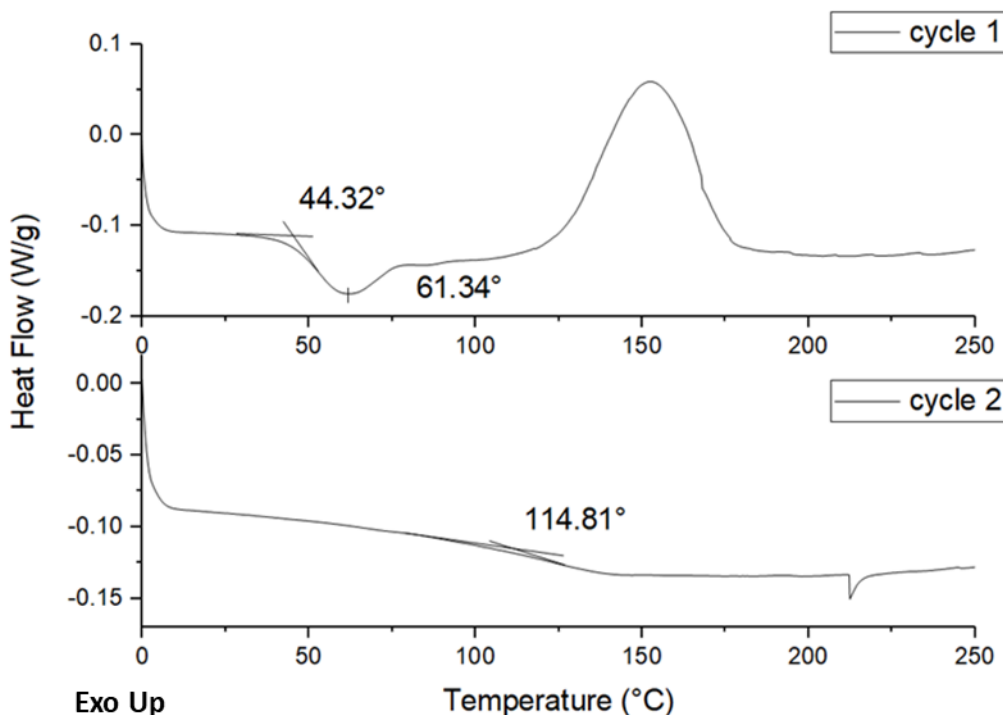


Figure 26: DSC curves of DM1

The first compound, DM1 shows an atypical DSC curve in a temperature range from 0 to 250°C repeated for two cycles (*Figure 26*). During the first cycle, two thermal phenomena occur at 44.3°C and 153°C which could correspond to the T_g of the DM1 and polymerization temperature of the compound respectively. During the last cycle, only one endothermic event is observed around 114.8°C. One hypothesis could be that this temperature is attributed to the glass transition temperature of the corresponding polymer (or oligomer) obtained from DM1 polymerization.

In order to complete our characterization on thermal properties on DM1, a DSC at low temperature under 150°C was carried out.

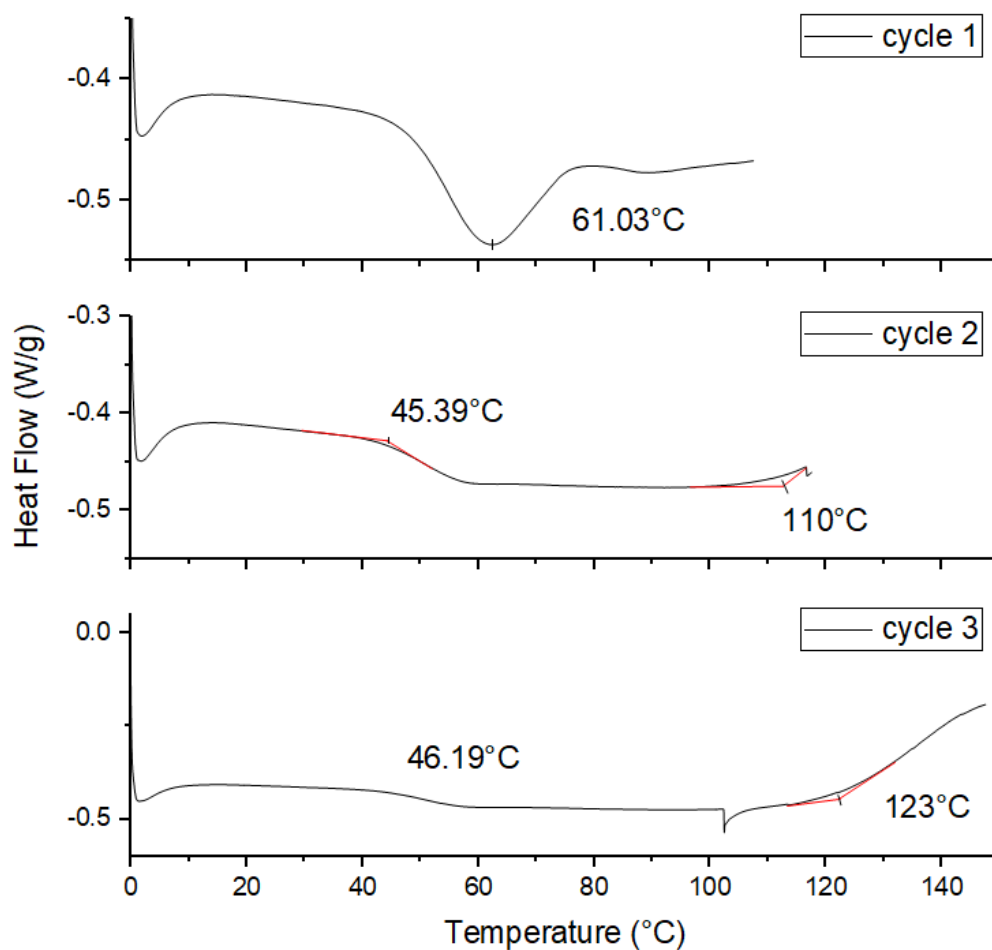


Figure 27: DSC low temperature experiment of DM1

The compound DM1 (Figure 27) during the first cycle exhibited firstly an endothermic event that resembles to a melting point at 61°C. During second and third cycle glass-transition temperature (T_g) at 45°C and an endothermic- process occurs after 110°C which might be the beginning of the polymerization.

Is important to note that after 100°C under DSC conditions DM1 molecule is modified in such way that T_g is modified for what we think is a polymerization.

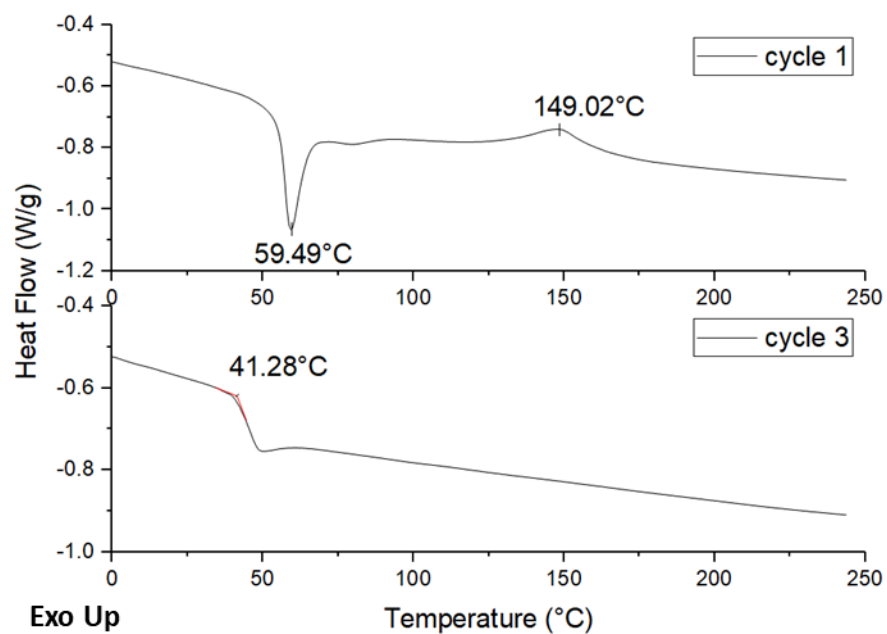


Figure 28 DSC curves of DM2

Concerning DSC of DM2 (Figure 28) two thermic events occur during the first cycle, a melting point and a small exothermic process but after the second and third cycle, compound's behavior remains stable and only one T_g is observed at 41.3 °C. Finally, compounds DM1 and DM2 exhibited glass-transition temperatures at 45.4 and 41.3 °C respectively. Surprisingly, no polymerization peak were observed in high temperature for DM2.

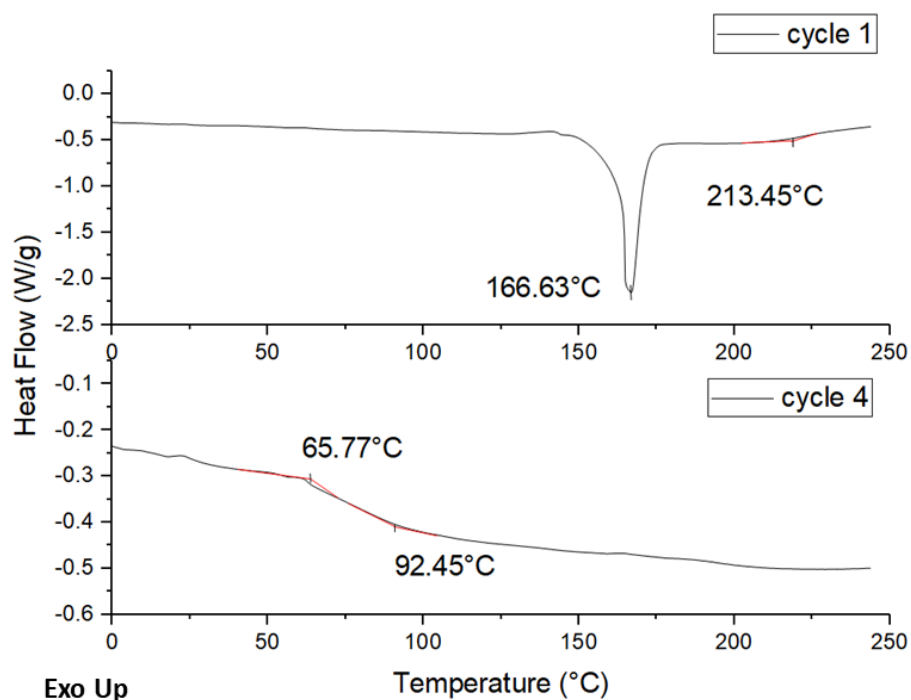


Figure 29 DSC curves of iDM1

DSC curves for 2,7- substituted carbazole based molecule iDM1 (Figure 29) show one melting point during the first scan at 166°C followed by an endothermic process after 213°C during the first cycle. However, this transition is much less pronounced in comparison to its 3,6- isomer DM1. From the second to fourth heating cycle, a glass transition was observed at 66°C. This low T_g suggest that it could not be the T_g of the corresponding polymer, like in the case of DM1 discussed above. The T_g of iDM1 is higher than that of DM1, which could be ascribed to the more steric hindrance of the 2,7- isomer.

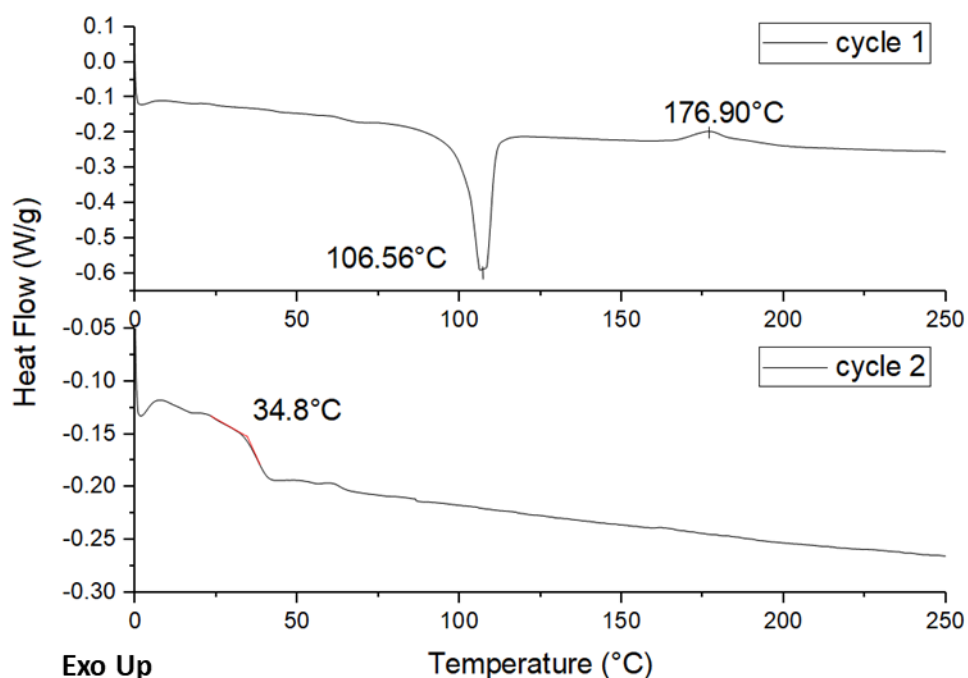


Figure 30 DSC curves of iDM2

When the benzyl side group (in iDM1) at the N-position was replaced by an aliphatic chain (in iDM2), the flexibility significantly increases, thus decreasing the melting point and glass transition temperature. As expected, DSC curves of iDM2 (Figure 30) showed during the first cycle, a melting point of 106°C (166°C for iDM1) followed by a small exothermic process at 176°C. During the second cycle only one T_g is observed at 34.8°C which is the lowest temperature observed for the whole studied compounds. As discussed for DM2, the phenomenon could be attributed to the glass transition of the monomer and no polymer was thermally formed. This curve specially help us to visualize how a long aliphatic chain as substituent dramatically decreases the final glass transition temperature. Low T_g is a non-desirable property since compounds in a real device will be subjected to higher temperatures than the 34.8°C shown by iDM2. Solar cell device under full sunlight irradiation could be heated to around 80°C.

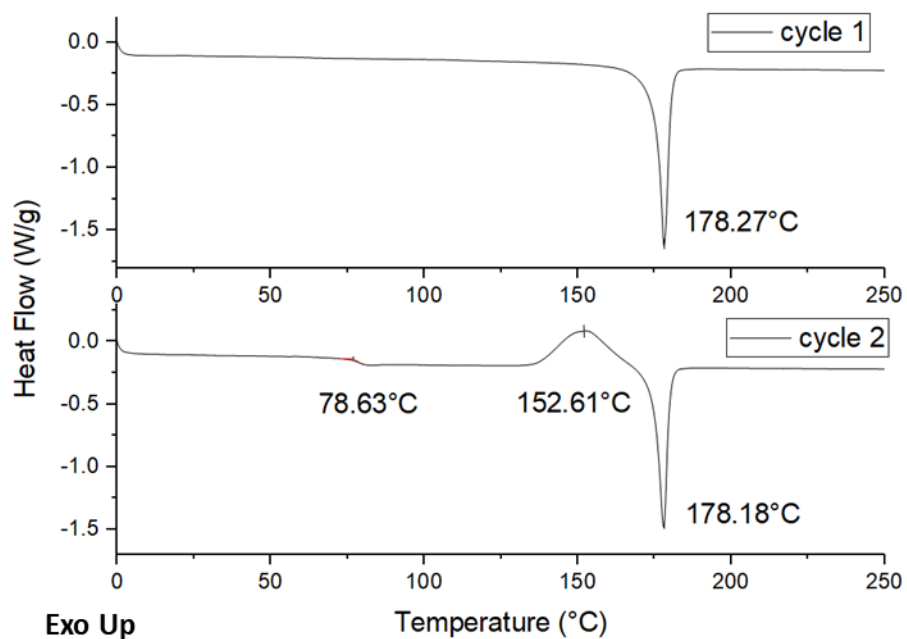


Figure 31: DSC curves of iDM3

The DSC curves of the compound iDM3 (Figure 31) shows during the first cycle an exothermic event considered as a melting point at 178°C. For the second cycle, a glass transition temperature (78°C), crystallization temperature (152°C) and melting point (178°C) are observed. The compound has both higher T_m and T_g in comparison with iDM1, attributed to its less flexible structure than that of iDM1 due to the absence of the flexible ethylene moiety.

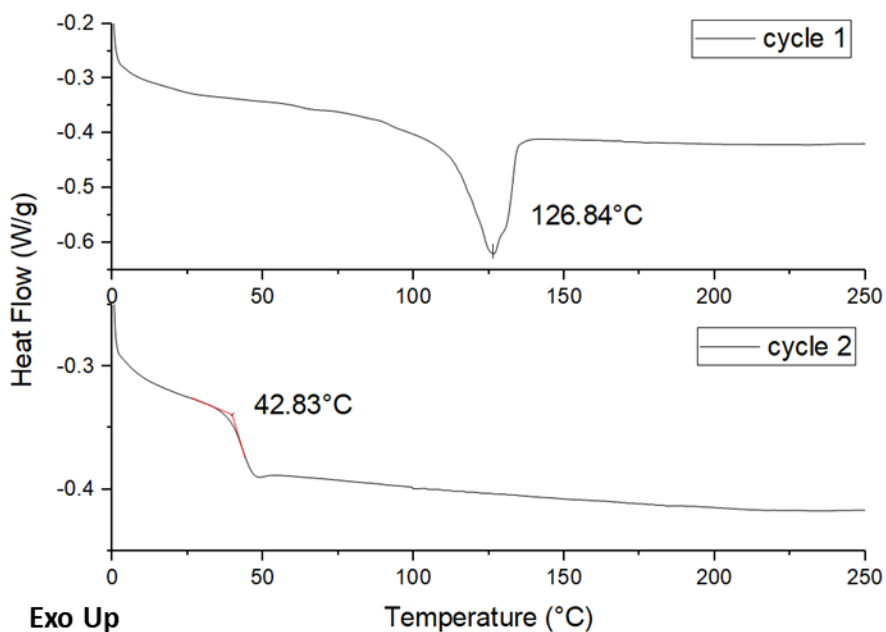


Figure 32 DSC curves of iDM4

As for iDM1 in comparison with iDM3, compound iDM4 disposes higher glass transition and melting point temperature in comparison with that of iDM2, thanks to the shorter aliphatic chain, thus less flexible configuration. DSC curves of iDM4 (Figure 32) during the first cycle a with only one endothermic event at 126°C, with no further crystallization (exothermic) process as for iDM3 case. During the second cycle, only one glass transition temperature is observed at a relative low temperature 42°C.

The thermal properties (T_d , T_g and T_m) of DMx and iDMx series are summarized in the Table 4

Table 4 Thermal properties decomposition, exothermic event and glass transition temperatures of DMx and iDMx series.

Compound	$T_d(^{\circ}\text{C})$	Exo E. ($^{\circ}\text{C}$)	$T_g (^{\circ}\text{C})$	Compound	$T_d(^{\circ}\text{C})$	Exo E. ($^{\circ}\text{C}$)	$T_g (^{\circ}\text{C})$
DM1	415	61	45	iDM1	425	166	65
DM2	379	59	41	iDM2	353	106	34
				iDM3	387	178*	78
				iDM4	350	126	42

As summarized in Table 4, some general trends are observed for these two series.

- All compounds are thermally stable with decomposition temperatures higher than 350°C, which are high enough for application in electronic devices.
- The 2,7-isomer iDM1 and iDM3 are thermodynamically more stable with higher T_g which is ascribed to the higher molecular steric hindrance.
- In both families, DMx and iDMx melting points are lower for alkylated substituted molecules than for those with phenyl substitutions. This can be explained by considering that linear alkane chains present many possible conformations, and thus are more geometrically irregular leaving more space on average between the molecules. Phenyl rings are a rigid structure, and so molecules containing them are more sterically constrained and have much less of motion around C=C bonds; this allows for the molecules to be, on average, closer to each other, providing, in turn, higher Van der Waals interactions derived from π -interactions, and consequently increasing their melting temperature.¹⁹⁶
- Targeted compounds with alkene moiety on the side chain have distinct DSC features in comparison with non-alkene containing molecules, showing an exothermic transition at high temperature, which could be lead to the formation of the oligomers/polymers. This transition was completely absent from the DSC curves of the non-alkene containing iDM3 and iDM4 compounds.

Clearly we can observe that thermodynamically speaking carbazole based molecules substituted on the position 2,7- are more resilient to thermal treatment, making of them a more reliable solution as HTM on photovoltaic devices on thermodynamic terms. These results come to be a surprise due to the lack of 2,7- substituted carbazole molecules on the literature where instead predominates research based on 3,6- carbazole HTMs.

2.4.2 Optical properties

The optical absorption properties of DMx and iDMx series were investigated in both, dichloromethane (DCM) solution and spin-coated thin film over a quartz glass substrate. UV-vis absorption spectra of the DMx series are presented in *Figure 33*. As can be seen, both compounds

have identical optical absorption features, both in solution and in solid state. DMx compounds series bearing 3,6-substituted carbazole, have π - π^* absorption band observed at 275–350 nm with a maximum peak at 310 nm, and less intensive lower energy absorption bands, that can be assigned as n - π^* bands observed at >350 nm.

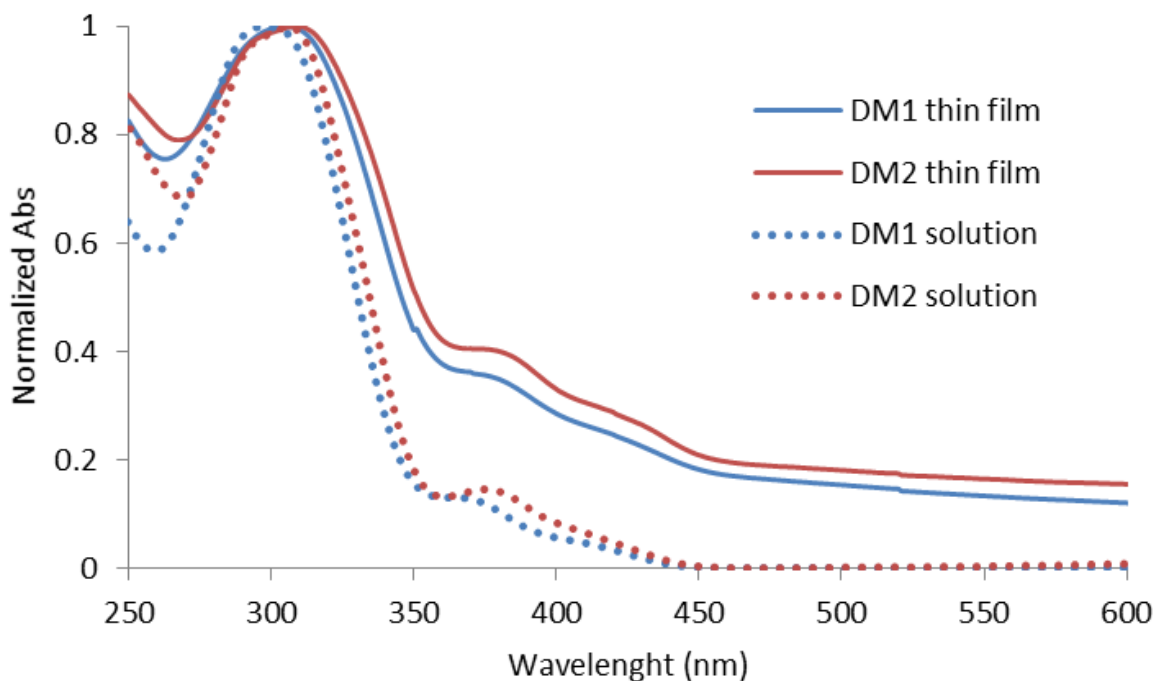


Figure 33: UV-vis spectra of DM1 and DM2 in solution and thin film

Film absorption experiments show a slight bathochromic shift to longer wavelength value (less than 5 nm) values. Consequently, we presume a low nanostructuration appearing on film at room temperature. The presence of phenyl group in DM1 induce a negligible a π - π stacking effect on film.

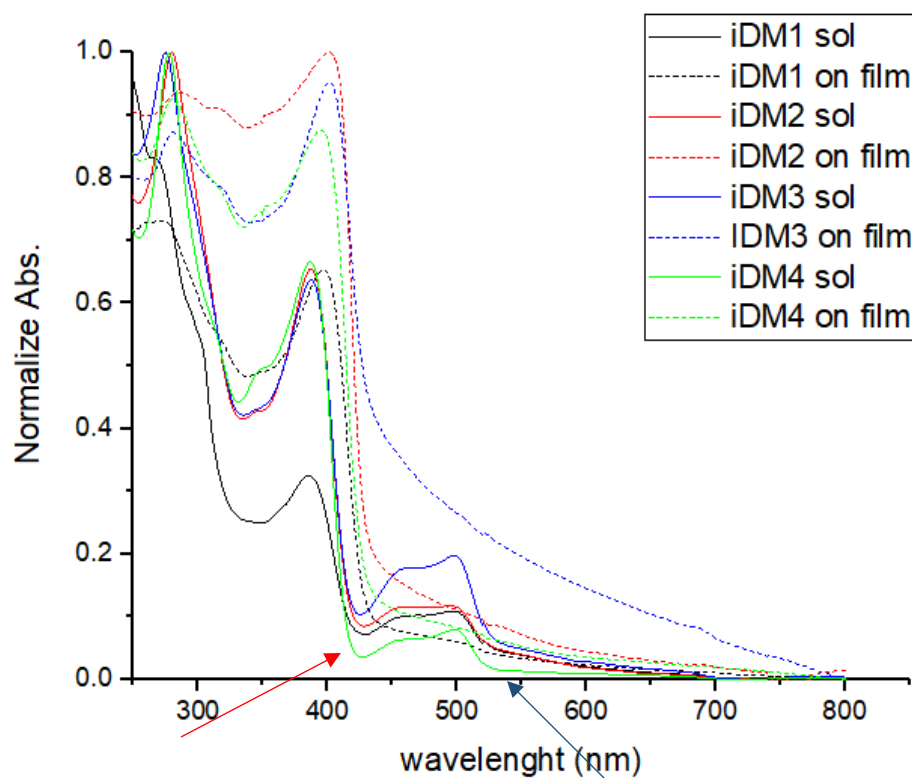


Figure 34 UV-vis spectra of iDMx series solution and thin film

The absorption of iDMx series is given in Figure 34. Compared to 3,6-substituted carbazole, the same pattern is observed on film for the iDMx series bearing 2,7- substituted carbazole, with a π - π^* absorption band is observed at 350–430 nm with a maximum peak at 400 nm. Moreover, a new absorption band is also observed around 500 nm that is absent in the DMx isomer counterparts. The main interpretation for this peak resides on the fact that molecules are partially oxidized. iDMx oxidized molecules present a new peak in visible domain. This has been demonstrated Leijtens *et al.*¹⁹⁷ through the partial oxidation of a 2,7-substitued carbazole molecule named EH44 with silver tetrafluorosulfonimide (TFSI) resulting in a new absorption band close to 500 nm. Same behavior was observed by Spiro-OMeTAD¹⁹⁸ after being oxidized with the TFSI were results showed improved operating stability for solar cells manufactured with Spiro-TFSI. This tendency of iDMx to oxidation could have some benefits on its application on solar cells devices, relying on the fact that HTM must be partially oxidized by dopant agents influencing its hole transport properties.

On thin film measurements, 500 nm peak disappears, certainly due to its low absorptivity, where such peak is overlapped by the main absorption curve. For our purposes, the absorption onset indicated with a red arrow (Figure 34) was used to calculate the HOMO-LUMO bandgap.

For the iDMx series of 2,7-substituted carbazole, bathochromic shift of the $\pi-\pi^*$ absorption band is observed, in comparison with 3,6-substituted analogues due to the larger π -conjugated system that goes through carbon-carbon bond in the carbazole core. Absorption of the iDMx series is somewhat closer to that of Spiro-OMeTAD (306, 385 nm)¹⁹⁹. In general, both compounds series absorb mostly in the UV region with a very weak absorption in the visible range of spectrum, which is advantageous for the application in the PSC, as HTM absorption contribution will not be significant competing.

Finally, we can conclude that light absorption of both series are appropriate for photovoltaic means and no significant parasitical light absorption with perovskite material is observed, making of both of series viable candidates for perovskite solar cells.

2.4.3 Electrochemistry measurements

The redox properties of the two series were studied by electrochemical cyclic voltammetry (CV) in dilute solution. Cyclic voltammograms of DMx and iDMx series were prepared with a concentration 1.0×10^{-3} M, recorded in 1.0×10^{-2} M TBAPF₆/CH₂Cl₂ solution and scan rate was 100 mV s^{-1} .

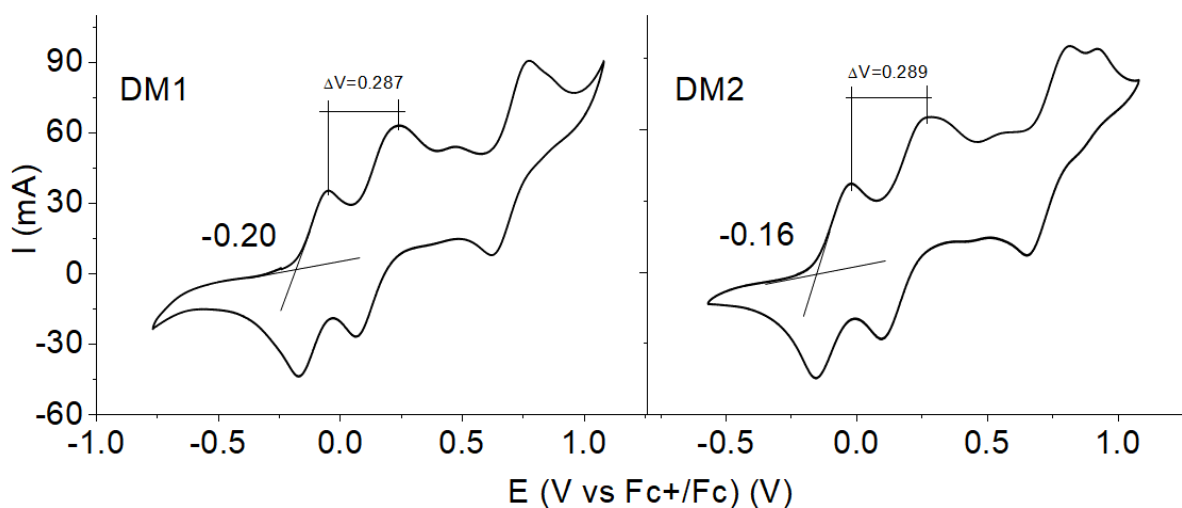


Figure 35 CV curves of DM1 and DM2

The CV curves corresponding to 3,6- carbazole compounds (*Figure 35*) display three reversible oxidation potentials. Usually the peak at higher potential values is assigned to the carbazole core. The first two peaks are assigned to the peripheral amines in positions 3- and 6- are attributed to the sequent oxidation of the two 4-methoxydiphenylamine (DPA) moieties by a single electron transfer processes. Both compounds possesses well defined oxidation states, reflected on a gap between oxidation peaks (ΔV) of around 0.29 V.

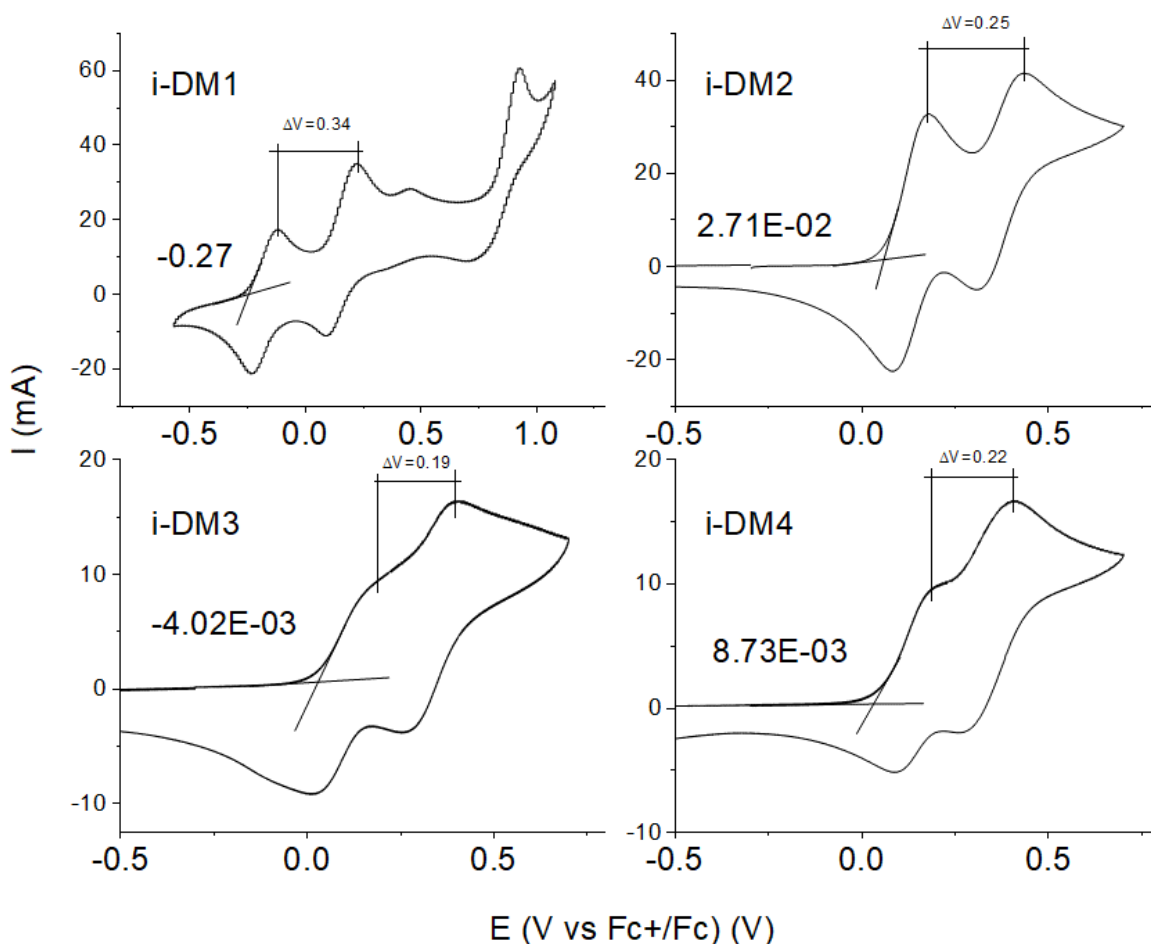


Figure 36 CV curves of iDMx series

Cyclic voltammetry curves of iDMx series (*Figure 36*) present the same behavior as DMx series counterpart. Two oxidation peaks, assigned to both amine groups are observed for the four molecules. Interestingly iDM2, iDM3 and iDM4 have higher oxidation onset than iDM1 by ≈ 0.06

V. iDM1 shows higher potential gap between the first and second oxidation peaks, which can be translate as a very well defined oxidation states on the molecule. By observation and practical experience the bigger the gap between oxidation peaks (ΔV) better the electronic performance. Thus for our purposes $\Delta V = 0.34$ V is a good sign of its hole mobility property.

The later proposal is based on the fact that after $1e^-$ subtraction (Figure 37), the first oxidation state, generates a radical-cation, which has different possible resonance structures that stabilizes the radical-cation structure. Such radical cation helps and enables its carrier property function. After $2e^-$ subtraction, on the second oxidation state, two positive charges are locked over each nitrogen atoms.

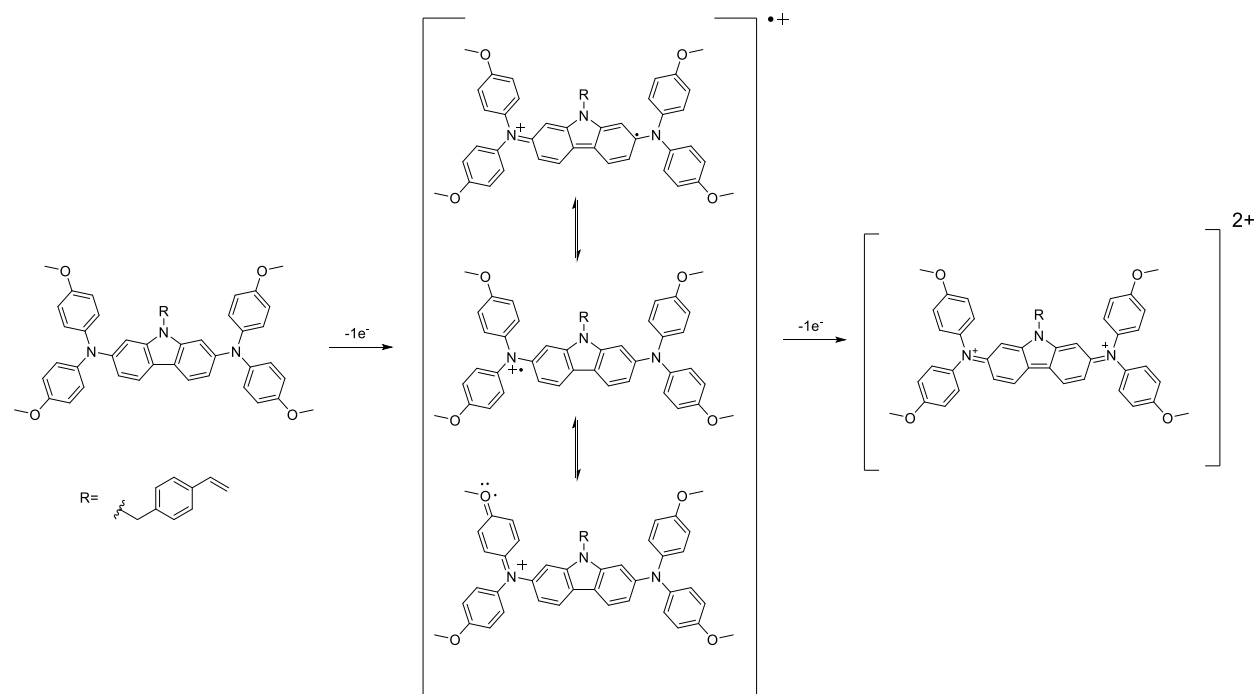


Figure 37 Proposed resonance structures for iDM1 radical-cation and dication

Table 5 DMx and iDMx potential values

Compound	E_{Ox1} [V]	E_{Ox2} [V]	ΔV [V]	E_{Red1} [V]	$1E_{ox/red}$ [V]
DM1	-0.04	0.23	0.28	-0.17	-0.11
DM2	-0.01	0.27	0.28	-0.15	-0.08
iDM1	-0.12	0.22	0.34	-0.23	-0.17
iDM2	0.18	0.43	0.25	0.08	0.13
iDM3	0.19	0.38	0.19	0.01	0.10
iDM4	0.18	0.40	0.22	0.08	0.13

Table 5 summarizes the oxidation potentials, the potential difference between first and second oxidation peak and the calculated standard potential of both series. From all revised compounds, iDM1 show the most atypical values, showing the lowest standard potential and the higher delta between their two oxidation peaks. Such results implies that styrene group is definitely playing a role on the electrical behavior of the molecule, while the phenyl without styrene group (iDM3) substituted molecule has, on the contrary the lowest $\Delta V = 0.199$ V of both series. Our first suggestion to explain this phenomenon relays on the steric effect derived from vinyl group on iDM1 that involves an arrangement over the DPA moieties. Nevertheless, as it can be seen on DFT modelisation results (chap.2.4.5), both structures (iDM1 and iDM3) are similar between each other with no significant differences. Otherwise, photovoltaic performance of both molecules could give a hint of such issue.

2.4.4 General physical properties table of DMx and i-DMx series

Electrochemical characterization along with the optical information allows to calculate experimentally the values of HOMO-LUMO energy levels. Experimental values of the DMx and iDMx series are shown in *Table 3* and plotted on *Figure 38* and *Figure 39*, and compared to perovskite levels and the HTM reference standard Spiro-OMeTAD. Found values for all the proposed molecules are suitable for the HTM role for PSCs. Their HOMO energy levels are higher than that of the perovskite, thus, enabling an efficient hole transfer from perovskite toward the HTM layer. Their high-lying LUMO level suggest that they have electron-blocking property, avoiding recombination at the perovskite/HTM interface.

The general table helps to compare physical and optoelectronic values of the studied series DMx and iDMx. As it was noted previously, in general, iDM1 and iDM3 (those bearing N-substituted phenyl rings) from iDMx serie are thermodynamically more stable than is counterpart DM1.

Table 6 General thermal, optical and electronic characteristics of DMx and iDMx

Compound	T _d (°C) ^[a]	T _g (°C) ^[b]	λ _{max} (nm) ^[c]	λ _{onset} (nm) ^[c]	E _{gap} (eV) ^[d]	E _{ox} (V) (Fc/Fc ⁺)	HOMO ^[IP] (eV)	LUMO ^[EA] (eV)
DM1	415	45	305, 375	443	2.80	-0.20	-4.60	-1.80
DM2	414	41	307, 372	444	2.80	-0.16	-4.65	-1.85
iDM1	424	65	264, 389	425	2.92	-0.27	-4.53	-1.61
iDM2	356	38	348, 385	424	2.92	0.03	-4.83	-1.91
iDM3	390	78	340, 385	426	2.91	0.00	-4.80	-1.89
iDM4	350	43	346, 383	427	2.90	0.01	-4.81	-1.90

^[a]Obtained from TGA measurements. ^[b]Obtained from DSC measurements. ^[c] Measured in CH₂Cl₂ solution 1 x 10⁻⁶ M. ^[d] Measured in CH₂Cl₂ 1.0 x 10⁻² M TBAPF₆ solution. Analyte 1 x 10⁻⁴ M. All E_{ox} data are reported relative to ferrocene²⁰⁰ which has a value of ionization potential (IP) 4.8 eV for ferrocene and 0.27 V for Fc/Fc⁺ against Au/Au⁺. The concentration of the complexes used in this experiment was 1.0 x 10⁻³ M and scan rate was 100 mV s⁻¹. E_{gap}= hc/λ_{onset}= 1240 eVnm/λ_{onset}; IP=E_{ox}+4.8; EA = IP - E_{gap}

The HOMO-LUMO values of DMx represented on Figure 38, shows how close they are compared with Spiro-OMeTAD. This leads us to propose that DMx could have a good performance as HTM.

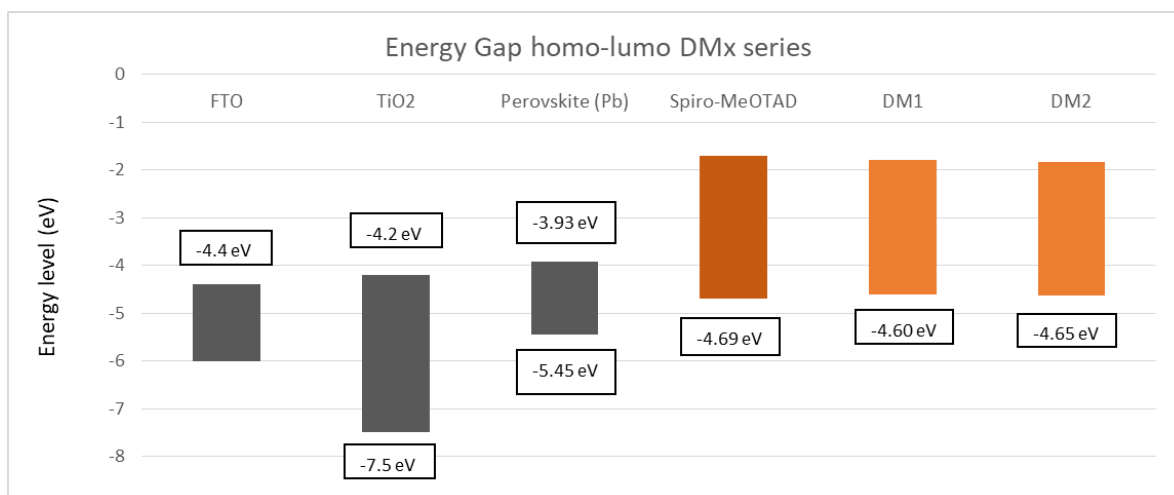


Figure 38 HOMO-LUMO values of DMx series

Except for iDM1, iDMx series, which has a slightly deeper HOMO values that bring them closer to the HOMO from perovskite layer. The later could be a hint for a good hole extraction property. All compounds energy values are quite close from each other indicating thus a small influence over the HOMO-LUMO, derived from substitution position and the group attached to the N atom on the carbazole core.

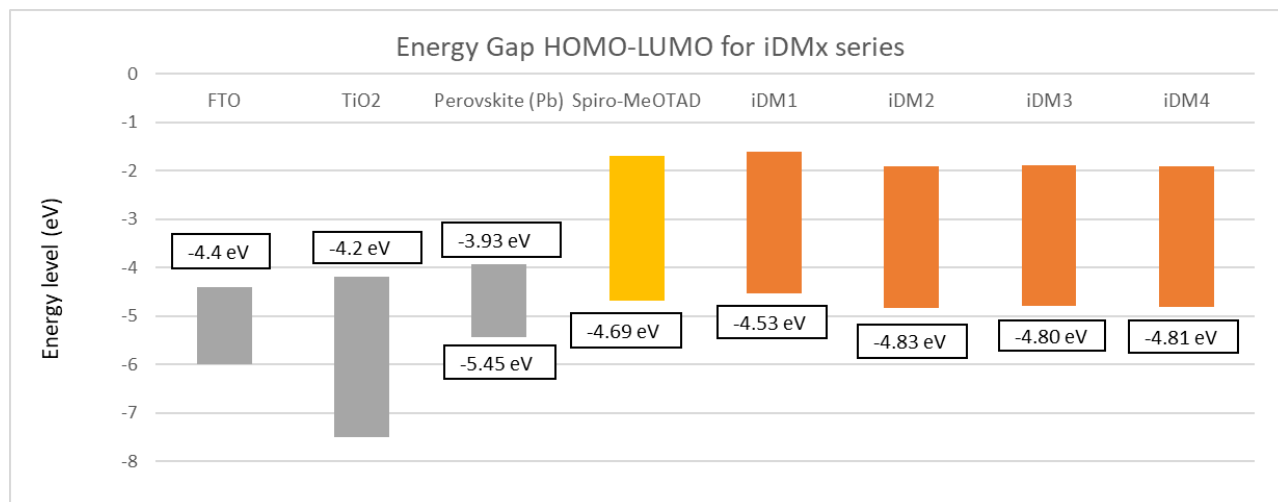


Figure 39 HOMO-LUMO values of iDMx series

Moreover, optical properties studied through UV-vis spectroscopy show a suitable light absorption by the DMx series, with more red shifted absorption in comparison with the iDMx. This absorption do not compete with perovskite so, no screen effect is expected.

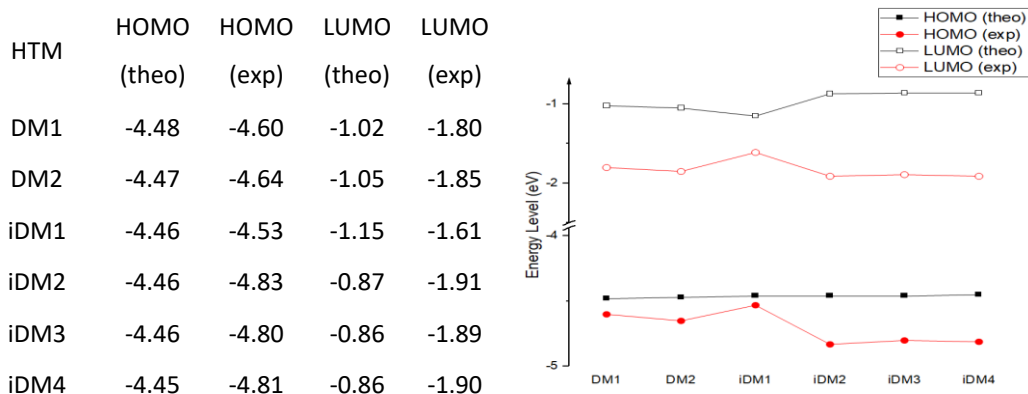
The last information represents what theoretically is a good candidate HTM for PSCs. Nevertheless, different factors must be observed in order to perform as a good HTM. Parameters as hole mobility and drift velocity can give also a more accurate clue of its final performance. Other factors like the interaction with the perovskite layer are difficult to predict but still quite important. In our case, the compounds with the previously showed molecular orbital (MO) energy values, thermal and optoelectronic properties are worth enough to test them on real devices and analyze their performance.

2.4.5 Computational studies

All molecular geometries for DMx and iDMx were optimized using density functional theory (DFT) calculations. Calculations were carried out using Gaussian 09²⁰¹ suite of programs.

Ground state geometries of DMx and iDMx series were fully optimized without imposing any symmetry constraints by employing the 6-31G(d,p) basis set. HOMO and LUMO energy levels are modeled, as shown in *Figure 40* and *Table 7*. The HOMO distribution for both series is localized along the whole molecule, that implies good charge distribution. For those molecules bearing an N-alkyl (DM2, iDM2, iDM4) and N-benzyl (iDM3) substitution, the LUMO orbital main contribution is localized on the carbazole core, whereas DM1 and iDM1 present a different LUMO distribution, localized on the styrene moiety separated of the entire molecular skeleton. The observation indicates that styrene's role could have some influence on the electronic features for DM1 and iDM1 molecules. Nevertheless, LUMO level for an HTM in a PSC is not involved on the final operation of the PSC.

Table 7 Calculated MO values against experimental of DMX and iDMX



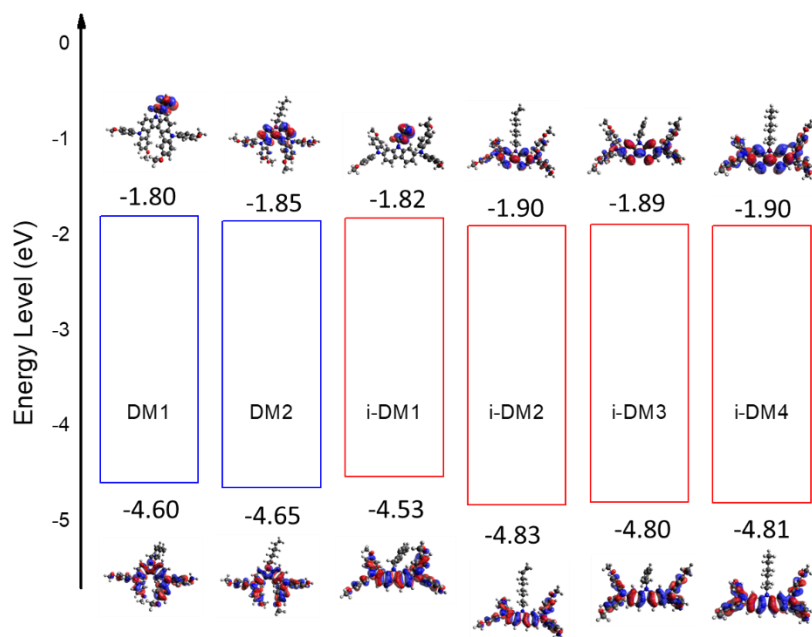


Figure 40 Calculated energy values for DMx and iDMx

HOMO and LUMO energy levels of DMx and iDMx series show very close values in accordance with those found experimentally, especially for HOMO location. Considering that DFT calculation is made on gas phase, the energy difference between theoretical and experimental values resides on the interaction between several molecules on solution giving thus differences between calculated and experimental values.

Moreover, DMx and iDMx show a tridimensional structure with $\approx 70^\circ$ on their dihedral angles between carbazole and benzene rings contained on the DPA groups, decreasing thus the possibilities to form regular aggregations that conduct to a crystalline state. Is important to note that none of the DMx and iDMx compounds where able to form crystals, which can be partially confirmed by the 3D models of the molecules.

2.4.6 Surface morphology studies by atomic force microscopy

The standard procedure to deposit an HTM film is by the spin coating method. After the HTM deposition is important to observe the quality and topology of the HTM films. The quality of the film is essential in order to decrease the charge trap and charge recombination and thus attaining better contact with the cathode which is expected in a hole mobility improvement. Optimal interface morphology between the hole transport layer and the metal electrode can be

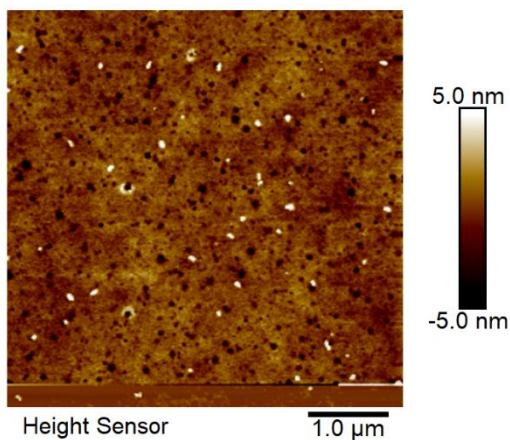
partially confirmed by the surface quality of HTM,²⁰² which is likely to result in an overall enhancement of J_{sc} , V_{oc} and FF.

Morphology of DM1, DM2 and iDM1 (*Figure 41*) made films with additives over glass substrates are studied by Atomic Force Microscopy (AFM).

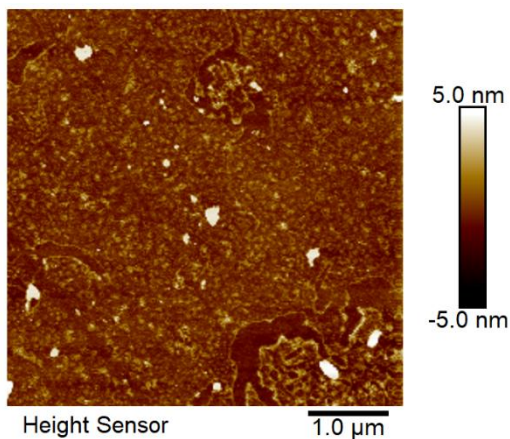
The films were made using the following procedure. A solution was prepared by dissolving 72 mg of HTM in 1 ml chlorobenzene. Then, 17.5 μ L of bis(trifluoromethylsulfonyl)imide lithium salt solution (LiTFSI) solution (520 mg in 1 mL ACN), 28.8 μ L of TBP (tert-butylpyridine) and 6 μ L of tris(2-(1H-pyrazol-1-yl)-4-tert-butylpyridine)cobalt(III)tri[bis(trifluoromethane)sulfonimide] (FK 209 Co(III) TFSI salt) (300 mg in 1 mL ACN) were added to this solution. Using 35 μ L of the HTM solution, the film is spin-coated at 4000 rpm, with an acceleration of 4000 rpm/s during 20 s.

Compound

DM1



DM2



iDM1

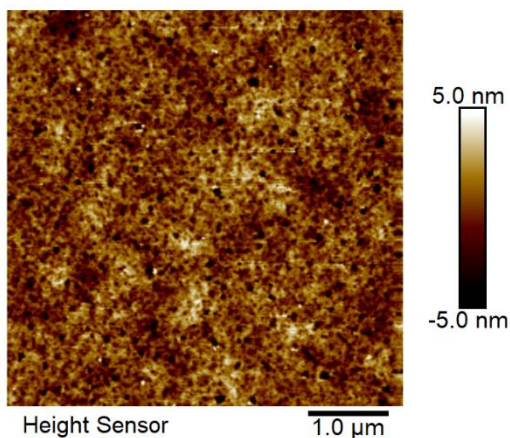
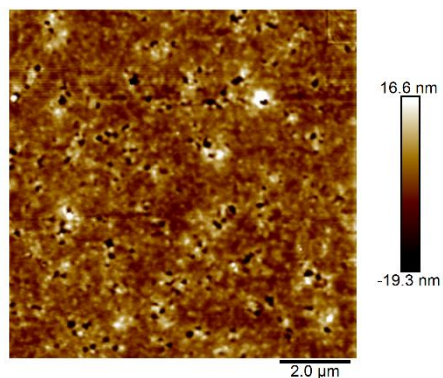


Figure 41 DM1, DM2 and iDM1 films AFM images

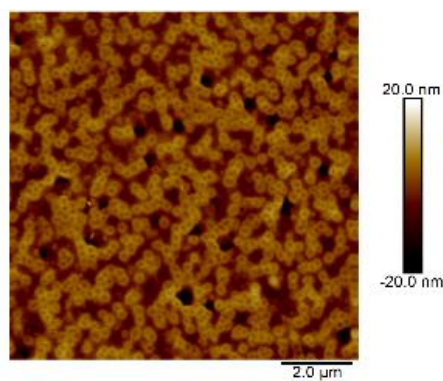
Homogenous surface for iDM1, DM1 and DM2 with root mean square roughness (R_q) values of 1.59, 1.60 and 0.96 nm are observed. From a general perspective, all compounds tend to form continuous films with low aggregates. More particularly, iDM1 seems to have a smoother surface with homogenous coating. This result could be related to the good solubility index and film formation ability observed during experiments.

Compound

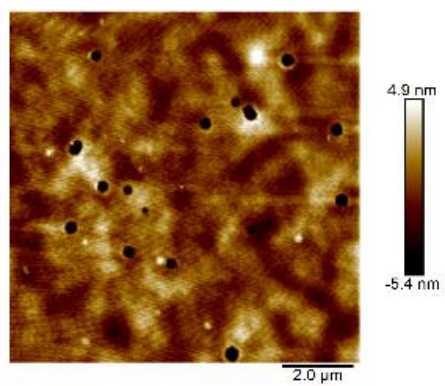
iDM1



iDM2



iDM3



iDM4

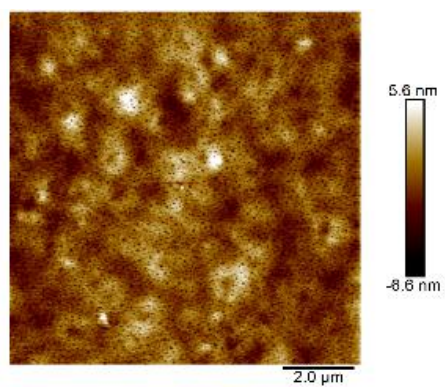


Figure 42 iDMx film AFM images

Morphology analysis (Figure 42) and roughness measurements (Table 8) of iDMx reveal a smooth surface, with relatively compact, continuous layers which display no abrupt grain formation with a root mean square roughness (R_q) close to the roughness standards of the hole transport layer that eventually will be reflected on a better the charge transport property. However, aggregate sizes are more visible from iDM2 and also iDM3 and iDM4 (from 300 nm to 500 nm). This morphology differences could be one of the causes of the low photovoltaic efficiency values for iDM2 and iDM4 revised on chapter 2.5.1. Certainly, a poor interface contact with the metal top electrode could explain such low performance, involving high charge trap and charge recombination rate.

Table 8 Root mean square roughness (R_q) and arithmetical mean deviation (R_a) for iDM1, 2, 3 and 4

Compound	R_q	R_a
iDM1	1.60	1.03
iDM2	3.38	4.25
iDM3	1.2	1.69
iDM4	1.27	1.64

2.5 Photovoltaic measurements

Device elaboration (Figure 43) and photovoltaic results have been carried out in *the Institut de Recherche de Chimie Paris* with Professor T. Pauporté's team.

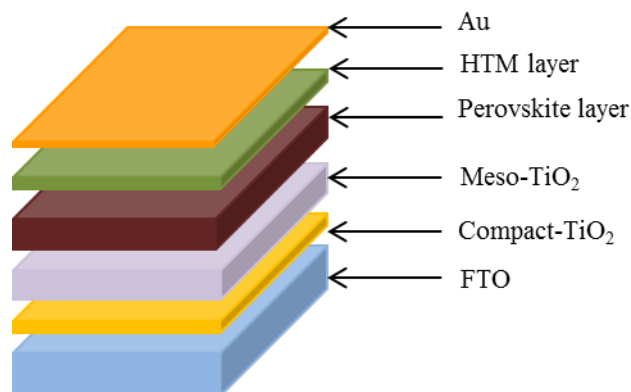


Figure 43 PSC diagram of configuration FTO/blocking layer TiO₂/mesoporous-TiO₂/CH₃NH₃PbI₃/HTM/Au

Substrate

The F-doped tin oxide coated glass (TEC7, Pilkington) was cut, and etched patterned using HCl 10% and Zn powder. They were then cleaned by using a concentrated 2.5 mol.L⁻¹ NaOH solution, rinsed with water, clean with a detergent, rinsed with MilliQ water and dried with compressed air. The substrates were then annealed 30 min at 500°C.

Blocking layer

A precursor solution was prepared by mixing 0.6 mL of titanium isopropoxide (TTIP), 0.4 mL of acetyl acetone in 7 mL of isopropanol. The substrate was placed on a hotplate at 455°C for 20°C prior to start the spraying. The deposited layer was then annealed at 455°C for 20 min before to let it to cool down. 50µL of this solution was deposited on the substrate, spin-coated at 4000 rpm for 35s and then placed on a hot-plate at 60 °C for 10 min. Finally annealed at 500°C for 30 min. The thickness of this layer is around 30-35 nm (Figure 44).

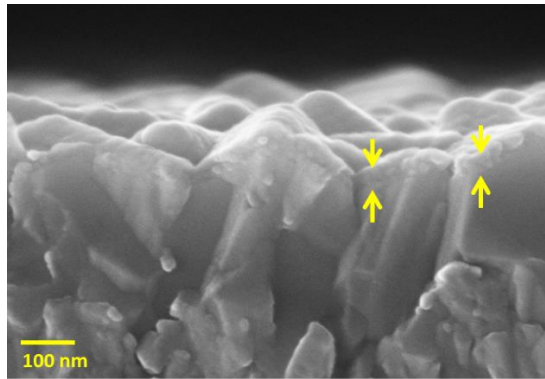


Figure 44 Cross-sectional SEM view of blocking layer

Mesoporous layer

The mesoporous TiO_2 layer was prepared by diluting the NR30-D paste from Dyesol with ethanol (1:10 mass ratio). 50 μL of the solution was deposited on the blocking layer and spin-coated 20s at 5000 rpm. The layer was then dried on a hotplate at 100°C for 10 min and subsequently annealed at 500°C for 30 min. The average thickness is 100-150 nm.

Perovskite layer

2-step (DM1, DM2, DM1P, iDM1)

The $\text{CH}_3\text{NH}_3\text{PbI}_3$ (MAPI) layer was prepared using a 2-step technique. 50 μL of a PbI_2 precursor solution consisting of acidified 1 mol.L^{-1} PbI_2 in DMF was spin-coated at 4000 rpm for 30s. Then, 100 μL of a methylammonium (MAI) solution containing 40 mg of MAI in 1 mL of 2-propanol was deposited on the PbI_2 layer, left to react for 20s and spun at 4000 rpm for 30s. The perovskite layer was annealed at 115°C for 1h on a hotplate. The samples were then removed from the hotplate and left to cool down to room temperature during 10 min.

1-step (B74, B186, iDM1, iDM2, iDM4, DM1, DM2, DM1P)

The $\text{CH}_3\text{NH}_3\text{PbI}_3$ (MAPI) precursor solution was prepared by mixing 553 mg of PbI_2 and 190 mg of MAI (Dyesol) in 1 mL of DMSO solvent. The solution was heated at 70°C until full dissolution. 50 μL of this solution was deposited on the substrate, and spin at 6000 rpm for 35s. The layer was dripped with 100 μL chlorobenzene after 25s. The perovskite layer was finally annealed at 105°C for 1h on a hotplate. The samples were then removed from the hotplate and let to cool down to room temperature during 10 min. The cells prepared with this perovskite layer are denoted MAPI in the following. The layer thickness is around 290-330 nm.

HTM layer

All HTM layers were prepared by following procedure. A solution was prepared by dissolving 72 mg of HTM in 1 ml chlorobenzene. Then, 17.5 μ l of bis(trifluoromethylsulfonyl)imide lithium salt solution (LiTFSI) solution (520 mg in 1 mL ACN), 28 μ L of TBP (tert-butylpyridine) and 6 μ L of tris(2-1H-pyrazol-1-yl)-4-tert-butylpyridine)-cobalt(III)-tris(bis(trifluoromethylsulfonyl)-imide) (300 mg in 1 mL ACN) were added to this solution. 35 μ L of the HTM solution was spin-coated at 4000 rpm for 20 s. The thickness of this layer is around 200 nm.

Gold contact

Finally, the device was completed by thermally evaporating a 70-80 nm thick gold back contact on the HTM layer.

2.5.1 Characterization of solar cells

J-V measurements

The *J-V* curves were recorded by a Keithley 2400 digital source-meter, using a 0.10 V.s⁻¹ voltage scan rate. The solar cells were illuminated with a solar simulator (Abet Technology Sun 2000) filtered to mimic AM 1.5G conditions. The illuminated surface was delimited by a black mask with an aperture diameter of 3 mm. The power density was calibrated to 100 mW.cm⁻² by the use of a reference silicon solar cell.

2.5.2 Analysis and discussion

2.5.3.1 Photovoltaic performance of DMx

The DMx compounds were tested in a PSC with the configuration FTO/blocking layer TiO₂/mesoporous-TiO₂/CH₃NH₃PbI₃/HTM/Au and the results are shown in Figure 45 and Table 9.

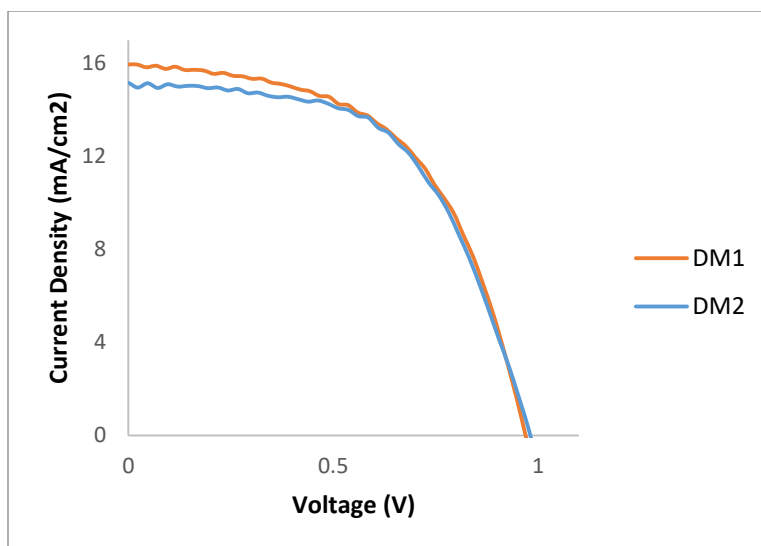


Figure 45 Photovoltaic performance of DMx

Photovoltaic performance (Figure 45 and Table 9) of DM1 and DM2 show a high short circuit current (J_{sc}) and power (V_{oc}) but low fill factor, as consequence a lower efficiency is obtained. Same V_{oc} and FF implies that the role of moiety attached on the N atom has a small or insignificant influence on the final performance. Same interface conditions are inferred from the observed morphologies by AFM experiments. Even if the thermal properties are different between DM1 and DM2 this do not reflected on the photovoltaic results.

Table 9 Photovoltaic results of DMx series

HTM-Layer	V_{oc} (V)	J_{sc} (mA cm ⁻²)	FF	PCE (%)
Spiro-OMeTAD	1.01	22.1	78.7	17.7
DM1	0.96	22.6	54.5	11.9
DM2	0.97	21.3	56.2	11.7

Many parameters could affect the photocurrent, for example the film quality, nanoscale morphologies (with stacking effect or not) and recombination rate (depending of additives quantity). Photovoltaic performances for DMx series are lower than Spiro-OMeTAD (17.6%) standard but still, they are promising considering that different steps could be optimized as notably additive quantity and HTM coating process with thermal step.

2.5.3 Photovoltaic performance of iDMx

In the same way that DMx molecules, iDMx series was tested using the configuration FTO/blocking layer TiO₂/mesoporous-TiO₂/CH₃NH₃PbI₃/HTM/Au. Results and discussions will only concern IDM1, IDM2, IDM4 and the Spiro-OMeTAD as reference. Main results are summarized in Figure 46 and Table 10. Unfortunately, due to a problem with the host laboratory, IDM3 could not be tested on photovoltaic prototypes.

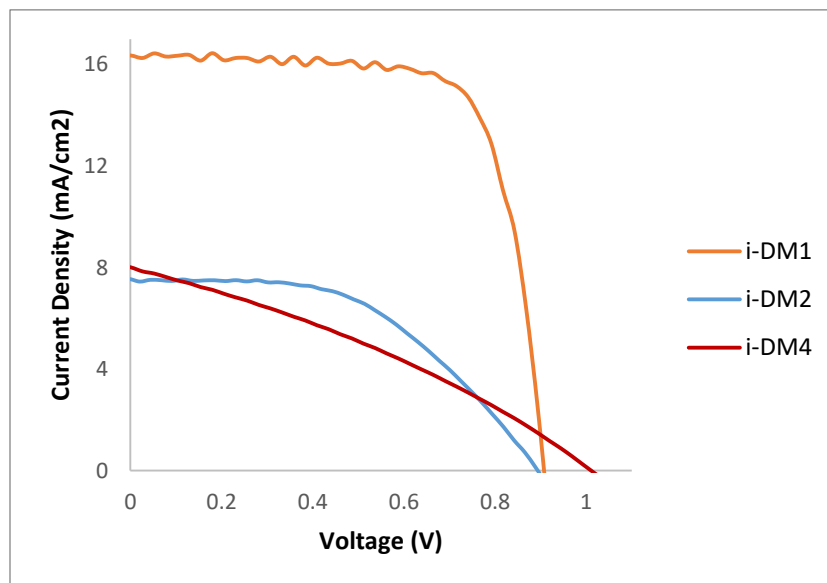


Figure 46 Photovoltaic Performance of iDMx series.

The 2,7-substitued carbazole (Cz) molecule iDM1 shows (Figure 46) the best performance of both molecular series with a PCE of 15.04 %, fill factor 73.4% and short circuit current of 22.59 mA cm⁻². This seems to be a direct consequence of the 2,7-Cz configuration where conjugation goes through the carbon-carbon bonding, being this comparable to the one observed in the Spiro-OMeTAD. In contrast, the rest of iDM2 and iDM4 show a poor performances, which could be a consequence, of its low thermal stability reflected on low T_g values or not well defined oxidation states. The previous results are a surprise even when N-alkyl-2,7-Cz molecules with similar T_g to ours (≈45°C) have been reported with good results^{172,197}.

Table 10 Photovoltaic results iDMx series

HTM-Layer	V _{oc} (V)	J _{sc} (mA cm ⁻²)	FF	PCE (%)
Spiro-OMeTAD	1.01	22.15	78.75	17.68
iDM1	0.90	22.59	73.40	15.04
iDM2	0.89	10.62	50.76	4.80
iDM4	1.00	11.31	32.23	3.68

However, electronic properties of iDM1 are different among the whole group of studied molecules: iDM1 present the lowest oxidation potential, the largest ΔV between first and second oxidation peaks, that can be interpreted as a well-defined single electron oxidation state, smaller bandgap on the iDMx series, good thermal stability and finally a more shift blue UV-vis absorption.

Comparison with DMx results

For the matter of comparison between both series with different substitutions, iDM1 bearing 2,7-Cz substitution, shows a better incident photocurrent conversion efficiency than DMx compounds. This has been recently observed by Zhu et al.¹⁸⁸ where 2,7-Cz rivals the 3,6-Cz in hole extraction as well as hole transport ability. One of their compounds exhibit a better efficiency (16.7 %PCE) than Spiro-OMeTAD (15.0 %PCE) in the same conditions. A possible explanation of this phenomenon is that iDM1 (2,7-Cz) is that in some way, styrene group is playing an important role, either by locking the molecule in a fix position due to steric effect and thus promoting an amorphous-random aggregation or by playing some role on the intermolecular charge transfer capacity. On the other hand, HTMs with larger conjugated as for the 2,7-Cz systems may lead to more efficient $\pi-\pi$ stacking in HTM films.¹⁷¹

2.5.4 Contact angle over MAPbI₃ surface

Contact angle measurement is a complementary analysis which help us to predict the stability under ambient conditions of the device, through the analysis of HTM film surface

wettability. Effectively, perovskite materials like MAPI is sensible to moisture, consequently, a hydrophobic coating layer could prevent his degradation and device stabilization.

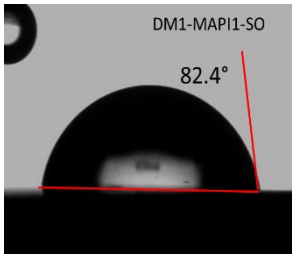
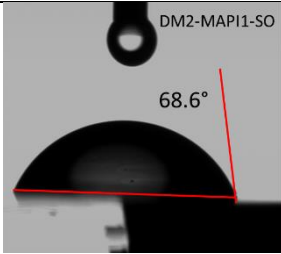
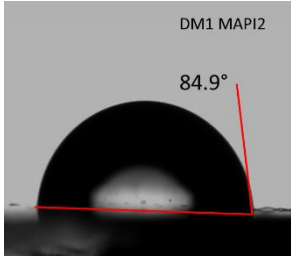
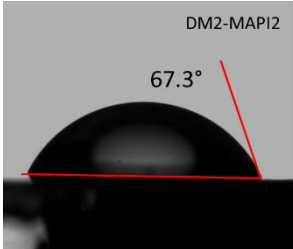
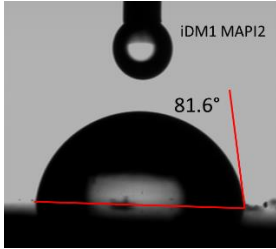
Contact angle is measured between the HTM film surface and a drop (20 μ L) of deionized water. To calculate hydrophobicity of the coated film, a picture is taken under white light emitting diode (LED) module, from where the contact angle between the film surface and the water drop is measured.

Contact angle is an important factor of an HTM characterization and a good hydrophobic (> 90°)²⁰³ character of the film layer is a desired feature. In addition, observation of the contact angle can helps to establish a relation between HTM molecular structure and its repelling water properties.

Table 11 Angle contact values obtained from each surface

	DM1	DM2	iDM1
MAPI1	82 \pm 4	68 \pm 3	-
MAPI2	85 \pm 2	67 \pm 2	82 \pm 2

Table 12 Contact angle images of DM1, DM2 and iDM1 and its arithmetic deviation value coated and different perovskite surface

	DM1	DM2	iDM1
MAPI1			
MAPI2			

**AFM images are a representation and real values are obtained automatically by the software*

Hydrophobicity and contact angle is measured (Table 11 and Table 12) for molecules with good photovoltaic results (DM1, DM2 and iDM1). Films are spin-coated using the same methodology as for the AFM experiments (2.4.6 Surface morphology studies by atomic force microscopy) over perovskite layer designated as MAPI1 (one-step method) and MAPI2 (two-step method) described on section 2.5 Photovoltaic measurements.

Contact angle measurements are done by depositing five times a water drop of 20 μ L of deionized water on the HTL surface and measuring the angle contact between the HTL and the water drop. Contact angle images (Table 12) are representative and the value showed on the image is arithmetic deviation of five values.

DM1, DM2 and iDM1, present a hydrophobic character close to Spiro-OMeTAD (77°)¹⁹⁷. Molecules bearing a N-styrene group, DM1 and iDM1 have very similar values around 80° . On the other hand, DM2 has a stronger hydrophilic character compared with DM1 and iDM1, presenting an average contact angle value of 67° . If a relation on molecular structure and water affinity film

properties, it can be noted that DM2 tends to be less water repellent than is aromatic counter parts DM1 and iDM1. A possible explanation to these results could be that aliphatic chain on DM2 tends to aggregate on a micellar way, exposing the methoxy groups from DPA to the exterior, thus creating more active sites to make hydrogen bonds with water and consequently increasing its hydrophilic character.

2.5.5 Light soaking effect

PSC devices using DM1 and DM2 as HTM are specially analyzed due to particular effect we observed during photovoltaic measurements. PSC modules, manufactured using the 1-step method (described in detail in section 2.5 Photovoltaic measurements), show a peculiar behavior. After 30 min under 1.5AM illumination at laboratory conditions, the so-called “*light soaking effect*”²⁰⁴ is observed. When the PV module is exposed to illumination, current output stabilizes after about 30 minutes, showed on Figure 47. Photocurrent and derived total efficiency increase, until reaching a maximum fill factor (FF) value under illumination.

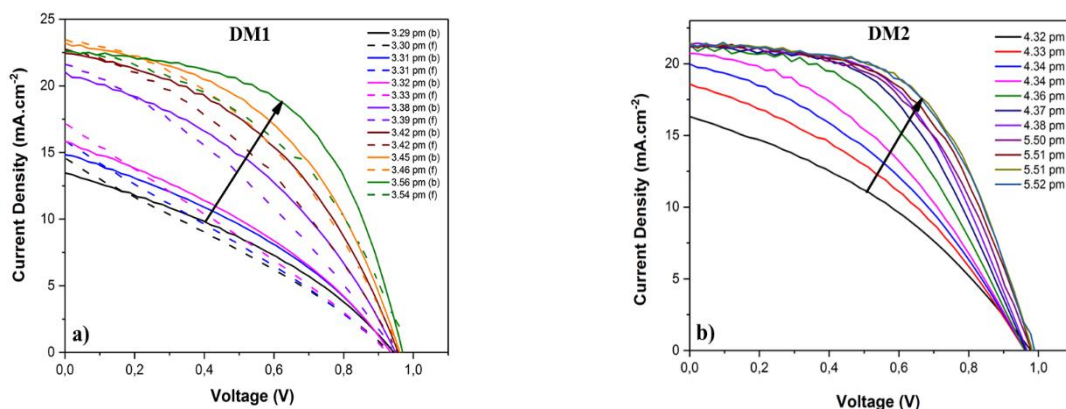


Figure 47 DM1 and DM2 photovoltaic performance evolution showing “*light soaking effect*” on MAPI 1 surface. Inset captions reveal the time in which the measurements have been made. (b) and (f) means backward and forward scans

Looking to understand the causes of these phenomena, a series of AFM experiments were designed in order to elucidate the origins of this effect.

The objective is to identify changes on the surface after 0, 10 and 60 minutes under 1.5 AM illumination and correlate the observed surface changes with the *light soaking effect*. Perovskite solar cells are manufactured using the 1-step (MAPI1) and 2-step (MAPI2) perovskite deposition method, and reference over ITO glass, were chosen to analyze their morphology by Atomic Force Microscopy (AFM). Modules will include DM1, DM2 and iDM1 as HTM. iDM1 is used as reference of molecule with no soaking effect. The total of the taken images from all substrates films are included in Annex 1. Average values of Roughness square root (Rq) and Roughness average (Ra) from each image are presented on the Table 13.

Logically, films coated over glass, present the smoothest surface, showing the lowest roughness values from of the three substrates, indicating a more homogeneous and regular films. The HTM coated over MAPI is related with a roughness increase.

Table 13 Average values of Roughness square root (Rq) and Roughens average (Ra)

			initial	10 min	60 min	$\Delta Rq(t_0-t_{60})$
DM1	Glass	Rq	1.60	1.13	1.21	-0.39
		Ra	1.03	0.85	0.82	
	MAPI 1	Rq	7.92	7.44	6.92	-1.00
		Ra	6.54	5.56	4.50	
	MAPI 2	Rq	2.51	2.59	2.94	+0.43
		Ra	1.81	2.02	2.35	
DM2	Glass	Rq	0.96	0.75	0.76	-0.20
		Ra	0.57	0.54	0.58	
	MAPI1	Rq	4.93	7.76	9.17	+4.24
		Ra	3.90	5.68	7.13	
	MAPI2	Rq	11.27	8.84	4.44	-6.83
		Ra	8.01	6.30	3.16	
iDM1	Glass	Rq	1.59	1.75	1.69	+0.10
		Ra	1.09	1.23	1.19	
	MAPI1	Rq	3.28	3.87	4.82	+1.54
		Ra	2.44	2.92	4.08	
	MAPI2	Rq	5.72	5.29	6.01	+0.29
		Ra	4.42	3.96	4.47	

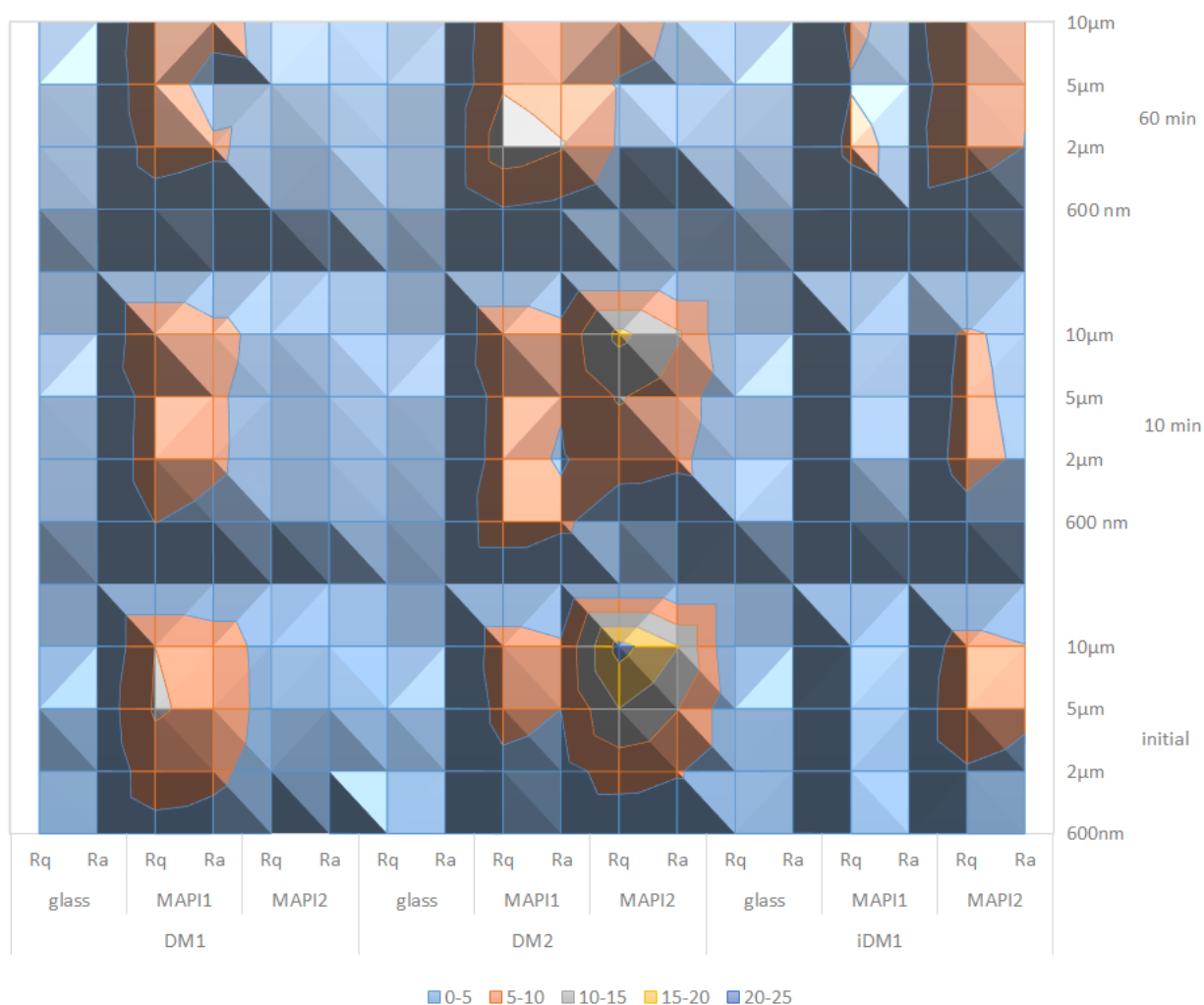


Figure 48 Image representation of Roughness square root (R_q) and Roughness average (R_a)

In order to help visualize all the data from AFM studies over time, the next tridimensional graphic is proposed. Roughness values are represented by the color change in function of time and scale measurements.

To compare different results on AFM measurements, the roughness square root (R_q) were preferentially used as more representative of the roughness for small size photography. Nevertheless, a relation between surface modification and *light soaking effect* is not evident by AFM means. However, a sensitive difference in R_q in DMx/MAPI1 compared to iDM1/MAPI1 could suggest that higher roughness of the MAPI1 surface could involve or reveal the soaking effect. It has been found that big interface area of high roughness surfaces also benefit the charge transport, improving short-circuit current of photovoltaic devices.²⁰⁵

We can conclude that, module's surface roughness isn't modified by 1.5AM illumination at AFM (500 nm) scale. Is evident that roughness deviation is derived from deposition of the perovskite film itself with only small differences between 1-step or 2-step perovskite deposition method. By visual examination of the AFM pictures it can be inferred, that film homogeneity is better for 2-step deposition method than for the 1-step.

After no consistent surface variations observable under AFM conditions, we can conclude that light soaking effect should have an underlying molecular reason.

Light exposure of modules produce some sort of stabilization that influences the final module power output and stability. Observing the T_g temperature for DM1 (45°C) and DM2 (41°C) and after measure the temperature reached by modules exposed to illumination (around 40°C), we can expect that DM1 and DM2 are close to their glass transition state, where molecules begins to flow, filling the perovskite layer porous and consequently increasing surface contact.

For the later reasons, we think that light soaking effect for 1-step deposition method of the perovskite layer, has a thermodynamic component that is evident thanks to the low glass transition temperature of DM1 and DM2. A posterior experiments to help prove our hypothesis, could be the observation by AFM of perovskite layer made with 1-step method and compare with the 2-step method.

2.6 Conclusions

In conclusion, we have designed, synthesized and tested six new carbazole derivatives as small molecule hole transport materials. These molecules were thought to be structural isomers distinguished from each other on the substitution positions over the carbazole core. The relationship between carbazole substitution and solar cell performance was demonstrated. For the 2,7-Cz substituted compounds, iDM1 outperform the rest of the compounds on the series, iDM2 and iDM4, maybe due to their low T_g 38°C and 43°C respectively. One possible explanation could be that, iDM1 with 2,7- configuration has a larger conjugated system may lead to more efficient π - π stacking that improves the intermolecular charge transfer on HTM layer and in consequence, a better efficiency (PCE 15.04%) is observed. In contrast, the 3,6-carbazole substituted compounds exhibit similar results (PCE=11.7% and 11.9%) independently of the N-substituted alkyl chain showing that its influence is not so important, on the 3,6- configuration.

Certainly, for a matter of synthesis simplicity, 3,6- carbazole are the chosen option instead the 2,7- isomeric counterpart. This study demonstrates that 2,7- substituted carbazole could be a reliable and interesting option as HTM, showing that the internal conjugation of the molecule plays a fundamental role on the final performance of PSC devices.

The relative facile synthesis, high power conversion efficiency as well as good stability demonstrate that specially iDM1 and in some degree DMx series, could stand as a good alternative HTMs for perovskite solar cells.

3. Carbazole-based polymeric/oligomeric hole transporting materials

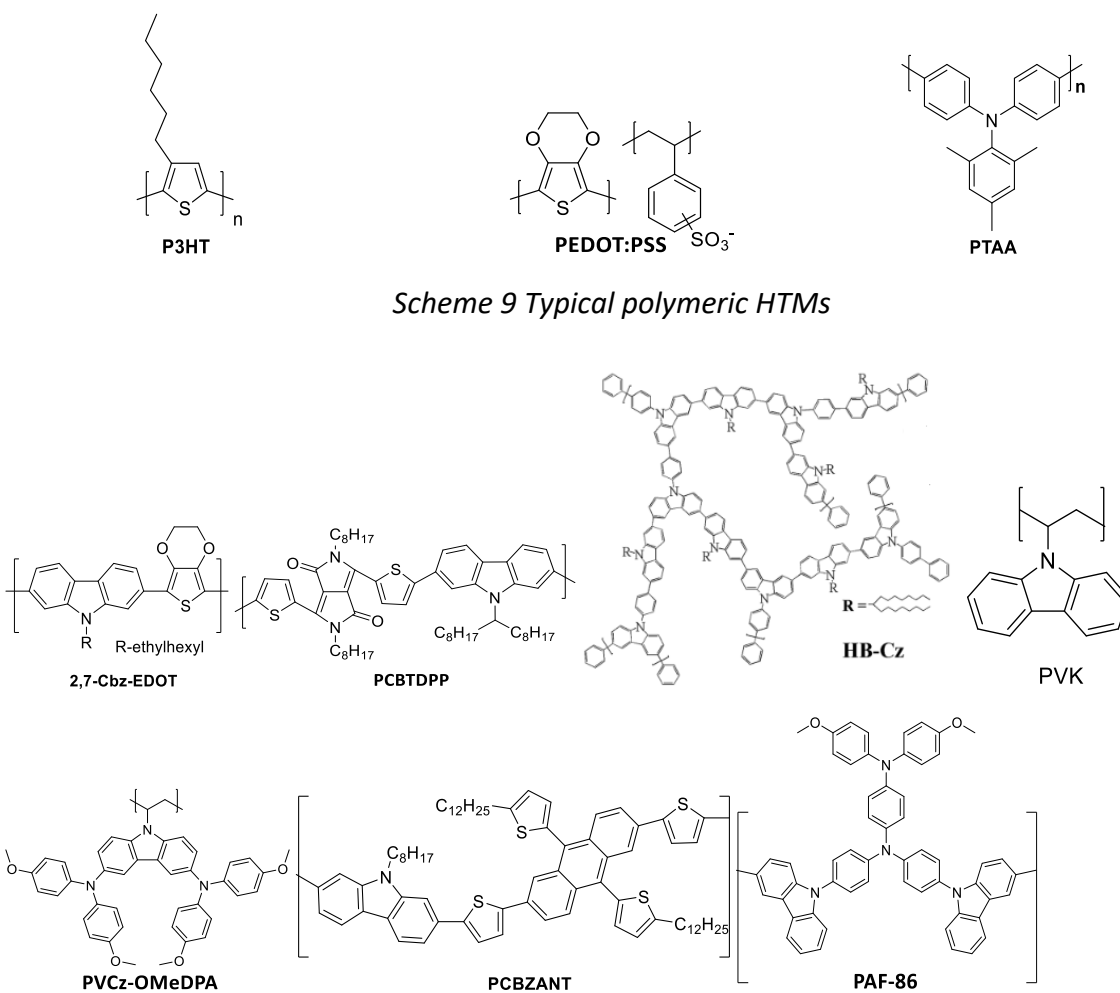
3.1 State of the art

Since the discovery of polyaniline in 19th century²⁰⁶ until the 2000 Nobel Prize in Chemistry²⁰⁶ “*for the discovery and development of conductive polymers*” conductive polymers had found a very important place in the organic electronics field, mostly as an emitting or charge transport layer in organic light-emitting diodes (OLEDs).^{207,208} Polymers, similar to small molecules, can function as a HTM in solar cells. A huge number of polymers have been already tested and reported. Several typical examples will be cited herein and related photovoltaic data are summarized in Table 14.

π -Conjugated polythiophenes have been well employed as electron donor materials in organic photovoltaics. Naturally they have been tested as hole transport materials in perovskite solar cells (PSC). Poly(3-hexylthiophene) (P3HT, Scheme 9) and PEDOT:PSS (poly(3,4-ethylenedioxythiophene):polystyrene sulfonate^{209,210} have been the most popular polymeric HTMs. While P3HT gave low performance, PEDOT:PSS has provided PSC devices with efficiency of higher than 18% PCE (Table 14). However, PEDOT:PSS film has been deposited from aqueous dispersion, thus, rendering it only suitable for inverted PSC device. In another hand, its acidity is also corrosive for the perovskite layer. Poly(triarylamine) (PTAA, Scheme 1) has also widely employed and it has successfully given satisfactory solar cell device performance (22% PCE).²¹¹ Recently, pendant non-conjugated polymer poly(9-vinylcarbazole) (PVK) PCE = 15 % has been explored as an efficient HTM in order to replace the PEDOT:PSS in inverted planar heterojunction PSC.²¹² In the same trend, the bisdi(4-methoxyphenyl)amine-substituted PVK (named as PVCz-OMeDAD, Scheme 10)²¹³, has been prepared and employed in PSCs. It is important to note that PVCz-OMeDAD has led to PSC devices with 16.9% PCE without additives. However, PVCz-OMeDAD has been synthesized in low yield. In terms of linear carbazole-based conjugated polymers, example of efficient co-polymers has been reported such as PCBZANT²¹⁴ (PCE 15.50%). Another interesting study with two different linear conjugated carbazole/EDOT co-polymers named poly(2,7-Cbz-EDOT) and poly(3,6-Cbz-EDOT), (Scheme 10). Structurally, these two polymers are different to each other by the connection position in the carbazole core and the impact of the molecular structure on the photovoltaic properties was investigated. When used as HTM in normal (or inverse) PSC devices, poly(2,7-Cbz-EDOT) has given better performance

than the linear poly(3,6-Cbz-EDOT). This is ascribed to the higher hole mobility and the deeper HOMO energy level.¹⁷⁰

In other hand, a carbazole-based hyper-branched polymer HB-Cz (PCE = 14%)²¹⁵ has been also developed for PSC applications. This highly branched systems disposed in a three-dimensional macromolecular network, have received big attention due to their advantages of facile synthesis, low cost, low viscosity, and good solubility. Highly branched polymers have been widely used as light-emitting materials and HTMs in OLED^{216,217} but their application in PSCs is rare.



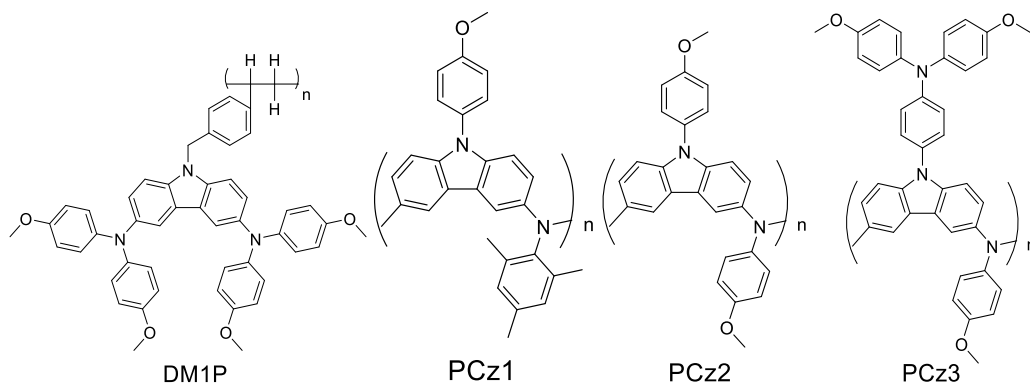
All the selected examples demonstrate the huge potential of carbazole-based (co)/polymers in perovskite-based photovoltaics technology. In comparison to molecular materials, polymers can present potential downsides like indistinct molar mass due to their poly-dispersity, batch-to-

batch reproducibility, purity, and stability under low vacuum conditions¹³⁷. Nevertheless, their main advantage is the improved long-term physicochemical stability and now they are starting to be extensively studied due to the mentioned characteristics. Nowadays the record efficiency for polymeric-HTM based PSC's with 22.6% comes from a research conducted by Seok et al.²¹⁸ The chosen HTM for such device is PTAA leaving besides the use of the traditional Spiro-MeOTAD standard²¹⁸. The choice on the use of PTAA relies on the fact that no dopant treatment is necessary for its coating and device stability tends to improve due to its hydrophobic properties.²¹⁹ Moreover, no obvious hysteresis is observed on devices using PTAA. Given the obtained results, most of the revised polymers showed good performance. Is for these reasons that polymer's use need to be revised in detail as an alternative option to small molecules as HTM.

Table 14 Carbazole based polymeric compounds used as HTM

HTM	Hole Mobility (cm ² V ⁻¹ s ⁻¹)	HOMO	LUMO	V _{oc} (V)	J _{sc} (mA cm ⁻²)	FF	PCE	Year/ Reference
PCBZANT	-	-5.15	-2.56	0.91	21.4	58.22	11.36	2018 ²¹⁴
PTAA	-	-5.18	-2.22	1.11	25	0.817	22.6	2017 ²¹⁸
PEDOT:PSS	-	-5.0	-	1.1	20.9	0.79	18.2	2017 ^{160,220}
P3HT	8.2 x 10 ⁻⁴	-5.18	-3.93	0.87	16.97	0.61	9.05	2017 ²¹⁵
PVK	-	-	-	0.96	22.0	0.71	15.16	2017 ²¹²
PAF-86	2.23 x 10 ⁻⁵	-	-2.27	0.91	18.23	0.59	9.84	2017 ²²¹
2,7-Cbz- EDOT	5.1 x 10 ⁻⁶	-5.21	-2.9	0.81	16.5	0.32	4.47/4.14 (P3HT)	2016 ¹⁷⁰
3,6-Cbz- EDOT	3.5 x 10 ⁻⁷	-5.09	-2.5	0.8	14.7	0.33	3.9/4.1 (P3HT)	2016 ¹⁷⁰
HB-Cz	8.4 x 10 ⁻⁴	-5.18	-2.42	0.97	20.88	0.69	14.07/9.05 (P3HT)	2017 ²¹⁵
PVCz- OMeDPA	3.44 x 10 ⁻⁴	-5.24	-2.49	1.085	21.96	0.67	16.09/18.5 (Spiro)	2017 ²¹³
PCBTDP	0.02	-5.4	-	1.15	4.47	0.59	5.55	2013 ²²²

Inspired from the success of the pendant modified PVK and the PTAA polymers, in this work we designed and prepared several new polymeric/oligomeric HTMs. The molecular structures of these new polymers are given in Scheme 11.



Scheme 11 Schematic representation of the synthesized polymer

Structurally, side chain polymer DM1P is based on polystyrene backbone meanwhile PCz1, PCz2 and PCz3 were designed from carbazole/aniline oligomer systems. Carbazole was substituted at N-position by strong electron donor groups such as methoxyphenyl (PCz1 and PCz2) or triphenylaminy (PCz3). These groups contribute to tune not only the electrochemical properties but also the thermal properties of the targeted materials. In addition, the presence of methoxy group increases the solubility of the targeted oligomers. Methoxy group can also increase the affinity with the perovskite layer via interaction occurred between the HTM methoxy groups and the perovskite methylammonium site.²²³

The use of the bulky mesitylene, a structural feature found in the popular PTAA, can significantly influence the morphological and optoelectrochemical properties of the final polymer. Through the work, we fully investigate their properties in order to understand and establish a structure/property relationship. This will help us to define what could be the best option for our working conditions comparing the efficiency results of small molecules versus polymeric HTMs. In the next paragraph, we firstly discuss the DM1P.

3.2 Carbazole non-conjugated polymer DM1P

3.2.1 Material synthesis

As discussed in Chapter II, one of the objectives of alkene group on DM1, DM2 and iDM1, iDM2 was to synthesize molecules with a polymerizable function (terminal alkene moiety or styrene). The later allow us to obtain the derived polymers (DM1P) and compare its performance in photovoltaic devices. As given in Chapter II, four molecules were designed for this purpose, being two structural isomers bearing 2,7- and 3,6- position substitution in the carbazole core center. However, only one of them, DM1 (Figure 49) could be successfully transformed into the corresponding polymer DM1P. Herein we described in detail different tested polymerization procedures (anionic and radical using different conditions and initiators like BPO and AIBN as is known for classic alkene polymerization). As an alternative polymerization path, chain radical polymerization and thermal annealing process were tested as well.

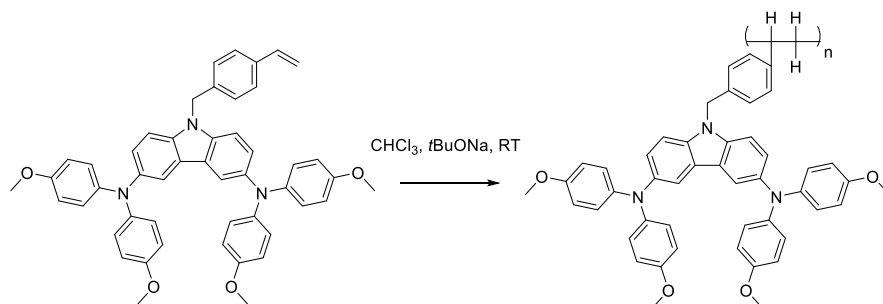


Figure 49 Structure and synthesis pathway of DM1P

Radical polymerization

Alkene moiety is known to react by free-radical polymerization (FRP) to form non conjugated polymer by which a polymer forms by the successive addition of free-radical building blocks. Free radicals are usually formed involving initiator or catalysts. After the radical generation, the starting radical, reacts with (non-radical) monomer units, triggering the polymer chain growth.²²⁴ Different polymerization attempts have been carried out using two different radical initiators Azobisisobutyronitrile (AIBN) and Benzoyl peroxide (BPO) (Figure 50) over DM1, DM2 and iDM1, iDM2 isomer pairs described in chapter 2. Next table resumes all experiments performed with different molar equivalents (between 2-20 mol %) of initiator with respect to monomer.



Figure 50 Benzoyl peroxide (BPO) and Azobisisobutyronitrile (AIBN) radical initiators

Only one positive result was achieved using BPO as initiator with low synthetic yields and styrene as a co-monomer with a 1:1 ratio. We also tested the polymerization reactions of DM1 in the presence divinylbenzene (DVB) (co-monomer, cross linking agent) without success.

Table 15 Reaction conditions for DM1 radical polymerization

Catalyst	Co-monomer/ Cross linking agent			Solvent			
	non	Styrene	DVB	Toluene	Chlorobenzene	Cyclohexanone	THF
AIBN	x	x	x	x	x	x	x
BPO	x	15%	x	x	x	x	<10% Yield

Note: in order to test catalyst reagents reactivity, parallel reactions were carried out of polyvinylcarbazole and polystyrene with positive results.

Anionic polymerization with no CHCl_3

Anionic addition polymerization involves vinyl monomers with strong electronegative groups.²²⁴ The anionic polymerization occurs with vinyl monomers only if the substituents on the double bond must be able to stabilize a negative charge. This polymerization is carried out through a carbanion active species and delocalization of the negative charge. Like all chain-growth polymerizations, it takes place in three steps: chain initiation, chain propagation, and

chain termination. Living polymerizations, which lack a formal termination pathway, occur in many anionic addition polymerizations. The advantage of living anionic addition polymerizations is that they allow for the control of structure and composition. Following the procedure for polyvinyl naphthalene²²⁵, two anionic polymerization were essayed on DM1 monomer using as catalyst: tert-butyllithium and sodium methoxide in toluene and THF as solvent. Unfortunately, No positive results were obtained using this method.

Thermal Polymerization in Solution

Based on the observation from the DSC of the monomer DM1, we decided to subject DM1 to thermal polymerization tests without a chemical initiator. The most widely accepted pathway for the spontaneous generation of radicals in the thermal polymerization of styrene was proposed in 1961.²²⁶ Styrene reaction and the identification of the radicals that initiate polymerization have remained speculative and controversial. The definitive experiment confirming this mechanism in 1977 was based on the retardation of the propagation step on the thermal polymerization of styrene with FeCl_3 in DMF. The resulting oligomers containing between six and fourteen monomer units were characterized by ^1H NMR and HR-MS proving then the possibility of polymerization with heat treatment.^{227,228}

After the analysis of the DSC curves, where monomer DM1's T_g is shifted to high temperatures after the heating cycle at 250°C , we theorized that polymerization/oligomerization could be taking place in solid state inside of the capsule during DSC experiments.

Several experiments were done to test the polymerization ability in solution of DM1, using different solvents at different temperatures under argon atmosphere. Moreover, using the same strategy as in radical polymerization, a crosslinking agents were added as well in parallel reactions, looking for positive polymerization results. All experimental conditions are given in Table 16, with the reaction temperature at which reactions were carried out, depending on the solvent boiling point. Unfortunately, no trace of polymer was detected even when a crosslinking agent was added, results are marked with an X on the table. We think that these results are due to the much lower concentration of the monomer in comparison with solid state found inside the DSC capsule, where polymerization by thermal ways is occurring.

Table 16 Thermal experiments table

	Crosslinking agent		no cross linking agent	Solvents		
	EDOT	DVB (divinylbenzene) and Styrene		Toluene 110°C	Chlorobenzene 132°C	Cyclohexanone 156°C
DM1 Annealing	X	X	X	X	X	X

Thermal polymerization was also tested by annealing process in solid state over thin film deposited on glass substrate. The films have been tested under inert (glove box) nitrogen atmosphere and ambient conditions at 150°C. Even physical changes occurred over the DM1 monomer made films, characterization was difficult and no further progress was done using this technique.

Chain transfer polymerization

Halomethanes used as chain transfer agents (CTA), which include chloroform, carbon tetrachloride, carbon tetrabromide, and bromotrichloromethane, have been widely used as CTA²²⁹ (telogens) for the preparation of telomers. The perhalomethanes (e.g. carbon tetrachloride, carbon tetrabromide, and bromotrichloromethane) react in the chain transfer process to exchange a halogen atom and form a perhaloalkyl radical that initiates a new propagating chain. The proposed mechanism for this reaction is depicted in Figure 51.

The halohydromethanes (e.g. chloroform) can in principle react by either H-atom or halogen-atom abstraction, thus for chloroform is listed in Table 17 with the chain transfer constants for different halomethanes and monomers. Styrene data could be compared with the monomer of this study, being styrene moiety who is susceptible to polymerization.

Chain transfer agent (CTA)	C _{tr} X 10 ⁴			
	MMA	MA	AN	Sty
CBR ₄	0.19	0.41	0.19	8.8
CCl ₄	18.5	1.0	0.85	92
CHCl ₃	1.77	-	5.6	3.4

For a matter of comparison, chloroform has the smaller chain transfer rate, anyways is still affective in its polymer formation function, which can give us an idea of its role in the presented reaction.

Chemical reaction scheme showing the radical polymerization of 4-vinylbenzyl chloride initiated by a trichloromethyl radical ($\cdot\text{CCl}_3$).

The reaction proceeds via a chain-growth mechanism:

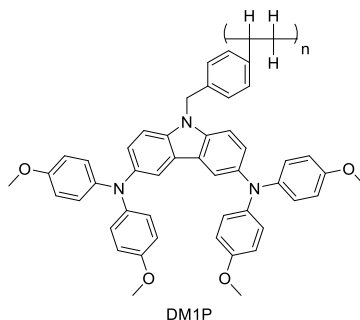
- Initiation: $\cdot\text{CCl}_3$ adds to the vinyl group of 4-vinylbenzyl chloride to form a radical intermediate.
- Propagation: The radical intermediate adds to another monomer, and this process repeats n times to form a polymer chain.

The final product is a polymer chain consisting of repeating units of 4-vinylbenzyl chloride, with a terminal radical group.

Polymerization can be achieved in two different ways. After the Buchwald–Hartwig amination (2.3.1.3 General synthesis procedure for compounds DM1 and DM2.), polymerization can take place on the addition of chloroform into the reaction mixture with a spontaneous polymerization by a chain halomethan-transfer reaction^{224,230–233} catalyzed by chloroform and the strong base conditions as illustrated in Figure 52.

Characterization

N-Poly-(4-benzyl-6-vinyl)-3,6-bis(4,4'-dimethoxydiphenylaminyl)carbazole (DM1P)



Elemental Analysis $C_{49}H_{43}N_3O_4$, Elem. Analysis (%) Exp. C 78.86, H 5.88, N 5.47, O 8.39; Calculated C 79.79, H 5.82, N 5.72, O 8.63.

1H 250 MHz (C_6D_6) δ 0.29 to 0.45 (m, 3H), 3.29 (s, 12H), 5.08 (s, 2H), 6.2-6.7 (m, 10H), 6.7-7.2 (m, 10H), 7.5-8.2 (m, 6H).

^{13}C NMR: no data, tested many times different concentration but no signals are observed

Gel permeation chromatography (GPC) analysis of three different batches show the following molecular weight (M_w) molecular number (M_n) and polydispersity index. (PDI).

Batch/kDa	M_n	M_w	PDI
1	18,90	62,12	3,28
2	25,28	32,80	1,57
3	17,33	29,93	1.72

3.2.3 Characterization of DM1P

3.2.3.1 Thermal Properties

Thermal stability of DM1P is evaluated by thermogravimetric analysis (TGA). The TGA curve of the polymer and that of the monomer are given in Figure 53 for comparison purpose. As can be seen, both materials are thermally stable with similar decomposition temperature ($T_d = 407^\circ C$ for the polymer which is comparable to its monomer DM1 $T_d = 415^\circ C$).

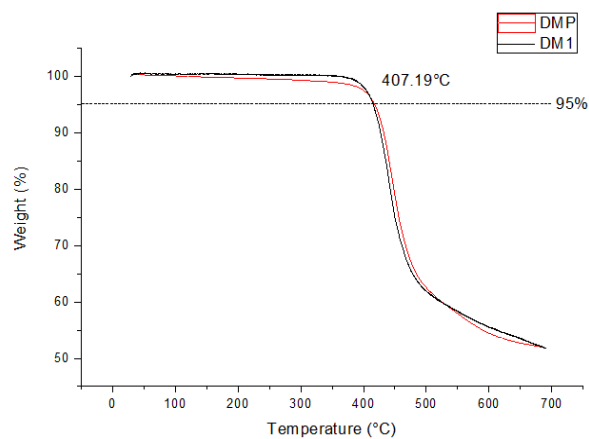


Figure 53 TGA analysis of DM1P and DM1

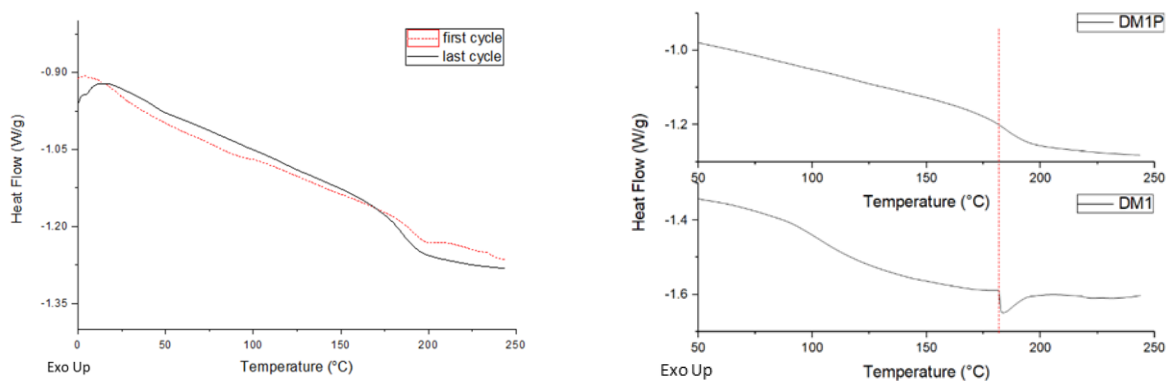


Figure 54 DSC analysis of DM1P and comparison with DM1

The thermal properties of the 3,6- carbazole substituted polymer DM1P was also examined by DSC (Figure 54). As can be seen, the polymer DM1P exhibited only one endothermic event at 184°C for the first cycle and 186 °C after the second cycle that we attributed to the T_g of the polymer.

It is interesting to note that DM1 during the second and third heating cycle presented an endothermic event similar to a glass transition temperature around 182°C that almost matches the value presented for DM1P. This leads us to theorize that polymerization could occur by annealing process at high temperature. Based on this information, many annealing experiments were essayed in different conditions (atmospheric conditions, under glove box, in solution, etc.) to achieve polymerization but none of them showed positive results as discussed above.

3.2.3.2 Optical Properties

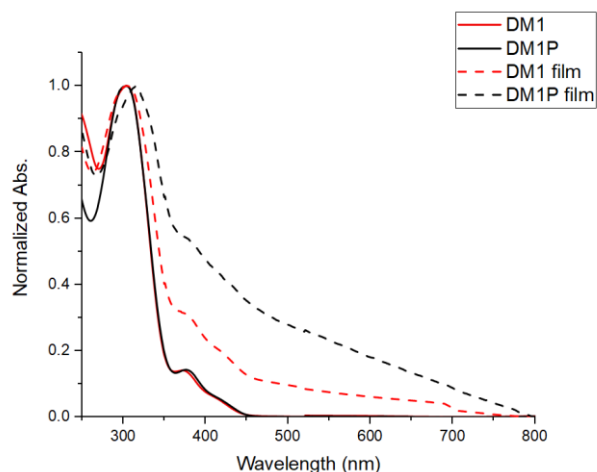


Figure 55 UV-vis spectra of DM1P and DM1 monomer

UV-vis absorption spectra of DM1P (0.8mg/100mL) and DM1 (1.1×10^{-3} mM) is recorded dichloromethane solution (0.8mg/100mL) DM1 (1×10^{-3} mM) are shown in Figure 55. DM1P and DM1 present the same maximum absorption features. An intense $\pi-\pi^*$ absorption band observed at 275–350 nm with a maximum peak at 310 nm with a slight hypochromic effect compare with its monomer. Such decrease on the absorption intensity is due to the lack of conjugation between alkene moiety and the benzene ring, which disappears after the polymerization to transform on the aliphatic chain. A less intensive lower energy absorption bands are observed at >350 nm, that can be assigned as $n-\pi^*$. For thin film deposited over glass, a hyperchromic effect appears due to the stacking effect and the increased molecular absorption directly dependent on film thickness. A similar effect on the absorption is observed as with DMx and iDMx family, and in general all compounds that are measure over films. While this effect is quite pronounced for the polymer more than the monomer, molar absorption can be modulated depending on the thickness of the film. In general, DM1P's wavelength absorption remains the same as the starting monomer, showing no overlap absorption with the perovskite film, making this polymer a suitable candidate for PSC device.

3.2.3.3 Electrochemistry

Cyclic voltammograms (Figure 56) of DM1 and DM1P solutions were prepared with a concentration 1.0×10^{-3} M considering a monomer unit for its molecular weight, recorded in 1.0×10^{-2} M TBAPF₆/ CH₂Cl₂ solution at a scan rate of 100 mV s⁻¹. The data are summarized in Table

18. The highest occupied molecular orbital (HOMO) energy levels were determined from the half-wave oxidation potential of the first oxidation value, considering as reference the redox couple Fc^+/Fc at -4.8 eV versus vacuum. In both case, no reduction peaks were observed and only the anodic part of the voltamograms are given in the Figure 56.

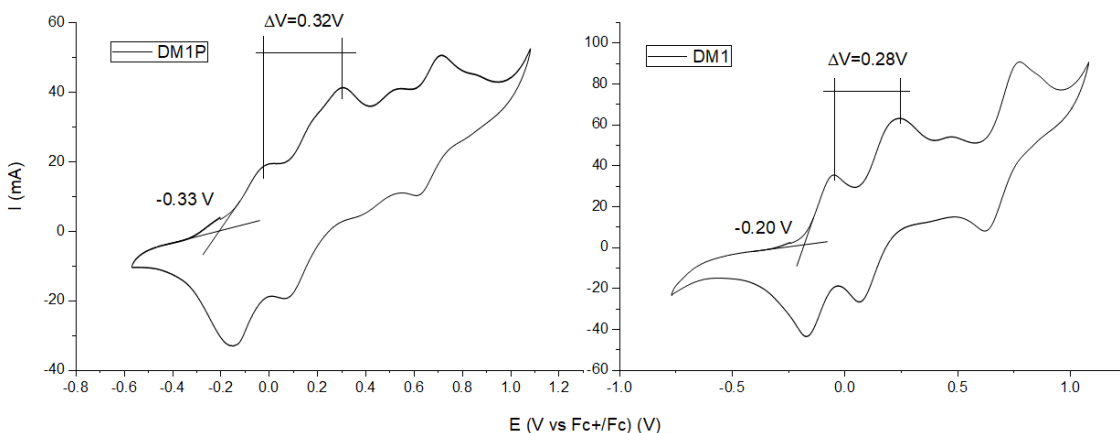


Figure 56 Cyclic voltammetry of DM1 and its derivative polymer DM1P

As can be observed, DM1 displays three main oxidation peaks. The two first ones correspond to the successive oxidation of two diphenylamine moieties. The third one at higher potential is ascribed to the oxidation of the carbazole core. As expected, DM1P has similar electrochemical behavior compared to DM1, except that these oxidations peaks are less-defined. The first oxidation potential (E_{ox}^1) of the polymer is shifted to positive values resulting in a higher HOMO (-4.47 eV (IP), Table 18) compared with its monomer DM1 (-4.60 eV). From the HOMO energy level and the optical bandgap, the LUMO energy level is estimated. Values are summarized in Table 18

Table 18 DM1P and DM1 oxidation potential values

HTM	E_{Ox1} [V]	E_{Ox2} [V]	ΔV [V]
DM1P	-0.022	0.3059	0.328
DM1	-0.049	0.238	0.288

On Table 18 are summarized the oxidation values of DM1P and compared with its monomer DM1. A larger ΔV , can be attributed to a larger number of the oxidations states within the polymer

on each one of its units, giving as a result a peak where the oxidation state is the average for the whole polymer.

3.2.3.4 Surface morphology

Atomic force microscopy (AFM) images show a compact, continuous coverage film showed on Figure 57. Hole transport layer surface homogeneity is an important feature to look at for decreasing current leakage and attaining contact with the cathode which leads to an increased hole collection.²³⁴ Optimal interface morphology between the active layer and the metal electrode can be partly confirmed by the surface quality of HTL, which will give an overall enhancement of J_{sc} , V_{oc} and FF. The best film formation ability of DM1P among the DMx series, which restrains the regular packing effectively, and present good solubility as its monomer counterpart. High solubility of DM1P helps to increases pore filling in the $MAPbI_3$ layer and improving the performance of photovoltaic device. Morphology of these samples present a root mean square and arithmetic mean roughness of R_q 14.0 and R_a 11.2 nm. Experimental conditions for the film deposition are described on 2.4.6 Surface morphology studies by atomic force microscopy.

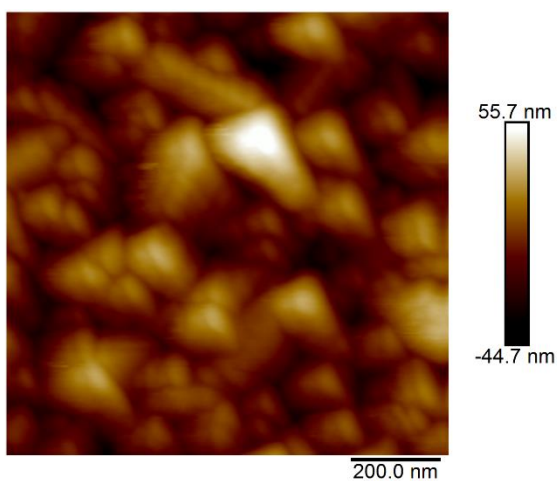


Figure 57 DM1P film AFM image. Thin film spin-coated on glass substrate

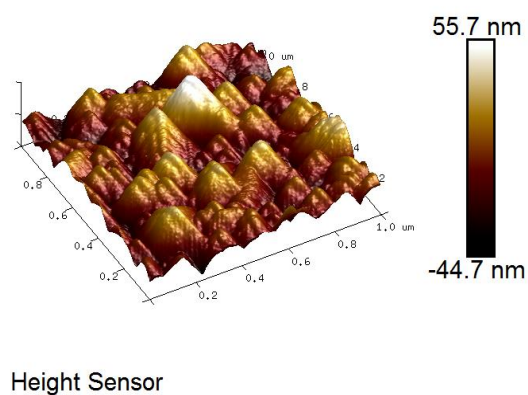


Figure 58 DM1P film AFM 3D image

3.2.3.5 Computational Studies

The DM1P polymer was studied by density functional theory (DFT) calculations. Calculations were carried out using the Gaussian 09²⁰¹ suite of programs. Ground state geometries of DM1P series were fully optimized imposing a 120° and 180° arrangement symmetry constraints by employing the 6-31G(d,p) basis set. Two different experiments were set up in order to visualize the possible conformation that DM1P takes.

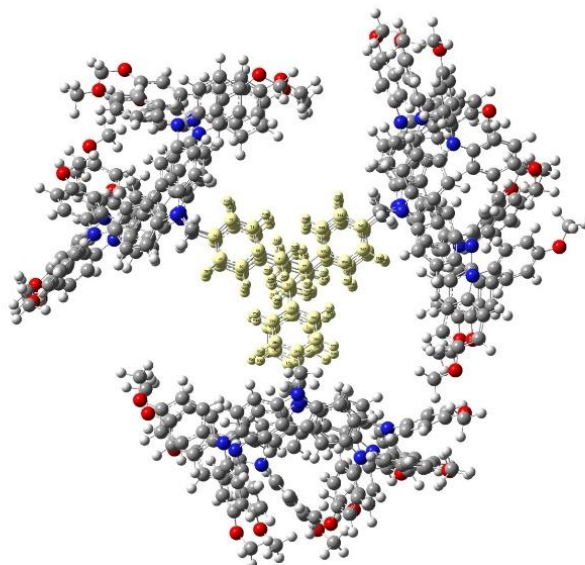


Figure 59 DM1P 120° “triangular” conformation

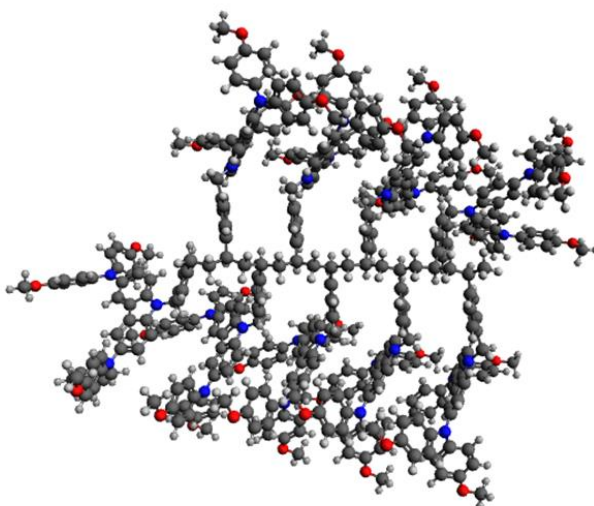


Figure 60 DM1P proposed configuration 180°

A preliminary structure was obtained with a 120° (triangular) configuration as shown in Figure 59. A second possibility for the polymer organization is a 180° (linear) configuration (Figure 60). Both conformations 120° and 180° have the same number of DPA-carbazole units (nine in total). The di(4-methoxyanilino) groups (DPA) substituted over Cz are closer to each other in a 180° -conformation (Figure 60), making less probable to occur due to steric hindrance as compared to 120° -conformation showed in Figure 59 where molecules have more free space to arrange in a triangular conformation.

Given the overcrowded structure of this polymer, for a clearer view, the non-conductive polystyrene is highlighted in yellow fragments in the 120° triangular conformation. In Figure 60, there are nine pending groups in the model to highlight the impact of the linking topology in the 180° -conformation.

Whatever the stability order between the two structures, a combination should be found in the amorphous state between both of them. The more stable arrangement should give an idea of the dominant conformer with triangular- 120° disposition. This information could give insights on the results of the hole transport properties observed for real devices compared with its monomer. Final results showed that DM1P has better results than DM1 (13% vs 11%), so this could be an explanation. A better packing improves hole transport properties.

Using DFT modelisation, we try to explain why polymerization of iDM1 (2,7-Cz substituted) didn't occur. In order to test the possibility to obtain the polymer derived from iDM1, the DPA groups linked at the 3,6 positions are highlighted in green in Figure 12 whereas the 2,7- positions are highlighted in red.

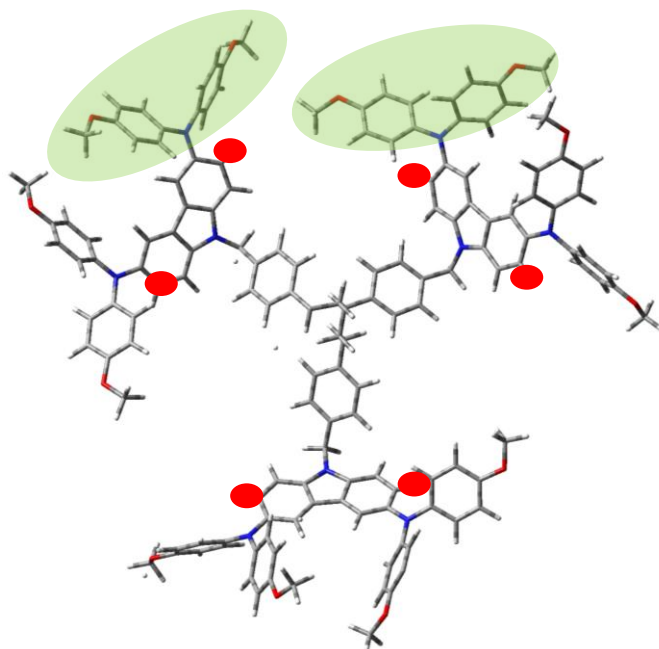


Figure 61 2,7- positions marked in red suggesting the lack of space for iDM1 derivate polymer to exist.

It can be easily seen that for the 3,6- isomer, the DPA groups can still avoid each other. As for the 2,7-isomer, the figure suggests that the DPA groups should point directly toward each-other, thus hindering the polymerization because there is not enough space for such polymer structure.

3.2.4 General physical properties of DM1P

All physical, optical and electronic properties of the polymer are given on Table 19 and their HOMO LUMO energy levels are illustrated in comparison with DM1 and common HTM Spiro-OMeTAD and the perovskite MAPI (Figure 62).

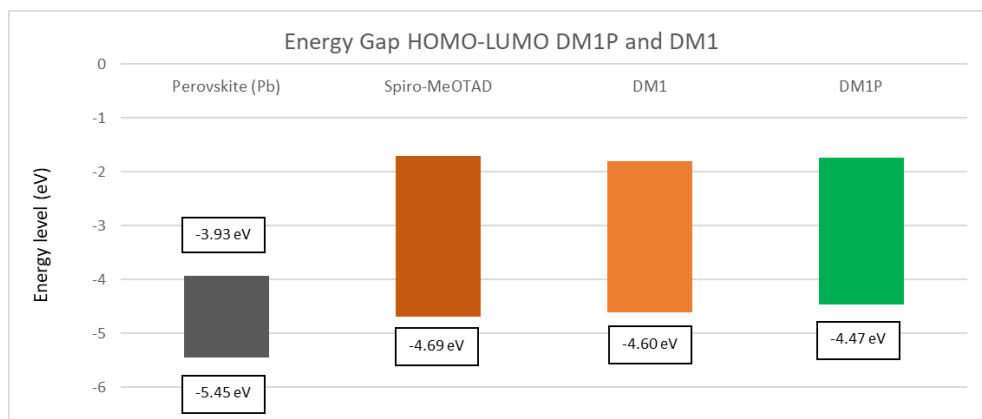


Figure 62 HOMO-LUMO values for DM1P and comparison with its monomer DM1

It can be observed that the frontier energy levels of the polymer are nearly identical to those observed for the monomer and very close to that of the Spiro-OMeTAD. The HOMO level is located slightly higher than that of perovskite, which will ensure an efficient hole transfer from perovskite to HTL at the interface. Otherwise, its LUMO energy level is much higher than that of perovskite, avoiding back electron recombination. These properties suggest that the polymer is a suitable candidate as HTMs for PSC. We can remark that the best improvement compared with its origin monomer resides on its high thermal stability where the glass transition temperature increases to 186°C, which is 120° higher than is monomer (Table 19).

Table 19 General physical, optical and electronic characteristics of DM1P

Compound	T _d (°C) ^[a]	T _g (°C) ^[b]	λ _{max} (nm) ^[c]	λ _{onset} (nm) ^[c]	E _{gap} (eV) ^[d]	E _{ox} (V) (Fc/Fc ⁺)	HOMO ^[l] P] (eV)	LUMO [EA] (eV)
DM1P	407	186	309, 382	454	2.73	-0.33	4.47	1.74

^[a]Obtained from TGA measurements. ^[b]Obtained from DSC measurements. ^[c] Measured in CH₂Cl₂ solution 1 x 10⁻⁶ M (Single unit equivalent).. ^[d] Measured in CH₂Cl₂ 1.0 x 10⁻² M TBAPF₆ solution. Analyte 1 x 10⁻⁴ M (Single unit equivalent). All E_{ox} data are reported relative to ferrocene²⁰⁰ which has a value of ionization potential (*IP*) 4.8 eV for ferrocene and 0.27 V for Fc/Fc⁺ against Au/Au⁺. The concentration of the complexes used in this experiment was 1.0 x 10⁻³ M and scan rate was 100 mV s⁻¹. E_{gap}= hc/λ_{onset}= 1240 eVnm/λ_{onset}; IP=E_{ox}+4.8; EA = IP - E_{gap}

3.2.5 Photovoltaic Performances

The polymer and the monomer were then coated on PSC device using the classic device architecture: Glass/FTO/cTiO₂/mpTiO₂-Perovskite/HTM/Au using the same methodology described in section 2.5.3.1. Optimized photovoltaic properties are summarized in Table 20. The photovoltaic properties of the Spiro-OMeTAD were also provided for comparison purpose.

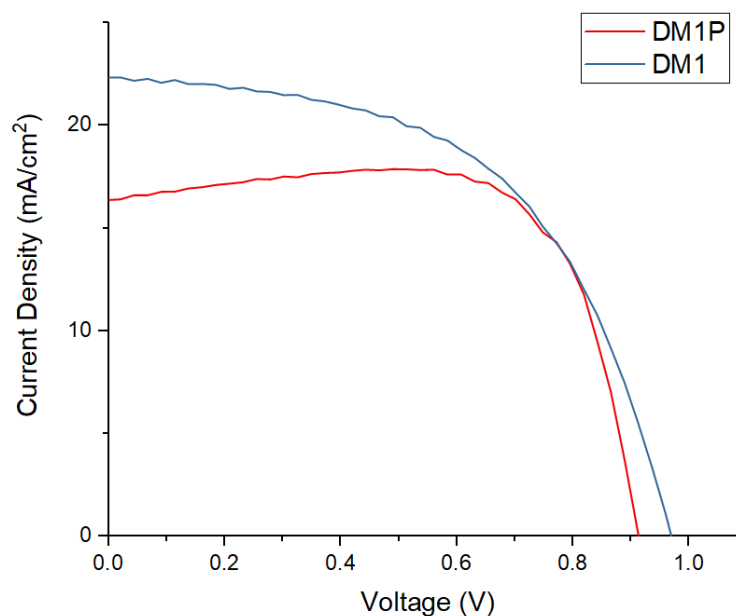


Figure 63 Photovoltaic results of DM1 and DM1P with dopants

Without dopant, the efficiency of DM1P cells was very low (below 0.7%). Their *J-V* curves are typical of highly resistive devices and problems of charge injection and transport occurred. For DM1P HTM, without doping, the device suffered from a very low FF that can be attributed to a low HTM conductivity and therefore high charge transport resistances.

Table 20 Photovoltaic results of DM1P (with Spiro-OMeTAD as reference)

HTM	Scan direction	V_{oc} (V)	J_{sc} (mA.cm ⁻²)	FF(%)	η (%)
DM1P with dopants	Rev (Best)	0.92	18.98	75.53	13.24
	For (Best)	0.95	16.94	48.01	7.70
	Rev (Avg)	0.91	15.95	76.04	11.09
	For (Avg)	0.93	17.98	42.62	7.18
Spiro-OMeTAD	Rev (Best)	1.01	22.15	78.75	17.68
	For (Best)	1.00	22.72	63.02	14.45
	Rev (Avg)	1.01	21.32	75.63	16.33
	For (Avg)	1.01	22.14	62.81	14.05
DM1 with dopants		0.96	22.58	54.40	11.91

For polymer carbazole based HTM, the V_{oc} of the cells were lower than that of the Spiro-OMeTAD. It suggests the occurrence of more recombination at the perovskite/HTM interface. Nevertheless DM1P devices show a good fill factor (best result: 76%) and current density (best result :19 mA.cm⁻²) resulting a promising PCE equal to 13.2% which is higher than those obtained by the monomer DM1 HTM counterpart, implying that in this case polymer derivative can be an improvement factor for device final performance results. Fill factor is higher with DM1P cells compared to monomer DM1 demonstrating a better interface with the polymer. However, these performances are still lower than those of the Spiro-OMeTAD as control device.

3.2.6 Conclusions

A polymer derived from DM1 was obtained and tested in photovoltaic cells. DM1P polymer showed better properties in comparison to its monomer counterpart. The thermal and film forming properties are importantly improved. Its glass transition temperature shifts from 45°C (monomer) to 186°C (polymer). This improved thermal stability also avoids effects like the “light soaking effect” previously presented by monomers DM1 and DM2, thus allowing the manufacture of more stable devices with a longer life expectancy. Finally, an improved efficiency was observed from 11% for DM1 to a 13% for DM1P polymer, proving that polymer derivate in this particular case is an advantage than its origin monomer for PSC devices.

3.3 Carbazole based conjugated Oligomer

3.3.1 Synthesis objective

Inspired by PTAA and its good performance on PSC's devices, three new polymers named PCz1, PCz2 and PCz3 (Figure 64) are proposed looking for a reliable HTM option with enhanced physical properties. These polymers are expected to give longer life expectancy as it has been found for polymers⁵⁴, better thermal properties making of them more resilient materials, and better carrier properties. The molecular conception of these materials has been described at the beginning of this chapter. In the next, the synthesis of these polymers and related intermediates compounds will be presented. The targeted polymers will be then fully characterized.

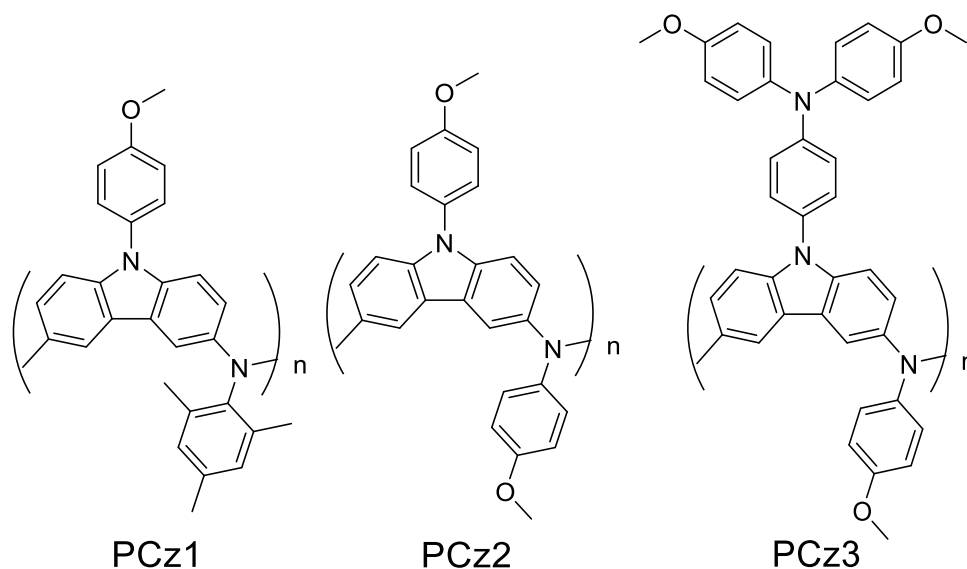


Figure 64 Series of conjugated carbazole based polymer PCzX

In this study, we want notably to observe and compare the influence of the number of methoxy groups attached to the phenyl ring. DFT calculations have shown that Spiro-OMeTAD interaction with the perovskite layer relies on its affinity for the methylammonium groups or its absence (anchoring on the methyl ammonium site, replacing it) on the surface, which is repulsive with the iodides and attractive with the Pb(II) ion.²³⁵ Trough DFT study is concluded that hole transfer yield is higher on non-polar surfaces.²³⁶

With the latter in mind, we propose a series of polymers PCzX (Figure 64) to observe the raising differences, depending on the number of methoxy groups comprehended within the molecule

and its interaction perovskite layer through their performance on PSC devices. The number of methoxy groups is increased over PCz1>PCz2>PCz3. So if the later is true, we will see an improvement on the final performance according decreasing number of MeO- groups included on the monomer unit.

3.3.2 Synthesis of PCzX series

As an alternative to PTAA, which is one of the most expensive HTM but at the same time one of the most efficient and long-term stable (21.2%) HTM. Retaining its efficiency for more than 1000h at 93%⁴³ of its initial capacity, represents one of the most reliable options to Spiro-OMeTAD. Moreover, opens the insight to new ways to design HTMs. A fundamental discussion on the role of key components of Spiro-OMeTAD like methoxy terminal groups is questioned due to the good results achieved by molecules that lack of them, like PTAA.

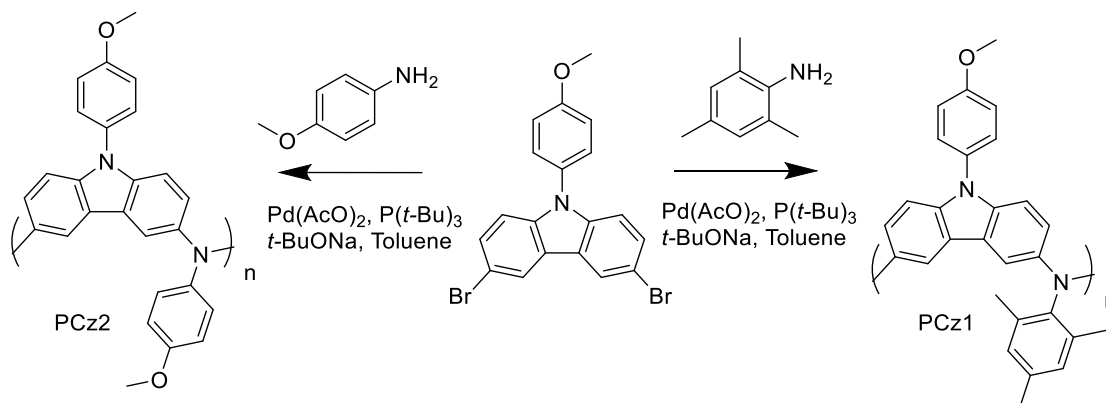
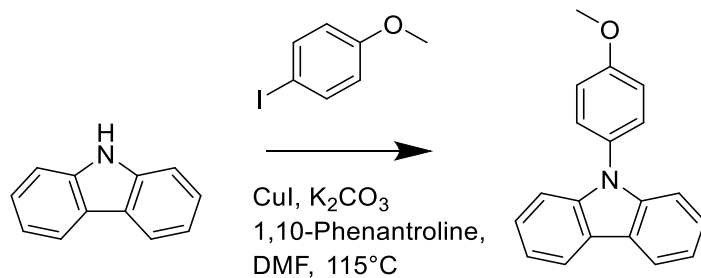


Figure 65 Resumed synthetic path for PCz1 and PCz2

Three oligomers where designed and synthetize using a simple path of metal catalyzed cross-coupling reaction to obtain the N-substituted-Cz derivative, followed by a bromination over the positions 3,6- on the carbazole core. The latter molecule can be directly coupled with the selected phenylamino linking agent to obtain the derived co-polymer (Figure 65).

Synthetic procedures

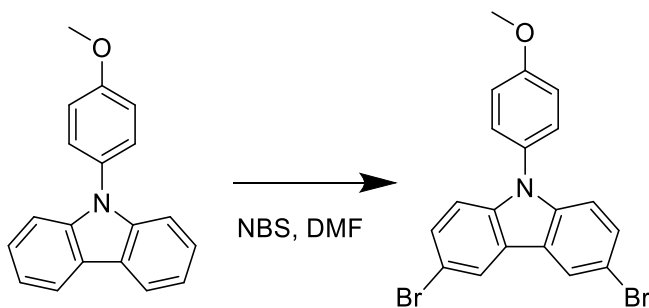
General synthesis procedure for N-phenylcarbazole.



In a dry 100 mL schlenk flask, carbazole (12 mmol, 1 eq) and p-iodoanisole, p-iodonitrobenzene, p-iodobenzonitrile (12 mmol, 1 eq), copper (I) iodide (1.93 mmol, 0.1 eq), potassium carbonate K₂CO₃ (17 mmol, 1.5 eq) and 1,10- Phenanthroline (2.69 mmol, 0.22 eq) were dissolved in DMF (200 mL) and charged. Reaction conditions are at 115°C for 24h. The mixture is allowed to cool at room temperature, filter by flash column with eluent gradient P_{eth}/chloroform (1/0- 1/0.2 v - v). Different fractions are collected, dried over anhydrous MgSO₄ filtered and concentrated under vacuum. The crude product is dissolved in methanol and recrystallized at 0°C affording a white solid 85%.

¹H NMR 250 MHz (DMSO-d₆) δ (ppm) 3.88 (s, 3H), 7.21 (d, 2H), 7.28 (d, 4H), 7.39-7.45 (d, 2H), 7.48-7.55 (d, 2H), 7.23 (d, 2H).

Synthesis of 3,6-dibromo-9-(4-methoxyphenyl)carbazole (Br₂CzPhOMe).

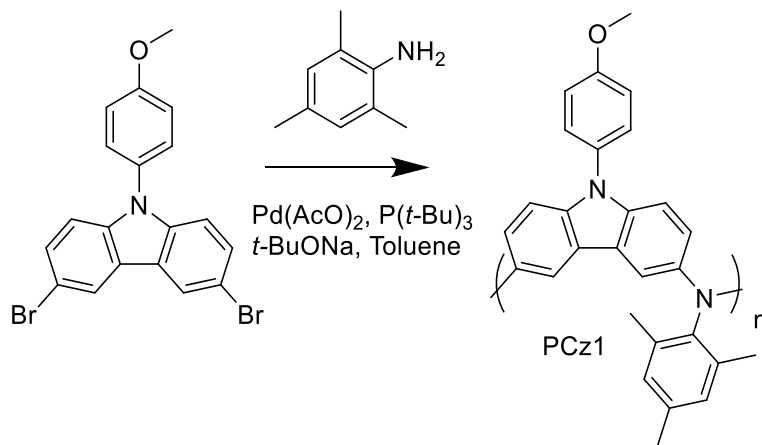


In a dry 100 round bottom flask placed in an ice bath, CzPhOMe (3.65 mmol, 1 eq) is dissolved in DMF (40 mL) followed by the addition of N-Bromosuccinimide (NBS) (2.23 mmol, 2.1 eq) dissolved in DMF (20 mL) and let it react for 2 hrs. Then ice bath is removed allowing the reactin mixture to reach room temperature in 1 hr. The reaction is quenched by adding water-brine (250 mL) and filtered. Raw product is dissolved in CHCl₃ and washed 3 times with water, MgSO₄ dried and solvent removed under vacuum. Precipitated in a CH₂Cl₂/petroleum ether (1-1 v-v) mixture at 0°C yielding an 83% of a white amorphous solid.

¹H NMR 250 MHz (DMSO-d₆) δ (ppm) 3.83 (s, 3H), 7.15-7.27 (m, 4H), 7.44-7.62 (m, 4H), 8.54-8.59 (m, 2H).

¹³C {¹H} NMR 62.9 MHz (DMSO-d₆); δ (ppm) 55.97, 112.27, 112.61, 115.87, 123.74, 124.09, 128.72, 128.84, 129.83, 140.19, 159.37.

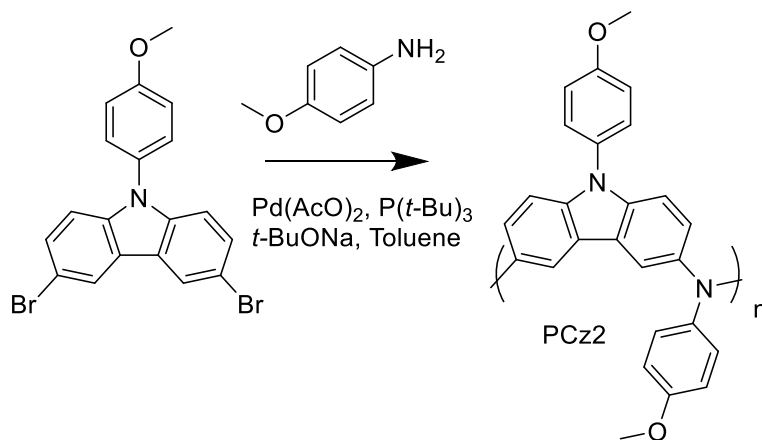
Synthesis of Poly(N-(4-methoxyphenyl)-3-(2,4,6-trimethylanilino)carbazole) (PCz1).



In a dry 100 mL schlenk flask under Ar atmosphere, Br₂CzPhOMe (1.16 mmol, 1 eq) and 2,4,6-trimethylaniline (1.16 mmol, 1 eq), palladium (II) acetate (0.057 mmol, 0.05 eq), tri-tert-butylphosphine (0.011 mmol, 0.1 eq) and sodium tert-butoxide (5.79 mmol, 5 eq) were charged and dissolved in toluene (30 mL). The mixture reaction is left to react at 115°C for 48h. The reaction is quenched by adding ethyl acetate (150 mL) and then filtered through a short silica pad. Solvent was removed under vacuum and the residue was dissolved in a minimal amount of CHCl₃ and two drops of toluene. This mixture was added to petroleum ether to promote its precipitation. The product is filtered and washed with petroleum ether several times to yield a yellow amorphous solid in 70% yield.

¹H NMR 250 MHz (DMSO-d₆) δ (ppm) 1.75-2.35 (m, 9H), 3.82 (s, 3H), 6.24-6.63 (m, 2H), 6.69-7.23 (m, 8H), 7.29-7.65 (m, 2H).

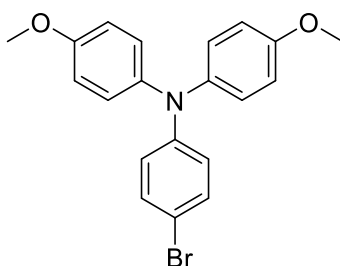
Synthesis of Poly(N-(4-methoxyphenyl)-3-(4-methoxyanilino)carbazole) (PCz2).



In a dry 100 mL schlenk flask under Ar atmosphere, $\text{Br}_2\text{CzPhOMe}$ (1.15 mmol, 1 eq) and p-anisidine (1.27 mmol, 1.1 eq), palladium (II) acetate (0.057 mmol, 0.05 eq), tri-tert-butylphosphine (0.011 mmol, 0.1 eq) and sodium tert-butoxide (6.95 mmol, 6 eq) were charged and dissolved in toluene (15 mL). Let it react at 115°C for 48h. The reaction is quenched by adding ethyl acetate (150 mL) and then filtered through a short silica pad. Solvent was removed under vacuum and the residue was dissolved in a minimal amount of CHCl_3 and three drops of toluene. This mixture is added to methanol to promote its precipitation. The product is filtered and washed with methanol several times to yield a yellow amorphous solid in 42% yield.

$^1\text{H NMR}$ 250 MHz (DMSO-d_6) δ (ppm) 3.49-4.03 (m, 6H), 6.07-7.92 (m 14H).

Synthesis of 4-bromo-N,N-bis(4-methoxyphenyl)aniline (TPA).

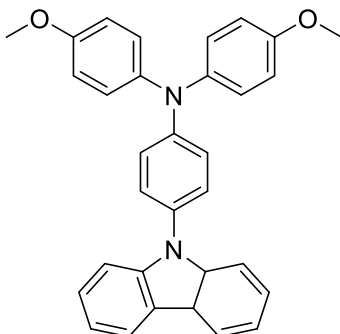


In a dry 100 mL schlenk flask under Ar atmosphere, p-iodoanisole (17 mmol, 3 eq) and p-bromoaniline (6 mmol, 1 eq), copper (I) chloride (0.58 mmol, 0.05 eq), potassium hydroxide (88 mmol, 15 eq) and 1,10-Phenanthroline (1.74 mmol, 0.05 eq) were charged and dissolved in toluene (15 mL) and let it react at 120°C for 24h. The reaction is quenched by adding HCl (0.01 M) solution (10 mL) and extracted with CHCl_3 (3 x 40mL). Organic fractions collected and washed with water (x3) then dried over anhydrous MgSO_4 , filtered and solvent removed under vacuum.

The product is purified by solid deposition column with an eluent mixture of P_{eth}/AcOEt (8-1 v-v). Fractions collected and solvent reduced to a minimal amount and product precipitated at 0°C. A dark pale amorphous solid is collected in 74% yield.

¹H NMR 250 MHz (DMSO-d₆) δ (ppm) 3.78 (s, 6H), 6.84-7.15 (m, 4H), 7.24-7.54 (m, 4H), 8.1-8.22 (m, 4H).

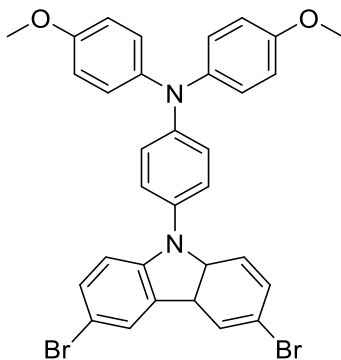
Synthesis of N-(4-(N,N-bis(4-methoxyphenyl)aniline)carbazole (CzTPA).



In a dry 100 mL schlenk flask under Ar atmosphere, carbazole (5.98 mmol, 1 eq) and TPA (5.08 mmol, 0.85 eq), palladium (II) acetate (0.29 mmol, 0.05 eq), tert-butylphosphine (0.59 mmol, 0.1 eq) and sodium tert-butoxide (36 mmol, 6 eq) were dissolved in toluene (14 mL) and charged into the flask. Let it react at 115°C for 24h. The reaction is quenched adding ethyl acetate (50 mL) and silica filtered. The product is column purified with a solvent mixture of P_{eth}/AcOEt (9-1 v-v). Fractions collected, solvent removed under vacuum and precipitated in CHCl₃/P_{eth} (50/50) at 0°C. A brownish amorphous solid is collected in 60% yield.

¹H NMR 250 MHz (DMSO-d₆) δ (ppm) 3.77 (s, 6H), 6.85-7.03 (m, 6H), 7.07-7.47 (m, 12H), 8.13-8.27 (m, 2H).

Synthesis of 3,6-dibromo-N-(4-(N,N-bis(4-methoxyphenyl)aniline)carbazole (Br₂CzTPA).



In a dry 100 round bottom flask in an ice bath CzTPA (1.06 mmol, 1 eq) is dissolved on DMF (17 mL) followed by the addition of N-Bromosuccinimide (NBS) (2.23 mmol, 2.1 eq) and let it react for 2h allowing it to reach room temperature. The reaction is quenched adding water-brine (200 mL) and filtered. Raw product is dissolved in CHCl₃ and washed x3 with water, MgSO₄ dried and solvent removed under vacuum. The product is column purified with a solvent mixture of Pet_h/CHCl₃ (1-2 v-v). Fractions collected, solvent removed under vacuum to obtain a dark purple amorphous solid in 49% yield.

¹H NMR 250 MHz (DMSO-d₆) δ (ppm) 3.75 (m, 6H), 6.82-7.07 (m, 4H), 7.08-7.60 (m, 12H), 8.13-8.55 (m, 2H).

Synthesis of Poly[3-(anisol)-N-(4-(N,N-bis(4-methoxyphenyl)aniline)carbazole] (PCz3).

In a dry 100 mL schlenk flask under Ar atmosphere, Br₂CzTPA (0.54 mmol, 1 eq) and p-methoxyaniline (0.59 mmol, 1.1 eq), palladium (II) acetate (0.027 mmol, 0.05 eq), tert-butylphosphine (0.054 mmol, 0.1 eq) and sodium tert-butoxide (2.7 mmol, 5 eq) were charged and dissolved in toluene (24 mL). Let it react at 105°C for 48h. The reaction is quenched by adding ethyl acetate (150 mL) and silica filtered. The excess of solvent is removed under vacuum and dissolved in a minimal amount of CHCl₃ and two drops of toluene. This mixture is added to methanol to promote its precipitation. The product is filtered and washed with methanol several times to yield a yellow amorphous solid with 80% efficiency.

¹H NMR 250 MHz (DMSO-d₆) δ (ppm) 3.56-3.86 (m, 9H), 6.73-7.48 (m, 20H), 7.67-7.81(m, 1H), 8.2-8.27 (m, 1H).

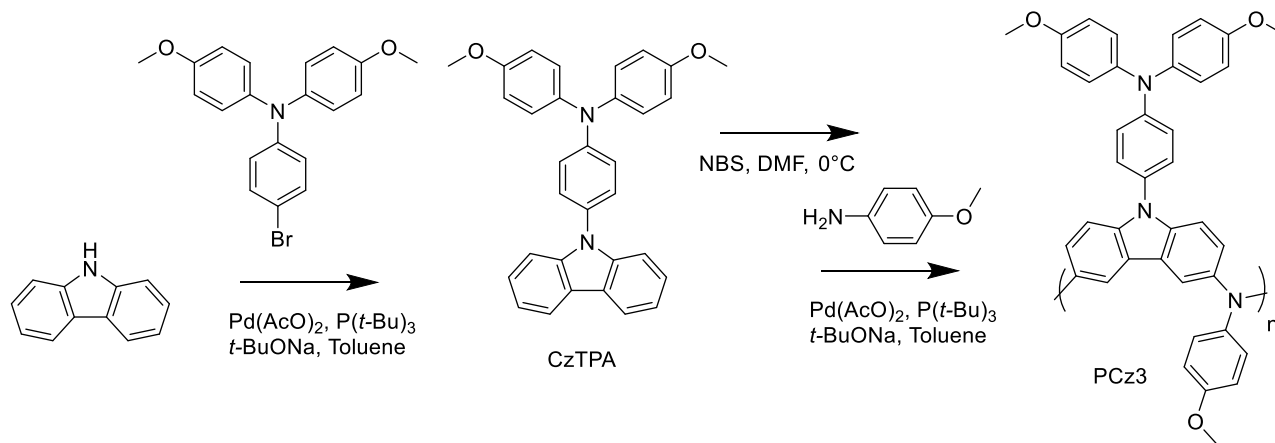


Figure 66 General synthesis of PCz3

3.3.3 Characterization

3.3.3.1 Thermal Properties

The thermal stability of these PCzX (X=1, 2, 3) oligomers were analyzed TGA. Figure 67 shows the TGA curves of PCz1, PCz2 and PCz3 with a single stage decomposition in a range that goes from 0 to 700°C . More specifically, a plateau that extends to around 300°C is observed for all three polymers, PCz1 being the more stable with a temperature of 344°C . Moreover, a slightly lower temperature decomposition is observed for PCz2 and PCz3 probably due to steric hindrance of the triphenylamine group for PCz3 and the methoxy groups for both oligomers, PCz2 and PCz3.

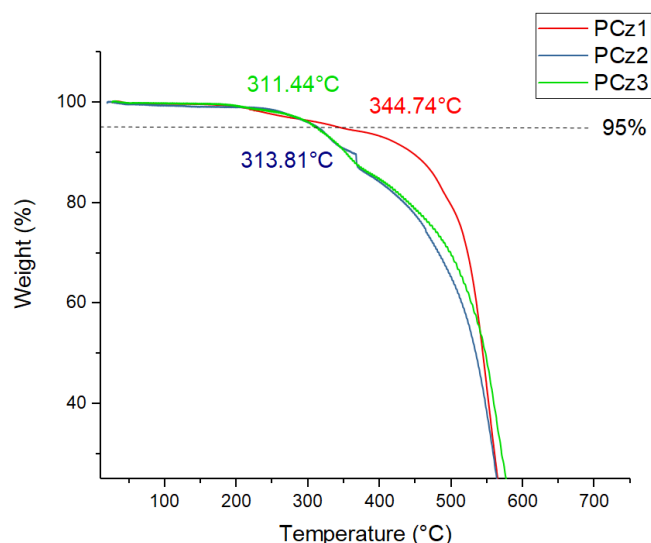


Figure 67 TGA of PCzX series

The thermal properties of PCzX series were examined by DSC between 0 and 250°C (Figure 68). The polymer PCz1 exhibited glass-transition temperatures (T_g) with a first endothermic event at 153°C followed by an exothermic event corresponding to a crystallization at 185°C and an endothermic event that represents a melting point at 229°C.

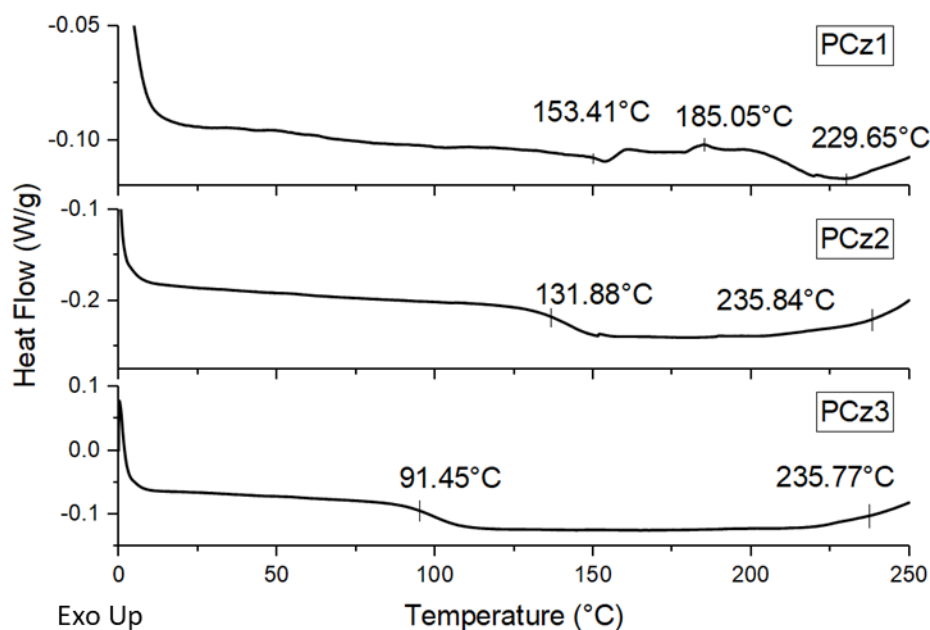


Figure 68 DSC (2nd cycle) of PCzX series

For PCz2 and PCz3 exhibit one endothermic event, interpreted as a glass transition temperature T_g at 131°C and 91°C respectively. After glass transition temperatures both oligomers show an

oxidation behavior after 235°C, meaning that oligomers undergo through a degradation process. Nevertheless, all glass transition temperatures for PCzX remain on the working range for a PSC, making of them a thermodynamically suitable candidates. Similar to T_d , PCz1 proved to be more stable than PCz2 and PCz3, demonstrating that methoxy groups, for this series, lower the thermodynamic stability of the oligomer, demonstrating that trimethylamine containing oligomer, is more resilient in both senses, thermostable and thermodynamic oligomer.

We can conclude that a full conjugated oligomer with a π -system running all along the chain will restrain the flexibility of the oligomer, making it more sensitive to thermal degradation. Regarding to glass transition temperatures we can observe how they are gradually reduced with the addition of bulky groups, in the following order PCz1>PCz2>PCz3.

There is no significant difference between PCz1 and PCz2, but the addition of triphenylamine for PCz3 reduces dramatically the glass transition temperature.

3.3.3.2 Optical Properties

UV–Vis absorption spectra recorded on 1×10^{-6} M (monomer unit equivalent) DCM solution of the PCzX oligomers series are presented in Figure 69.

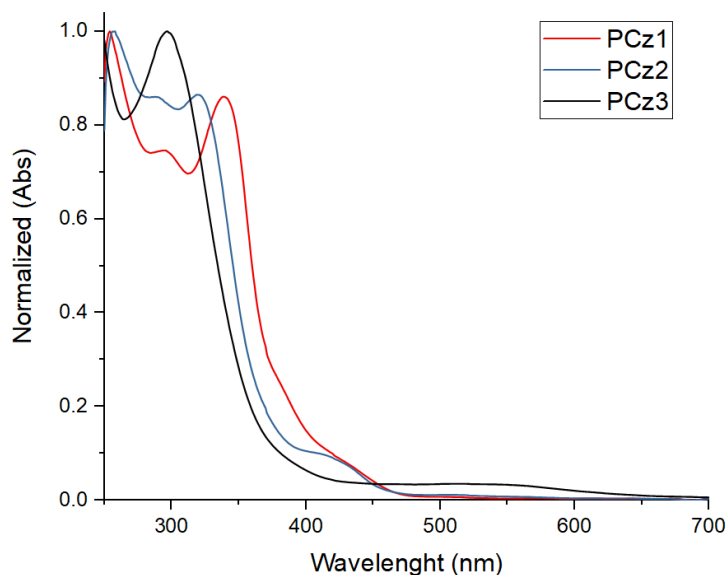


Figure 69 UV-vis spectra of PCzX series (X=1,2,3)

They have a π - π^* absorption band from the conjugated oligomer, with a maximum peak at 254 nm, and lower energy absorption bands, that can be assigned as n - π^* bands observed at >350 (295 and 338 nm). Absorption curves of PCz1 and PCz2 are quite similar, PCz2 shows a small hypsochromic shift (around 10 nm) in wavelength due to the presence of one extra methoxy group per unit, which increase also the absorption on the 300 nm band.

In the case of PCz3, hypsochromic shift of 46 nm which indicates a conjugation interruption, probably due to the lack of interaction of the methyl groups from the diphenyl amine group and the carbazole core or a smaller conjugation length

The oligomer family PCzX (X=1,2,3) present an adequate absorption, mostly in the UV spectral domain which will not cause parasitic interference in the absorption range of the perovskite material.

3.3.3.3 Electrochemistry measurements

All new oligomers are investigated by cyclic voltammetry (CV) are given in Figure 70 and the resumed values on Table 21. The CV curves corresponding to PCzX oligomers (Figure 70) display multiple oxidation processes and well defined oxidation waves. Due to the present of multiple triarylamine-type functions in the polymer, it is difficult to localize the first oxidation state.

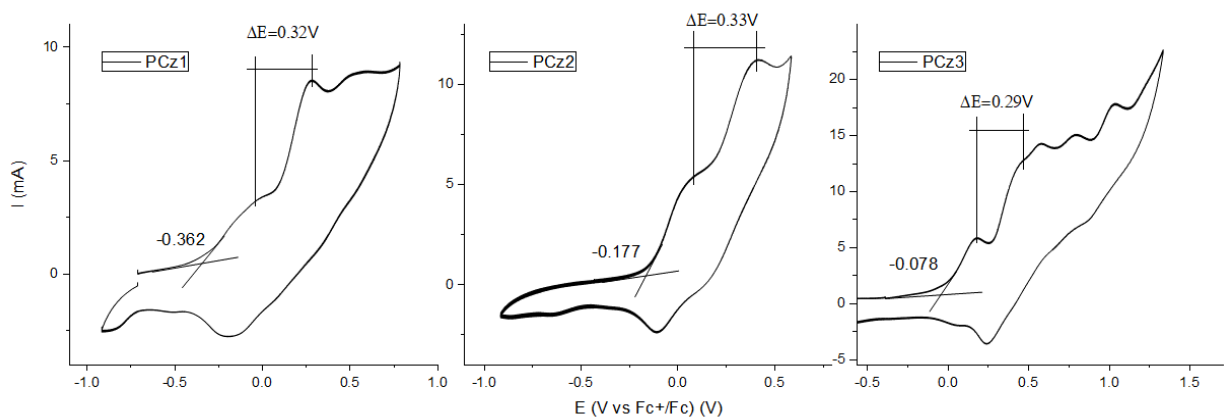


Figure 70 PCzX series voltammogram

The CV curves corresponding to PCzX oligomers (Figure 70) display at least one reversible oxidation peak. Due to the extended conjugation through the polymer chain, the first oxidation

state presents a more diffuse character along the whole chain. It's also worth to notice that PCz1 and PCz2 have a more extended oxidation peak. In other hand PCz3 voltammogram has a well defined first oxidation peak indicating thus a stable first oxidation state. PCzX oligomers possess a longer potential range between oxidation states, reflected on a gap between oxidation peaks (ΔV) of around 0.3 V.

Table 21 Oxidation values of PCzX series

Polymer	E_{Ox1} [V]	E_{Ox2} [V]	ΔV [V]
PCz1	-0.04	0.28	0.32
PCz2	0.08	0.42	0.34
PCz3	0.17	0.47	0.30

From the potential of the first oxidation, HOMO energy level of PCzX oligomers were estimated. Using the HOMO energy level and the optical bandgap, the LUMO energy level can be estimated. All thermal and optoelectrochemical properties of these oligomers are summarized in Table 22

Table 22 General thermal, optical and electrochemical characteristics of PCzX series

Compound	T_g (°C) ^[a]	T_d (°C) ^[b]	$\lambda_{max}(nm)$ ^[c]	$\lambda_{onset}(nm)$ ^[c]	$E_{gap}(eV)$ ^[d]	$E_{ox}(V)$ (Fc/Fc ⁺)	HOMO ^[IP] (eV)	LUMO ^[EA] (eV)
PCz1	153.4	344	339,256	460	2.7	-0.36	4.44	1.7
PCz2	131.8	313	321, 258	462	2.7	-0.15	4.64	2.0
PCz3	95.4	311	298	408	3.0	-0.08	4.72	1.7

^[a]Obtained from TGA measurements. ^[b]Obtained from DSC measurements. ^[c] Measured in CH₂Cl₂ solution 1 x 10⁻⁶ M (Single unit equivalent).. ^[d] Measured in CH₂Cl₂ 1.0 x 10⁻² M TBAPF₆ solution. Analyte 1 x 10⁻⁴ M (Single unit equivalent). All E_{ox} data are reported relative to ferrocene²⁰⁰ which has a value of ionization potential (IP) 4.8 eV for ferrocene and 0.27 V for Fc/Fc⁺ against Au/Au⁺. The concentration of the complexes used in this experiment was 1.0 x 10⁻³ M and scan rate was 100 mV s⁻¹. $E_{gap} = hc/\lambda_{onset} = 1240 \text{ eVnm}/\lambda_{onset}$; $IP = E_{ox} + 4.8$; $EA = IP - E_{gap}$

The frontier energy levels of these materials are given in Figure 71 against that of Spiro-OMeTAD and perovskite for comparison purpose. As can be seen, HOMO-LUMO energy levels suggest that these oligomers could assure efficient hole transfer from perovskite into the HTL. It could also efficiently block electron charge recombination. The later results suggest that these polymers could be used as HTM in PSC device.

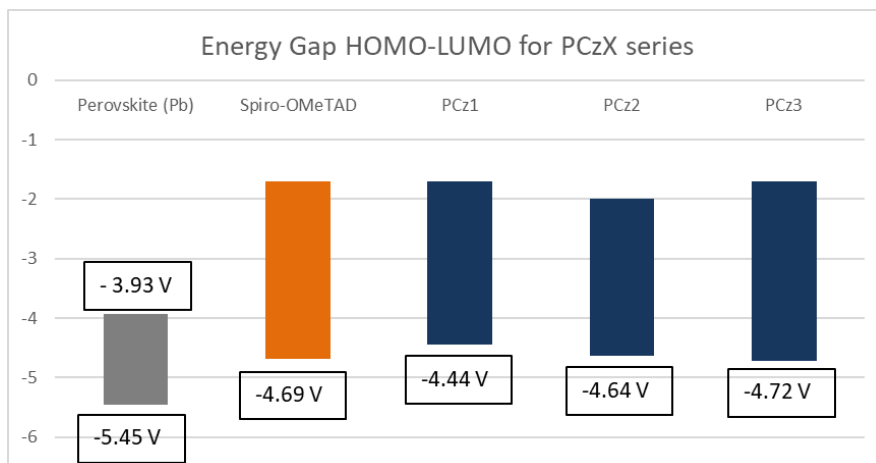


Figure 71 Energy Gap HOMO-LUMO for PCzX series

3.3.3.4 Surface Morphology

The surface roughness parameter is an important parameter of HTL for decreasing current losses and attaining better contact with the cathode. Optimal interface morphology between the active layer and the metal electrode can be partly confirmed by the surface quality of HTL.²⁰² Moreover, low surface roughness can ensure a good contact between the hole transport layer (HTL) and the perovskite layers.

The films were prepared using the same procedure as described on Chapter 2. A solution was prepared by dissolving 60 mg of HTM in 1 ml chlorobenzene. Then, 17.5 μ l of bis(trifluoromethylsulfonyl)imide lithium salt solution (LiTFSI) solution (520 mg in 1 mL ACN), 28.8 μ l of TBP (tert-butylpyridine) and 6 μ l of tris (2-1H-pyrazol-1-yl) - 4-tert-butylpyridine – cobalt (III) -tris (bis (trifluoromethylsulfonyl) imide) (300 mg in 1 mL ACN) were added to this solution. 35 μ l of the HTM solution was spin-coated at 4000 rpm, 4000 rpm/s for 20 s.

Morphology of PCz1, PCz2 and PCz3 made films with additives over glass substrates are studied by AFM and images are given in Figure 72. The roughness is given in Table 23. All films show

uniform and smooth surface morphology implying thus very good film formation properties. The three of them show small roughness values, being the lowest value for PCz3. This can be explained by its good solubility thanks to steric effect of the triphenylamine moiety and the numerous methoxy groups contained on the polymer unit (three in total).

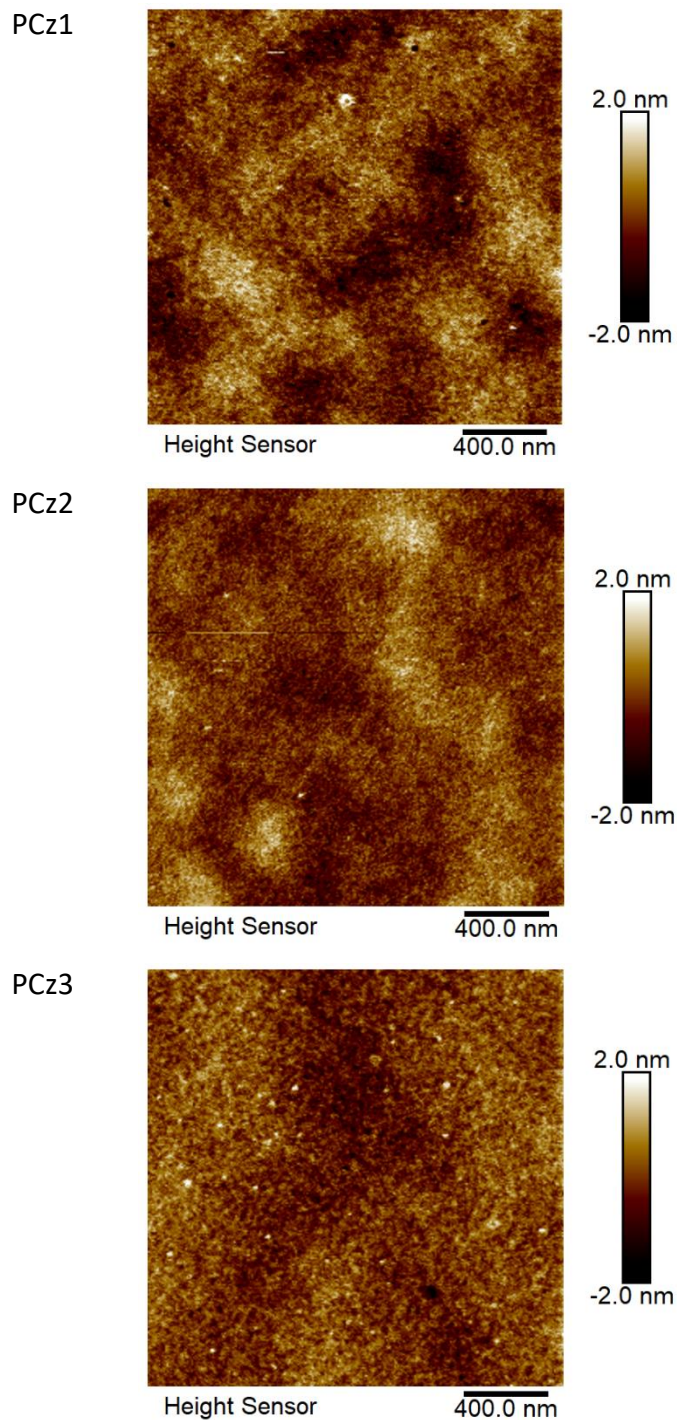


Figure 72 Film AFM images of PCzX polymers at 2 μ m scale

Table 23 PCzX average roughness values from AFM images

		600 nm	2 μ m	5 μ m	10 μ m
PCz1	Rq	0.65	0.97	2.44	0.86
	Ra	0.52	0.77	1.99	0.68
PCz2	Rq	0.59	2.4	2.64	0.6
	Ra	0.44	1.17	1.00	0.42
PCz3	Rq	0.46	0.55	0.68	1.56
	Ra	0.32	0.44	0.55	1.19

If the root mean square and the arithmetic mean roughness values calculates as their name say, the average of the height asperities on the film surface. More smooth and homogenous is the surface formed film, smaller both values are going to be. In the case of PCzX, the film forming ability is remarkable. We noted that both PCz1 and PCz2 show higher values on the 5 μ m area of the picture. We can conclude that some deeps or valleys are always formed, making some defects or anomalies on the film without being an issue for PSC purposes.

3.3.3.5 Computational Studies

All calculations reported in this work were carried out using the Gaussian 09²⁰¹ suite of programs. Ground state geometries of fragment composed by 4 units from oligomers PCz1, PCz2 and PCz3 were fully optimized without imposing any symmetry constraints by employing the 6-31G(d,p) basis set. HOMO and LUMO orbitals are localized, both, along the center chain (Figure 73). Computational values do not represent the carrier dynamics of the oligomer; nevertheless, a good approximation can be done by computational analysis of a chain fragment.

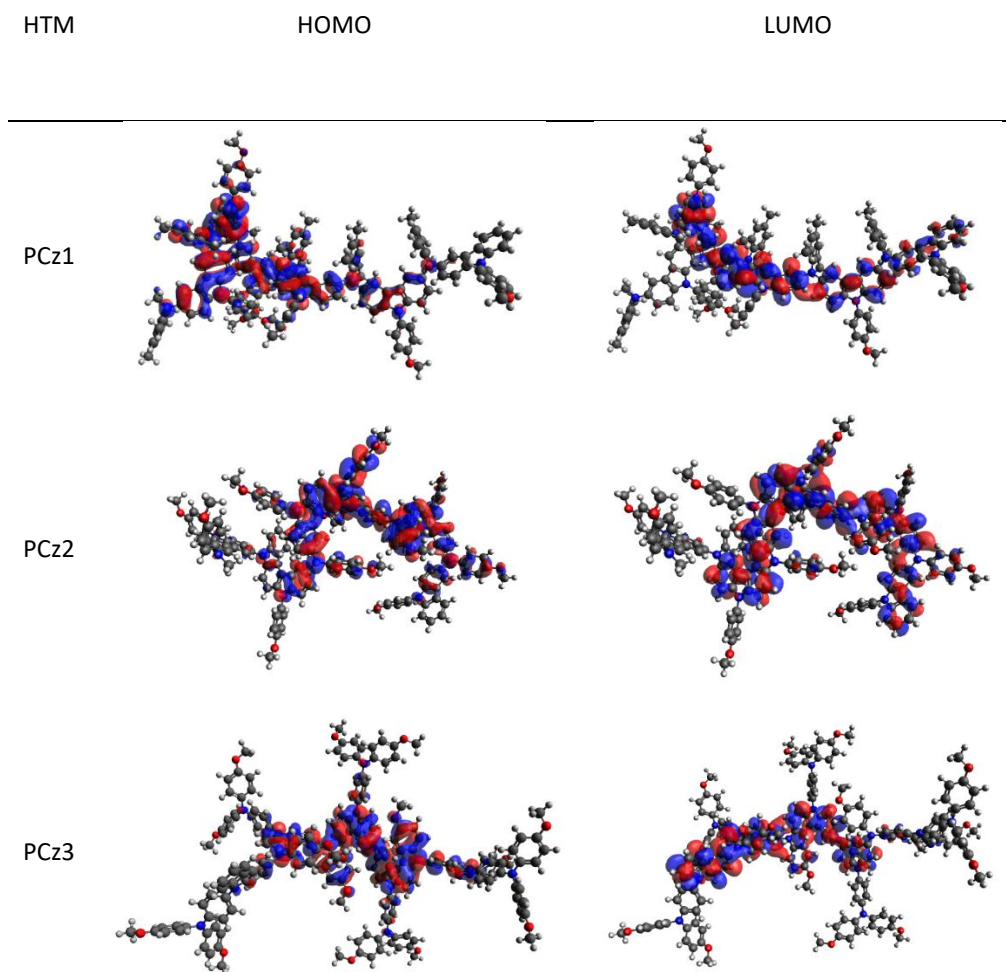


Figure 73 Calculated molecular orbitals for PCzX series

Table 24 Experimental and theoretical values of PCzX series

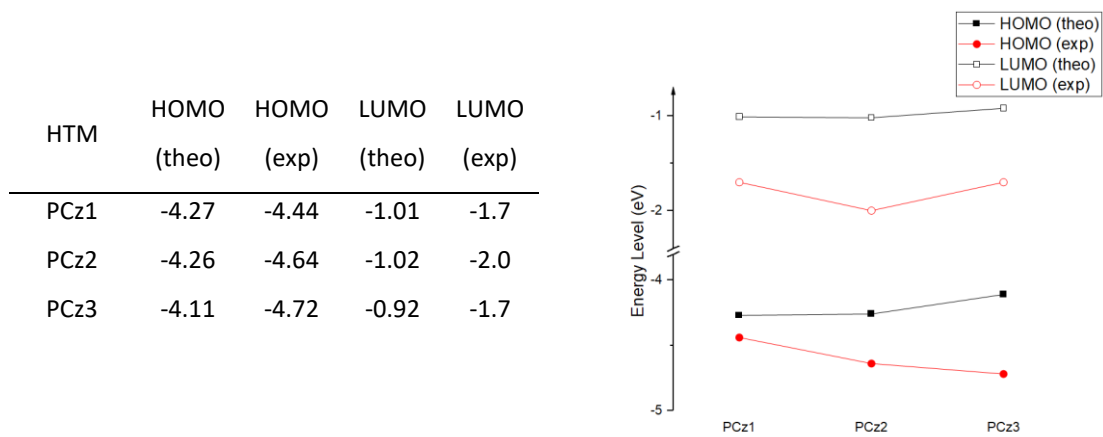


Table 24. Calculated values tend to be higher in energy compared with experimental values. In the same way LUMO energy values follow the same trend, higher values than its experimental couple. The later results indicate an accurate approximation in the calculations for the PCzX series.

3.3.3.6 Contact angle measurements

Contact angles of the water drop on the oligomer films deposited on glass substrates are measured in order to estimate the relative hydrophobicity of these films. Highly hydrophobic films are expected in order to protect the perovskite layer from moisture. Pinholes can be formed in the film and promote the degradation of the perovskite, and thus good hydrophobicity of the layer is a desired feature. In addition, this study can establish a relation between HTL molecule structure and its repelling water properties. PCzX (Figure 74) series show a clear tendency to decrease the contact angle as they increase the number of methoxy groups in the polymer unit, making evident the effect that such groups have over the water repellent character of film. Hydrophobicity and contact angle is measured over the films prepared using the method for the previous AFM experiments. All the measurements were repeated five times depositing 10 μ L of deionized water over the HTL and measuring the contact angle and calculating its arithmetic deviation. Images in Figure 74 are a representation of the angle formed between the water drop and HTL film. Real values are calculated automatically and contact angle average values are shown below.

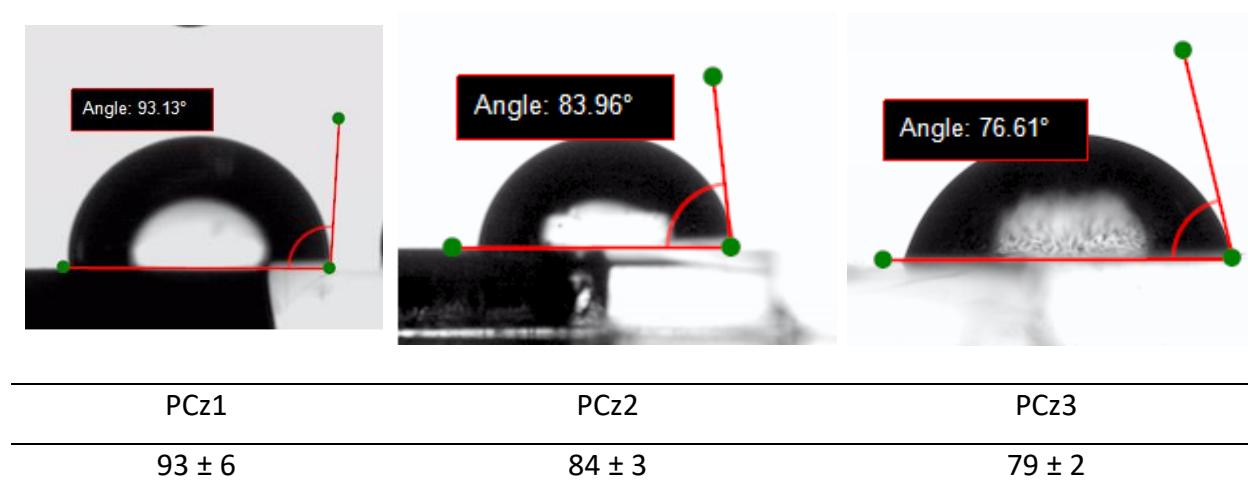


Figure 74 Contact angle of PCzX films average values and representative image

3.3.4 Conclusions

Three new oligomers are designed, synthesized and characterized for the purpose of application as HTM in perovskite photovoltaic devices.

These oligomers present advantages like easy and affordable synthesis, simplified purification through precipitation process in common solvents like methanol or petroleum ether.

The three oligomers due to their relatively high molecular weight have high glass temperature, ideal to work on photovoltaic prototypes. This thermodynamic advantage make oligomers a resilient option for their use as hole transport materials.

We propose the use of trimethylanilino moiety on PCz1, as an alternative of methoxy-substituted molecules in hole transport materials. Thermal, morphological, optical and electrochemical characterizations suggest that these oligomers could be suitable for the role of HTM.

Their test on real PV devices could help to elucidate the role, of fully conjugated oligomers against single molecules and the influence on the number of methoxy groups per monomer units.

4. Bicarbazylum and 1,4-bicarbazolyl--benzene HTMs

4.1 State of the art

Conjugation through side to side carbazole based polymers or oligomers where the polymer backbone is covalently connected to n -number of carbazole moieties, is expected to improve the hole transporter properties. A good hole mobility is one of the most important and desired characteristics on final molecules, thus the aim for the design and synthesis of functional conjugated polymers can be achieved in two different manners: Carbazole can be coupled by 1) oxidative coupling²³⁷ or 2) catalyzed coupling reactions²³⁸.

Oxidative coupling is achieved by two different ways: electrochemical oxidation or by oxidative FeCl_3 catalyzed polymerization. In order to have positive results, it is needed to understand firstly carbazole electronic properties and oxidation/reduction mechanism in order to design useful reactions and molecules that allow them to undergo by subsequent reactions and thus finally obtaining functional polymers.

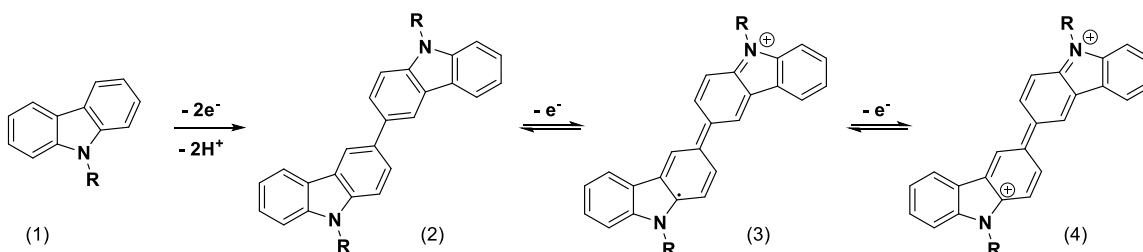


Figure 75 Dimerization and mechanism for the electrochemical oxidation of (1) N-carbazole into (2) 3,3'-bicarbazyl and further (3) bicarbazyl radical-cation and (4) dication.²³⁹

For both oxidative coupling reactions (electrochemical and catalyzed), bicarbazyl dication is stabilized by the delocalization of the positive charges through the whole molecule π -system including the two nitrogen atoms, which hinders following reactions and polymerization.

Siove *et al.*²³⁷ demonstrated that oxidative polymerization catalyzed by FeCl_3 is possible in sterically impeded carbazole molecule 1,4,5,8,9-pentamethylcarbazole. Due to the high steric hindrance, the twisted derivative bi-carbazyl dication, leads to a reduced conjugation between the monomer units. This non-coplanar structure conduces to the destabilization of the oxidized 3,3'-bicarbazyl dimer breaking the π -conjugation allowing for the first time, to a carbazole compound to be converted in high polymer by the dehydrocoupling route using FeCl_3 as the oxidizing agent.

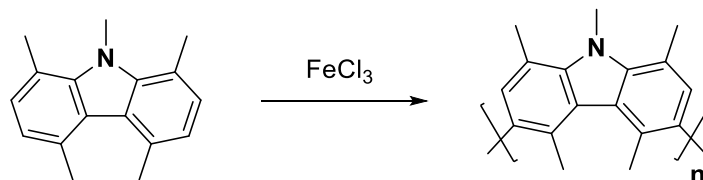


Figure 76 Oxidative polymerization of 1,4,5,8,9-pentamethylcarbazole²³⁷

Nevertheless, of the final structure of the carbazole compound of interest, knowledge of its electronic properties is crucial to its practical application. A complete data of the properties of carbazole monomer and their potential polymers are of great importance, and represent the basics for designing suitable carbazole-based polymeric derivatives with the desired properties.

4.2 Carbazole oxidative coupling

With the aim to test the polymerization capacity of carbazole under the right conditions, we want to propose a series of carbazole compounds that can function as a potential monomers in order to test their polymerization ability. Our proposal is based on the fact that, linking carbazole through the nitrogen-containing conjugated structure enables it to react by obtaining a polycarbazole.²⁴⁰ Such polymer will be electron-rich and conjugated which, may enhance conductivity making of it a suitable candidate for exploration its use as an organic polymer for PSC.

4.2.1 Synthesis objective

The process to form polymer by oxidative catalysis has cost-effective advantages such as using a common catalyst, mild reaction conditions, and requiring a single monomer unit. Because no other functional groups such as halogen atoms (chlorine, bromine, iodine) or dioxaborolane¹⁶⁴ derivatives are required for coupling polymerization, properties derived from monomers are likely to be fully retained and structures of final polymers are easier to characterize. A series of 1,4-bicarbazolyl-benzene is synthesized to test their polymerization ability using oxidative coupling FeCl_3 catalyzed method. The series tend to be progressive in the sense that, only one position is modified in consecutive synthetic steps.

With the use of this series we pretend to map their electronic properties through their evolution by the integration of different electron rich groups and to sketch their potential use as functional hole transport materials for perovskite solar cells.

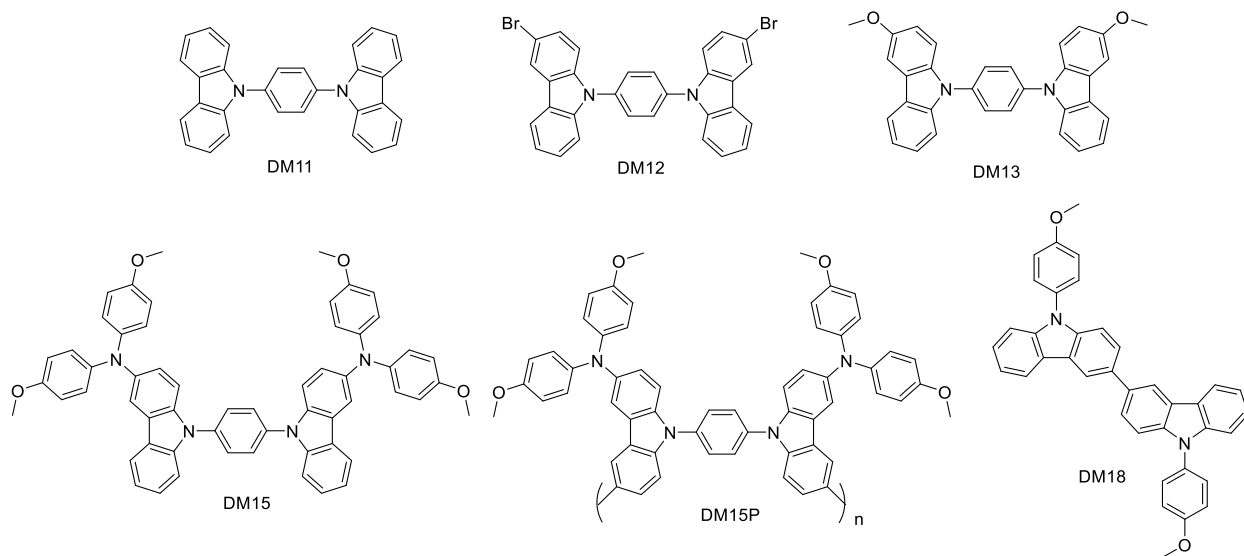
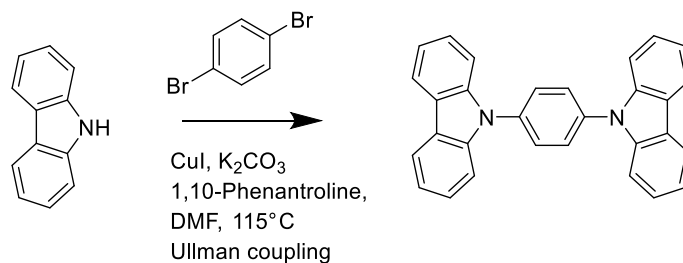


Figure 77 Series of 1,4-bicarbazolyl-benzene DM1X

4.2.2 Synthetic procedures

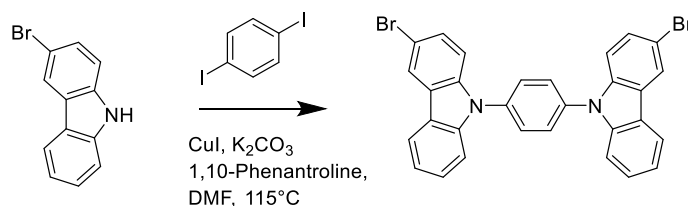
General synthesis procedure for 1,4-bis(carbazol-9-yl)benzene (DM11). In a dry 100 mL schlenk flask under Ar atmosphere, 9H-carbazole (8,97 mmol, 1 eq) and p-dibromobenzene (4,03 mmol, 0,45 eq), cupper (I) iodide (0,68 mmol, 0,17 eq), potassium carbonate (4,03 mmol, 1 eq) and 1,10-Phenanthroline (2,01 mmol, 0,225 eq) were dissolved in DMF (15 mL) and charged into the flask. Let it react at 120°C for 24h. The reaction is quenched adding water-brine (100 mL) and filtered. The raw product in is dissolved in CHCl₃ and washed with water-brine. Fractions collected and MgSO₄ dried, solved removed to minimal and petroleum ether is added to induce precipitation at 0°C. Precipitation is carried two times to yield 67% of a white amorphous solid.



^1H NMR 250 MHz (DMSO- d_6) δ (ppm) 7.34 (t, 4H, $J = 7.1\text{Hz}$), 7.51 (t, 4H, $J = 8.37$), 7.62 (d, 4H, $J = 8.2$), 7.94 (s, 4H), 8.31 (d, 4H, $J = 7.74$).

^{13}C { ^1H } NMR 62.9 MHz (DMSO- d_6); δ (ppm) 110.29, 120.76, 121.07, 123.32, 126.83, 128.72, 136.20, 140.49.

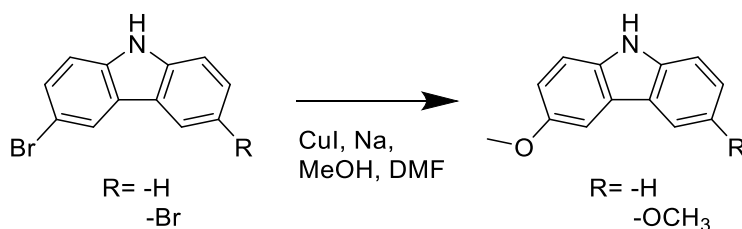
General synthesis procedure for 1,4-bis(3-bromo-carbazol-9-yl)benzene (DM12). In a dry 100 mL schlenk flask under Ar atmosphere, 3-bromo-9H-carbazole (4 mmol, 1 eq) and p-diiodobenzene (1.97 mmol, 0.48 eq), copper (I) iodide (0.33 mmol, 0.17 eq), potassium carbonate (1.97 mmol, 1 eq) and 1,10-phenanthroline (0.91 mmol, 0.225 eq) were dissolved in DMF (15 mL) and charged into the flask. The reaction mixture reacts at 115°C for 24h. The reaction is quenched adding water-brine (100 mL) and filtered. The raw product is dissolved in CH_2Cl_2 and silica filtered to remove rest of inorganics. Fractions collected and MgSO_4 dried and solvent removed to minimal volume. Petroleum ether is added to induce precipitation at 0°C. A white amorphous solid is obtained with 90%.



^1H NMR 250 MHz (DMSO- d_6) δ (ppm) 7.28-7.45 (m, 2H), 7.49-7.7 (m, 6H), 7.94 (s, 4H), 8.31-8.43 (m, 2H), 8.53-8.62 (m, 2H), 8.67-8.77 (m, 2H).

General synthesis procedure for 3-methoxy-9H-carbazole and 3,6-dimethoxy-9H-carbazole. In a two neck 250 mL round-bottom flask on ice bath at 0°C, equipped with a condenser and under Ar atmosphere, 60 mL of distilled DMF and 40 mL of absolute MeOH are loaded with 4.6 gr of metallic sodium (203 mmol, 20 eq). Two hours later, ice bath is removed and metallic sodium is dissolved forming sodium methoxide. Then catalyzer copper (I) iodide (20 mmol, 2 eq) is added

and let it stir for 30 min while the solution turns to green. Then, 3-bromocarbazole (10 mmol, 1 eq) is added and let it react for 24 hours at 115°C. Water is added to quench the reaction and ceramic funnel filtered, and washed with brine. The obtained solid (raw 3-methoxy-carbazole) that remains on filter is dissolved on AcOEt and silica filtered to remove solids. The product containing solution is washed with water and brine 3x, MgSO₄ dried and solvent removed under vacuum. Crude product is recrystallized from CHCl₃/Petroleum ether (50/50) to give a white crystalline product with a 72 % of efficiency. Note: same procedure is used to synthesized 3,6-dimethoxy-9H-carbazole using 3,6-dibromo-9H-carbazole as starting material and double equivalent of catalyzer and metallic sodium. A white crystalline powder is obtained with 56% of efficiency.

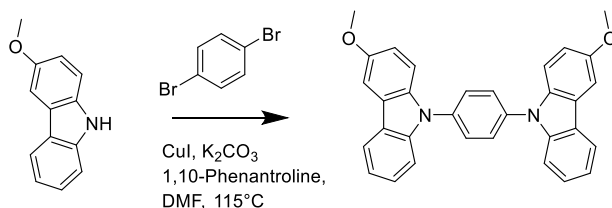


3-bromo-9H-carbazole ¹H NMR 250 MHz (DMSO-d₆) δ (ppm) 7.21 (t, 1H, *J* = 7.11Hz), 7.43 (t, 1H, *J* = 6.97), 7.48-7.54 (m, 3H), 8.17 (d, 1H, *J* = 7.43Hz), 8.30 (s, 1H), 10.5 (s, N-H).

3-methoxy-9H-carbazole ¹H NMR 250 MHz (DMSO-d₆) δ (ppm) 3.88 (s, 3H), 7.03 (dd, 1H, *J* = 8.69 Hz, *J* = 2.37Hz), 7.13 (t, 1H, *J* = 7.4Hz), 7.35 (t, 1H, *J* = 8.21), 7.41 (d, 1H, *J* = 8.69), 7.47 (d, 1H, *J* = 8.21), 7.67 (d, 1H, *J* = 2.37Hz), 10.13 (s, N-H)

General synthesis procedure for 1,4-bis(3-methoxy-carbazol-9-yl)benzene (DM13). In a dry 100 mL Schlenk flask under Ar atmosphere, 3-methoxy-9H-carbazole (2,53 mmol, 1 eq) and p-dibromobenzene (1,14 mmol, 0,45 eq), palladium (II) acetate (0,12 mmol, 0,05 eq), tri-tert-butylphosphine (0,278 mmol, 0,11 eq) and sodium tert-butoxide (15,2 mmol, 6 eq) were dissolved in toluene (15 mL) and charged into the flask. The reaction mixture reacts at 110°C for 24h. The reaction is quenched adding ethyl acetate (50 mL) and silica filtered. The raw product is dissolved in CHCl₃ and washed with water-brine. Fractions collected and MgSO₄ dried, the solvent is removed to a minimal quantity and petroleum ether is added to induce precipitation at 0°C. Precipitation is made two times to yield a white amorphous solid with 67%.

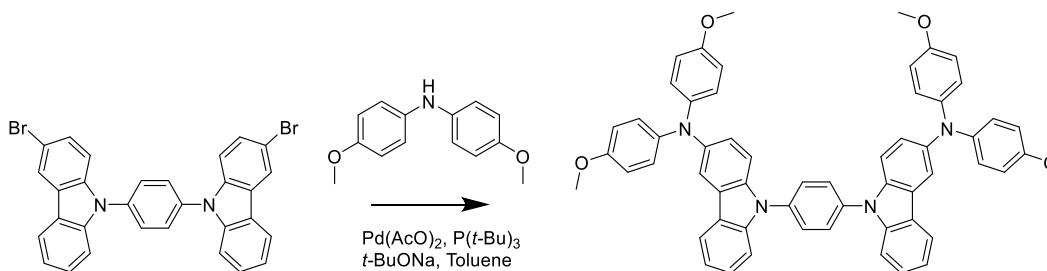
¹H NMR 250 MHz (DMSO-d₆) δ (ppm) 3.77 (s, 6H), 6.85-7.03 (m, 6H), 7.07-7.47 (m, 12H), 8.13-8.27 (m, 2H).



General synthesis procedure for 1,4-bis(3,3'-(bis(4,4'-dimethoxyphenyl)amine)carbazol-9-yl)benzene (DM15). In a dry 100 mL Schlenk flask under Ar atmosphere, 1,4-bis(3-bromocarbazol-9-yl)benzene (0,59 mmol, 1 eq) and 4,4'-dimethoxydiphenylamine (1,48 mmol, 2,5 eq), palladium (II) acetate (0,029 mmol, 0,05 eq), tert-butylphosphine (0,059 mmol, 0,1 eq) and sodium tert-butoxide (3,57 mmol, 6 eq) were dissolved in toluene (13 mL) and charged into the flask. Let it react at 115°C for 24h. The reaction is quenched adding ethyl acetate (50 mL) and silica filtered. The product is column purified with a solvent gradient of P_{eth}/AcOEt (3-1 > 1-1 v-v). Fractions collected, solvent removed under vacuum to yield a yellow amorphous solid with 45%.

¹H NMR 250 MHz (DMSO-d₆) δ (ppm) 3.71 (s, 12H), 6.35-7.34 (m, 30H), 7.35-7.99 (m, 4H).

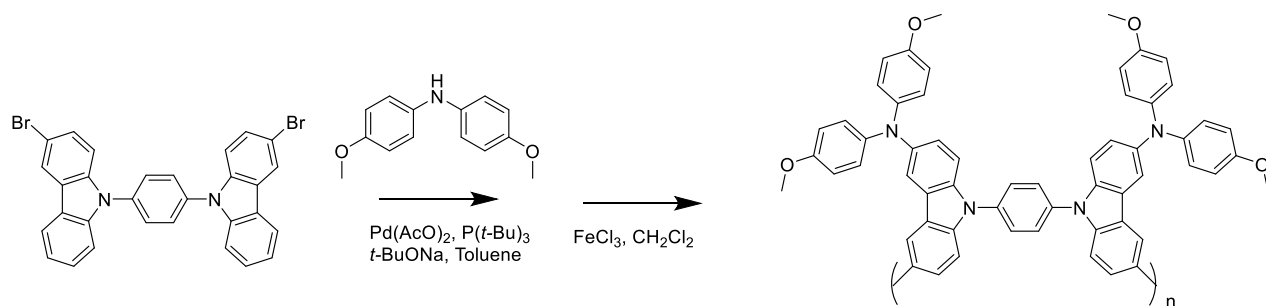
HR-MS: m/z=863.3580 [M+H]⁺



General synthesis procedure for Poly[1,4-bis(3,3'-(bis(4,4'-dimethoxyphenyl)amine)carbazol-9-yl)benzene] (DM15P)? In a two neck 100 mL round-bottom flask, equipped with a condenser and under Ar atmosphere, FeCl₃ (2,08 mmol, 6 eq) is dissolved in 20 mL of CH₂Cl₂ and loaded with 1,4-bis(3,3'-(bis(4,4'-dimethoxyphenyl)amine)carbazol-9-yl)benzene (1,1 mmol, 1 eq) dissolved in 17 mL CH₂Cl₂ and let it react for 48h at 40°C. The solvent amount is reduced to approximately 10 mL and product then precipitated in MeOH (150 mL) and filtered and washed with abundant MeOH.

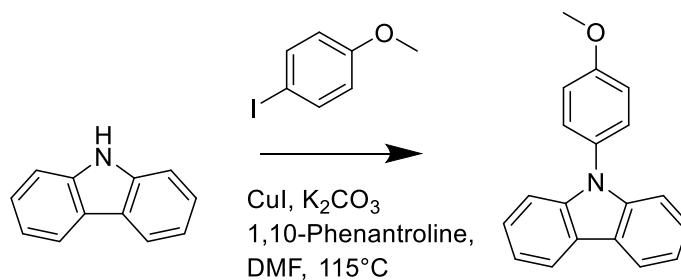
Raw product is dissolved in CHCl_3 and washed (3x) with and HCl (0,01 M) solution. The fractions are collected, MgSO_4 dried and solvent removed under vacuum to yield a 53% on weight of amorphous blue solid.

^1H NMR (17-11-02/2) 250 MHz (DMSO-d_6) δ (ppm) 3.74-4.10 (m, 12H), 6.66-7.77 (m, 20H), 7.81-8.20 (m, 8H), 8.22-8.56 (m, 2H), 8.66-9.09 (m, 2H).



4.2.3 Synthesis of dimer (DM18) by oxidative coupling

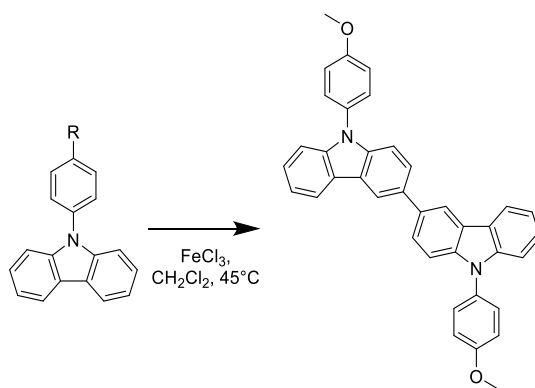
General synthesis procedure for N-(4-methoxybenzyl)carbazole. In a dry 100 mL schlenk flask, carbazole (12 mmol, 1 eq) and p-iodoanisole, p-iodonitrobenzene, p-iodobenzonitrile (12 mmol, 1 eq), copper (I) iodide (1.93 mmol, 0.1 eq), potassium carbonate K_2CO_3 (17 mmol, 1.5 eq) and 1,10-Phenanthroline (2.69 mmol, 0.22 eq) were dissolved in DMF (200 mL) and charged. Reaction conditions are at 115°C for 24h. The mixture is allowed to cool at room temperature, filter by flash column with eluent gradient $P_{\text{eth}} - P_{\text{eth}}/\text{Chloroform}$ (1- 1/0.2 v - v). Different fractions are collected, dried over anhydrous MgSO_4 filtered and concentrated under vacuum. The crude product is dissolved in methanol and recrystallized at 0°C affording a white solids with 85% yield.



General synthesis procedure for 9,9'-(4-methoxyphenyl)-3,3'-bicarbazole (DM18). In a two neck 100 mL round-bottom flask, equipped with a condenser and under Ar atmosphere, FeCl_3 (6.58 mmol, 6 eq) is dissolve in 20 mL of CH_2Cl_2 and loaded in with N-(4-nitrophenyl)carbazole (1,1 mmol, 1 eq) dissolved in 25 mL CH_2Cl_2 an let it react for 24h at 40°C . The reaction mixture is

precipitated in MeOH 250mL and washed with abundant MeOH. Product is dissolved in CHCl₃/MeOH (50/50 v-v) and recrystallize it at 0 °C. A 83% of a white solid is collected.

¹H NMR 250 MHz (DMSO-d₆) δ (ppm) 3.89 (s, 6H), 7.21-7.28 (m, 4H), 7.29-7.36 (m, 4H), 7.37-7.50 (m, 4H), 7.53-7.62 (m, 4H), 7.87 (d, 2H, *J* = 8.68Hz), 8.38 (d, 2H, *J* = 7.28), 8.65-8.69 (m, 2H).



4.2.4 Characterization

4.2.4.1 Thermal Properties

To evaluate their thermal stability, DM1X series is analyzed by Thermal Gravimetric Analysis (TGA). Figure 78 and Figure 79 are shown the thermogravimetric curves for the whole series. For DM11, DM13 and DM18 shows a two steps decomposing process while only a single stage decomposition is observed for DM15 and DM15P from 0 to 600 °C.

A plateau that extends from 250°C is observed for DM11, DM12 and DM13 while for DM15, DM15P and DM18 a longer plateau is extended until 300°C. This confirms the observation done on Chapter 2 that a higher number of phenyl rings give an extra thermodynamic bond energy that can be translated as an increment on the *T_d*. In case of DM18 (379°C), higher *T_d* is observed compared with the rest of the compounds that implies an extra thermal stability. As the molecule structure suggest, the potential planarity derived from its aromaticity, will confer a molecular aggregation conducted by π -stacking interaction and thus increasing the thermal stability.

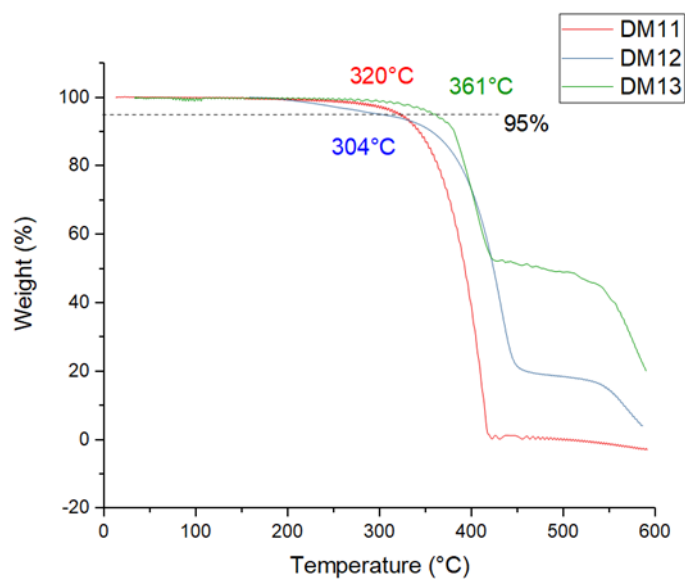


Figure 78 TGA curves of DM11, DM12 and DM13

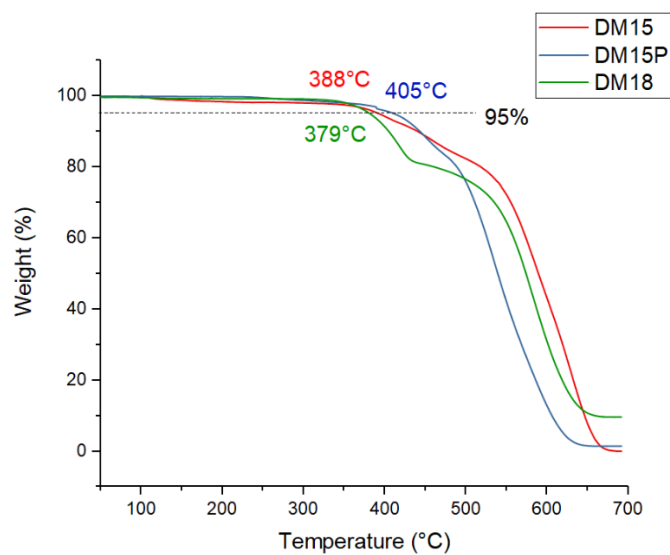


Figure 79 TGA curves of DM15, DM15P and DM18

As is expected, the molecule derived from DM15 (388°C), DM15P (405°C) show a higher T_d than its origin molecule, consequence of a larger linkage between molecules that gives more stability to the polymer raising thus, the decomposition temperature.

The thermal properties of the N,N'-bicarbazolyl-1,4-benzene series DM1X were examined by Differential Scanning Calorimetry (DSC).

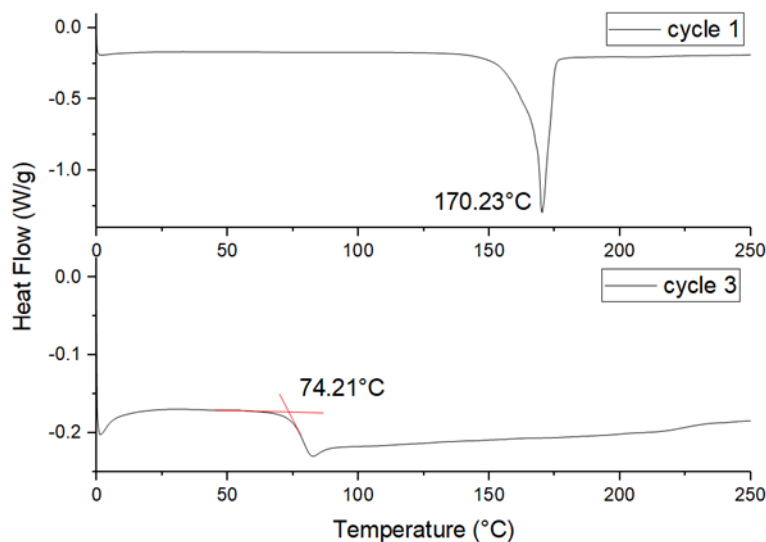


Figure 80 DSC curves DM13

DSC curves of DM13 (Figure 80) present only one event during the first cycle, corresponding to a melting point at 170.23°C. During the second cycle, a glass transition temperature is observed at 74.21°C which is the lowest temperature observed for the studied compounds. Even if this temperature is the lowest one, is highly enough for a HTM to work in device at laboratory conditions. This DSC curve helps to visualize how the structure of carbazole confers a very good stability for a compound with a relatively low molecular weight.

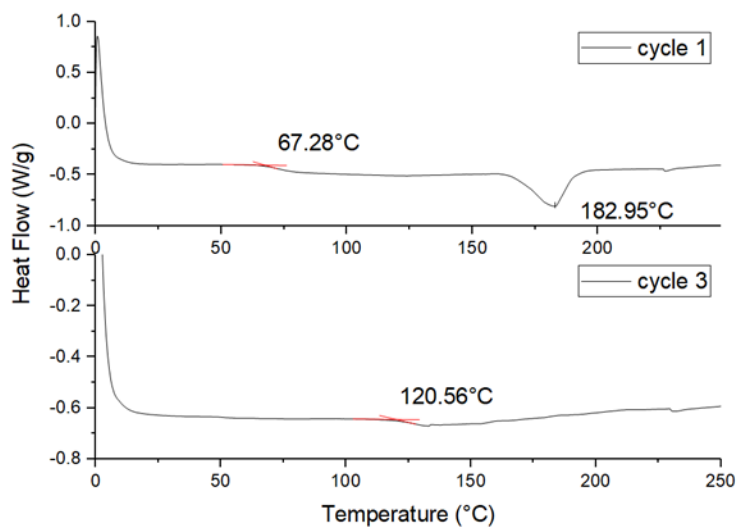


Figure 81 DSC curves DM15

In DSC curves of DM15 (Figure 81), two events are observed: a first event, not so clear, that resembles to a glass transition at 67°C and a second event corresponding to a melting point at 182.95°C. During the second cycle, only one glass transition temperature is observed at 120.56°C. This thermic behavior fits perfectly for the working range on a photovoltaic device, making of DM15 a heat resilient compound for its use as an HTM.

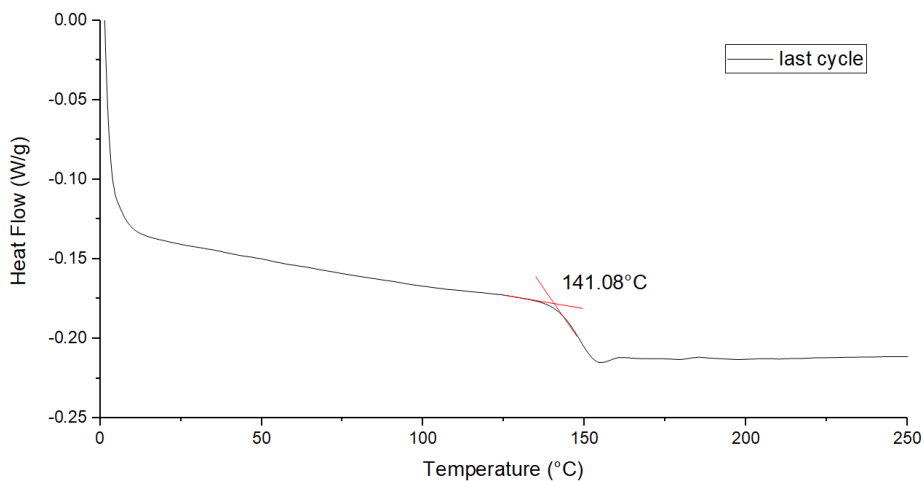


Figure 82 DSC curves DM15P

First cycle shows DSC curves of DM15P (Figure 82) only one event is observed corresponding to a glass transition temperature 141.08°C. Compared to its monomer the glass transition temperature is increased by twenty degrees, that is a hint that a larger molecules is obtained.

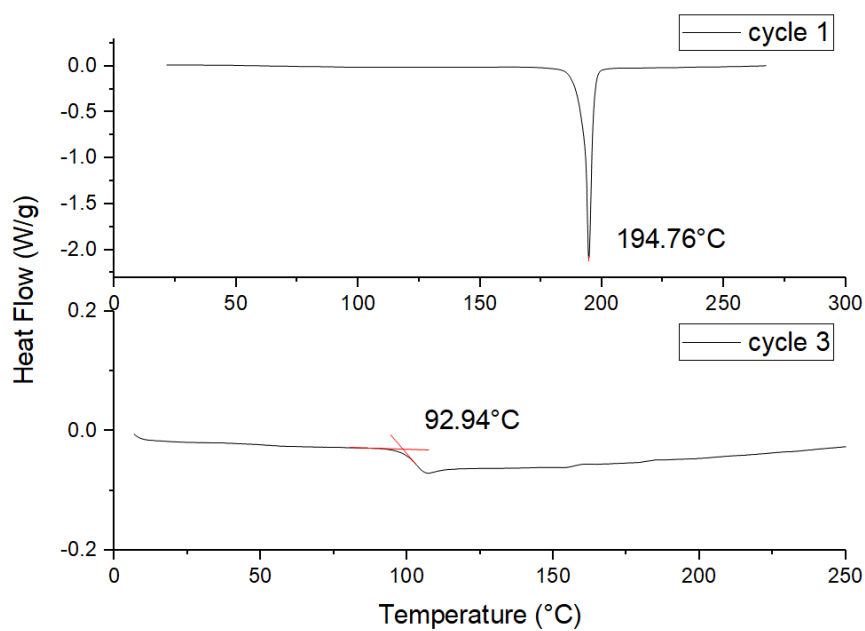


Figure 83 DSC curves of DM18

On DSC curves of DM18 (Figure 83) only one event is observed show during the first cycle, corresponding to a melting point at 194.74°C, being this temperature the highest melting temperature for the whole series and compounds presented in this work. During the second cycle, a glass transition temperature is observed at 92.94°. No crystallization or oxidation events are observed, making of this small molecule a quite resilient one. Furthermore, such high melting temperature observed for DM18 is a good example of how a bicarbazylum structure and its π -stacking interaction can improve is thermal properties. Another important point is that, DM18 has no rotation bonds on its rigid structure, giving this peculiar melting and glass transition temperature.

On Table 25 are resumed all different degradation and glass temperatures for DM1X series. In general, all presented compound are potentially good HTM candidates with appropriate temperatures for PSC proposes with DM13 exception (74°C). The later demonstrates that bicarbazylum or and bicarbazolyl compounds are good option as synthetic path to obtain compounds with a good thermodynamic performance.

Table 25 Melting, glass transition and decomposition temperature for DM1X series

Compound	T _m (°C)	T _g (°C)	T _d (°C)
DM13	170	74	361
DM15	182	120	388
DM15P	-	141	405
DM18	194	92	379

4.2.4.2 Optical properties

UV-vis absorption spectra of DM1X series is recorded on DCM 1 x 10⁻⁶M solution. UV-vis spectra are presented in Figure 84 and Figure 85.

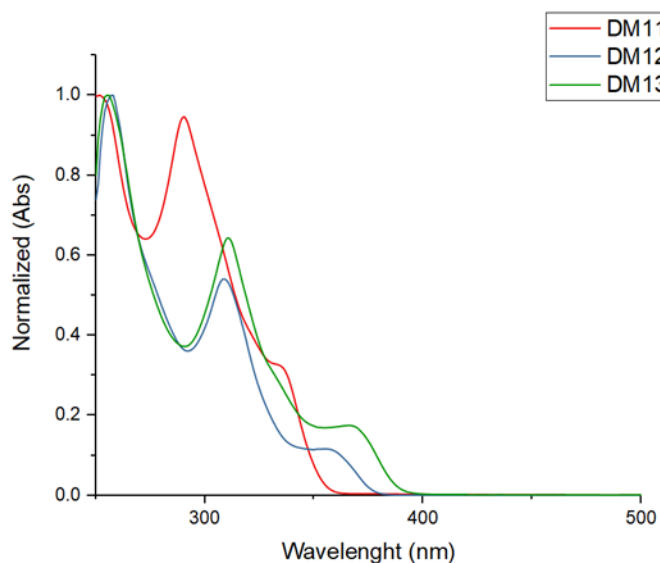


Figure 84 UV-vis spectra of DM11, DM12 and DM13

DM1X compounds series composed of two carbazole molecules, have an intense π - π^* absorption band observed at around 310 nm, and less intensive lower energy absorption bands, that can be assigned as n - π^* bands observed at >350 nm. Between DM12 and DM13 a same absorption pattern is observed, while DM12 is bearing two bromine atoms and DM13 is bearing

methoxy groups in their place, with the only difference that we observe a bathochromic (red values) shift by DM13.

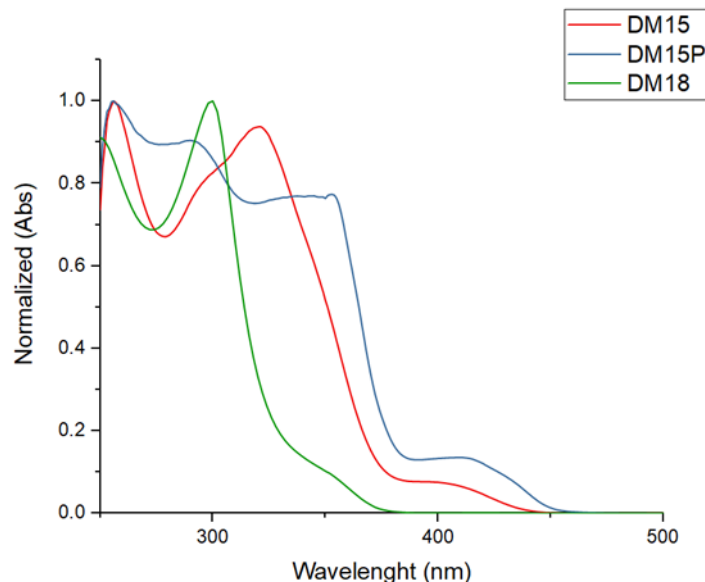


Figure 85 UV-vis spectra of DM15, DM15P and DM18

Absorption of DM15 and DM15P are reach visible domain, with 437 and 452 nm as absorption onsets respectively: Main explanation is to its longer conjugation π -orbital that extends throught both DPA groups on the molecules and the carbazole centers. This same effect is observed for the derived molecule DM15P with an even lower absorption onset that goes as far as 450 nm. DM15P lower absorption onset doesn't really compromise its role as HTM, because such absorption overlap doesn't represent a parasitic or competitive absorption. In other hand DM18 has absorption onset at 376 nm, that makes of it an ideal candidate in terms of non competitive light absorption. It's worth to notice that, bicarbazylum plays an important role, which can be considered as desirable. If we compare DM18 with DM13 that are structurally speaking similar, we can see that even if the π orbital is longer in DM18 its absorption is shifted to a higher values than those for DM13.

We can conclude that on light absorption terms, all the presented compounds are suitable candidates for HTM applications. The evolution and changes on the spectra of DM11, DM12, DM13, DM15 and DM15P is tracked according to the addition of different moieties on the molecule, showing a progressive shift to red values (bathochromic) associated to a longer conjugated π -orbitals. The latter absorption curves are an example of how light absorption can

be tuned with the addition or subtraction of elements in one molecule or through its internal connectivity like the case of DM18 that having a bigger molecular weight than DM13, its closer relative, its absorption is shifted to blue values (hypsochromic effect).

4.2.4.3 Electrochemistry measurements

The redox properties of the two series were studied by electrochemical cyclic voltammetry (CV) in dilute solution. Cyclic voltammograms of DM1X series were prepared with a concentration $1.0 \times 10^{-3} \text{ M}$, recorded in $1.0 \times 10^{-2} \text{ M}$ TBAPF₆/ CH₂Cl₂ solution and scan rate was 100 mV s^{-1} .

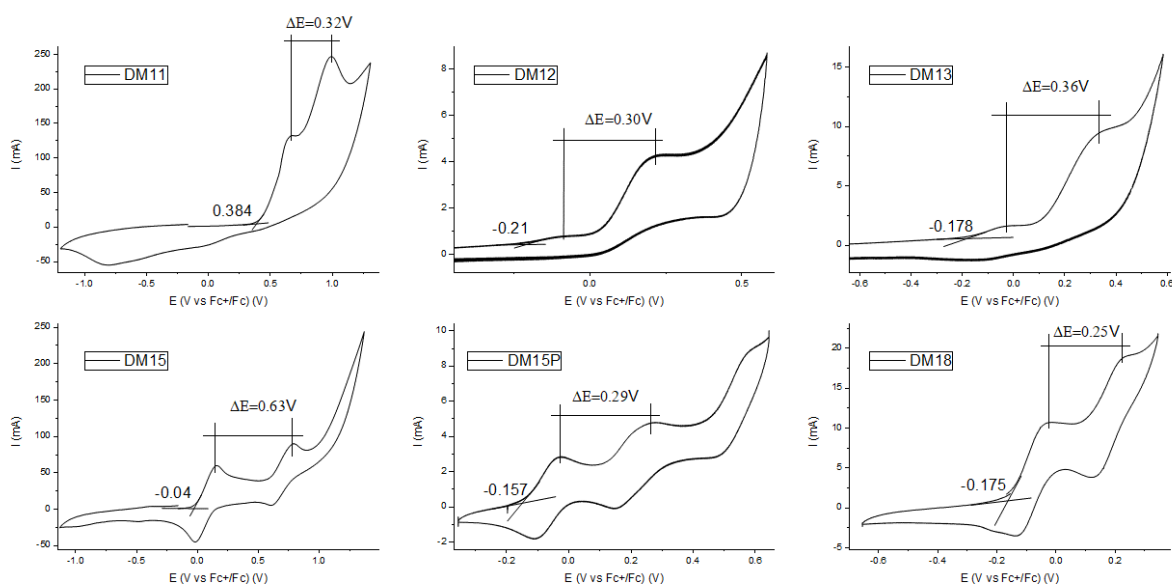


Figure 86 Cyclic voltammetry curves for DM1X series

The CV curves corresponding to DM1X compounds (Figure 86) display two oxidation peaks on showed potential range.

In chapter two of this thesis for DMx and iDMx, the first two peaks are assigned to peripheral amines contained on the diphenylamino (DPA) group. The CV curves here presented show how the shape of the CV is modified by the absence of such groups, especially over the presence of the reduction peaks. Nevertheless, on the present case, molecules based on biscarbazolyl-1,4-benzene, still two oxidation peaks are observed, that can be assigned to a dication formed by de subtraction of two electrons. DM11, DM12 and DM13 presents a similar pattern, with no defined

oxidation peaks and almost absent reduction peaks, which can give a hint of its poor electrochemical performance.

With the addition of the DPA group, can be seen clearly the difference and how the reduction peaks are well defined.

Usually, the first two peaks are assigned to the peripheral amines are attributed to the sequent oxidation of the two 4-methoxydiphenylamine (DPA) moieties by a single electron transfer processes on DM15 and DM15P. Nevertheless, the CV shape observed previously, suggest that DM18 is behaving on the same way, where the methoxy-benzene linked to the nitrogen atom on the carbazole confers the previously observed CV shape for DMx and iDMx family.

Among all DM1X compounds here analyzed, DM15 possesses a very well defined oxidation states, reflected on a gap between first and second oxidation peaks (ΔV) of 0.63 V, being such value the highest one observed for the whole compounds revised on this thesis. Thus, we would like to theorize that it would be very worth to test DM15 molecule's performance as an HTM. Additionally, the evaluation of DM15 against its derived polymer DM15P, could help to unveil the role that plays a full conjugation over a final molecule.

Table 26 DM1X oxidation potential and reduction values

Compound	E_{Ox1} [V]	E_{Ox2} [V]	ΔV [V]
DM11	0.669	0.995	0.325
DM12	-0.086	0.217	0.303
DM13	-0.029	0.333	0.362
DM15	0.149	0.782	0.634
DM15P	-0.029	0.264	0.293
DM18	-0.025	0.225	0.251

4.2.5 General properties physical properties of DM1X series

On Table 27 are resumed the physical, optical and electronic data for all the DM1X series, where can be noted that all the compounds contained on the series are, in theory, suitable candidates as HTMs for PSC.

Table 27 General thermal, optical and electronic characteristics of DM1X

Compound	T _d (°C) ^[a]	T _g (°C) ^[b]	λ _{max} (nm) ^[c]	λ _{onset} (nm) ^[c]	E _{gap} (eV) ^[d]	E _{ox} (V) (Fc/Fc ⁺)	HOMO ^[IP] (eV)	LUMO ^[EA] (eV)
DM11	320.1	-	334, 290, 251	359	3.45	0.384	-5.18	-1.73
DM12	304.01	-	358, 310, 258	380	3.26	-0.021	-4.78	-1.52
DM13	361.49	74	366, 311, 255	394	3.15	-0.178	-4.62	-1.47
DM15	388.78	120	400, 318, 256	440	2.82	-0.04	-4.76	-1.94
DM15P	405.23	141	409, 350, 289, 257	452	2.74	-0.157	-4.64	-1.90
DM18	379.29	92	298, 250	413	3.00	-0.175	-4.63	-1.62

^[a]Obtained from TGA measurements. ^[b]Obtained from DSC measurements. ^[c] Measured in CH₂Cl₂ solution 1 x 10⁻⁶ M (Single unit equivalent).. ^[d] Measured in CH₂Cl₂ 1.0 x 10⁻² M TBAPF₆ solution. Analyte 1 x 10⁻⁴ M (Single unit equivalent). All E_{ox} data are reported relative to ferrocene²⁰⁰ which has a value of ionization potential (IP) 4.8 eV for ferrocene and 0.27 V for Fc/Fc⁺ against Au/Au⁺. The concentration of the complexes used in this experiment was 1.0 x 10⁻³ M and scan rate was 100 mV s⁻¹. E_{gap}= hc/λ_{onset}= 1240 eVnm/λ_{onset}; IP=E_{ox}+4.8; EA = IP - E_{gap}

Degradation temperature is high for all the studied compounds being over 350°C, temperature range that ensures no degradation under PV conditions. Although, glass transition temperatures, for all the compounds can be considered high enough for real device working conditions, except for DM13. DSC results allow us to understand the role of substituents over the bicarbazolyl-1,4-benzene core, where two carbazole molecules give extra thermodynamic stability, increasing T_g for a relatively low molecular weight compounds.

Moreover, optical properties studied by UV-vis spectroscopy; show an appropriate light absorption performance by the DM1X group, with only DM15 and DM15P having a blue shifted absorption due to a longer π-conjugation in comparison with the rest of DM1X group.

Electrochemical characterization along with the optical information allows to calculate experimentally HOMO-LUMO energy levels.

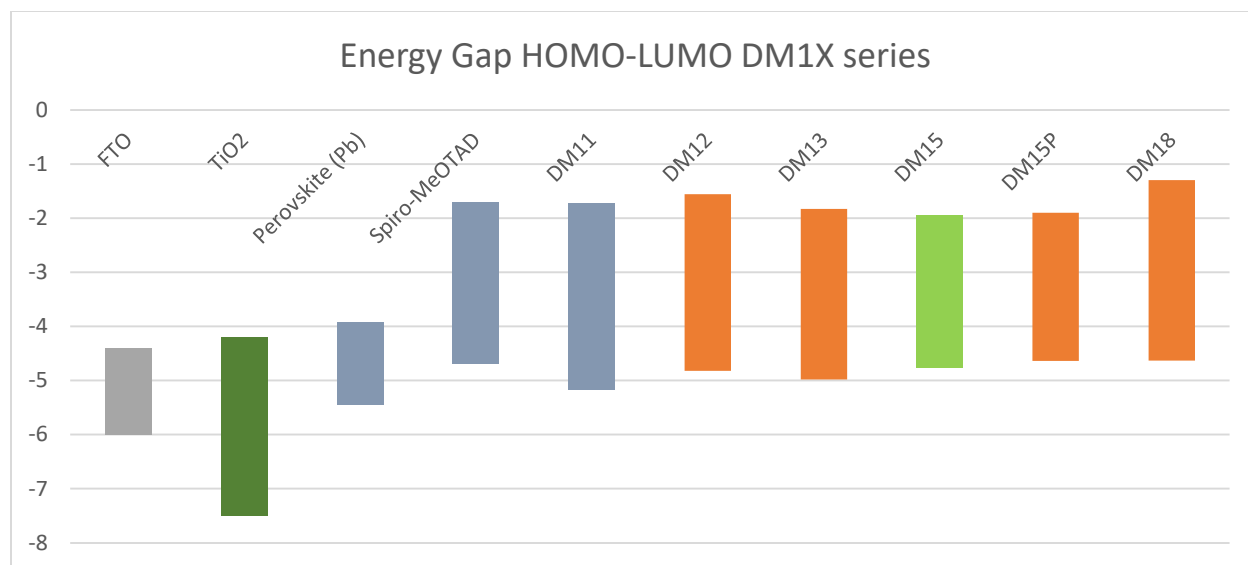


Figure 87 Experimental HOMO-LUMO values of DM1X series

Found values for all the proposed molecules are suitable for the role of HTM on PSCs. Experimental values of the DM1X series are plotted on Figure 87 and compared to perovskite levels and the HTM reference standard Spiro-OMeTAD. DM1X values are really close to those given by Spiro-OMeTAD, with wide enough band gap values, that avoid undesired hole recombination and eventually a bad performance on PCS devices. We can conclude that especially for DM15, DM15P and DM18 it worth to test them on real devices and compare its performance.

4.2.6 Computational Studies

All molecular geometries of DM1X were optimized, HOMO and LUMO energy levels shown in Figure 88 and Table 28 were simulated using density functional theory calculation at B3LYP/6–311G(d,p) ran over Gaussian 09 program package²⁰¹. The HOMO and LUMO of DM11 and DM12 are distributed along the whole molecule, having no defined parts on the structure for each molecular orbital. We can observe how DM11 among the rest of the molecules in the group, is the only one that remains almost planar. The introduction of bromine atom on DM12 and methoxy moiety on DM13, tends to increase the dihedral angle between the carbazoyl group and its benzene center, from 24.5° (DM11) to 58.2° (DM12) and 56.3° (DM13).

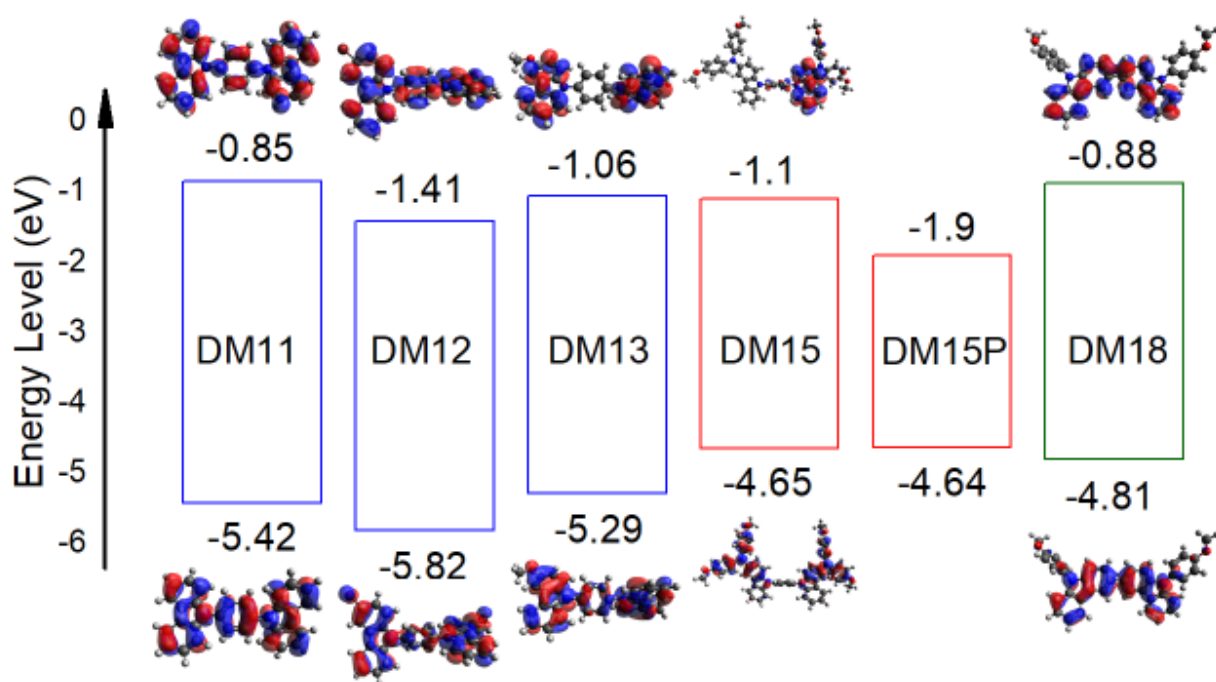


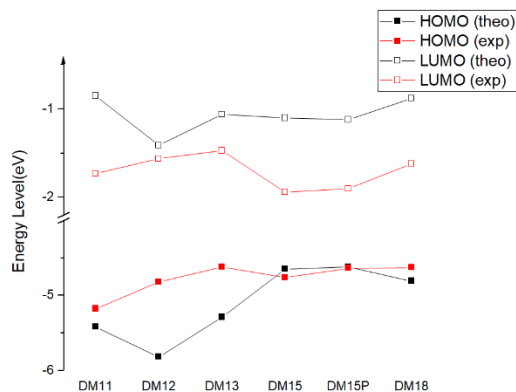
Figure 88 DM1X optimized geometries and calculated HOMO-LUMO energy levels

Usually, is expected that HOMO and LUMO localized in different regions within the molecular structure will have a good role as a charge carrier.

Following the latter description, DM13 and DM15 present such defined HOMO-LUMO localized on different parts of the molecular structure. DM13's HOMO level is localized along the whole molecule while the LUMO will occur over the carbazole groups, leaving out the benzene center.

Table 28 Calculated OM energy values for DM1X

HTM	HOMO (theo)	HOMO (exp)	LUMO (theo)	LUMO (exp)
DM11	-5.42	-5.18	-0.85	-1.73
DM12	-5.82	-4.82	-1.41	-1.56
DM13	-5.29	-4.62	-1.06	-1.47
DM15	-4.65	-4.76	-1.1	-1.94
DM15P	-4.62	-4.64	-1.12	-1.9
DM18	-4.81	-4.63	-0.88	-1.62



For DM15 case, the HOMO distribution is localized over the diphenylamine (DPA) groups, implying that donor capacity of the molecule resides over the DPA. For the LUMO distribution, this is mainly localized in one of the two carbazole groups and the benzene center of the molecule. For its derivative polymer DM15P, only a two-unit dimer is rendered, results show to follow the same pattern as the monomer, while the HOMO is localized over the peripheral DPA groups, its LUMO is situated over half of its chain center.

For DM18, we can observe that not all regions on the molecule are contemplated for the HOMO nor for LUMO, leaving the methoxy-benzene attached to the carbazole, without participation on the molecular carrier function. In addition, calculations show that DM18 is not planar having a dihedral angle between both carbazole molecules of 39.8°.

Calculated values are compared with those obtained experimentally and it is worth to notice that they follow the same tendency as the experimental values. Implying thus that computational calculations approaches in a very assertive way to experimental values.

2.4.7 Surface morphology studies by atomic force microscopy

Films were prepared using the following procedure. A solution was prepared by dissolving 72 mg of HTM in 1 ml chlorobenzene. Then, 17.5 μ l of bis(trifluoromethylsulfonyl)imide lithium salt solution (LiTFSI) solution (520 mg in 1 mL ACN), 28.8 μ L of TBP (tert-butylpyridine) and 6 μ L of tris (2-(1H-pyrazol-1-yl) - 4-tert-butylpyridine) – cobalt (III) -tris (bis (trifluoromethylsulfonyl) imide) (300 mg in 1 mL ACN) were added to this solution. 35 μ L of the HTM solution was spin-coated at 4000 rpm, 4000 rpm/s for 20 s.

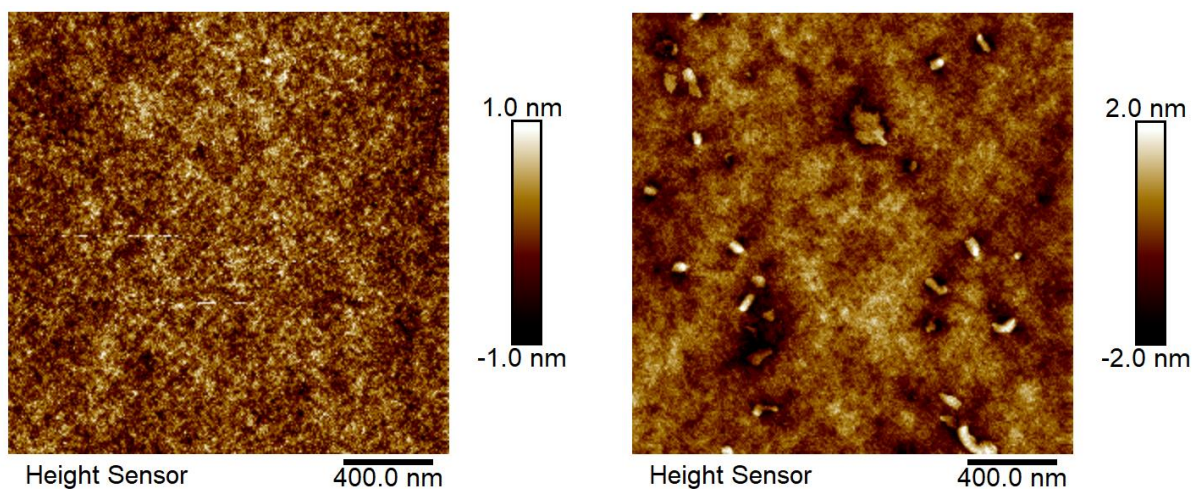


Figure 89 AFM images of D15 and DM15P

The morphology and roughness of the films coated over FTO were analyzed by atomic force microscope. AFM images can be seen in Figure 89(a) for DM15 with a smooth and continues surface with no grain or aggregation defect. It roughness values Rq and Ra (≈ 280 nm and 220 nm) which is to lowest value found for all the compounds observed during this work. This is a very desirable quality for an HTM since; a good quality layer will have less defects and better contact with the cathode and perovskite layer. Moreover, a good film formation is an indicative that solubility is good enough for film deposition purposes.

In other hand, the derivative compound, DM15P shows a different morphology with presence of aggregates with sizes that goes around 50 to 100 nm. Such aggregates indicates certainly a lower solubility by DM15P, but still, surface roughness has acceptable values. Given that, solution for used to coat the films was prepared taking in count the concentration of the DM15P same as the monomer. A difference in DM15P solubility could be a probable reason for such aggregates.

Root mean square and arithmetic mean values at different scan dimension are summarized on Table 29.

Table 29 Root mean square (Rq) and arithmetic mean (Ra) for DM15 and DM15P in different area scale

		600 nm	2 μ m	5 μ m	10 μ m
DM15	Rq	0.27	0.29	0.29	0.27
	Ra	0.22	0.23	0.23	0.21
DM15P	Rq	0.55	0.71	1.69	1.35
	Ra	0.43	0.56	1.41	0.93

4.2.8 Angle Contact

Contact angle images were measured under white LED module. All the measurements are repeated five times, applying one drop of deionized water (10 μ L) to characterize hydrophobic character of the film. Hydrophobicity is a desired feature because helps to prevent that moisture get in contact with the perovskite and will help eventually extend the lifetime of the devices. In addition, this study can establish a relation between DM15 structure and its repelling water properties after polymerization.

Hydrophobicity and contact angle is measured for DM15 $81 \pm 1^\circ\text{C}$ and DM15P $93 \pm 2^\circ\text{C}$ using the films prepared used for the previous AFM experiments.

Figure 16 shows us a higher hydrophobic character for the derived compound DM15P ($\theta=92.6^\circ$) compared to the small molecules from the same unit ($\theta=81.0^\circ$). The arrangement of the molecules in some sort of way that methoxy groups are not exposed at the surface of the sample of DM15P film could explain this behavior: Structure of DM15P reduces the possibility of free rotation of moieties and consequently the number of methoxy groups at the surface.

4.2.6 Conclusions

A series of small molecules based on bicarbazolyl-1,4-benzene are presented as an alternative option for hole transport materials. This series was done with two purposes: firstly, to probe at what degree can a carbazole based HTM retains its carrier properties while its structure and molecular weight is reduced to a minimum. Second, to design a molecule that allows a potential polymerization by oxidative coupling.

Finally, best candidates for PSC application could be DM15, DM15P and DM18 as HTMs. We expect to reveal and compare the raising differences between a monomer and a derived molecule. In this way, we will try to understand how we can improve the performance of an HTM using small molecules that lead to less use of resources, synthetic steps, catalyzers, etc. and simplify their manufacture with a view to scale up their production.

It is important to emphasize that carbazole oxidative reactivity; constitutes an interesting tool that has not been widely used. Synthesis using oxidative coupling could be an effective way to take advantage of carbazole as a building block for future HTMs.

General Conclusions and Perspectives

In this thesis we presented the synthesis and characterization of carbazole (Cz) based small molecules and polymer derivatives for their application as hole transport materials (HTM) in hybrid perovskite photovoltaic solar cells (PSC). The main objective of this study was to design and synthesize alternative and reliable molecules to those ones existing today as classical HTM references like Spiro-OMeTAD small molecule or PTAA a conjugated polymer.

First, we propose a comparative study of a series of positional (3,6- versus 2, 7-) substituted carbazole isomers. Properties like, thermal stability, optical absorption and electrical behavior, are analyzed and compared, in order to present a comprehensive analysis of their derived properties based on their structural differences.

We found that thermodynamic stability tends to be higher for those bearing a 2,7- substitution over the carbazole core. Through computational analysis we can conclude that steric hindrance limits (restrains) their spatial movement especially for those with a phenyl substituent (iDM1 and iDM3) increasing its glass transition temperature and thus making of them more thermally resilient.

Second point of this thesis, was to test the polymerization ability, of alkene bearing functionalized compounds, DM1, DM2 and complementary isomers iDM1 and iDM2 molecules. Due to the poor bond activation by the terminal alkene moiety, no positive polymerization results were achieved for DM2 and iDM2. Concerning to DM1 and iDM1 bearing a styrene function, only DM1 was able to render a functional polymer (DM1P) under our working conditions. Experimental polymerization results match computational results, indicating a spatial restriction for compound iDM1, that is sterically impeded, denying thus (that avoids) a successful polymerization.

In roughness terms, AFM studies demonstrate morphology significant differences arise from 1-step and 2-step perovskite deposition and coating over glass deposition. Film roughness values of DM1, iDM1 and DM1P deposited over glass are smaller than those over perovskite, implying then, that film homogeneity comes from perovskite deposition itself and not from HTM's.

For final photovoltaic results, among series DMx and iDMx, the best efficiencies were observed for DM1 (11%), DM1P (13%) and iDM1 (15%). We consider that, the better performance displayed for 2,7- substituted carbazole iDM1 is related to the structural resemblance to Spiro-

OMeTAD. This leads us to theorize that, internal molecule conjugation through carbon-carbon bond in the heterocycle 2,7-Cz molecules presents better carrier properties than the conjugation through the N atom presented by 3,6-Cz substitution.

Due to the lack of proposals of carbazole based conjugated oligomers as HTMs on the literature; we propose three new oligomers in order to compare their potential role as HTM's. Given the good results showed by PSC using the conjugated polymer PTAA in their final efficiency and enhanced lifespan, we designed carbazole oligomers that could emulate its good performance on photovoltaic devices. As is likely for n-oligomer, PCzX series have higher glass transition temperatures than small molecules. In addition, a larger conjugation is expected to change its carrier properties compared with small molecules. Contrary of what is expected for larger molecules; PCzX retains its good solubility properties, thanks to a flexible chain and methoxy groups which increase their solubility and film formation abilities reflected on their low roughness values observed by AFM on films made with PCzX series.

Through the observation of the water repellent ability by contact angle studies, we can estimate or relate the presence of methoxy groups to its hydrophobic properties. A clear pattern is observed that links the number of methoxy groups per molecule unit on the oligomer and the observed contact angle values. The lower the number of methoxy groups per oligomer unit like PCz1, the higher the contact angle between the film and the water droplet. The latter suggests, that the use of methoxy groups which helps polymer solubility, also compromises the hydrophobic character of the film.

Moreover, we would like to highlight that one of the main advantages of PCzX series, is the easy synthetic route, consisting of three steps, all of them with high yields and simple purification procedure that set PCzX series as a potential alternative due to the capability to scale up its production.

The latter PCzX series needs to be tested on real devices, preliminary studies, show promising results for the PCz1 about PCE = 18%. Moreover, better studies about oligomerization rates and index has to be carried out in order to standardize its production and reproducibility.

The latter study opens the possibility to exploit these kind of oligomers and study their performance over real devices. Moreover, the above mentioned oligomers are based on a 3,6-Cz conjugation, that leaves a whole new open possibility to explore 2,7-Cz conjugated oligomers that are practically inexistent on the literature.

Finally, for Chapter 4, molecules based on bicarbazolyl (DM13, DM15, DM15P) and bicarbazylum (DM18) were designed. The use of DM1X family, searches to take advantage of the ability to carbazole to couple by oxidative ways. In order to couple Cz molecules by oxidative ways, a stable bicarbazylum dication formation that hinders consecutive coupling reactions, must be avoided. This facet of carbazole reactivity is quite attractive from a synthetic perspective due the lack of functional groups such as halogen atoms or borolane for example, required for coupling reactions. Moreover, electrochemical polymerization can potentially be attained, for its use on inverted configuration perovskite devices, or even different applications like those on organic electronics where electrochemical film deposition is needed.

Molecules comprehended on DM1X family have physical, electrochemical and optical values that match the requirement for a HTM candidate on PSC. It is difficult to predict their role on PSC final devices, so it is expected that DM1X molecules can be tested on real modules.

In general, we have presented a work that explores in a broad way the different synthetic ways in which carbazole can be used. Thanks to the versatility of carbazole reactivity, we have proposed three different alternatives based on its reactivity (small molecules, polymeric and oxidative). It is important to emphasize that its unique reactivity and its potential use can be of great help in the design of new hole transport materials.

In perspective, the present work examines key points for the improvement in the design of Cz designed HTM's. Analyzing basic points such as, the influence of the internal connectivity within the molecule for the case of 2,7- and 3,6- positional isomers, the comparison between small molecules and polymers (DM1 vs DM1P), and the use of synthetic ways that reduce the use of materials and catalysts as in the case of oxidative coupling (DM18). We consider that our work, proposes an innovative path for a new generation of carbazole based HTM's.

We trust that future research can take advantage of our experience and design Cz-based HTMs centered on our findings that help to improve the final efficiency of PSC.

Bibliography

- (1) BP. Statistical Review of World Energy. *BP Stat. Rev. World Energy* **2016**, No. June, 1–48.
- (2) Coddington, O.; Lean, J. L.; Pilewskie, P.; Snow, M.; Lindholm, D. A Solar Irradiance Climate Data Record. *Bull. Am. Meteorol. Soc.* **2016**, 97 (7), 1265–1282.
- (3) Global Exergy Resource Chart - GCEP
<http://gcep.stanford.edu/research/exergy/resourcechart.html> (accessed Jun 21, 2018).
- (4) Mouchot, A. La Chaleur solaire et ses applications industrielles : Augustin Bernard Mouchot, Augustin Mouchot : Free Download, Borrow, and Streaming : Internet Archive
<https://archive.org/details/lachaleursolair00moucgoog> (accessed Jun 25, 2018).
- (5) International Energy Agency (IEA). World Energy Outlook 2016. **2016**.
- (6) Philipps, S. Photovoltaics Report, Updated: 27 August 2018. **2018**, No. August.
- (7) POWER Data Access Viewer <https://power.larc.nasa.gov/data-access-viewer/> (accessed Jun 26, 2018).
- (8) Tsao, J.; Lewis, N.; Crabtree, G. Solar FAQs. *US Dep. Energy* **2006**, 1–24.
- (9) IEA-PVPS Reporting Countries; Becquerel Institute (BE); RTS Corporation (JP). Snapshot of Global Photovoltaic Markets (1992-2016), IEA PVPS Task 1, International Energy Agency Power Systems Programme, Report IEA PVPS T1-31-2017. **2017**, 1–16.
- (10) Rubel, M. H. K.; Miura, A.; Takei, T.; Kumada, N.; Mozahar Ali, M.; Nagao, M.; Watauchi, S.; Tanaka, I.; Oka, K.; Azuma, M.; et al. Superconducting Double Perovskite Bismuth Oxide Prepared by a Low-Temperature Hydrothermal Reaction. *Angew. Chemie Int. Ed.* **2014**, 53 (14), 3599–3603.
- (11) Seshadri, R.; Hervieu, M.; Martin, C.; Maignan, A.; Domenges, B.; Raveau, B.; Fitch, A. N. Study of the Layered Magnetoresistive Perovskite La 1.2 Sr 1.8 Mn 2 O 7 by High-Resolution Electron Microscopy and Synchrotron X-Ray Powder Diffraction . *Chem. Mater.* **2002**, 9 (8), 1778–1787.
- (12) Park, N. G. Perovskite Solar Cells: An Emerging Photovoltaic Technology. *Mater. Today* **2015**, 18 (2), 65–72.
- (13) Harvey, N. A history of luminescence from the earliest times until 1900
https://archive.org/stream/historyoflumines00harv/historyoflumines00harv_djvu.txt (accessed Jun 25, 2018).
- (14) Efficiency-chart NREL <https://www.nrel.gov/pv/assets/images/efficiency-chart.png> (accessed Jun 25, 2018).
- (15) Yoshikawa, K.; Kawasaki, H.; Yoshida, W.; Irie, T.; Konishi, K.; Nakano, K.; Uto, T.; Adachi, D.; Kanematsu, M.; Uzu, H.; et al. Silicon Heterojunction Solar Cell with Interdigitated Back Contacts for a Photoconversion Efficiency over 26%. *Nat. Energy* **2017**, 2 (5), 17032.
- (16) Tai, Q.; You, P.; Sang, H.; Liu, Z.; Hu, C.; Chan, H. L. W.; Yan, F. Efficient and Stable Perovskite Solar Cells Prepared in Ambient Air Irrespective of the Humidity. *Nat. Commun.* **2016**, 7, 11105.
- (17) Park, N.-G.; Grätzel, M.; Miyasaka, T.; Zhu, K.; Emery, K. Towards Stable and Commercially Available Perovskite Solar Cells. *Nat. Energy* **2016**, 1 (October), 16152.
- (18) Li, Y.; Meng, L.; Yang, Y. (Michael); Xu, G.; Hong, Z.; Chen, Q.; You, J.; Li, G.; Yang, Y.; Li, Y. High-Efficiency Robust Perovskite Solar Cells on Ultrathin Flexible Substrates. *Nat. Commun.* **2016**, 7, 10214.
- (19) Assadi, M. K.; Bakhoda, S.; Saidur, R.; Hanaei, H. Recent Progress in Perovskite Solar Cells. *Renew. Sustain. Energy Rev.* **2018**, 81 (June 2017), 2812–2822.
- (20) Qiu, L.; Ono, L. K.; Qi, Y. Advances and Challenges to the Commercialization of Organic–Inorganic Halide Perovskite Solar Cell Technology. *Mater. Today Energy* **2018**, 7, 169–189.
- (21) Zuo, C.; Vak, D.; Angmo, D.; Ding, L.; Gao, M. One-Step Roll-to-Roll Air Processed High Efficiency Perovskite Solar Cells. *Nano Energy* **2018**, 46 (January), 185–192.
- (22) Das, S.; Yang, B.; Gu, G.; Joshi, P. C.; Ivanov, I. N.; Rouleau, C. M.; Aytug, T.; Geohegan, D. B.; Xiao, K. High-Performance Flexible Perovskite Solar Cells by Using a Combination of Ultrasonic Spray-

- Coating and Low Thermal Budget Photonic Curing. *ACS Photonics* **2015**, 2 (6), 680–686.
- (23) Rong, Y.; Ming, Y.; Ji, W.; Li, D.; Mei, A.; Hu, Y.; Han, H. Toward Industrial-Scale Production of Perovskite Solar Cells: Screen Printing, Slot-Die Coating, and Emerging Techniques. *J. Phys. Chem. Lett.* **2018**, 9 (10), 2707–2713.
 - (24) O'Regan, B.; Gratzel, M. A Low-Cost, High-Efficiency Solar-Cell Based on Dye-Sensitized Colloidal TiO₂ Films. *Nature* **1991**, 353 (6346), 737–740.
 - (25) Kakiage, K.; Aoyama, Y.; Yano, T.; Oya, K.; Fujisawa, J.; Hanaya, M. Highly-Efficient Dye-Sensitized Solar Cells with Collaborative Sensitization by Silyl-Anchor and Carboxy-Anchor Dyes. *Chem. Commun.* **2015**, 51 (88), 15894–15897.
 - (26) Lee, J.; Rahman, M.; Sarker, S.; Nath, N. C. D.; Ahammad, A. J. S.; Lee, J. K. Metal Oxides and Their Composites for the Photoelectrode of Dye Sensitized Solar Cells. *Adv. Compos. Mater. Med. Nanotechnol.* **2010**, 181–210.
 - (27) Chen, X.; Mao, S. S. Titanium Dioxide Nanomaterials: Synthesis, Properties, Modifications, and Applications. *Chem. Rev.* **2007**, 107 (7), 2891–2959.
 - (28) Obotowo, I. N.; Obot, I. B.; Ekpe, U. J. Organic Sensitizers for Dye-Sensitized Solar Cell (DSSC): Properties from Computation, Progress and Future Perspectives. *J. Mol. Struct.* **2016**, 1122, 80–87.
 - (29) Wu, J.; Lan, Z.; Lin, J.; Huang, M.; Huang, Y.; Fan, L.; Luo, G. Electrolytes in Dye-Sensitized Solar Cells. *Chem. Rev.* **2015**, 115 (5), 2136–2173.
 - (30) Grätzel, M. Recent Advances in Sensitized Mesoscopic Solar Cells. *Acc. Chem. Res.* **2009**, 42 (11), 1788–1798.
 - (31) Chung, I.; Lee, B.; He, J.; Chang, R. P. H.; Kanatzidis, M. G. All-Solid-State Dye-Sensitized Solar Cells with High Efficiency. *Nature* **2012**, 485 (7399), 486–489.
 - (32) Zhang, W.; Anaya, M.; Lozano, G.; Calvo, M. E.; Johnston, M. B.; Míguez, H.; Snaith, H. J. Highly Efficient Perovskite Solar Cells with Tunable Structural Color. *Nano Lett.* **2015**, 15 (3), 1698–1702.
 - (33) Frost, J. M.; Walsh, A. What Is Moving in Hybrid Halide Perovskite Solar Cells? *Acc. Chem. Res.* **2016**, 49 (3), 528–535.
 - (34) Fong, D. D.; Stephenson, G. B.; Streiffer, S. K.; Eastman, J. A.; Auciello, O.; Fuoss, P. H.; Thompson, C.; Li, H.; Ryan, P.; Wang, L.-P.; et al. Ferroelectricity in Ultrathin Perovskite Films. *Science* (80-.). **2004**, 304 (5677), 1650–1653.
 - (35) Baikie, T.; Fang, Y.; Kadro, J. M.; Schreyer, M.; Wei, F.; Mhaisalkar, S. G.; Graetzel, M.; White, T. J. Synthesis and Crystal Chemistry of the Hybrid Perovskite (CH₃NH₃)PbI₃ for Solid-State Sensitised Solar Cell Applications. *J. Mater. Chem. A* **2013**, 1 (18), 5628–5641.
 - (36) Mitzi, D. B. Templating and Structural Engineering in Organic-Inorganic Perovskites. *J. Chem. Soc. Dalton Trans.* **2001**, No. 1, 1–12.
 - (37) Ponseca, C. S.; Savenije, T. J.; Abdellah, M.; Zheng, K.; Yartsev, A.; Pascher, T.; Harlang, T.; Chabera, P.; Pullerits, T.; Stepanov, A.; et al. Organometal Halide Perovskite Solar Cell Materials Rationalized: Ultrafast Charge Generation, High and Microsecond-Long Balanced Mobilities, and Slow Recombination. *J. Am. Chem. Soc.* **2014**, 136 (14), 5189–5192.
 - (38) Kojima, A.; Teshima, K.; Shirai, Y.; Miyasaka, T. Organometal Halide Perovskites as Visible-Light Sensitizers for Photovoltaic Cells. *J. Am. Chem. Soc.* **2009**, 131 (17), 6050–6051.
 - (39) Im, J.-H.; Lee, C.-R.; Lee, J.-W.; Park, S.-W.; Park, N.-G.; Sargent, E. H.; Cho, K.-S.; Lee, E. K.; Joo, W.-J.; Jang, E.; et al. 6.5% Efficient Perovskite Quantum-Dot-Sensitized Solar Cell. *Nanoscale* **2011**, 3 (10), 4088.
 - (40) Kim, H.-S.; Lee, C.-R.; Im, J.-H.; Lee, K.-B.; Moehl, T.; Marchioro, A.; Moon, S.-J.; Humphry-Baker, R.; Yum, J.-H.; Moser, J. E.; et al. Lead Iodide Perovskite Sensitized All-Solid-State Submicron Thin Film Mesoscopic Solar Cell with Efficiency Exceeding 9%. *Sci. Rep.* **2012**, 2 (7436), 591.
 - (41) Stranks, S. D.; Eperon, G. E.; Grancini, G.; Menelaou, C.; Alcocer, M. J. P.; Leijtens, T.; Herz, L. M.; Petrozza, A.; Snaith, H. J. Electron-Hole Diffusion Lengths Exceeding 1 Micrometer in an Organometal Trihalide Perovskite Absorber. *Science* (80-.). **2013**, 342 (6156), 341–344.

- (42) efficiency-chart.png (PNG Image, 1200 × 665 pixels) - Scaled (95%)
<https://www.nrel.gov/pv/assets/images/efficiency-chart.png> (accessed May 24, 2019).
- (43) Fu, Q.; Tang, X.; Huang, B.; Hu, T.; Tan, L.; Chen, L.; Chen, Y. Recent Progress on the Long-Term Stability of Perovskite Solar Cells. *Adv. Sci.* **2018**, 1700387.
- (44) Marinova, N.; Valero, S.; Delgado, J. L. Organic and Perovskite Solar Cells: Working Principles, Materials and Interfaces. *J. Colloid Interface Sci.* **2017**, 488, 373–389.
- (45) Wang, K.; Liu, C.; Du, P.; Chen, L.; Zhu, J.; Karim, A.; Gong, X. Efficiencies of Perovskite Hybrid Solar Cells Influenced by Film Thickness and Morphology of CH₃NH₃PbI₃-xCl_x Layer. *Org. Electron.* **2015**, 21 (February), 19–26.
- (46) Shi, Y.; Xing, Y.; Li, Y.; Dong, Q.; Wang, K.; Du, Y.; Bai, X.; Wang, S.; Chen, Z.; Ma, T. CH₃NH₃PbI₃ and CH₃NH₃PbI₃-xCl_x in Planar or Mesoporous Perovskite Solar Cells: Comprehensive Insight into the Dependence of Performance on Architecture. *J. Phys. Chem. C* **2015**, 119 (28), 15868–15873.
- (47) Tavakoli, M. M.; Gu, L.; Gao, Y.; Reckmeier, C.; He, J.; Rogach, A. L.; Yao, Y.; Fan, Z. Fabrication of Efficient Planar Perovskite Solar Cells Using a One-Step Chemical Vapor Deposition Method. *Sci. Rep.* **2015**, 5 (1), 14083.
- (48) Butler, K. T.; Frost, J. M.; Walsh, A. Band Alignment of the Hybrid Halide Perovskites CH₃NH₃PbCl₃, CH₃NH₃PbBr₃ and CH₃NH₃PbI₃. *Mater. Horizons* **2015**, 2 (2), 228–231.
- (49) Saliba, M.; Matsui, T.; Domanski, K.; Seo, J.-Y.; Ummadisingu, A.; Zakeeruddin, S. M.; Correa-Baena, J.-P.; Tress, W. R.; Abate, A.; Hagfeldt, A.; et al. Incorporation of Rubidium Cations into Perovskite Solar Cells Improves Photovoltaic Performance. *Science* (80-.). **2016**, 354 (6309), 206–209.
- (50) Wehrenfennig, C.; Eperon, G. E.; Johnston, M. B.; Snaith, H. J.; Herz, L. M. High Charge Carrier Mobilities and Lifetimes in Organolead Trihalide Perovskites. *Adv. Mater.* **2014**, 26 (10), 1584–1589.
- (51) Jiang, C. S.; Yang, M.; Zhou, Y.; To, B.; Nanayakkara, S. U.; Luther, J. M.; Zhou, W.; Berry, J. J.; Van De Lagemaat, J.; Padture, N. P.; et al. Carrier Separation and Transport in Perovskite Solar Cells Studied by Nanometre-Scale Profiling of Electrical Potential. *Nat. Commun.* **2015**, 6, 1–10.
- (52) Blancon, J.-C.; Tsai, H.; Nie, W.; Stoumpos, C. C.; Pedesseau, L.; Katan, C.; Kepenekian, M.; Soe, C. M. M.; Appavoo, K.; Sfeir, M. Y.; et al. Extremely Efficient Internal Exciton Dissociation through Edge States in Layered 2D Perovskites. *Science* (80-.). **2017**, 355 (6331), 1288–1292.
- (53) Kim, H.-S.; Hagfeldt, A.; Park, N.-G. Morphological and Compositional Progress in Halide Perovskite Solar Cells. *Chem. Commun.* **2019**, 55 (9), 1192–1200.
- (54) Christians, J. A.; Schulz, P.; Tinkham, J. S.; Schloemer, T. H.; Harvey, S. P.; Tremolet de Villers, B. J.; Sellinger, A.; Berry, J. J.; Luther, J. M. Tailored Interfaces of Unencapsulated Perovskite Solar Cells for >1,000 Hour Operational Stability. *Nat. Energy* **2018**, 3 (1), 68–74.
- (55) Mesquita, I.; Andrade, L.; Mendes, A. Perovskite Solar Cells: Materials, Configurations and Stability. *Renew. Sustain. Energy Rev.* **2018**, 82 (September 2017), 2471–2489.
- (56) Asghar, M. I.; Zhang, J.; Wang, H.; Lund, P. D. Device Stability of Perovskite Solar Cells – A Review. *Renew. Sustain. Energy Rev.* **2017**, 77 (July 2016), 131–146.
- (57) Troughton, J.; Hooper, K.; Watson, T. M. Humidity Resistant Fabrication of CH₃NH₃PbI₃ perovskite Solar Cells and Modules. *Nano Energy* **2017**, 39 (June), 60–68.
- (58) Mehmood, U.; Al-Ahmed, A.; Afzaal, M.; Al-Sulaiman, F. A.; Daud, M. Recent Progress and Remaining Challenges in Organometallic Halides Based Perovskite Solar Cells. *Renew. Sustain. Energy Rev.* **2017**, 78 (December 2015), 1–14.
- (59) Lee, M. M.; Teuscher, J.; Miyasaka, T.; Murakami, T. N.; Snaith, H. J. Efficient Hybrid Solar Cells Based on Meso-Superstructured Organometal Halide Perovskites. *Science* **2012**, 338 (6107), 643–647.
- (60) Lv, S.; Han, L.; Xiao, J.; Zhu, L.; Shi, J.; Wei, H.; Xu, Y.; Dong, J.; Xu, X.; Li, D.; et al. Mesoscopic TiO₂/CH₃NH₃PbI₃ Perovskite Solar Cells with New Hole-Transporting Materials Containing

- Butadiene Derivatives. *Chem. Commun.* **2014**, 50 (52), 6931.
- (61) Meng, L.; You, J.; Guo, T. F.; Yang, Y. Recent Advances in the Inverted Planar Structure of Perovskite Solar Cells. *Acc. Chem. Res.* **2016**, 49 (1), 155–165.
 - (62) Bai, S.; Wu, Z.; Wu, X.; Jin, Y.; Zhao, N.; Chen, Z.; Mei, Q.; Wang, X.; Ye, Z.; Song, T.; et al. High-Performance Planar Heterojunction Perovskite Solar Cells: Preserving Long Charge Carrier Diffusion Lengths and Interfacial Engineering. *Nano Res.* **2014**, 7 (12), 1749–1758.
 - (63) Cosnier, S.; Karyakin, A. *Electropolymerization: Concepts, Materials and Applications*; 2010.
 - (64) Yu, Z.; Sun, L. Recent Progress on Hole-Transporting Materials for Emerging Organometal Halide Perovskite Solar Cells. *Adv. Energy Mater.* **2015**, 5 (12), 1500213.
 - (65) Son, D.-Y.; Im, J.-H.; Kim, H.-S.; Park, N.-G. 11% Efficient Perovskite Solar Cell Based on ZnO Nanorods: An Effective Charge Collection System. *J. Phys. Chem. C* **2014**, 118 (30, SI), 16567–16573.
 - (66) Salim, T.; Sun, S.; Abe, Y.; Krishna, A.; Grimsdale, A. C.; Lam, Y. M. Perovskite-Based Solar Cells: Impact of Morphology and Device Architecture on Device Performance. *J. Mater. Chem. A* **2015**, 3 (17), 8943–8969.
 - (67) Bi, D.; Yi, C.; Luo, J.; Décoppet, J. D.; Zhang, F.; Zakeeruddin, S. M.; Li, X.; Hagfeldt, A.; Grätzel, M. Polymer-Templated Nucleation and Crystal Growth of Perovskite Films for Solar Cells with Efficiency Greater than 21%. *Nat. Energy* **2016**, 1 (10), 1–5.
 - (68) Anaraki, E. H.; Kermanpur, A.; Steier, L.; Domanski, K.; Matsui, T.; Tress, W.; Saliba, M.; Abate, A.; Grätzel, M.; Hagfeldt, A.; et al. Highly Efficient and Stable Planar Perovskite Solar Cells by Solution-Processed Tin Oxide. *Energy Environ. Sci.* **2016**, 9 (10), 3128–3134.
 - (69) Xin, X.; Scheiner, M.; Ye, M.; Lin, Z. Surface-Treated TiO₂ Nanoparticles for Dye-Sensitized Solar Cells with Remarkably Enhanced Performance. *Langmuir* **2011**, 27 (23), 14594–14598.
 - (70) Leijtens, T.; Lauber, B.; Eperon, G. E.; Stranks, S. D.; Snaith, H. J. The Importance of Perovskite Pore Filling in Organometal Mixed Halide Sensitized TiO₂-Based Solar Cells. *J. Phys. Chem. Lett.* **2014**, 5 (7), 1096–1102.
 - (71) Mesquita, I.; Andrade, L.; Mendes, A. Perovskite Solar Cells: Materials, Configurations and Stability. *Renew. Sustain. Energy Rev.* **2018**, 82 (July 2017), 2471–2489.
 - (72) Leijtens, T.; Eperon, G. E.; Pathak, S.; Abate, A.; Lee, M. M.; Snaith, H. J. Overcoming Ultraviolet Light Instability of Sensitized TiO₂ with Meso-Superstructured Organometal Tri-Halide Perovskite Solar Cells. *Nat. Commun.* **2013**, 4, 1–8.
 - (73) Snaith, H. J. Perovskites: The Emergence of a New Era for Low-Cost, High-Efficiency Solar Cells. *J. Phys. Chem. Lett.* **2013**, 4 (21), 3623–3630.
 - (74) Wojciechowski, K.; Saliba, M.; Leijtens, T.; Abate, A.; Snaith, H. J. Sub-150 °C Processed Meso-Superstructured Perovskite Solar Cells with Enhanced Efficiency. *Energy Environ. Sci.* **2014**, 7 (3), 1142–1147.
 - (75) Numata, Y.; Sanehira, Y.; Miyasaka, T. Impacts of Heterogeneous TiO₂ and Al₂O₃ Composite Mesoporous Scaffold on Formamidinium Lead Trihalide Perovskite Solar Cells. *ACS Appl. Mater. Interfaces* **2016**, 8 (7), 4608–4615.
 - (76) Matas Adams, A.; Marin-Beloqui, J. M.; Stoica, G.; Palomares, E. The Influence of the Mesoporous TiO₂ Scaffold on the Performance of Methyl Ammonium Lead Iodide (MAPbI₃) Perovskite Solar Cells: Charge Injection, Charge Recombination and Solar Cell Efficiency Relationship. *J. Mater. Chem. A* **2015**, 3 (44), 22154–22161.
 - (77) Leijtens, T.; Stranks, S. D.; Eperon, G. E.; Lindblad, R.; Johansson, E. M. J.; McPherson, I. J.; Rensmo, H.; Ball, J. M.; Lee, M. M.; Snaith, H. J. Electronic Properties of Meso-Superstructured and Planar Organometal Halide Perovskite Films: Charge Trapping, Photodoping, and Carrier Mobility. *ACS Nano* **2014**, 8 (7), 7147–7155.
 - (78) Jiang, Q.; Zhang, L.; Wang, H.; Yang, X.; Meng, J.; Liu, H.; Yin, Z.; Wu, J.; Zhang, X.; You, J. Enhanced Electron Extraction Using SnO₂ for High-Efficiency Planar-Structure HC(NH₂)₂PbI₃-Based Perovskite Solar Cells. *Nat. Energy* **2017**, 2 (1), 16177.

- (79) Wang, K.; Feng, J.; Zhu, X.; Priya, S.; Wu, C.; Liu, S.; Ren, X.; Yang, R.; Yang, D.; Fang, G. High Efficiency Planar-Type Perovskite Solar Cells with Negligible Hysteresis Using EDTA-Complexed SnO₂. *Nat. Commun.* **2018**, *9* (1).
- (80) Jiang, Q.; Chu, Z.; Wang, P.; Yang, X.; Liu, H.; Wang, Y.; Yin, Z.; Wu, J.; Zhang, X.; You, J. Planar-Structure Perovskite Solar Cells with Efficiency beyond 21%. *Adv. Mater.* **2017**, *29* (46), 1–7.
- (81) Liu, D.; Kelly, T. L. Perovskite Solar Cells with a Planar Heterojunction Structure Prepared Using Room-Temperature Solution Processing Techniques. *Nat. Photonics* **2014**, *8* (2), 133–138.
- (82) Etgar, L.; Gao, P.; Xue, Z.; Peng, Q.; Chandiran, A. K.; Liu, B.; Nazeeruddin, M. K.; Grätzel, M. Mesoscopic CH₃NH₃PbI₃/TiO₂ Heterojunction Solar Cells. *J. Am. Chem. Soc.* **2012**, *134* (42), 17396–17399.
- (83) Mei, A.; Li, X.; Liu, L.; Ku, Z.; Liu, T.; Rong, Y.; Xu, M.; Hu, M.; Chen, J.; Yang, Y.; et al. A Hole-Conductor-Free, Fully Printable Mesoscopic Perovskite Solar Cell with High Stability. *Science* (80-.). **2014**, *345* (6194), 295–298.
- (84) Jeng, J. Y.; Chiang, Y. F.; Lee, M. H.; Peng, S. R.; Guo, T. F.; Chen, P.; Wen, T. C. CH₃NH₃PbI₃ Perovskite/Fullerene Planar-Heterojunction Hybrid Solar Cells. *Adv. Mater.* **2013**, *25* (27), 3727–3732.
- (85) Zhu, Z.; Bai, Y.; Liu, X.; Chueh, C.-C.; Yang, S.; Jen, A. K.-Y. Enhanced Efficiency and Stability of Inverted Perovskite Solar Cells Using Highly Crystalline SnO₂ Nanocrystals as the Robust Electron-Transporting Layer. *Adv. Mater.* **2016**, *28* (30), 6478–6484.
- (86) Liu, Y.; Renna, L. A.; Page, Z. A.; Thompson, H. B.; Kim, P. Y.; Barnes, M. D.; Emrick, T.; Venkataraman, D.; Russell, T. P. A Polymer Hole Extraction Layer for Inverted Perovskite Solar Cells from Aqueous Solutions. *Adv. Energy Mater.* **2016**, *6* (20), 1–7.
- (87) Zheng, L.; Mukherjee, S.; Wang, K.; Hay, M. E.; Boudouris, B. W.; Gong, X. Radical Polymers as Interfacial Layers in Inverted Hybrid Perovskite Solar Cells. *J. Mater. Chem. A* **2017**, *5*, 23831–23839.
- (88) Xiao, Y.; Han, G.; Chang, Y.; Zhou, H.; Li, M.; Li, Y. An All-Solid-State Perovskite-Sensitized Solar Cell Based on the Dual Function Polyaniline as the Sensitizer and p-Type Hole-Transporting Material. *J. Power Sources* **2014**, *267*, 1–8.
- (89) Hosseini, A.; İçli, K.; Özenbaş, M.; Erçelebi. Fabrication and Characterization of Spin-Coated TiO₂ films. *Energy Procedia* **2014**, *60* (C), 191–198.
- (90) Lu, H.; Ma, Y.; Gu, B.; Tian, W.; Li, L. Identifying the Optimum Thickness of Electron Transport Layers for Highly Efficient Perovskite Planar Solar Cells. *J. Mater. Chem. A* **2015**, *3* (32), 16445–16452.
- (91) Ke, W.; Fang, G.; Wang, J.; Qin, P.; Tao, H.; Lei, H.; Liu, Q.; Dai, X.; Zhao, X. Perovskite Solar Cell with an Efficient TiO₂ compact Film. *ACS Appl. Mater. Interfaces* **2014**, *6* (18), 15959–15965.
- (92) Mohd Yusoff, A. R. bin; Ibrahim, M. A.; Yap, C. C.; Ahmad Ludin, N.; Mohamad Noh, M. F.; Daik, R.; Jang, J.; Mat Teridi, M. A.; Lim, E. L.; Teh, C. H. The Architecture of the Electron Transport Layer for a Perovskite Solar Cell. *J. Mater. Chem. C* **2017**, *6* (4), 682–712.
- (93) Chen, L.-C.; Tseng, Z.-L. ZnO-Based Electron Transporting Layer for Perovskite Solar Cells. In *Nanostructured Solar Cells*; InTech, 2017; pp 203–215.
- (94) Guarnera, S.; Abate, A.; Zhang, W.; Foster, J. M.; Richardson, G.; Petrozza, A.; Snaith, H. J. Improving the Long-Term Stability of Perovskite Solar Cells with a Porous Al₂O₃ Buffer Layer. *J. Phys. Chem. Lett.* **2015**, *6* (3), 432–437.
- (95) Yang, G.; Tao, H.; Qin, P.; Ke, W.; Fang, G. Recent Progress in Electron Transport Layers for Efficient Perovskite Solar Cells. *J. Mater. Chem. A* **2016**, *4* (11), 3970–3990.
- (96) Gagliardi, A.; Abate, A. Mesoporous Electron-Selective Contacts Enhance the Tolerance to Interfacial Ion Accumulation in Perovskite Solar Cells. *ACS Energy Lett.* **2018**, *3* (1), 163–169.
- (97) Xia, J.; Masaki, N.; Jiang, K.; Yanagida, S. Deposition of a Thin Film of TiO_x from a Titanium Metal Target as Novel Blocking Layers at Conducting Glass / TiO₂ Interfaces in Ionic Liquid Mesoscopic TiO₂ Dye-Sensitized Solar. **2006**, 25222–25228.

- (98) Leijtens, T.; Lauber, B.; Eperon, G. E.; Stranks, S. D.; Snaith, H. J. The Importance of Perovskite Pore Filling in Organometal Mixed Halide Sensitized TiO₂-Based Solar Cells. *J. Phys. Chem. Lett.* **2014**, 5 (7), 1096–1102.
- (99) Abdi-Jalebi, M.; Dar, M. I.; Sadhanala, A.; Senanayak, S. P.; Giordano, F.; Zakeeruddin, S. M.; Grätzel, M.; Friend, R. H. Impact of a Mesoporous Titania-Perovskite Interface on the Performance of Hybrid Organic-Inorganic Perovskite Solar Cells. *J. Phys. Chem. Lett.* **2016**, 7 (16), 3264–3269.
- (100) Colella, S.; Mosconi, E.; Fedeli, P.; Listorti, A.; Gazza, F.; Orlandi, F.; Ferro, P.; Besagni, T.; Rizzo, A.; Calestani, G.; et al. MAPbI₃-XCl_x Mixed Halide Perovskite for Hybrid Solar Cells: The Role of Chloride as Dopant on the Transport and Structural Properties. *Chem. Mater.* **2013**, 25 (22), 4613–4618.
- (101) Yao, E. P.; Sun, P.; Huang, W.; Yao, E. P.; Yang, Y.; Wang, M. Efficient Planar Perovskite Solar Cells Using Halide Sr-Substituted Pb Perovskite. *Nano Energy* **2017**, 36 (February), 213–222.
- (102) Chatterjee, S.; Pal, A. J. Influence of Metal Substitution on Hybrid Halide Perovskites: Towards Lead-Free Perovskite Solar Cells. *J. Mater. Chem. A* **2018**, 6, 3793–3823.
- (103) Im, J.-H.; Jang, I.-H.; Pellet, N.; Grätzel, M.; Park, N.-G. Growth of CH₃NH₃PbI₃ Cuboids with Controlled Size for High-Efficiency Perovskite Solar Cells. *Nat. Nanotechnol.* **2014**, 9 (11), 927–932.
- (104) Gao, H.; Bao, C.; Li, F.; Yu, T.; Yang, J.; Zhu, W.; Zhou, X.; Fu, G.; Zou, Z. Nucleation and Crystal Growth of Organic-Inorganic Lead Halide Perovskites under Different Relative Humidity. *ACS Appl. Mater. Interfaces* **2015**, 7 (17), 9110–9117.
- (105) Udayabhaskararao, T.; Kazes, M.; Houben, L.; Lin, H.; Oron, D. Nucleation, Growth, and Structural Transformations of Perovskite Nanocrystals. *Chem. Mater.* **2017**, 29 (3), 1302–1308.
- (106) Gloag, D. People Sources of Lead Pollution. *a* **1981**, 282 (January), 41–44.
- (107) Tong, S.; von Schirnding, Y. E.; Prapamontol, T. Environmental Lead Exposure: A Public Health Problem of Global Dimensions. *Bull. World Health Organ.* **2000**, 78 (9), 1068–1077.
- (108) De Wolf, S.; Holovsky, J.; Moon, S. J.; Löper, P.; Niesen, B.; Ledinsky, M.; Haug, F. J.; Yum, J. H.; Ballif, C. Organometallic Halide Perovskites: Sharp Optical Absorption Edge and Its Relation to Photovoltaic Performance. *J. Phys. Chem. Lett.* **2014**, 5 (6), 1035–1039.
- (109) Sadhanala, A.; Deschler, F.; Thomas, T. H.; Dutton, S. E.; Goedel, K. C.; Hanusch, F. C.; Lai, M. L.; Steiner, U.; Bein, T.; Docampo, P.; et al. Preparation of Single-Phase Films of CH₃NH₃Pb(I₁-XBr_x)₃ with Sharp Optical Band Edges. *J. Phys. Chem. Lett.* **2014**, 5 (15), 2501–2505.
- (110) Ali, R.; Hou, G.-J.; Zhu, Z.-G.; Yan, Q.-B.; Zheng, Q.-R.; Su, G. Predicted Lead-Free Perovskites for Solar Cells. *Chem. Mater.* **2018**, 30 (3), 718–728.
- (111) Abate, A. Perovskite Solar Cells Go Lead Free. *Joule* **2017**, 1 (4), 659–664.
- (112) Nie, R.; Mehta, A.; Park, B.; Kwon, H.-W.; Im, J.; Seok, S. I. Mixed Sulfur and Iodide-Based Lead-Free Perovskite Solar Cells. *J. Am. Chem. Soc.* **2018**, jacs.7b11332.
- (113) Chen, M.; Ju, M.-G.; Carl, A. D.; Zong, Y.; Grimm, R. L.; Gu, J.; Zeng, X. C.; Zhou, Y.; Padture, N. P. Cesium Titanium(IV) Bromide Thin Films Based Stable Lead-Free Perovskite Solar Cells. *Joule* **2018**, No. Iv, 1–13.
- (114) Giustino, F.; Snaith, H. J. Toward Lead-Free Perovskite Solar Cells. *ACS Energy Lett.* **2016**, 1 (6), 1233–1240.
- (115) Chen, J.; Park, N.-G. Inorganic Hole Transporting Materials for Stable and High Efficiency Perovskite Solar Cells. *J. Phys. Chem. C* **2018**, 122 (25), 14039–14063.
- (116) Hossain, M. I.; Alharbi, F. H.; Tabet, N. Copper Oxide as Inorganic Hole Transport Material for Lead Halide Perovskite Based Solar Cells. *Sol. Energy* **2015**, 120, 370–380.
- (117) Guo, Y.; Yin, X.; Que, W. NiOxmesoporous Films Derived from Ni(OH)₂nanosheets for Perovskite Solar Cells. *J. Alloys Compd.* **2017**, 722, 839–845.
- (118) Yue, S.; Liu, K.; Xu, R.; Li, M.; Azam, M.; Ren, K.; Liu, J.; Sun, Y.; Wang, Z.; Cao, D.; et al. Efficacious Engineering on Charge Extraction for Realizing Highly Efficient Perovskite Solar Cells. *Energy*

- Environ. Sci.* **2017**, *10* (12), 2570–2578.
- (119) Xie, F.; Chen, C.-C.; Wu, Y.; Li, X.; Cai, M.; Liu, X.; Yang, X.; Han, L. Vertical Recrystallization for Highly Efficient and Stable Formamidinium-Based Inverted-Structure Perovskite Solar Cells. *Energy Environ. Sci.* **2017**, *10*, 1942–1949.
 - (120) Liu, M.; Johnston, M. B.; Snaith, H. J. Efficient Planar Heterojunction Perovskite Solar Cells by Vapour Deposition. *Nature* **2013**, *501* (7467), 395–398.
 - (121) Ye, S.; Sun, W.; Li, Y.; Yan, W.; Peng, H.; Bian, Z.; Liu, Z.; Huang, C. CuSCN-Based Inverted Planar Perovskite Solar Cell with an Average PCE of 15.6%. *Nano Lett.* **2015**, *15* (6), 3723–3728.
 - (122) Mohamed, S. A.; Gasiorowski, J.; Hingerl, K.; Zahn, D. R. T.; Scharber, M. C.; Obayya, S. S. A.; El-Mansy, M. K.; Sariciftci, N. S.; Egbe, D. A. M.; Stadler, P. CuI as Versatile Hole-Selective Contact for Organic Solar Cell Based on Anthracene-Containing PPE-PPV. *Sol. Energy Mater. Sol. Cells* **2015**, *143*, 369–374.
 - (123) Rao, H.; Ye, S.; Sun, W.; Yan, W.; Li, Y.; Peng, H.; Liu, Z.; Bian, Z.; Li, Y.; Huang, C. A 19.0% Efficiency Achieved in CuOx-Based Inverted CH₃NH₃PbI₃-XCl_xsolar Cells by an Effective Cl Doping Method. *Nano Energy* **2016**, *27*, 51–57.
 - (124) Arora, N.; Dar, M. I.; Hinderhofer, A.; Pellet, N.; Schreiber, F.; Zakeeruddin, S. M.; Grätzel, M. Perovskite Solar Cells with CuSCN Hole Extraction Layers Yield Stabilized Efficiencies Greater than 20%. *Science* (80-.). **2017**, *358* (6364), 768–771.
 - (125) Qin, P.; Tanaka, S.; Ito, S.; Tetreault, N.; Manabe, K.; Nishino, H.; Nazeeruddin, M. K.; Grätzel, M. Inorganic Hole Conductor-Based Lead Halide Perovskite Solar Cells with 12.4% Conversion Efficiency. *Nat. Commun.* **2014**, *5* (May), 1–6.
 - (126) Darbost, U.; Cabana, J.; Demers, E.; Maris, T.; Wuest, J. Molecular Tectonics. Use of Br•••aryl Supramolecular Interactions for the Construction of Organized Networks from 9,9'-Spirobifluorene in the Crystalline State. *Chem* **2011**, *1* (1), 52–61.
 - (127) Park, S.; Heo, J. H.; Cheon, C. H.; Kim, H.; Im, S. H.; Son, H. J. A [2,2]Paracyclophane Triarylamine-Based Hole-Transporting Material for High Performance Perovskite Solar Cells. *J. Mater. Chem. A* **2015**, *3* (48), 24215–24220.
 - (128) Park, S.; Heo, J. H.; Cheon, C. H.; Kim, H.; Im, S. H.; Son, H. J. A [2,2]Paracyclophane Triarylamine-Based Hole-Transporting Material for High Performance Perovskite Solar Cells. Supporting Information. *J. Mater. Chem. A* **2015**, *3* (48), 24215–24220.
 - (129) Choi, H.; Park, S.; Kang, M.-S.; Ko, J. Efficient, Symmetric Oligomer Hole Transporting Materials with Different Cores for High Performance Perovskite Solar Cells. *Chem. Commun. Chem. Commun* **2015**, *51* (51), 15506–15509.
 - (130) Petrus, M. L.; Bein, T.; Dingemans, T. J.; Docampo, P. A Low Cost Azomethine-Based Hole Transporting Material for Perovskite Photovoltaics. *J. Mater. Chem. A* **2015**, *3* (23), 12159–12162.
 - (131) Liu, X.; Kong, F.; Guo, F.; Cheng, T.; Chen, W.; Yu, T.; Chen, J.; Tan, Z.; Dai, S. Influence of π -Linker on Triphenylamine-Based Hole Transporting Materials in Perovskite Solar Cells. *Dye. Pigment.* **2017**, *139*, 129–135.
 - (132) Cho, A.-N.; Chakravarthi, N.; Kranthiraja, K.; Reddy, S. S.; Kim, H.-S.; Jin, S.-H.; Park, N.-G. Acridine-Based Novel Hole Transporting Material for High Efficiency Perovskite Solar Cells. *J. Mater. Chem. A* **2017**, *5* (16), 7603–7611.
 - (133) Agarwala, P.; Kabra, D. A Review on Triphenylamine (TPA) Based Organic Hole Transport Materials (HTMs) for Dye Sensitized Solar Cells (DSSCs) and Perovskite Solar Cells (PSCs): Evolution and Molecular Engineering. *J. Mater. Chem. A* **2017**, *5* (4), 1348–1373.
 - (134) Nishimura, H.; Ishida, N.; Shimazaki, A.; Wakamiya, A.; Saeki, A.; Scott, L. T.; Murata, Y. Hole-Transporting Materials with a Two-Dimensionally Expanded π -System around an Azulene Core for Efficient Perovskite Solar Cells. *J. Am. Chem. Soc.* **2015**, *137* (50), 15656–15659.
 - (135) Wang, Y. K.; Jiang, Z. Q.; Liao, L. S. New Advances in Small Molecule Hole-Transporting Materials for Perovskite Solar Cells. *Chinese Chem. Lett.* **2016**, *27* (8), 1293–1303.
 - (136) Gratia, P.; Magomedov, A.; Malinauskas, T.; Daskeviciene, M.; Abate, A.; Ahmad, S.; Grätzel, M.;

- Getautis, V.; Nazeeruddin, M. K. A Methoxydiphenylamine-Substituted Carbazole Twin Derivative: An Efficient Hole-Transporting Material for Perovskite Solar Cells. *Angew. Chemie Int. Ed.* **2015**, *54* (39), 11409–11413.
- (137) Calió, L.; Kazim, S.; Grätzel, M.; Ahmad, S. Hole-Transport Materials for Perovskite Solar Cells. *Angew. Chemie - Int. Ed.* **2016**, *55* (47), 14522–14545.
- (138) Behrouznejad, F.; Shahbazi, S.; Taghavinia, N.; Wu, H.-P.; Wei-Guang Diao, E. A Study on Utilizing Different Metals as the Back Contact of $\text{CH}_3\text{NH}_3\text{PbI}_3$ Perovskite Solar Cells. *J. Mater. Chem. A* **2016**, *4* (35), 13488–13498.
- (139) Nouri, E.; Mohammadi, M. R.; Lianos, P. Construction of Perovskite Solar Cells Using Inorganic Hole-Extracting Components. *ACS Omega* **2018**, *3* (1), 46–54.
- (140) Rong, X.; Tian, H.; Bi, W.; Jin, H.; Zhang, T.; Guo, D.; Zhao, K. Impact of Metal Electrode Work Function of $\text{CH}_3\text{NH}_3\text{PbI}_3/\text{p-Si}$ Planar Heterojunction Perovskite Solar Cells. *Sol. Energy* **2017**, *158* (August), 424–431.
- (141) Sanehira, E. M.; Tremolet De Villers, B. J.; Schulz, P.; Reese, M. O.; Ferrere, S.; Zhu, K.; Lin, L. Y.; Berry, J. J.; Luther, J. M. Influence of Electrode Interfaces on the Stability of Perovskite Solar Cells: Reduced Degradation Using MoOx/Al for Hole Collection. *ACS Energy Lett.* **2016**, *1* (1), 38–45.
- (142) Cox, M.; Gorodetsky, A.; Kim, B.; Kim, K. S.; Jia, Z.; Kim, P.; Nuckolls, C.; Kymissis, I. Single-Layer Graphene Cathodes for Organic Photovoltaics. *Appl. Phys. Lett.* **2011**, *98* (12).
- (143) Shao, Y.; Wang, Q.; Dong, Q.; Yuan, Y.; Huang, J. Vacuum-Free Laminated Top Electrode with Conductive Tapes for Scalable Manufacturing of Efficient Perovskite Solar Cells. *Nano Energy* **2015**, *16*, 47–53.
- (144) Yaqub, G.; Hannan, A.; Akbar, E.; Usman, M.; Hamid, A.; Sadiq, Z.; Iqbal, M. Synthesis, Antibacterial, and Antifungal Activities of Novel Pyridazino Carbazoles. *J. Chem.* **2013**, *2013*, 1–7.
- (145) Bashir, M.; Bano, A.; Ijaz, A. S.; Chaudhary, B. A. Recent Developments and Biological Activities of N-Substituted Carbazole Derivatives: A Review. *Molecules* **2015**, *20* (8), 13496–13517.
- (146) Rotella, D. P.; McFarlane, G. R.; Greenfield, A.; Grosanu, C.; Robichaud, A. J.; Denny, R. A.; Feenstra, R. W.; Núñez-García, S.; Reinders, J. H.; Neut, M. van der; et al. Tetrahydrocarbazole-Based Serotonin Reuptake Inhibitor/Dopamine D2partial Agonists for the Potential Treatment of Schizophrenia. *Bioorganic Med. Chem. Lett.* **2009**, *19* (19), 5552–5555.
- (147) Patel, O. P. S.; Mishra, A.; Maurya, R.; Saini, D.; Pandey, J.; Taneja, I.; Raju, K. S. R.; Kanojiya, S.; Shukla, S. K.; Srivastava, M. N.; et al. Naturally Occurring Carbazole Alkaloids from *Murraya Koenigii* as Potential Antidiabetic Agents. *J. Nat. Prod.* **2016**, *79* (5), 1276–1284.
- (148) Gribble, G. W. *Indole Ring Synthesis*; John Wiley & Sons, Ltd: Chichester, UK, 2016.
- (149) Girard, P. R. Dioxazine Violet Pigments. *High Perform. Pigment. Second Ed.* **2009**, *8*, 195–204.
- (150) Saleh, M.; Baek, S. Bin; Lee, H. M.; Kim, K. S. Triazine-Based Microporous Polymers for Selective Adsorption of CO_2 . *J. Phys. Chem. C* **2015**, *119* (10), 5395–5402.
- (151) Saleh, M.; Kim, K. S. Highly Selective CO_2 Adsorption Performance of Carbazole Based Microporous Polymers. *RSC Adv.* **2015**, *5* (52), 41745–41750.
- (152) López-Olvera, A.; Sánchez-González, E.; Campos-Reales-Pineda, A.; Aguilar-Granda, A.; Ibarra, I. A.; Rodríguez-Molina, B. CO_2 capture in a Carbazole-Based Supramolecular Polyhedron Structure: The Significance of Cu(II) Open Metal Sites. *Inorg. Chem. Front.* **2017**, *4* (1), 56–64.
- (153) Al Mousawi, A.; Lara, D. M.; Noirbent, G.; Dumur, F.; Toufaily, J.; Hamieh, T.; Bui, T. T.; Goubard, F.; Graff, B.; Gigmes, D.; et al. Carbazole Derivatives with Thermally Activated Delayed Fluorescence Property as Photoinitiators/Photoredox Catalysts for LED 3D Printing Technology. *Macromolecules* **2017**, *50* (13), 4913–4926.
- (154) Wex, B.; Kaafarani, B. R. Perspective on Carbazole-Based Organic Compounds as Emitters and Hosts in TADF Applications. *J. Mater. Chem. C* **2017**, *5* (34), 8622–8653.
- (155) Zassowski, P.; Ledwon, P.; Kurowska, A.; Herman, A. P.; Lapkowski, M.; Cherpak, V.; Hotra, Z.; Turyk, P.; Ivaniuk, K.; Stakhira, P.; et al. 1,3,5-Triazine and Carbazole Derivatives for OLED Applications. *Dye. Pigment.* **2018**, *149* (July 2017), 804–811.

- (156) Zhuang, H.; Xu, X.; Liu, Y.; Zhou, Q.; Xu, X.; Li, H.; Xu, Q.; Li, N.; Lu, J.; Wang, L. Dual-Mechanism-Controlled Ternary Memory Devices Fabricated by Random Copolymers with Pendent Carbazole and Nitro-Azobenzene. *J. Phys. Chem. C* **2012**, *116* (48), 25546–25551.
- (157) Venkateswararao, A.; Thomas, K. R. J.; Lee, C. P.; Li, C. T.; Ho, K. C. Organic Dyes Containing Carbazole as Donor and π -Linker: Optical, Electrochemical, and Photovoltaic Properties. *ACS Appl. Mater. Interfaces* **2014**, *6* (4), 2528–2539.
- (158) Duvva, N.; Kanaparthi, R. K.; Kandhadi, J.; Marotta, G.; Salvatori, P.; De Angelis, F.; Giribabu, L. Carbazole-Based Sensitizers for Potential Application to Dye Sensitized Solar Cells. *J. Chem. Sci.* **2015**, *127* (3), 383–394.
- (159) Naik, P.; Su, R.; Elmorsy, M. R.; El-Shafei, A.; Adhikari, A. V. Investigation of New Carbazole Based Metal-Free Dyes as Active Photo-Sensitizers/Co-Sensitizers for DSSCs. *Dye. Pigment.* **2018**, *149* (September 2017), 177–187.
- (160) Liu, J.; Qi, X.; Jiang, T.; Lin, Z.; Chen, S.; Xie, L.; Fan, Q.; Ling, Q.; Zhang, H.; Huang, W. A Rectifying Diode with Hysteresis Effect from an Electroactive Hybrid of Carbazole-Functionalized Polystyrene with CdTe Nanocrystals via Electrostatic Interaction. *Sci. China Chem.* **2010**, *53* (11), 2324–2328.
- (161) Campbell, N.; Barclay, B. M. Recent Advances in the Chemistry of Carbazole. *Chem Rev* **1947**.
- (162) Li, J.; Liu, D.; Li, Y.; Lee, C. S.; Kwong, H. L.; Lee, S. A High Tg Carbazole-Based Hole-Transporting Material for Organic Light-Emitting Devices. *Chem. Mater.* **2005**, *17* (5), 1208–1212.
- (163) Kuwabara, Y.; Ogawa, H.; Inada, H.; Noma, N.; Shirota, Y. Thermally Stable Multilayered Organic Electroluminescent Devices Using Novel Starburst Molecules, 4,4',4''-Tri(N-Carbazolyl)Triphenylamine (TCTA) and 4,4',4''Tris(3-Methylphenylphenylamino)Triphenylamine (m-MTDATA), as Hole-Transport Materials. *Adv. Mater.* **1994**, *6* (9), 677–679.
- (164) Dubey, S.; Sarvaiya, J. N.; Seshadri, B. Temperature Dependent Photovoltaic (PV) Efficiency and Its Effect on PV Production in the World - A Review. *Energy Procedia* **2013**, *33*, 311–321.
- (165) O'Brien, D. F.; Burrows, P. E.; Forrest, S. R.; Koene, B. E.; Loy, D. E.; Thompson, M. E. Hole Transporting Materials with High Glass Transition Temperatures for Use in Organic Light-Emitting Devices. *Adv. Mater.* **1998**, *10* (14), 1108–1112.
- (166) Koene, B. E.; Loy, D. E.; Thompson, M. E. Asymmetric Triaryldiamines as Thermally Stable Hole Transporting Layers for Organic Light-Emitting Devices. *Chem. Mater.* **1998**, *10* (8), 2235–2250.
- (167) Justin Thomas, K. R.; Lin, J. T.; Tao, Y.-T.; Ko, C.-W. Light-Emitting Carbazole Derivatives: Potential Electroluminescent Materials. *J. Am. Chem. Soc.* **2001**, *123* (38), 9404–9411.
- (168) Agarwal, N.; Nayak, P. K.; Ali, F.; Patankar, M. P.; Narasimhan, K. L.; Periasamy, N. Tuning of HOMO Levels of Carbazole Derivatives: New Molecules for Blue OLED. *Synth. Met.* **2011**, *161* (5–6), 466–473.
- (169) Costa, J. C. S.; Taveira, R. J. S.; Lima, C. F. R. A. C.; Mendes, A.; Santos, L. M. N. B. F. Optical Band Gaps of Organic Semiconductor Materials. *Opt. Mater. (Amst.)* **2016**, *58*, 51–60.
- (170) Li, W.; Otsuka, M.; Kato, T.; Wang, Y.; Mori, T.; Michinobu, T. 3,6-Carbazole vs 2,7-Carbazole: A Comparative Study of Hole-Transporting Polymeric Materials for Inorganic-Organic Hybrid Perovskite Solar Cells. *Beilstein J. Org. Chem.* **2016**, *12*, 1401–1408.
- (171) Xu, B.; Sheibani, E.; Liu, P.; Zhang, J.; Tian, H.; Vlachopoulos, N.; Boschloo, G.; Kloo, L.; Hagfeldt, A.; Sun, L. Carbazole-Based Hole-Transport Materials for Efficient Solid-State Dye-Sensitized Solar Cells and Perovskite Solar Cells. *Adv. Mater.* **2014**, *26* (38), 6629–6634.
- (172) Sung, S. Do; Kang, M. S.; Choi, I. T.; Kim, H. M.; Kim, H.; Hong, M.; Kim, H. K.; Lee, W. I. 14.8% Perovskite Solar Cells Employing Carbazole Derivatives As Hole Transporting Materials. *Chem. Commun. (Camb.)* **2014**, *50* (91), 14161–14163.
- (173) Kang, M. S.; Sung, S. Do; Choi, I. T.; Kim, H.; Hong, M.; Kim, J.; Lee, W. I.; Kim, H. K. Novel Carbazole-Based Hole-Transporting Materials with Star-Shaped Chemical Structures for Perovskite-Sensitized Solar Cells. *ACS Appl. Mater. Interfaces* **2015**, *7* (40), 22213–22217.
- (174) Wang, H.; Sheikh, A. D.; Feng, Q.; Li, F.; Chen, Y.; Yu, W.; Alarousu, E.; Ma, C.; Haque, M. A.; Shi,

- D.; et al. Facile Synthesis and High Performance of a New Carbazole-Based Hole-Transporting Material for Hybrid Perovskite Solar Cells. *ACS Photonics* **2015**, 2 (7), 849–855.
- (175) Magomedov, A.; Paek, S.; Gratia, P.; Kasparavicius, E.; Daskeviciene, M.; Kamarauskas, E.; Gruodis, A.; Jankauskas, V.; Kantminiene, K.; Cho, K. T.; et al. Diphenylamine-Substituted Carbazole-Based Hole Transporting Materials for Perovskite Solar Cells: Influence of Isomeric Derivatives. *Adv. Funct. Mater.* **2018**, 1704351, 1–13.
- (176) Lim, I.; Kim, E.-K.; Patil, S. a.; Ahn, D. Y.; Lee, W.; Shrestha, N. K.; Lee, J. K.; Seok, W. K.; Cho, C.-G.; Han, S.-H. Indolocarbazole Based Small Molecules: An Efficient Hole Transporting Material for Perovskite Solar Cells. *RSC Adv.* **2015**, 5 (68), 55321–55327.
- (177) Ramos, F. J.; Rakstys, K.; Kazim, S.; Grätzel, M.; Nazeeruddin, M. K.; Ahmad, S. Rational Design of Triazatruxene-Based Hole Conductors for Perovskite Solar Cells. *RSC Adv.* **2015**, 5 (66), 53426–53432.
- (178) Daskeviciene, M.; Paek, S.; Wang, Z.; Malinauskas, T.; Jokubauskaite, G.; Rakstys, K.; Cho, K. T.; Magomedov, A.; Jankauskas, V.; Ahmad, S.; et al. Carbazole-Based Enamine: Low-Cost and Efficient Hole Transporting Material for Perovskite Solar Cells. *Nano Energy* **2017**, 32 (November 2016), 551–557.
- (179) Zhang, J.; Xu, B.; Johansson, M. B.; Vlachopoulos, N.; Boschloo, G.; Sun, L.; Johansson, E. M. J.; Hagfeldt, A. Strategy to Boost the Efficiency of Mixed-Ion Perovskite Solar Cells: Changing Geometry of the Hole Transporting Material. *ACS Nano* **2016**, 10 (7), 6816–6825.
- (180) Molina-Ontoria, A.; Zimmermann, I.; Garcia-Benito, I.; Gratia, P.; Roldán-Carmona, C.; Aghazada, S.; Graetzel, M.; Nazeeruddin, M. K.; Martín, N. Benzotrithiophene-Based Hole-Transporting Materials for 18.2 % Perovskite Solar Cells. *Angew. Chemie - Int. Ed.* **2016**, 55 (21), 6270–6274.
- (181) Lu, C.; Choi, I. T.; Kim, J.; Kim, H. K. Simple Synthesis and Molecular Engineering of Low-Cost and Star-Shaped Carbazole-Based Hole Transporting Materials for Highly Efficient Perovskite Solar Cells. *J. Mater. Chem. A* **2017**, 5 (38), 20263–20276.
- (182) Bui, T. T.; Goubard, F.; Troughton, J.; Watson, T. Simple 3,6-Bis(Diphenylaminyl)Carbazole Molecular Glasses as Hole Transporting Materials for Hybrid Perovskite Solar Cells. *J. Mater. Sci. Mater. Electron.* **2017**, 28 (23), 17551–17556.
- (183) Bui, T. T.; Shah, S. K.; Abbas, M.; Sallenave, X.; Sini, G.; Hirsch, L.; Goubard, F. Carbazole-Based Molecular Glasses as Hole-Transporting Materials in Solid State Dye-Sensitized Solar Cells. *ChemNanoMat* **2015**, 1 (3), 203–210.
- (184) Chen, Z.; Li, H.; Zheng, X.; Zhang, Q.; Li, Z.; Hao, Y.; Fang, G. Low-Cost Carbazole-Based Hole-Transport Material for Highly Efficient Perovskite Solar Cells. *ChemSusChem* **2017**, 10 (15), 3111–3117.
- (185) Yin, X.; Guan, L.; Yu, J.; Zhao, D.; Wang, C.; Shrestha, N.; Han, Y.; An, Q.; Zhou, J.; Zhou, B.; et al. One-Step Facile Synthesis of a Simple Carbazole-Cored Hole Transport Material for High-Performance Perovskite Solar Cells. *Nano Energy* **2017**, 40 (August), 163–169.
- (186) Zhang, M. D.; Zheng, B. H.; Zhuang, Q. F.; Huang, C. Y.; Cao, H.; Chen, M. D.; Wang, B. Two Dimethoxyphenylamine-Substituted Carbazole Derivatives as Hole-Transporting Materials for Efficient Inorganic-Organic Hybrid Perovskite Solar Cells. *Dye. Pigment.* **2017**, 146, 589–595.
- (187) Zong, X.; Qiao, W.; Chen, Y.; Sun, Z.; Liang, M.; Xue, S. A New Binaphthol Based Hole-Transporting Materials for Perovskite Solar Cells. *Tetrahedron* **2017**, 73 (24), 3398–3405.
- (188) Zhu, L.; Shan, Y.; Wang, R.; Liu, D.; Zhong, C.; Song, Q.; Wu, F. High-Efficiency Perovskite Solar Cells Based on New TPE Compounds as Hole Transport Materials: The Role of 2,7- and 3,6-Substituted Carbazole Derivatives. *Chem. - A Eur. J.* **2017**, 23 (18), 4373–4379.
- (189) Rakstys, K.; Paek, S.; Gao, P.; Gratia, P.; Marszalek, T.; Grancini, G.; Cho, K. T.; Genevicius, K.; Jankauskas, V.; Pisula, W.; et al. Molecular Engineering of Face-on Oriented Dopant-Free Hole Transporting Material for Perovskite Solar Cells with 19% PCE. *J. Mater. Chem. A* **2017**, 5 (17), 7811–7815.
- (190) Daškevičiūtė, Š.; Sakai, N.; Franckevičius, M.; Daškevičienė, M.; Magomedov, A.; Jankauskas, V.;

- Snaith, H. J.; Getautis, V. Nonspiro, Fluorene-Based, Amorphous Hole Transporting Materials for Efficient and Stable Perovskite Solar Cells. *Adv. Sci.* **2018**, *5* (4), 1700811.
- (191) Benhattab, S.; Cho, A. N.; Nakar, R.; Berton, N.; Tran-Van, F.; Park, N. G.; Schmaltz, B. Simply Designed Carbazole-Based Hole Transporting Materials for Efficient Perovskite Solar Cells. *Org. Electron. physics, Mater. Appl.* **2018**, *56* (October 2017), 27–30.
- (192) Li, D.; Shao, J.-Y.; Li, Y.; Li, Y.; Deng, L.-Y.; Zhong, Y.-W.; Meng, Q. New Hole Transporting Materials for Planar Perovskite Solar Cells. *Chem. Commun.* **2018**, *54*, 1651–1654.
- (193) Li, M.; Wang, Z.; Liang, M.; Liu, L.; Wang, X.; Sun, Z.; Xue, S. Low-Cost Carbazole-Based Hole-Transporting Materials for Perovskite Solar Cells: Influence of S,N-Heterocycle. *J. Phys. Chem. C* **2018**, *122*, acs.jpcc.8b09482.
- (194) Yin, C.; Lu, J.; Xu, Y.; Yun, Y.; Wang, K.; Li, J.; Jiang, L.; Sun, J.; Scully, A. D.; Huang, F.; et al. Low-Cost N,N''-Bicarbazole-Based Dopant-Free Hole-Transporting Materials for Large-Area Perovskite Solar Cells. *Adv. Energy Mater.* **2018**, *8* (21), 1–10.
- (195) Pitoňák, M.; Neogrády, P.; Řezáč, J.; Jurečka, P.; Urban, M.; Hobza, P. Benzene Dimer: High-Level Wave Function and Density Functional Theory Calculations. *J. Chem. Theory Comput.* **2008**, *4* (11), 1829–1834.
- (196) Ouellette, R. J.; Rawn, J. D.; Ouellette, R. J.; Rawn, J. D. 4 – Alkanes and Cycloalkanes Structures and Reactions. In *Organic Chemistry Study Guide*; Elsevier, 2015; pp 47–67.
- (197) Leijtens, T.; Giovenzana, T.; Habisreutinger, S. N.; Tinkham, J. S.; Noel, N. K.; Kamino, B. A.; Sadoughi, G.; Sellinger, A.; Snaith, H. J. Hydrophobic Organic Hole Transporters for Improved Moisture Resistance in Metal Halide Perovskite Solar Cells. *ACS Appl. Mater. Interfaces* **2016**, *8* (9), 5981–5989.
- (198) Nguyen, W. H.; Bailie, C. D.; Unger, E. L.; McGehee, M. D. Enhancing the Hole-Conductivity of Spiro-OMeTAD without Oxygen or Lithium Salts by Using Spiro(TFSI)₂ in Perovskite and Dye-Sensitized Solar Cells. *J. Am. Chem. Soc.* **2014**, *136* (31), 10996–11001.
- (199) Fantacci, S.; De Angelis, F.; Nazeeruddin, M. K.; Grätzel, M.; Grätzel, M. Electronic and Optical Properties of the Spiro-MeOTAD Hole Conductor in Its Neutral and Oxidized Forms: A DFT/TDDFT Investigation. *J. Phys. Chem. C* **2011**, *115* (46), 23126–23133.
- (200) Pommerehne, J.; Vestweber, H.; Guss, W.; Mahrt, R. F.; Bässler, H.; Porsch, M.; Daub, J. Efficient Two Layer Leds on a Polymer Blend Basis. *Adv. Mater.* **1995**, *7* (6), 551–554.
- (201) G09 | Gaussian.com <https://gaussian.com/glossary/g09/> (accessed Jan 24, 2019).
- (202) Choi, W. T.; Song, J.; Ko, J.; Jang, Y.; Kim, T. H.; Han, Y. S.; Lim, J.; Lee, C.; Char, K. Effect of Solvent Additives on Bulk Heterojunction Morphology of Organic Photovoltaics and Their Impact on Device Performance. *J. Polym. Sci. Part B Polym. Phys.* **2016**, *54* (2), 128–134.
- (203) Butt, H. J.; Roisman, I. V.; Brinkmann, M.; Papadopoulos, P.; Vollmer, D.; Semprebon, C. Characterization of Super Liquid-Repellent Surfaces. *Curr. Opin. Colloid Interface Sci.* **2014**, *19* (4), 343–354.
- (204) Deng, X.; Wen, X.; Zheng, J.; Young, T.; Lau, C. F. J.; Kim, J.; Green, M.; Huang, S.; Ho-Baillie, A. Dynamic Study of the Light Soaking Effect on Perovskite Solar Cells by In-Situ Photoluminescence Microscopy. *Nano Energy* **2018**, *46* (January), 356–364.
- (205) Zheng, L.; Ma, Y.; Chu, S.; Wang, S.; Qu, B.; Xiao, L.; Chen, Z.; Gong, Q.; Wu, Z.; Hou, X. Improved Light Absorption and Charge Transport for Perovskite Solar Cells with Rough Interfaces by Sequential Deposition. *Nanoscale* **2014**, *6* (14), 8171–8176.
- (206) Inzelt, G. *Conducting Polymers : A New Era in Electrochemistry*; Springer, 2008.
- (207) Burroughes, J. H.; Bradley, D. D. C.; Brown, A. R.; Marks, R. N.; Mackay, K.; Friend, R. H.; Burns, P. L.; Holmes, A. B. Light-Emitting Diodes Based on Conjugated Polymers. *Nature* **1990**, *347* (6293), 539–541.
- (208) Friend, R. H.; Gymer, R. W.; Holmes, A. B.; Burroughes, J. H.; Marks, R. N.; Taliani, C.; Bradley, D. D. C.; Dos Santos, D. A.; Brédas, J. L.; Lögdahl, M.; et al. Electroluminescence in Conjugated Polymers. *Nature* **1999**, *397* (6715), 121–128.

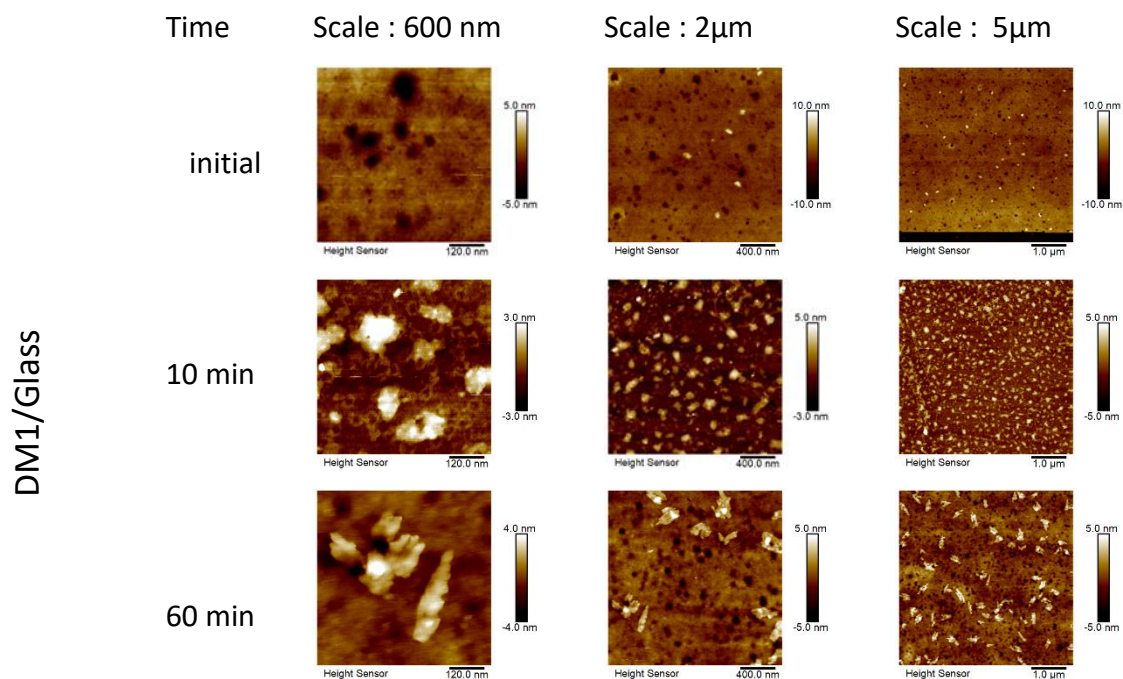
- (209) Nie, W.; Tsai, H.; Asadpour, R.; Blancon, J.-C.; Neukirch, A. J.; Gupta, G.; Crochet, J. J.; Chhowalla, M.; Tretiak, S.; Alam, M. A.; et al. High-Efficiency Solution-Processed Perovskite Solar Cells with Millimeter-Scale Grains. *Science* (80-.). **2015**, *347* (6221), 522–525.
- (210) Edri, E.; Kirmayer, S.; Cahen, D.; Hodes, G. High Open-Circuit Voltage Solar Cells Based on Organic-Inorganic Lead Bromide Perovskite. *J. Phys. Chem. Lett.* **2013**, *4* (6), 897–902.
- (211) Mali, S. S.; Shim, C. S.; Hong, C. K. Highly Stable and Efficient Solid-State Solar Cells Based on Methylammonium Lead Bromide (CH₃NH₃PbBr₃) Perovskite Quantum Dots. *NPG Asia Mater.* **2015**, *7* (8), e208-9.
- (212) Yang, L.; Yan, Y.; Cai, F.; Li, J.; Wang, T. Poly(9-Vinylcarbazole) as a Hole Transport Material for Efficient and Stable Inverted Planar Heterojunction Perovskite Solar Cells. *Sol. Energy Mater. Sol. Cells* **2017**, *163* (1), 210–217.
- (213) Xu, Y.; Bu, T.; Li, M.; Qin, T.; Yin, C.; Wang, N.; Li, R.; Zhong, J.; Li, H.; Peng, Y.; et al. Non-Conjugated Polymer as an Efficient Dopant-Free Hole-Transporting Material for Perovskite Solar Cells. *ChemSusChem* **2017**, *10* (12), 2578–2584.
- (214) Tong, T.; Tan, C.; Keller, T.; Li, B.; Zheng, C.; Scherf, U.; Gao, D.; Huang, W. Two Anthracene-Based Copolymers as the Hole-Transporting Materials for High-Performance Inverted (p-i-n) Perovskite Solar Cells. *Macromolecules* **2018**, *51* (18), 7407–7416.
- (215) Zhou, Z.; Zhao, Y.; Zhang, C.; Zou, D.; Chen, Y.; Lin, Z.; Zhen, H.; Ling, Q. A Facile One-Pot Synthesis of Hyper-Branched Carbazole-Based Polymer as a Hole-Transporting Material for Perovskite Solar Cells. *J. Mater. Chem. A* **2017**, *5* (14), 6613–6621.
- (216) Zhao, L. yun; Liu, Y. nan; Wang, S. fan; Tao, Y. tian; Wang, F. fang; Zhang, X. wen; Huang, W. Novel Hyperbranched Polymers as Host Materials for Green Thermally Activated Delayed Fluorescence OLEDs. *Chinese J. Polym. Sci. (English Ed.)* **2017**, *35* (4), 490–502.
- (217) Li, Z.; Liu, Y.; Yu, G.; Wen, Y.; Guo, Y.; Ji, L.; Qin, J.; Li, Z. A New Carbazole-Constructed Hyperbranched Polymer: Convenient One-Pot Synthesis, Hole-Transporting Ability, and Field-Effect Transistor Properties. *Adv. Funct. Mater.* **2009**, *19* (16), 2677–2683.
- (218) Yang, W. S.; Park, B.-W.; Jung, E. H.; Jeon, N. J. Iodide Management in Formamidinium-Lead-Halide – Based Perovskite Layers for Efficient Solar Cells. *Science* (80-.). **2017**, *356* (6345), 1376–1379.
- (219) Fu, F.; Feurer, T.; Weiss, T. P.; Pisoni, S.; Avancini, E.; Andres, C.; Buecheler, S.; Tiwari, A. N. High-Efficiency Inverted Semi-Transparent Planar Perovskite Solar Cells in Substrate Configuration. *Nat. Energy* **2017**, *2* (1), 16190.
- (220) Hu, L.; Sun, K.; Wang, M.; Chen, W.; Yang, B.; Fu, J.; Xiong, Z.; Li, X.; Tang, X.; Zang, Z.; et al. Inverted Planar Perovskite Solar Cells with a High Fill Factor and Negligible Hysteresis by the Dual Effect of NaCl-Doped PEDOT:PSS. *ACS Appl. Mater. Interfaces* **2017**, *9* (50), 43902–43909.
- (221) Wang, Y.; Zhang, S.; Wu, J.; Liu, K.; Li, D.; Meng, Q.; Zhu, G. Electropolymerization Porous Aromatic Framework Film As a Hole-Transport Layer for Inverted Perovskite Solar Cells with Superior Stability. *ACS Appl. Mater. Interfaces* **2017**, *9* (50), 43688–43695.
- (222) Cai, B.; Xing, Y.; Yang, Z.; Zhang, W.; Qiu, J. High Performance Hybrid Solar Cells Sensitized by Organolead Halide Perovskites. *Energy Environ. Sci.* **2013**, 1480–1485.
- (223) Saliba, M.; Orlandi, S.; Matsui, T.; Aghazada, S.; Cavazzini, M.; Correa-Baena, J.-P.; Gao, P.; Scopelliti, R.; Mosconi, E.; Dahmen, K.-H.; et al. A Molecularly Engineered Hole-Transporting Material for Efficient Perovskite Solar Cells. *Nat. Energy* **2016**, *1* (2), 15017.
- (224) Jenkins, A. D.; Jones, R. G.; Moad, G. Terminology for Reversible-Deactivation Radical Polymerization Previously Called “Controlled” Radical or “Living” Radical Polymerization (IUPAC Recommendations 2010). *Pure Appl. Chem.* **2009**, *82* (2), 483–491.
- (225) Nossarev, G. G.; Hogen-Esch, T. E. Livingtert-Butyllithium Initiated Anionic Polymerization of 2-Vinylnaphthalene in Toluene-Tetrahydrofuran Mixtures. *J. Polym. Sci. Part A Polym. Chem.* **2001**, *39* (17), 3034–3041.
- (226) Uraneck C. A., Hsieh H .L., B. O. G. Telechelic Polymers. *J. Polym. Sci., Part A Polym. Chem.* **1960**,

- 46 (148), 535–539.
- (227) Barr, N. J.; Bengough, W. I.; Beveridge, G.; Park, G. B. The Measurement of Rates of Initiation in the Thermal Polymerization of Styrene. *Eur. Polym. J.* **1978**, *14* (4), 245–250.
 - (228) Buzanowski, W. C.; Graham, J. D.; Priddy, D. B.; Shero, E. Spontaneous Polymerization of Styrene in the Presence of Acid: Further Confirmation of the Mayo Mechanism. *Polymer (Guildf)*. **1992**, *33* (14), 3055–3059.
 - (229) Chiefari, J.; Rizzardo, E. *Control of Free-Radical Polymerization by Chain Transfer Methods*; 2002.
 - (230) Mayo, F. R. Chain Transfer in the Polymerization of Styrene: The Reaction of Solvents with Free Radicals ¹. *J. Am. Chem. Soc.* **1943**, *65* (12), 2324–2329.
 - (231) Flory, P. J. The Mechanism of Vinyl Polymerizations. *J. Am. Chem. Soc.* **1937**, *59* (2), 241–253.
 - (232) Furuncuoğlu, T.; Uğur, I.; Degirmenci, I.; Aviyente, V. Role of Chain Transfer Agents in Free Radical Polymerization Kinetics. *Macromolecules* **2010**, *43* (4), 1823–1835.
 - (233) Matyjaszewski, K.; Davis, T. P. *Handbook of Radical Polymerization*; 2002; Vol. 125.
 - (234) Zhu, Q.; Bao, X.; Yu, J.; Zhu, D.; Qiu, M.; Yang, R.; Dong, L. Compact Layer Free Perovskite Solar Cells with a High-Mobility Hole-Transporting Layer. *ACS Appl. Mater. Interfaces* **2016**, *8* (4), 2652–2657.
 - (235) Torres, A.; Rego, L. G. C. Surface Effects and Adsorption of Methoxy Anchors on Hybrid Lead Iodide Perovskites: Insights for Spiro-MeOTAD Attachment. *J. Phys. Chem. C* **2014**, *118* (46), 26947–26954.
 - (236) Yin, J.; Cortecchia, D.; Krishna, A.; Chen, S.; Mathews, N.; Grimsdale, A. C.; Soci, C. Interfacial Charge Transfer Anisotropy in Polycrystalline Lead Iodide Perovskite Films. *J. Phys. Chem. Lett.* **2015**, *6* (8), 1396–1402.
 - (237) Siove, A.; Adès, D. Synthesis by Oxidative Polymerization with FeCl₃ of a Fully Aromatic Twisted Poly(3,6-Carbazole) with a Blue-Violet Luminescence. *Polymer (Guildf)*. **2004**, *45* (12), 4045–4049.
 - (238) Zhang, Z.-B.; Fujiki, M.; Tang, H.-Z.; Motonaga, M.; Torimitsu, K. The First High Molecular Weight Poly(N -Alkyl-3,6-Carbazole)s. *Macromolecules* **2002**, *35* (6), 1988–1990.
 - (239) Karon, K.; Lapkowski, M. Carbazole Electrochemistry: A Short Review. *J. Solid State Electrochem.* **2015**, *19* (9), 2601–2610.
 - (240) Chen, Q.; Liu, D. P.; Luo, M.; Feng, L. J.; Zhao, Y. C.; Han, B. H. Nitrogen-Containing Microporous Conjugated Polymers via Carbazole-Based Oxidative Coupling Polymerization: Preparation, Porosity, and Gas Uptake. *Small* **2014**, *10* (2), 308–315.

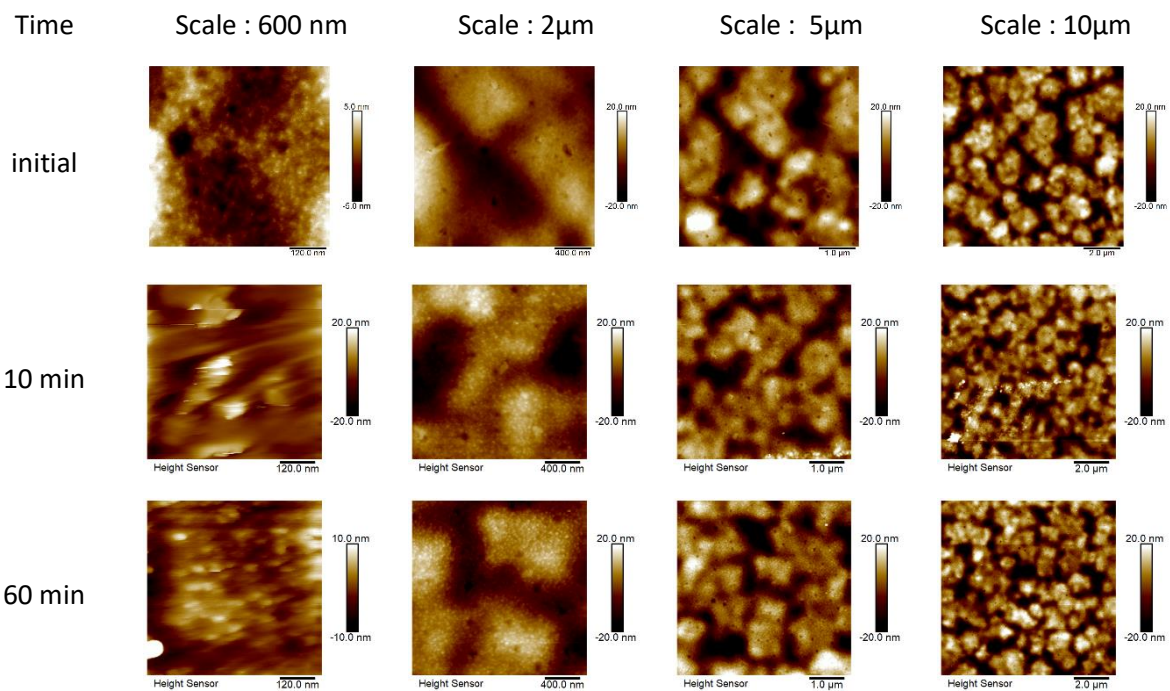
Annex

The films for AFM characterization were prepared using the following procedure. A solution was prepared by dissolving 72 mg of HTM in 1 ml chlorobenzene. Then, 17.5 μ l of bis(trifluoromethylsulfonyl)imide lithium salt solution (LiTFSI) solution (520 mg in 1 mL ACN), 28.8 μ L of TBP (tert-butylpyridine) and 6 μ L of tris (2-1H-pyrazol-1-yl) - 4-tert-butylpyridine – cobalt (III) -tris (bis (trifluoromethylsulfonyl) imide) (300 mg in 1 mL ACN) were added to this solution. 35 μ L of the HTM solution was spin-coated at 4000 rpm, 4000 rpm/s for 20 s.

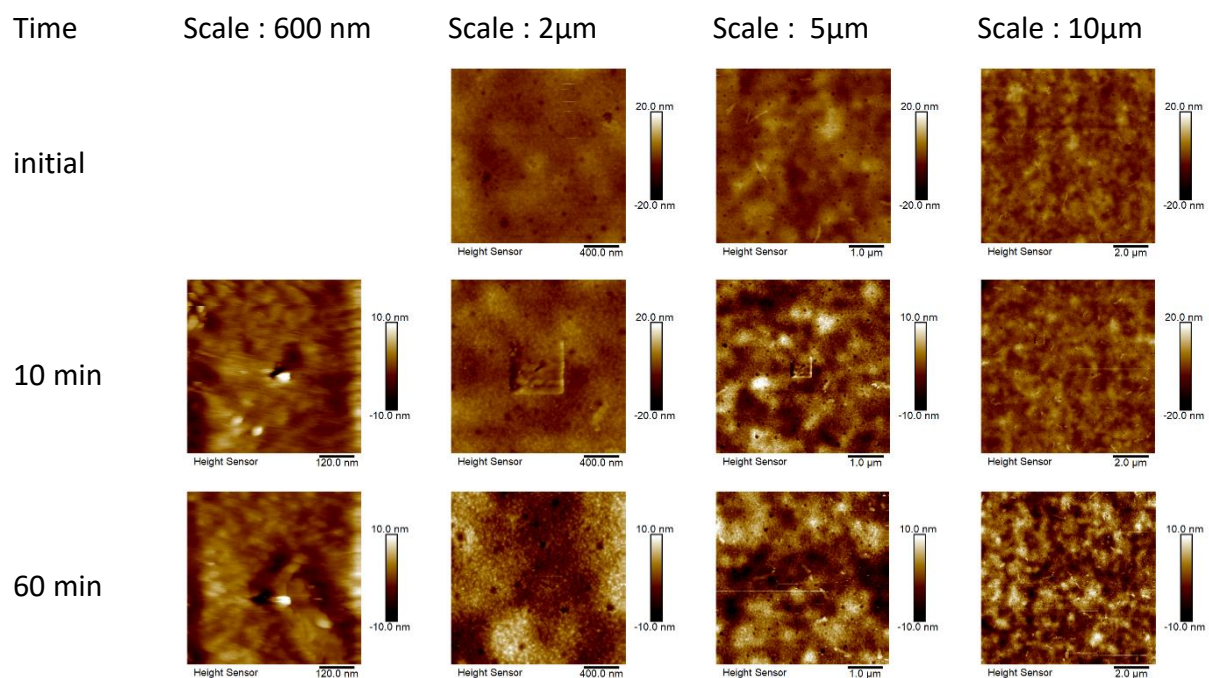
Different AFM measurements were done after 0, 10 and 60 minutes under illumination. PSC modules made with HTM DM1, DM2 and iDM1 were chosen as HTM on perovskite prototype modules and manufactured using the 1-step and 2-step perovskite deposition method, and referenced over ITO glass, to analyze their morphology.

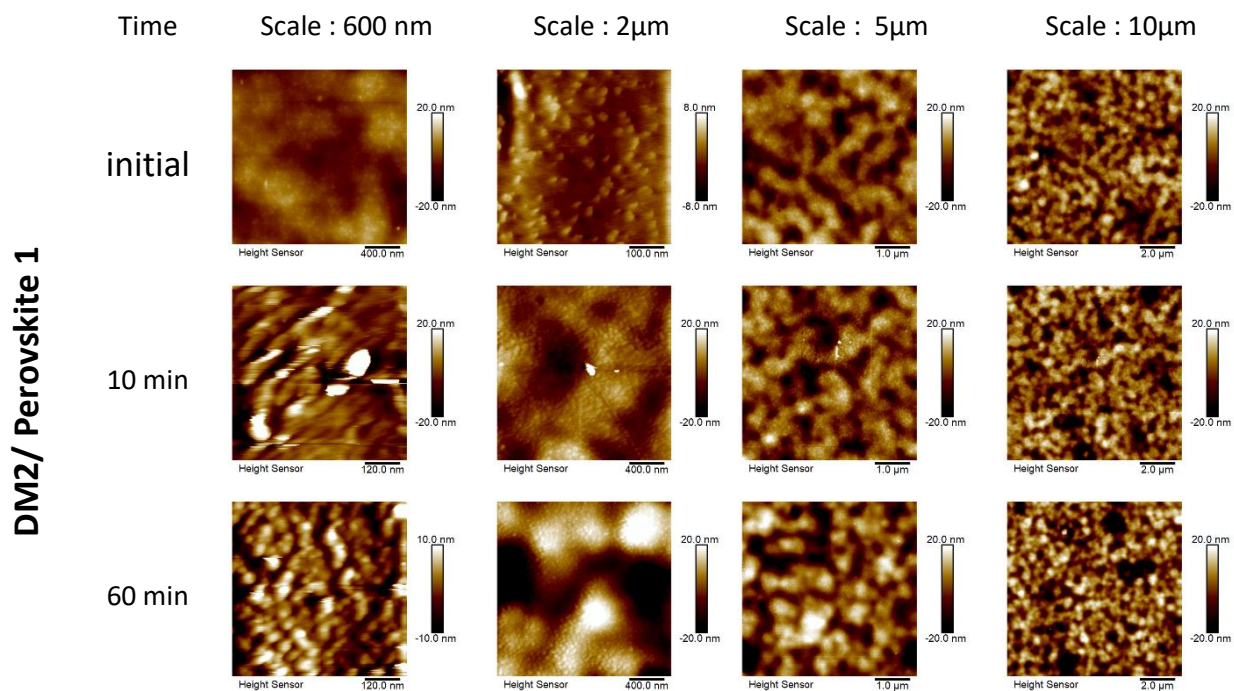
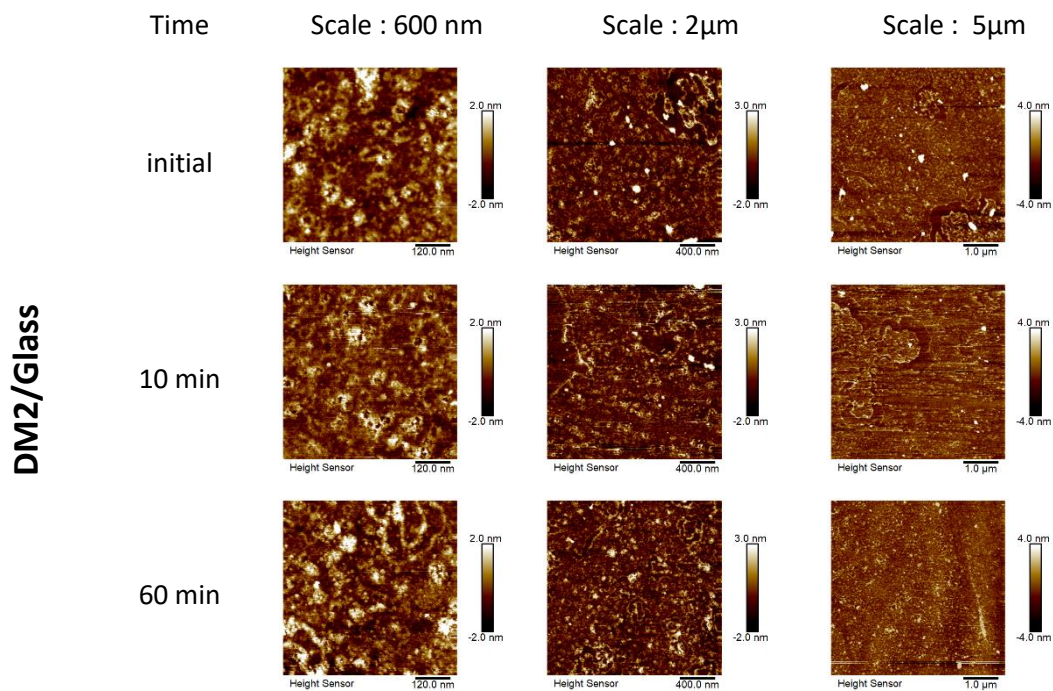


DM1/ Perovskite 1

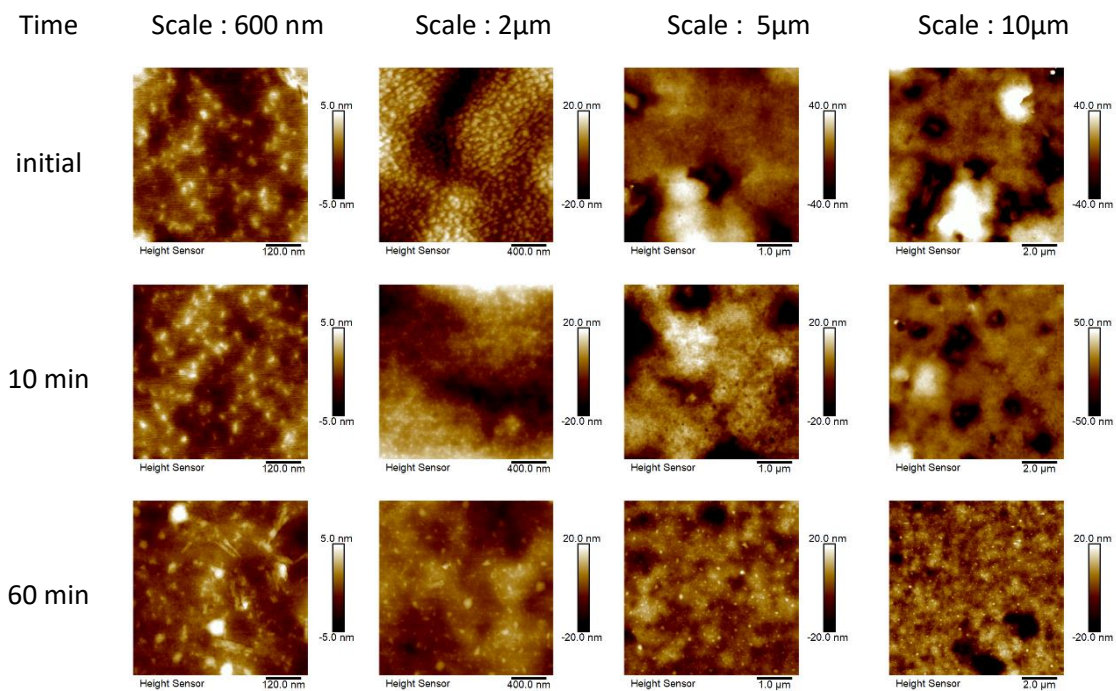


DM1/ Perovskite 2

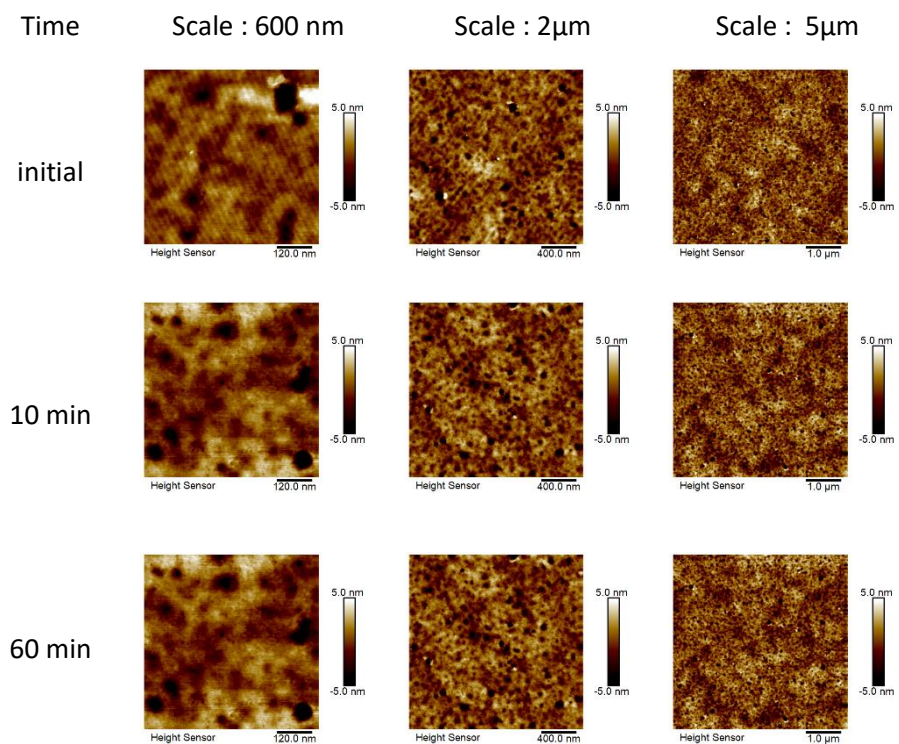




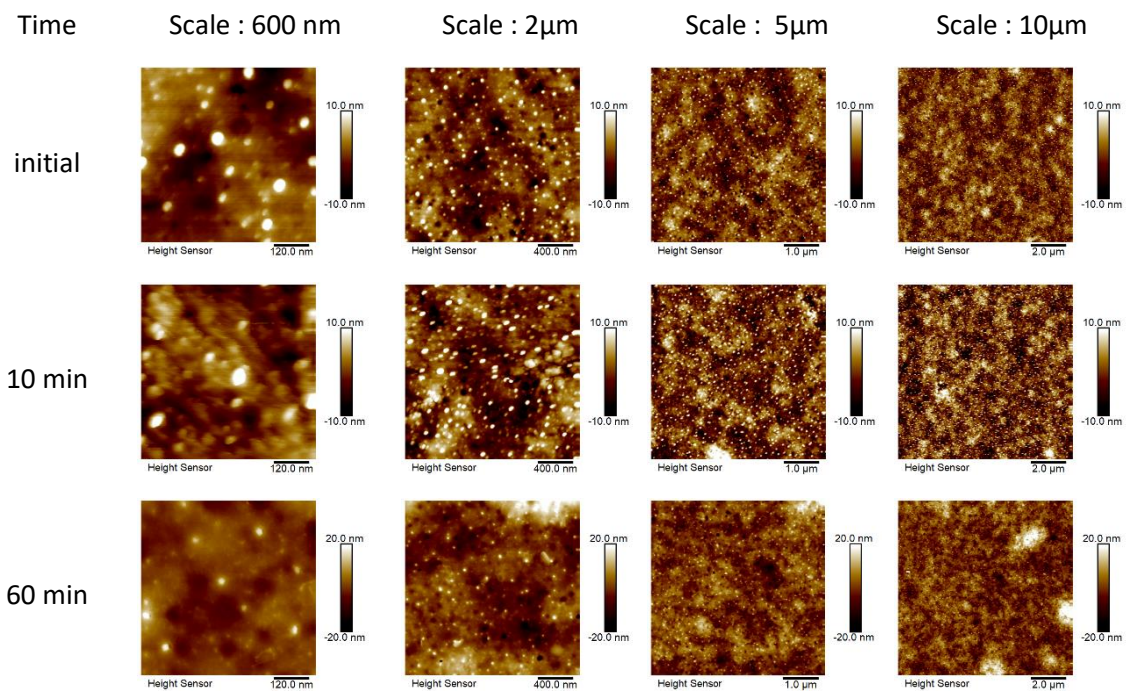
DM2/ Perovskite 2



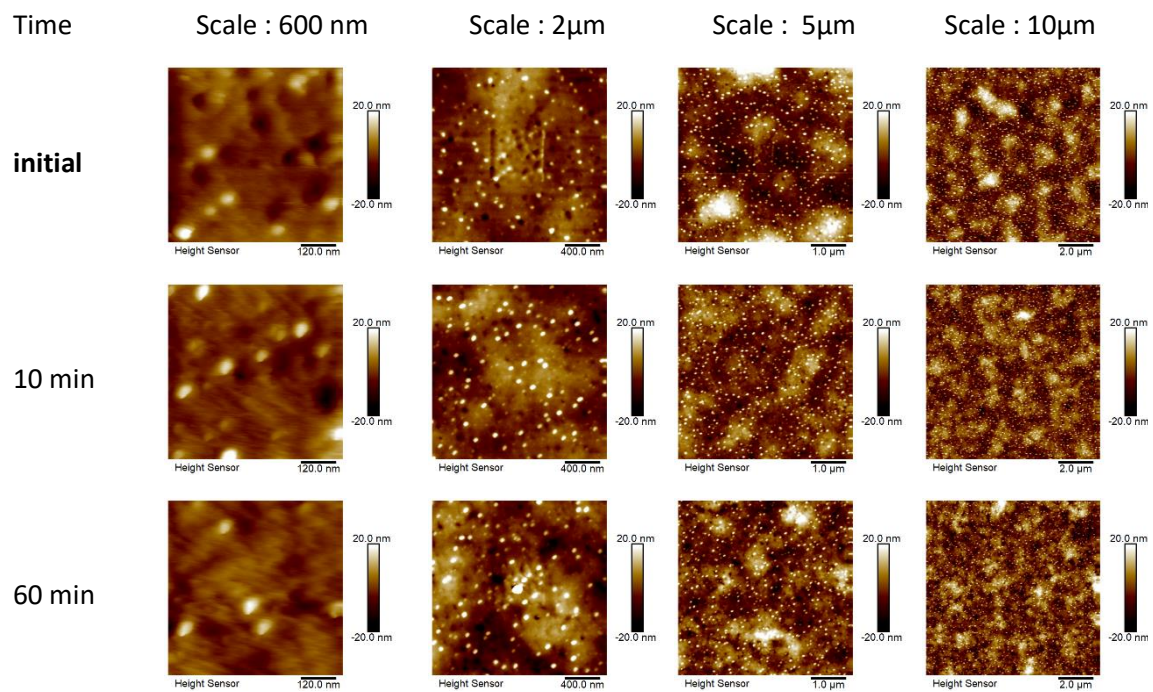
iDM1/ glass



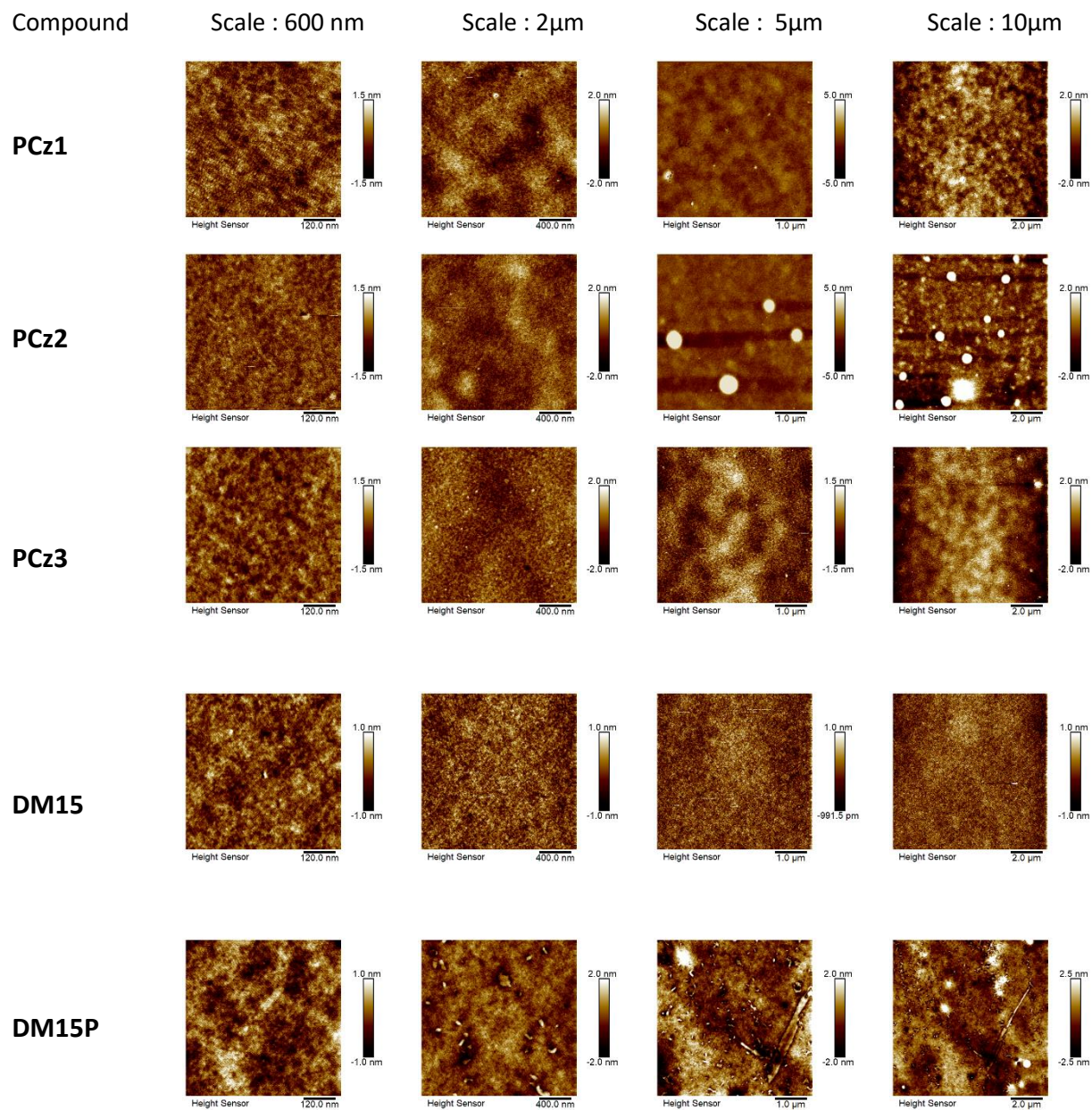
iDM1/ Perovskite 1



iDM1/ Perovskite 2

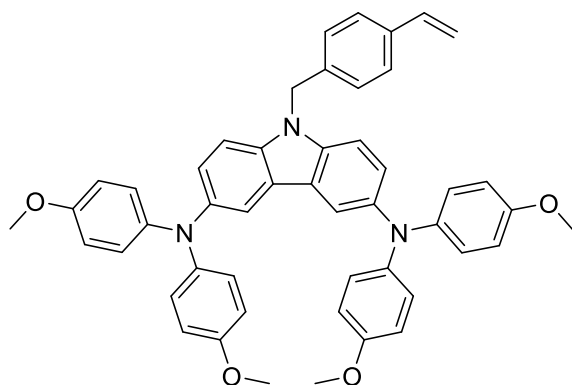


AFM images at different scales of the coated films of PCzX family and DM15 and its derivative polymer DM15P and AFM characterized over ITO glass.



Annex 2

DM1

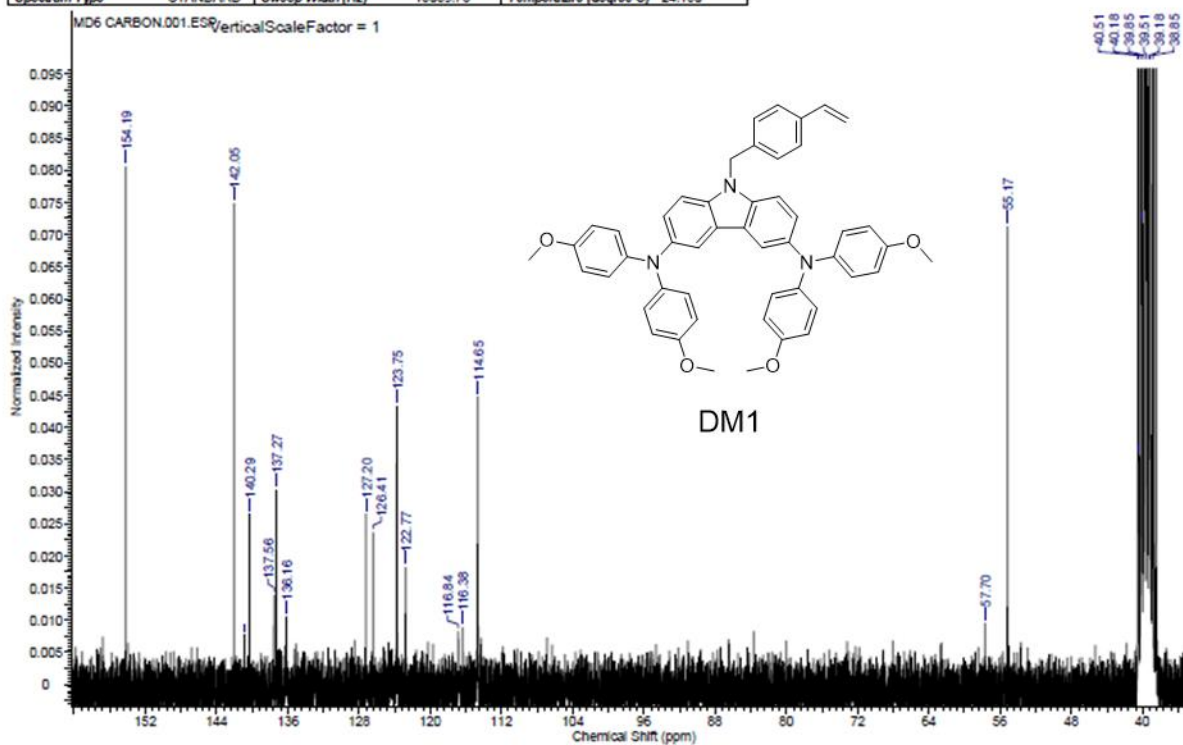


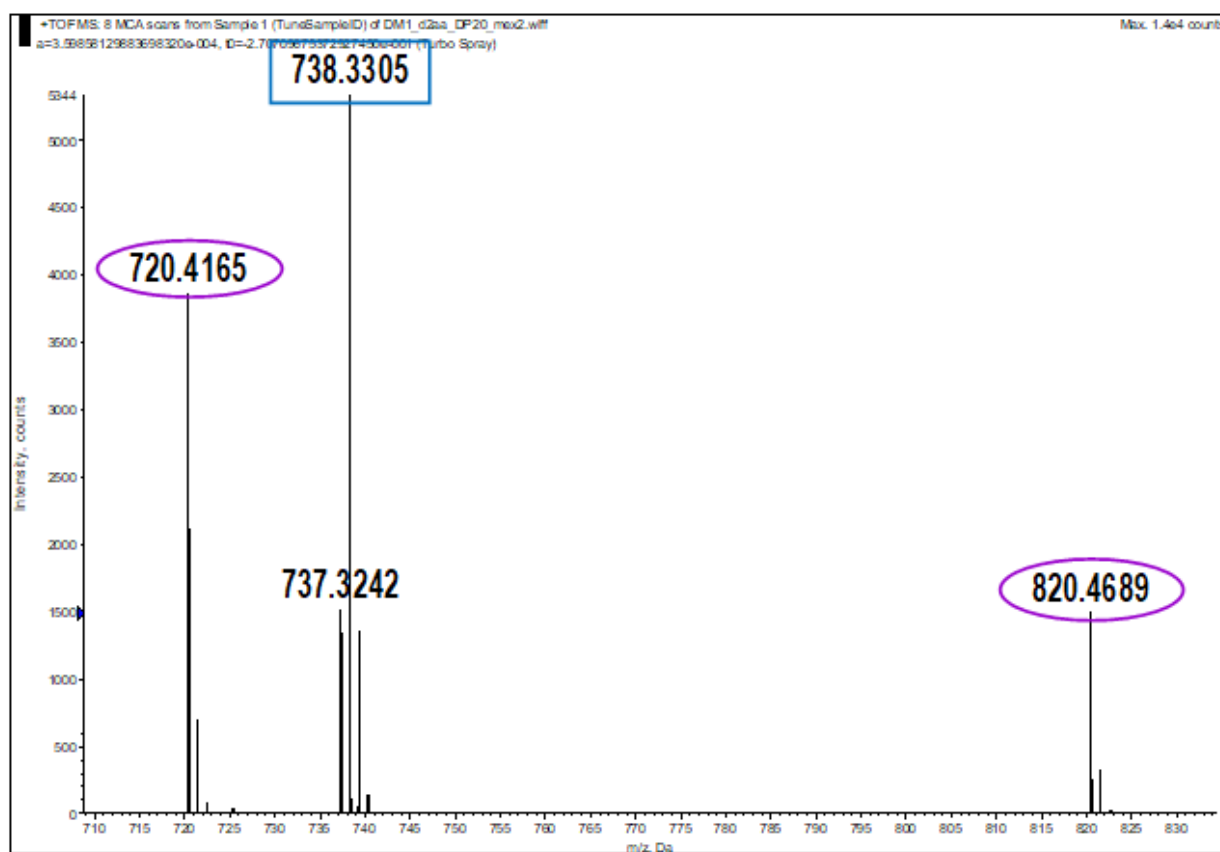
DM1

This report was created by ACD/NMR Processor Academic Edition. For more information go to www.acdlabs.com/nmrproc/

4/17/2019 7:55:32 PM

Acquisition Time (sec)	2.1758	Comments	MD6 carbon dans DMSO	Date	21 Oct 2015 08:06:56
Date Stamp	21 Oct 2015 08:06:56	File Name	E:\downloads\MD6 carbon\MD6 carbon1.tif	Origin	spect
Frequency (MHz)	62.90	Nucleus	¹³ C	Number of Transients	12124
Original Points Count	32768	Owner	root	Points Count	32768
Receiver Gain	6502.00	SW (cycles) (Hz)	15060.24	Pulse Sequence	zgpg30
Spectrum Type	STANDARD	Sweep Width (Hz)	15059.78	Solvent	DMSO-d6
		Temperature (degree C)	24.160	Spectrum Offset (Hz)	6261.5596



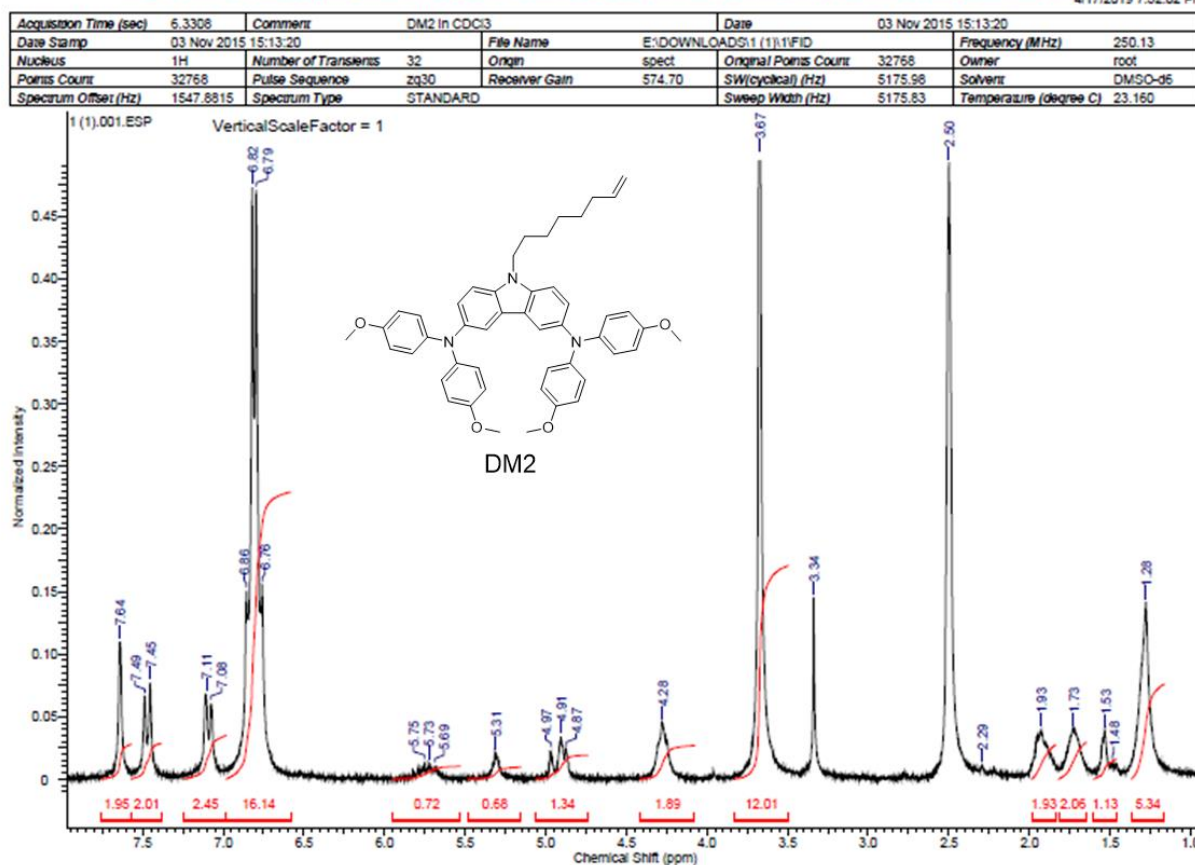


Spectre de masse haute résolution en mode electrospray positif de l'échantillon DM1 (exp. n° 2). L'ion ciblé est détecté à m/z 738.3305 et les pics retenus pour l'étalonnage interne sont observés respectivement à m/z 720.4165 et m/z 820.4689.

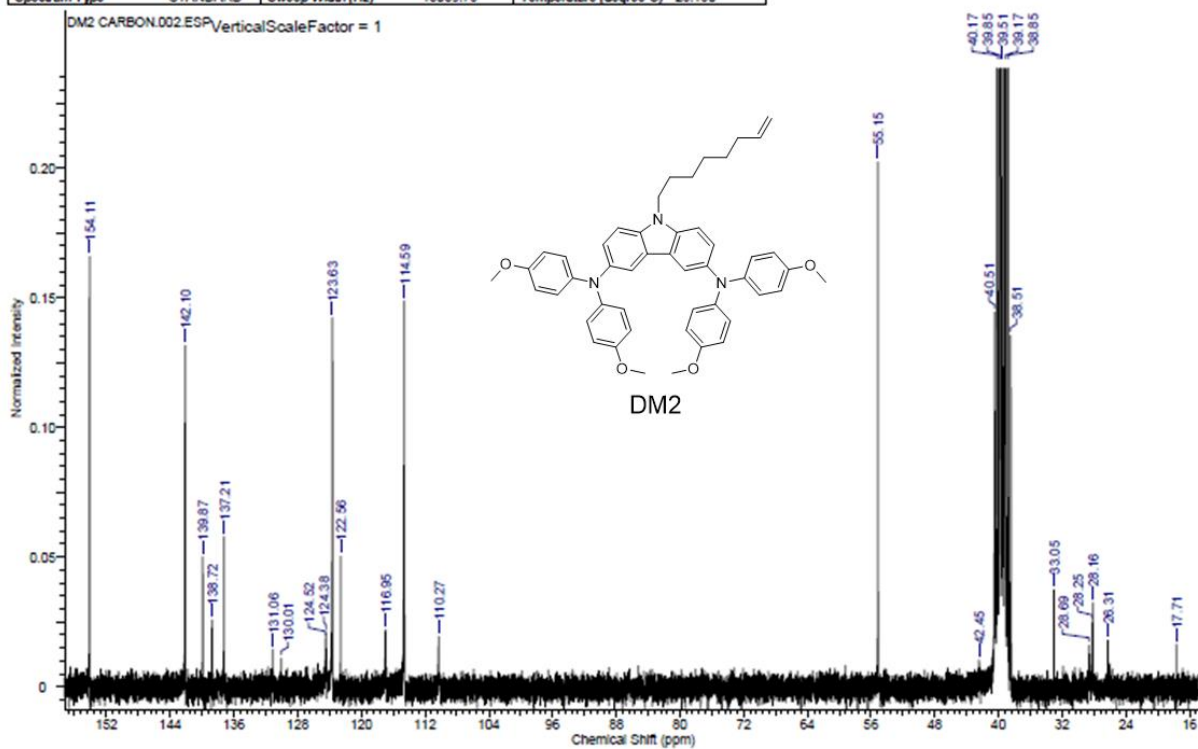
DM2

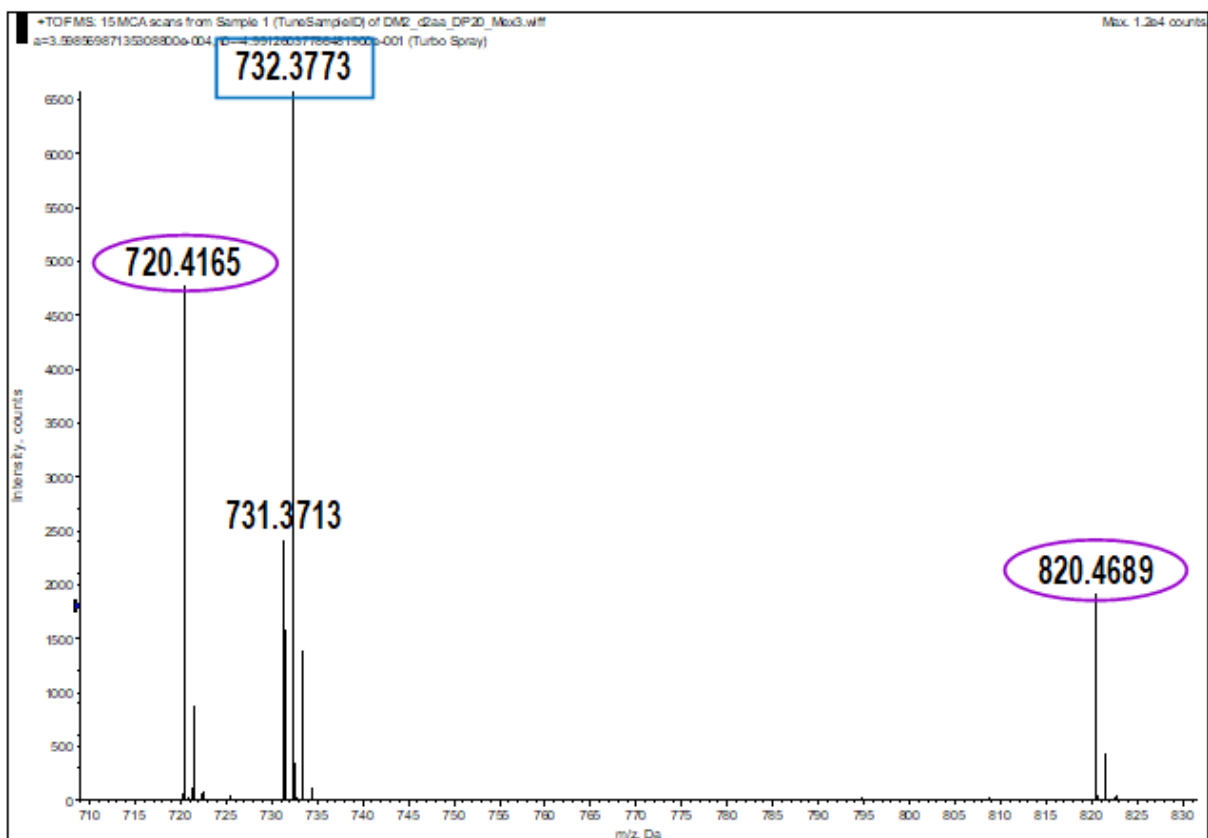
This report was created by ACD/NMR Processor Academic Edition. For more information go to www.acdlabs.com/nmrproc/

4/17/2019 7:52:02 PM



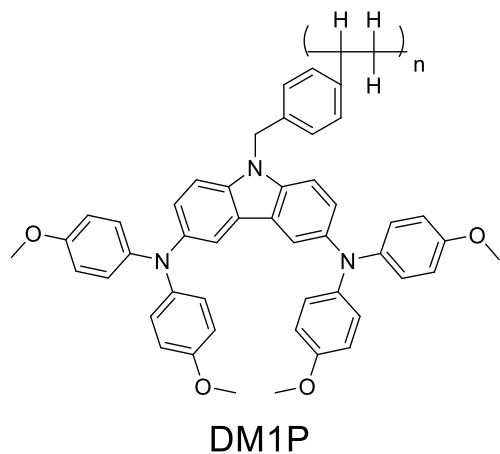
Acquisition Time (sec)	2.1758	Comment	DM2 carbon dans DMSO	Date	04 Nov 2015 07:15:28
Date Stamp	04 Nov 2015 07:15:28			File Name	E:\DOCTORADO\SYNTHESIS\DM2\DM2 CARBON 2\FID
Frequency (Mhz)	62.90	Nucleus	¹³ C	Number of Transients	12024
Original Points Count	32768	Owner	root	Origin	spect
Receiver Gain	6502.00	SW (cycles) (Hz)	15060.24	Pulse Sequence	zgpg30
Spectrum Type	STANDARD	Sweep Width (Hz)	15059.78	Spectrum Offset (Hz)	6261.1001
		Temperature (degree C)	23.160		



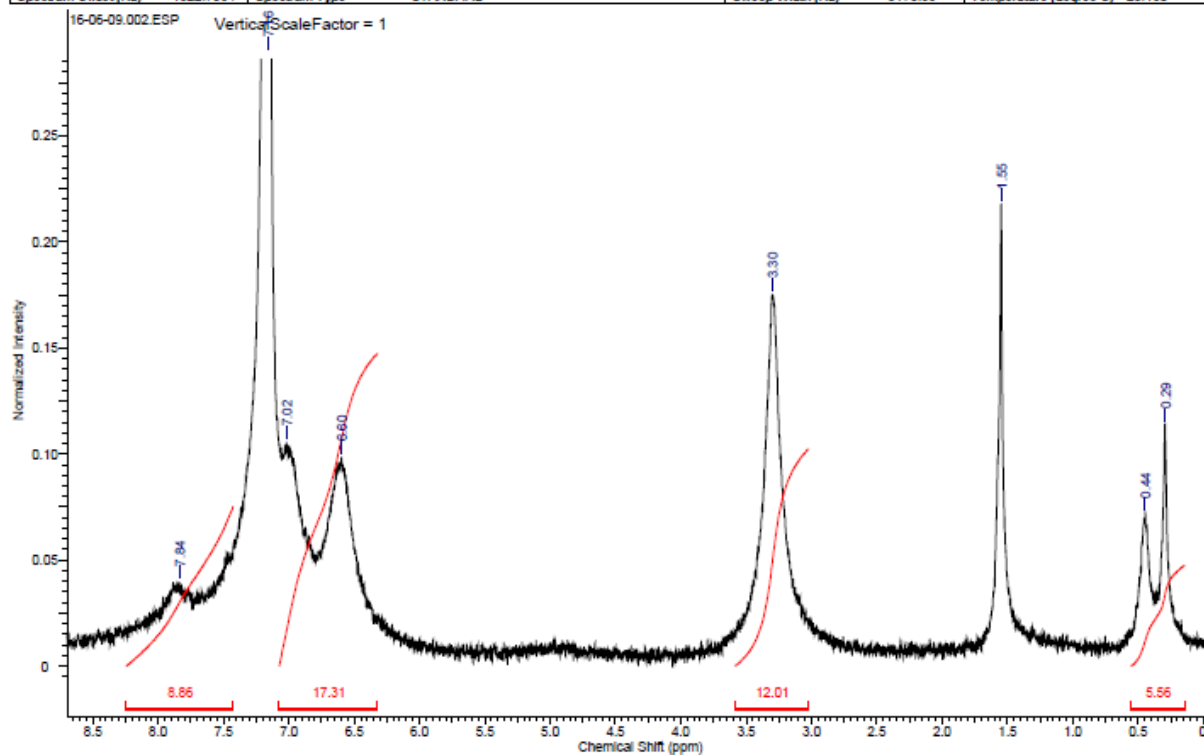


Spectre de masse haute résolution en mode electrospray positif de l'échantillon DM2 (exp. n° 3). L'ion ciblé est détecté à m/z 732.3773 et les pics retenus pour l'étalonnage interne sont observés respectivement à m/z 720.4165 et m/z 820.4689.

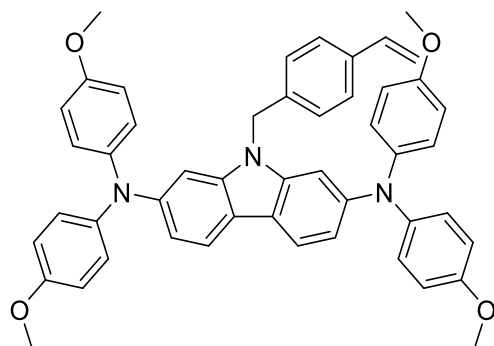
DM1P



Acquisition Time (sec)	6.3308	Comment	DM1 after polymerization	Date	09 Jun 2016 16:26:08
Date Stamp	09 Jun 2016 16:26:08	File Name	G:\16-06-09\2\FID	Frequency (MHz)	250.13
Nucleus	¹ H	Number of Transients	16	Origin	spect
Points Count	32768	Pulse Sequence	zg30	Receiver Gain	912.30
Spectrum Offset (Hz)	1522.7964	Spectrum Type	STANDARD	SW (cyclical) (Hz)	5175.98
				Solvent	BENZENE-d ₆
				Sweep Width (Hz)	5175.83
				Temperature (degree C)	25.160

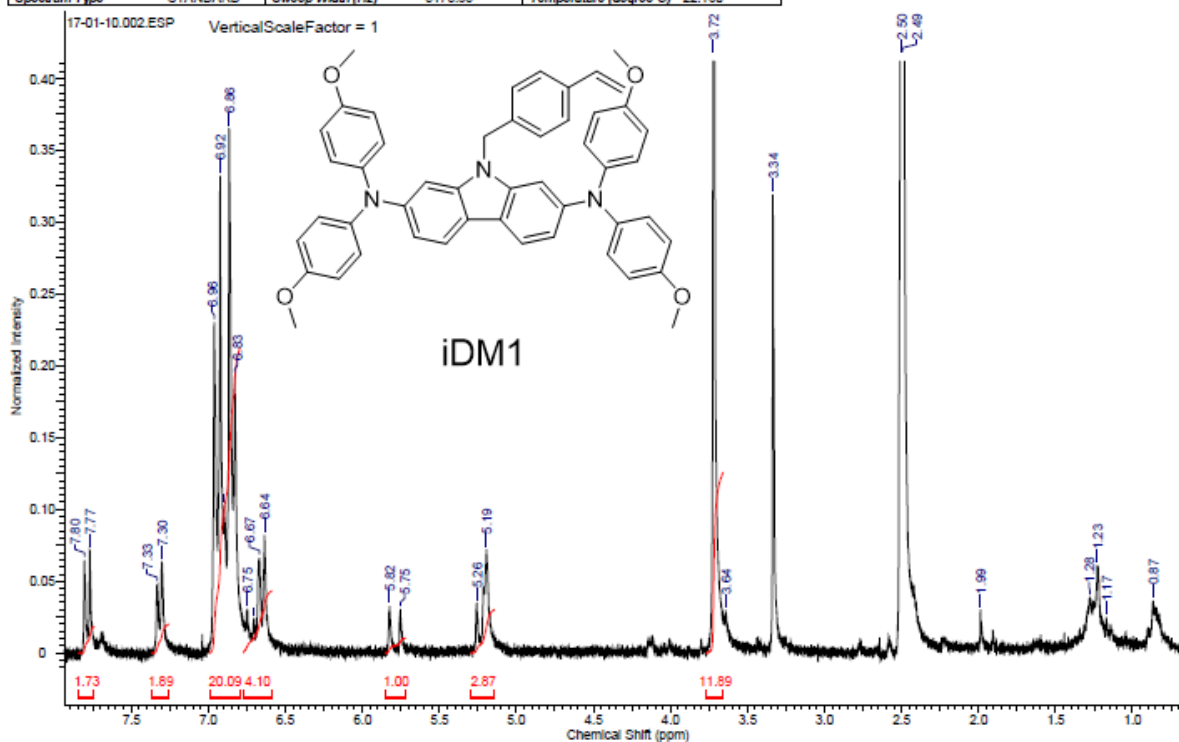


iDM1

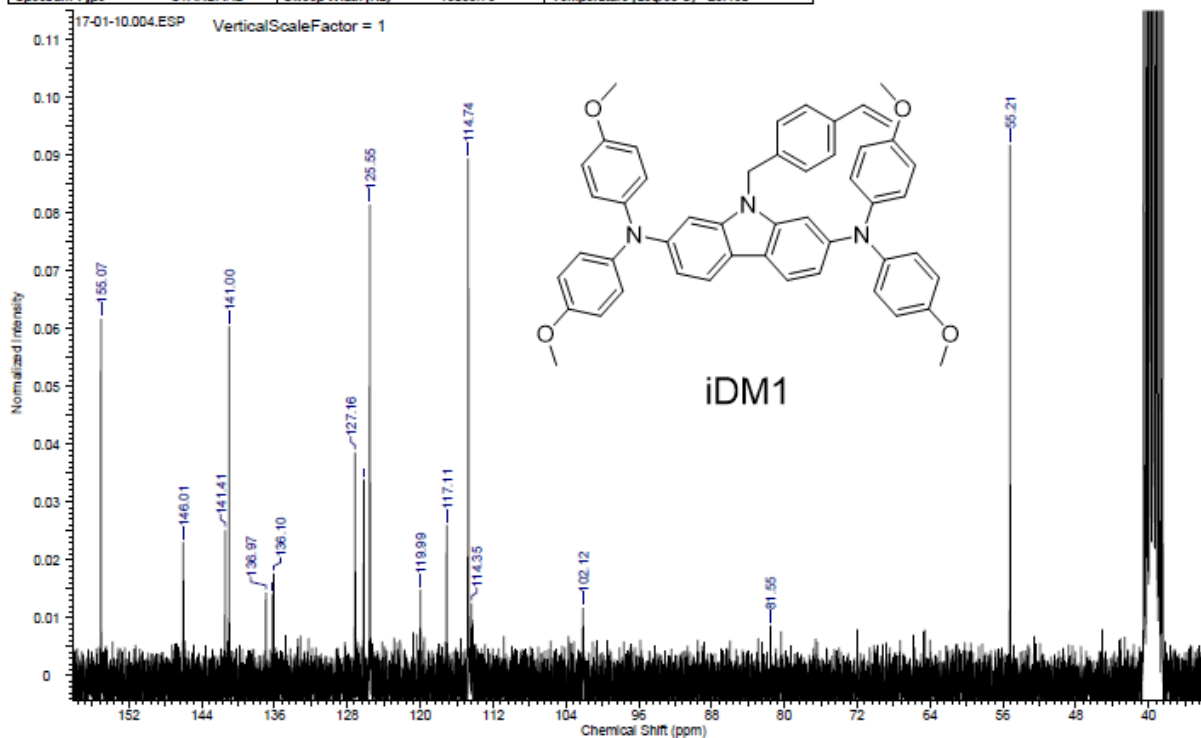


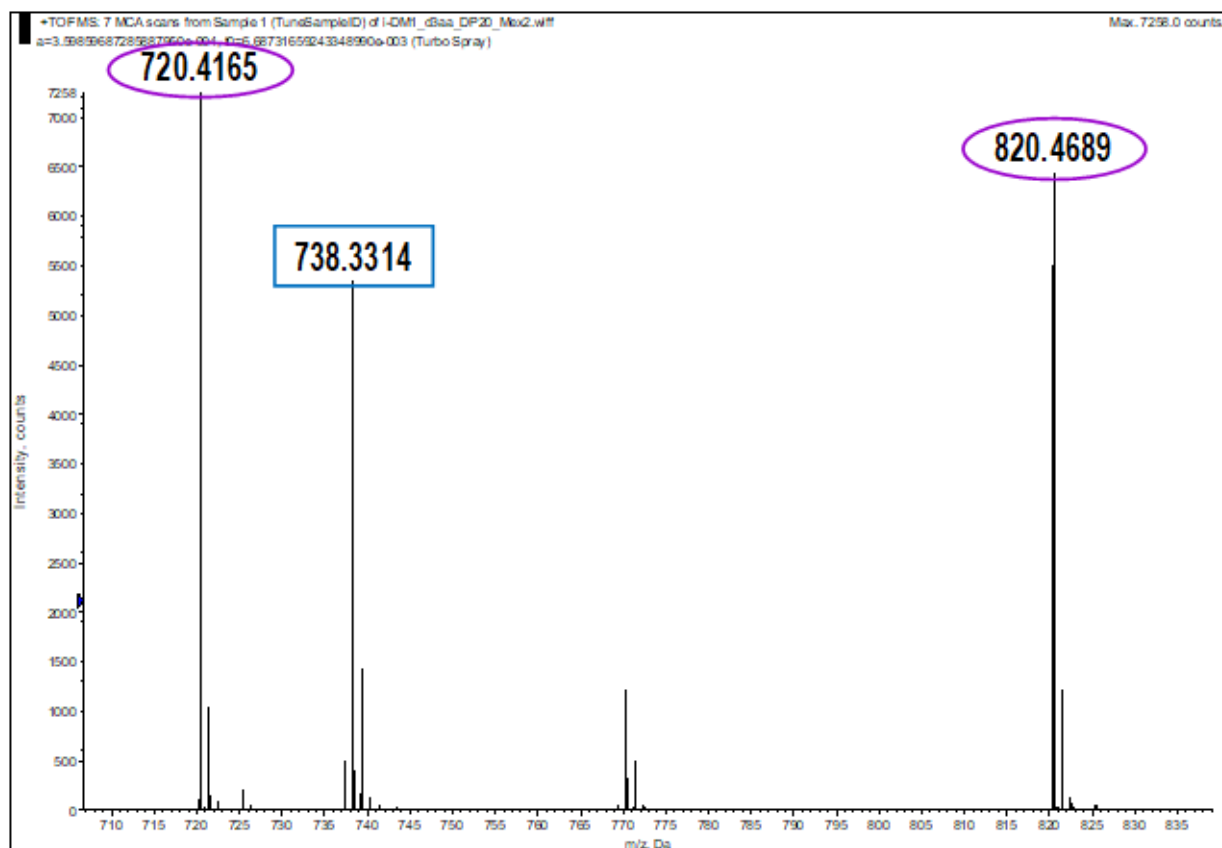
iDM1

Acquisition Time (sec)	6.3306	Comment	DM3 after column in DMSO	Date	10 Jan 2017 15:21:52
Date Stamp	10 Jan 2017 15:21:52			File Name	C:\USERS\ILANOVA\DOCUMENTS\DOCTORADO\SYNTHESIS\NMR\17-01-10\2\FID
Frequency (MHz)	250.13	Nucleus	¹ H	Number of Transients	16
Original Points Count	32768	Owner	root	Points Count	32768
Receiver Gain	912.30	SW(cyclical) (Hz)	5175.98	Solvent	DMSO-d5
Spectrum Type	STANDARD	Sweep Width (Hz)	5175.83	Temperature (degree C)	22.160
				Pulse Sequence	zg30
				Spectrum Offset (Hz)	1547.2496



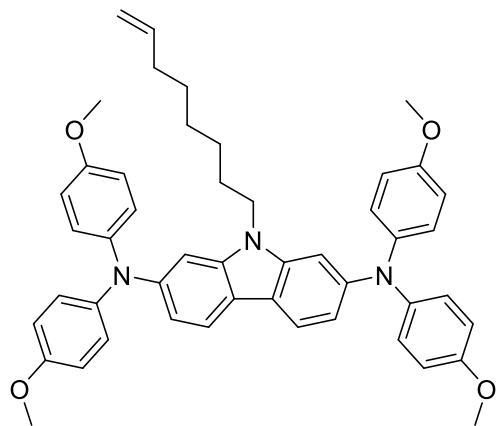
Acquisition Time (sec)	2.1758	Comment	DM3 after column in DMSO carbon	Date	11 Jan 2017 07:45:20
Date Stamp	11 Jan 2017 07:45:20	File Name	C:\USERS\LANOVA\DOCUMENTS\DOCTORADO\SYNTHESIS\NMR\17-01-10\4\FI D		
Frequency (MHz)	62.90	Nucleus	13C	Number of Transients	12024
Original Points Count	32768	Owner	root	Points Count	32768
Receiver Gain	6502.00	SW (cycles) (Hz)	15060.24	Solvent	DMSO-d6
Spectrum Type	STANDARD	Sweep Width (Hz)	15059.78	Temperature (degree C)	23.160
				Pulse Sequence	zgpg30
				Spectrum Offset (Hz)	6262.0190





Spectre de masse haute résolution en mode electrospray positif de l'échantillon i-DM1 (exp. n° 2). L'ion ciblé est détecté à m/z 738.3314 et les pics retenus pour l'étalonnage interne sont observés respectivement à m/z 720.4165 et m/z 820.4689.

iDM2

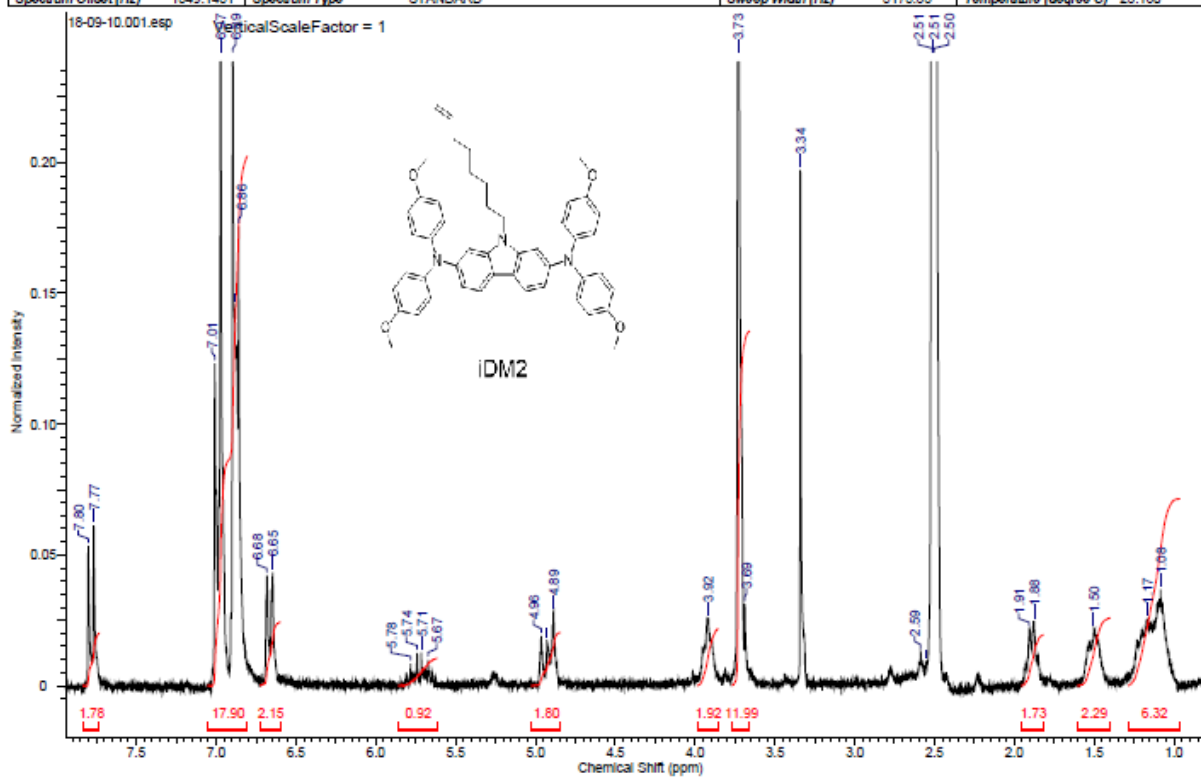


IDM2

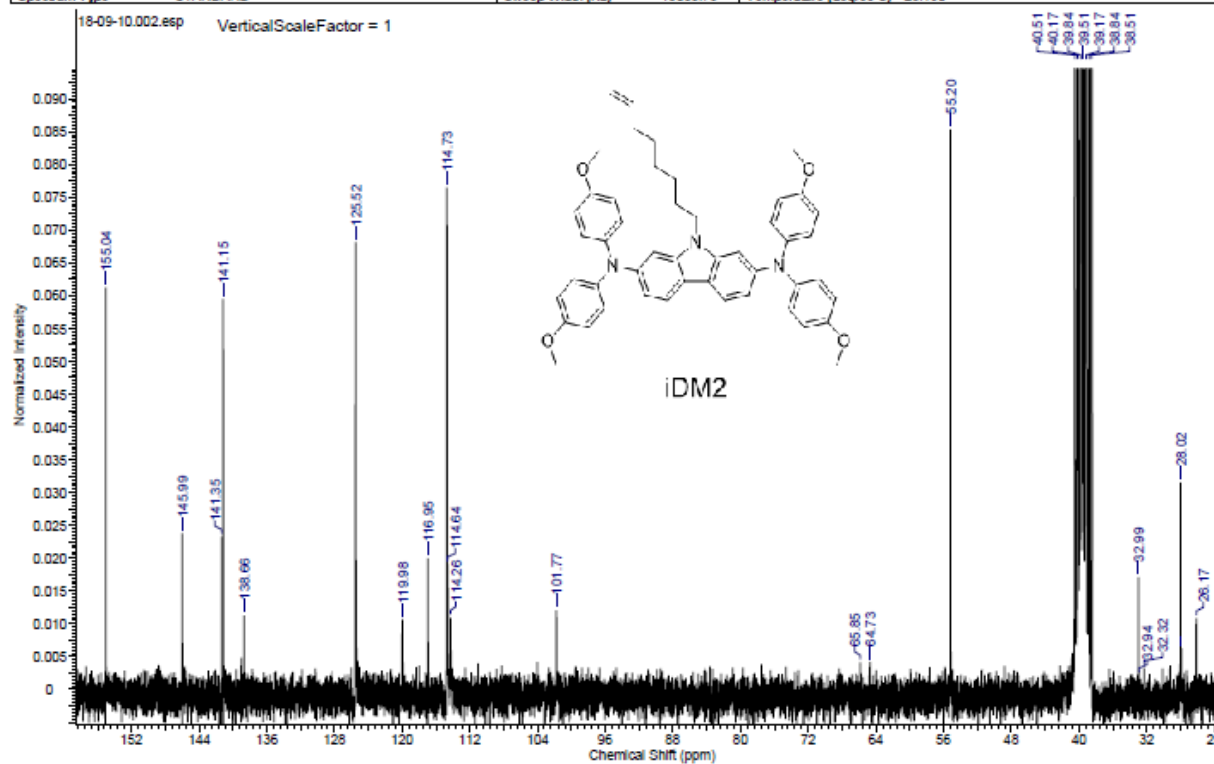
This report was created by ACD/NMR Processor Academic Edition. For more information go to www.acdlabs.com/nmrproc/

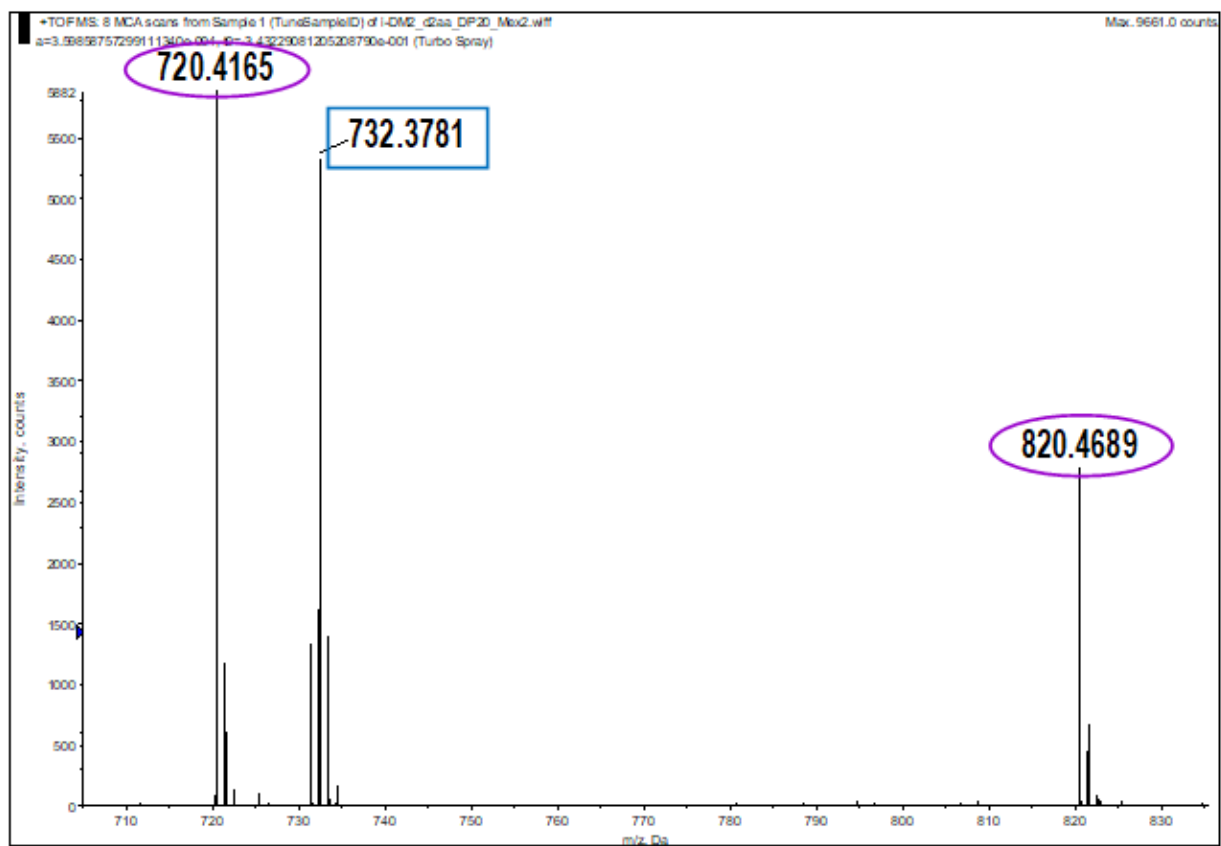
9/12/2018 10:33:11 AM

Acquisition Time (sec)	6.3308	Comment	IDM2 proton in DMSO	Date	10 Sep 2018 16:15:28
Date Stamp	10 Sep 2018 16:15:28	File Name	H:\18-09-10\1\FID	Frequency (MHz)	250.13
Nucleus	¹ H	Number of Transients	15	Original Points Count	32768
Points Count	32768	Pulse Sequence	zg30	Receiver Gain	912.30
Spectrum Offset (Hz)	1549.1451	Spectrum Type	STANDARD	SW (cyclical) (Hz)	5175.98
				Sweep Width (Hz)	5175.83
				Temperature (degree C)	23.160



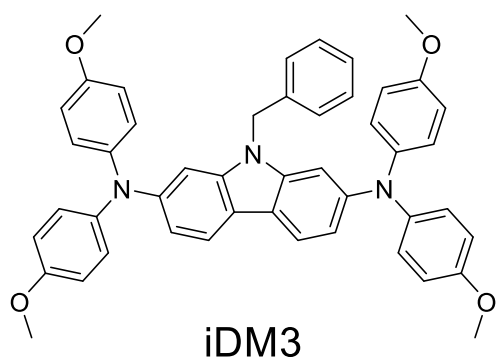
Acquisition Time (sec)	2.1758	Comment	i-DM2 carbon in DMSO	Date	11 Sep 2018 07:41:20
Date Stamp	11 Sep 2018 07:41:20	File Name	H:\18-09-10\2\FID		
Frequency (MHz)	62.90	Nucleus	¹³ C	Number of Transients	13024
Original Points Count	32768	Owner	root	Points Count	32768
Receiver Gain	6502.00	SW (cycles)	15060.24	Solvent	DMSO-d6
Spectrum Type	STANDARD	Sweep Width (Hz)	15059.78	Temperature (degree C)	23.160



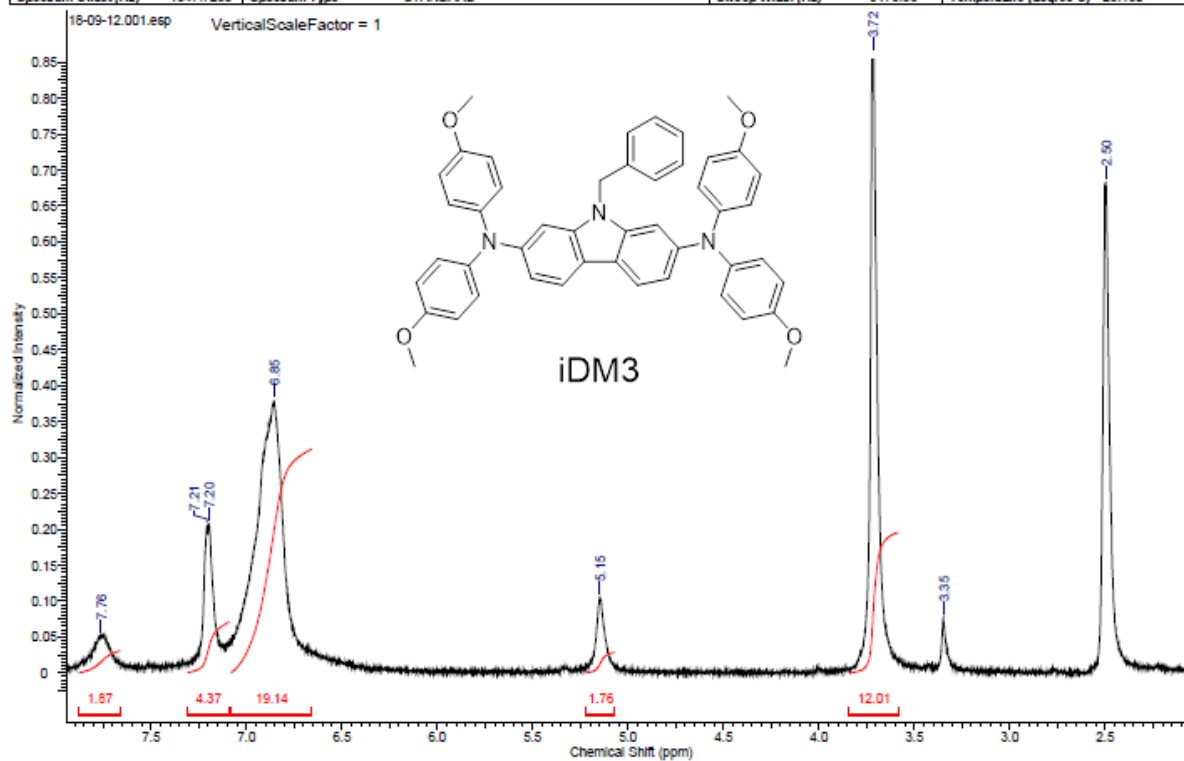


Spectre de masse haute résolution en mode electrospray positif de l'échantillon i-DM2 (exp. n° 2). L'ion ciblé est détecté à m/z 732.3781 et les pics retenus pour l'étalonnage interne sont observés respectivement à m/z 720.4165 et m/z 820.4689.

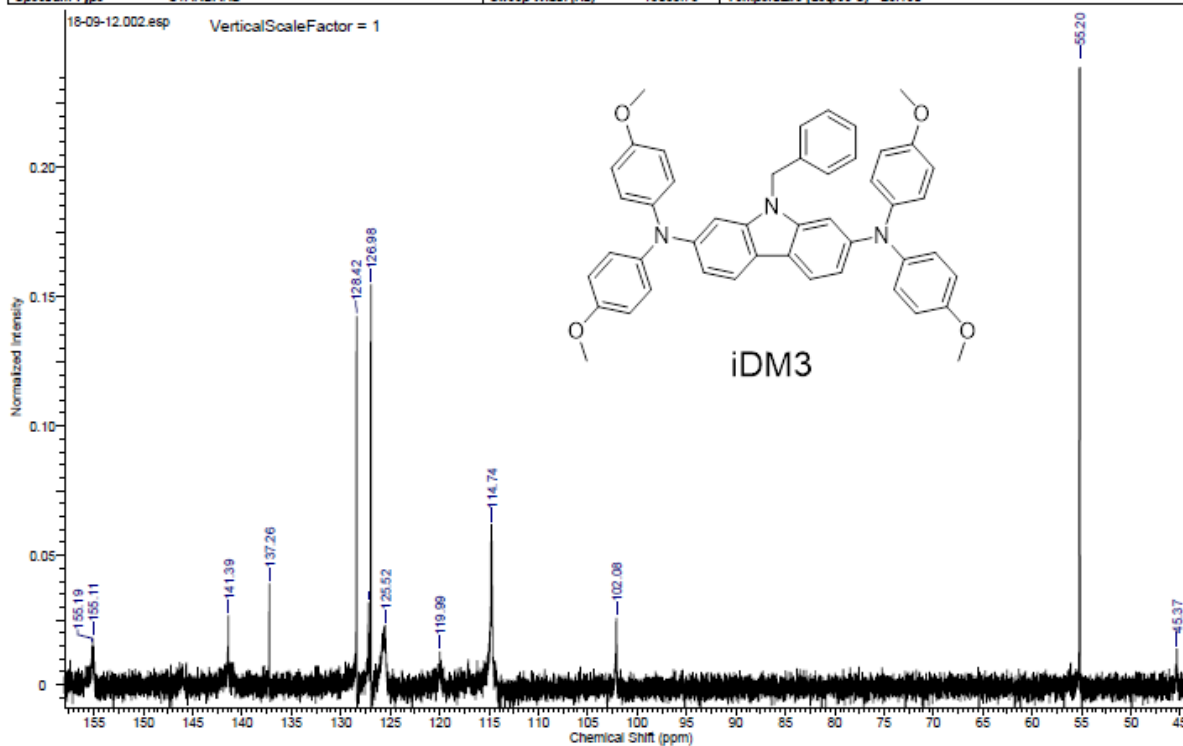
iDM3

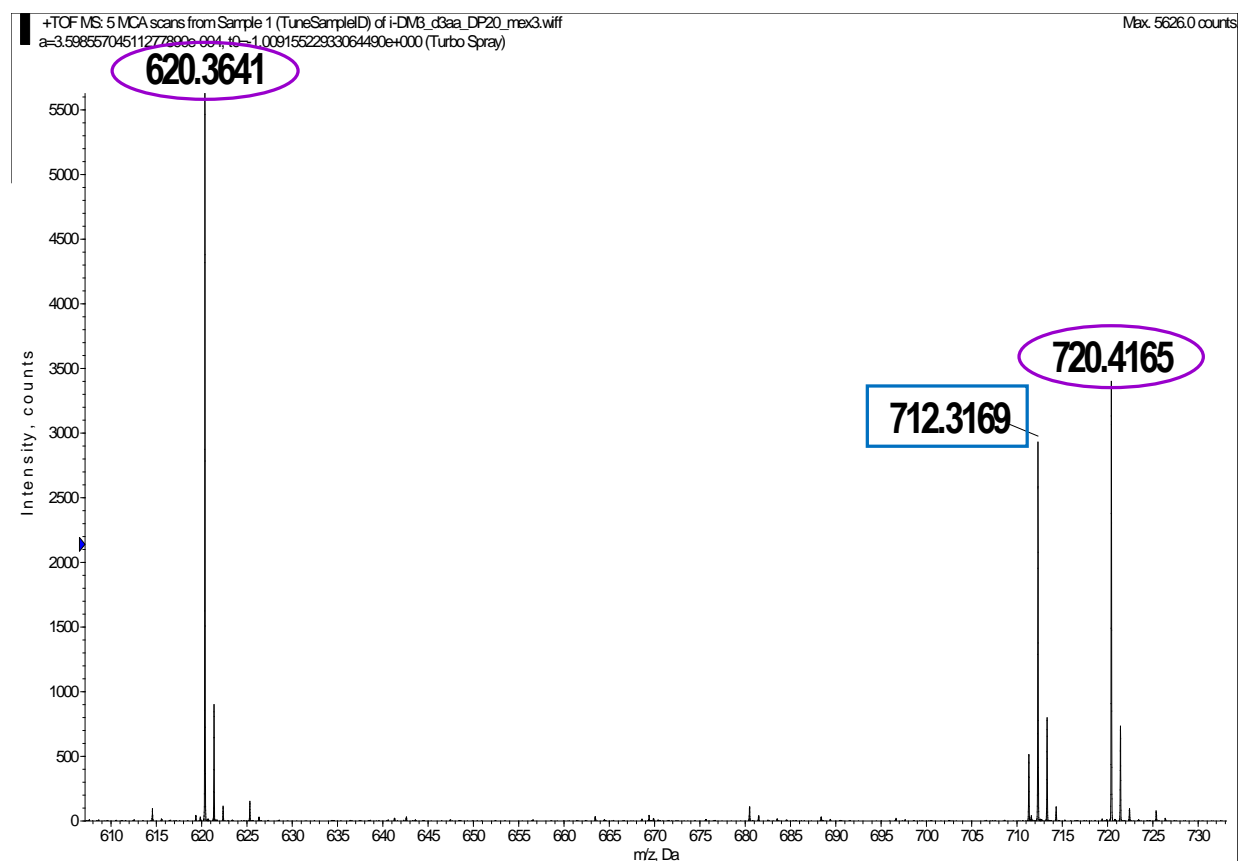


Acquisition Time (sec)	6.3308	Comment	i-DM3 proton in DMSO		Date	12 Sep 2018 16:32:32	
Date Stamp	12 Sep 2018 16:32:32		File Name	H:\18-09-12\1\FID	Frequency (MHz)	250.13	
Nucleus	¹ H	Number of Transients	16	Origin	spect	Original Points Count	32768
Points Count	32768	Pulse Sequence	zg30	Receiver Gain	912.30	SW (cycles) (Hz)	5175.98
Spectrum Offset (Hz)	1547.7235	Spectrum Type	STANDARD		Sweep Width (Hz)	5175.83	Solvent
							DMSO-d5
							Temperature (degree C)
							23.160



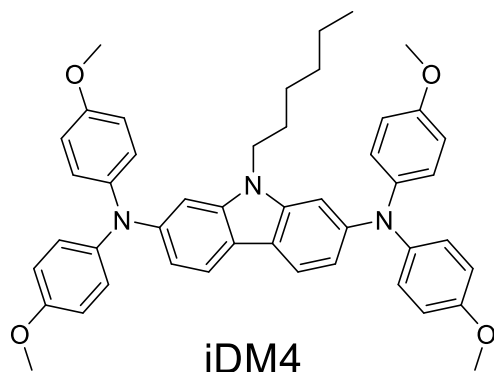
Acquisition Time (sec)	2.1758	Comment	i-DM3 carbon in DMSO		Date	13 Sep 2018 08:00:32	
Date Stamp	13 Sep 2018 08:00:32		File Name	H:\18-09-12\2\FID			
Frequency (MHz)	62.90	Nucleus	¹³ C	Number of Transients	13024	Origin	spect
Original Points Count	32768	Owner	root	Points Count	32768	Pulse Sequence	zgpg30
Receiver Gain	6502.00	SW(cyclical) (Hz)	15060.24	Solvent	DMSO-d6	Spectrum Offset (Hz)	6261.5596
Spectrum Type	STANDARD		Sweep Width (Hz)	15059.78	Temperature (degree C)	23.160	



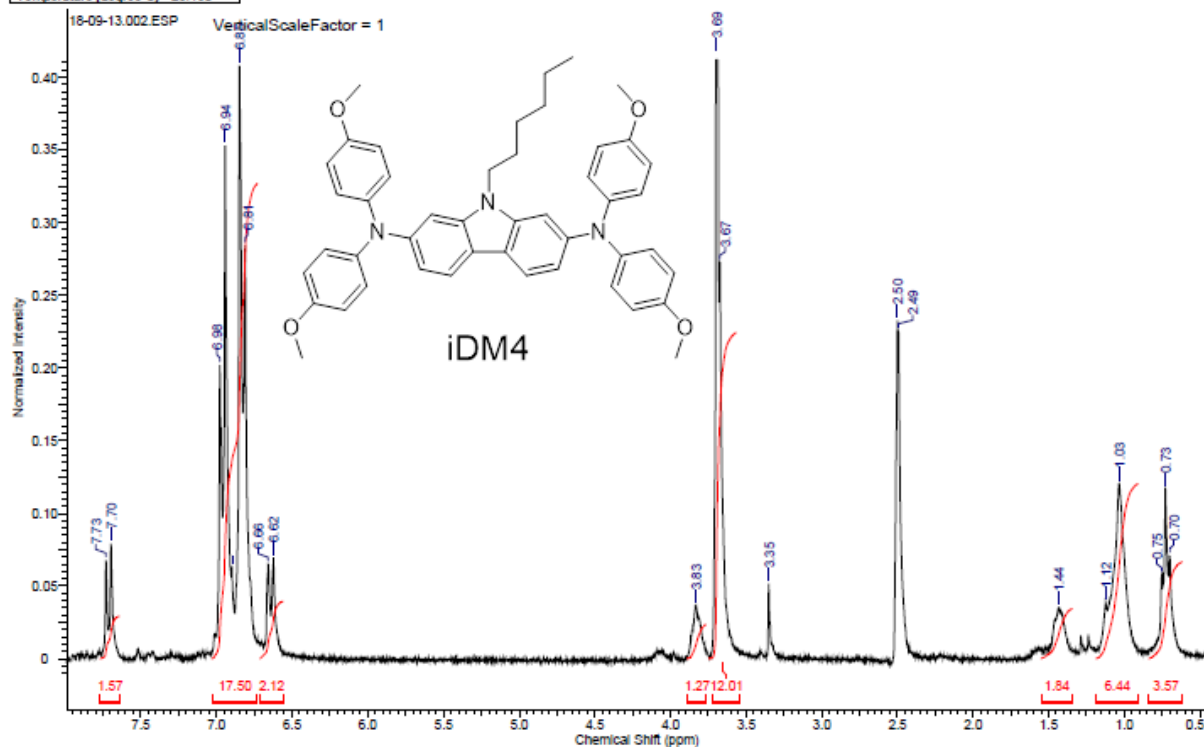


Spectre de masse haute résolution en mode electrospray positif de l'échantillon i-DM3 (exp. n° 3). L'ion ciblé est détecté à m/z 712.3169 et les pics retenus pour l'étalonnage interne sont observés respectivement à m/z 620.3641 et m/z 720.4165.

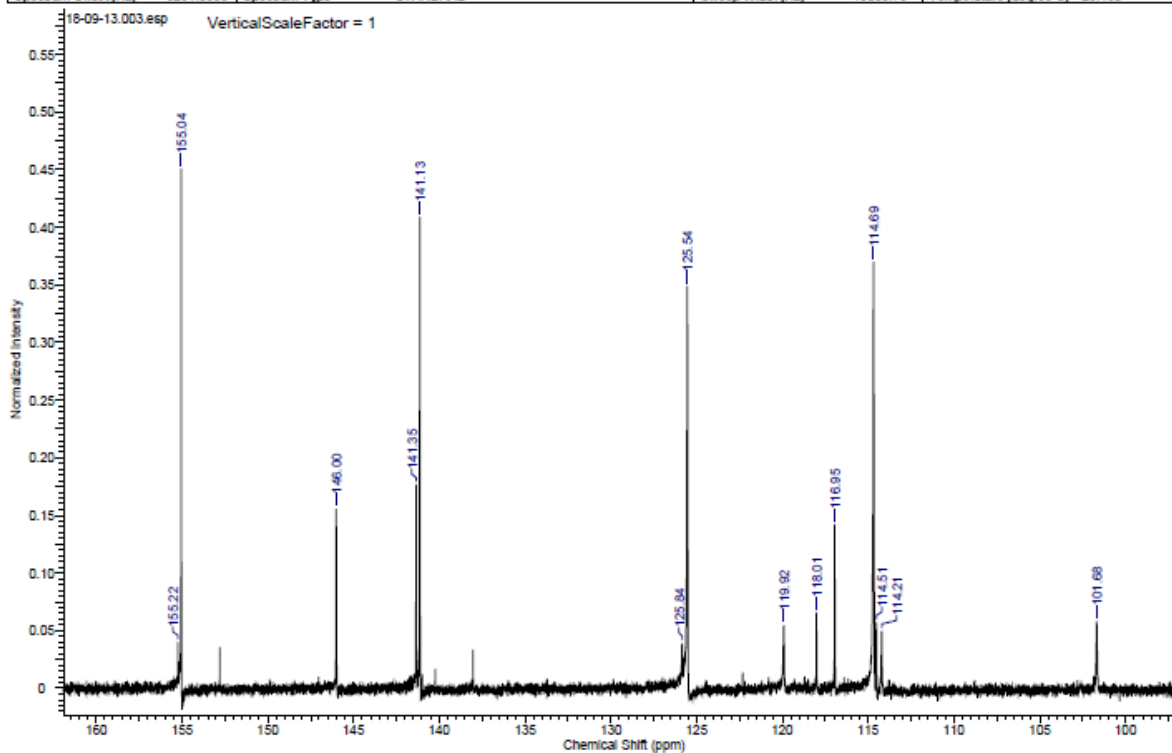
iDM4



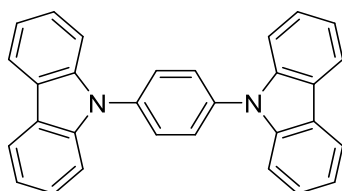
Acquisition Time (sec)	6.3306	Comment	IDM4	Date	13 Sep 2018 18:51:12		
Date Stamp	13 Sep 2018 18:51:12			File Name	H:\18-09-13\FID	Frequency (MHz)	250.13
Nucleus	¹ H	Number of Transients	16	Origin	spect	Original Points Count	32768
Points Count	32768	Pulse Sequence	zg30	Receiver Gain	912.30	SW (cycles) (Hz)	5175.98
Spectrum Offset (Hz)	1547.4077			Spectrum Type	STANDARD	Solvent	DMSO-d6
Temperature (degree C)	23.160					Sweep Width (Hz)	5175.83



Acquisition Time (sec)	2.1758	Comment	IDM4	Date	14 Sep 2018 09:04:32	
Date Stamp	14 Sep 2018 09:04:32			File Name	H:\18-09-13\FID	Frequency (MHz)
Nucleus	13C	Number of Transients	12024	Origin	spect	Original Points Count
Points Count	32768	Pulse Sequence	zgpg30	Receiver Gain	6502.00	32768
Spectrum Offset (Hz)	6261.5596	Spectrum Type	STANDARD	SW (cycles) (Hz)	15060.24	Solvent
				Sweep Width (Hz)	15059.78	DMF-d5
						Temperature (degree C)
						23.160

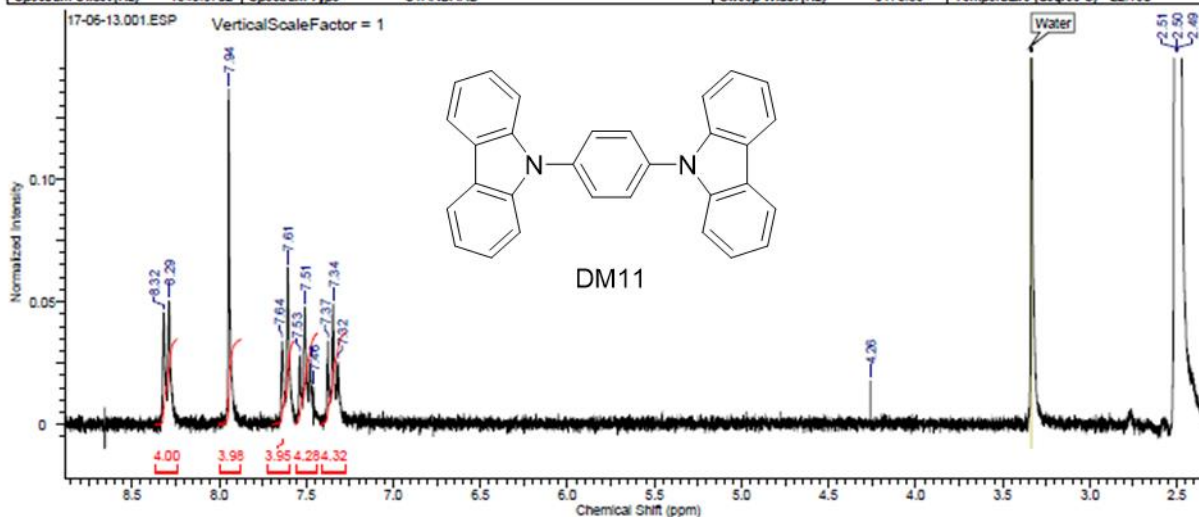


DM11

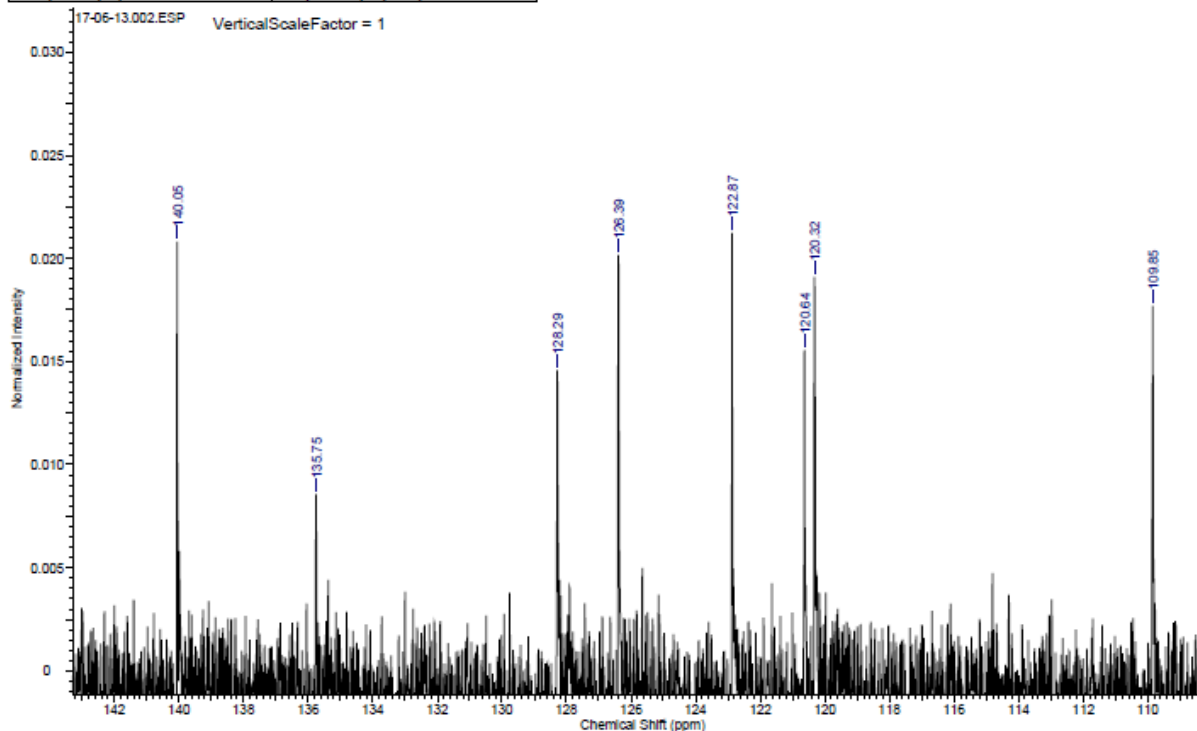


DM11

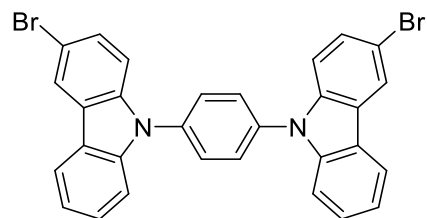
Acquisition Time (sec)	6.3308	Comment	CzPhCz in DMSO	Date	13 Jun 2017 17:57:52
Date Stamp	13 Jun 2017 17:57:52	File Name	G:\17-06-13\1\FID	Frequency (MHz)	250.13
Nucleus	¹ H	Number of Transients	16	Origin	spect
Points Count	32768	Pulse Sequence	zg30	Original Points Count	32768
Spectrum Offset (Hz)	1545.6702	Receiver Gain	912.30	SW(cyclical) (Hz)	5175.98
		Spectrum Type	STANDARD	Solvent	DMSO-d6
				Sweep Width (Hz)	5175.83
				Temperature (degree C)	22.160



Acquisition Time (sec)	2.1758	Comment	CzPhCz in DMSO	Date	14 Jun 2017 08:11:12
Date Stamp	14 Jun 2017 08:11:12	File Name	C:\USERS\RENOV\DOCUMENTS\MEGA\DOCTORADO\SYNTHESIS\NMR\17-06-13\2\FID	Frequency (MHz)	62.90
Nucleus	¹³ C	Number of Transients	12024	Origin	spect
Owner	root	Points Count	32768	Pulse Sequence	zgpg30
SW(cyclical) (Hz)	15050.24	Solvent	DMSO-d6	Receiver Gain	6502.00
Spectrum Offset (Hz)	15059.78	Temperature (degree C)	23.160	Spectrum Type	STANDARD



DM12

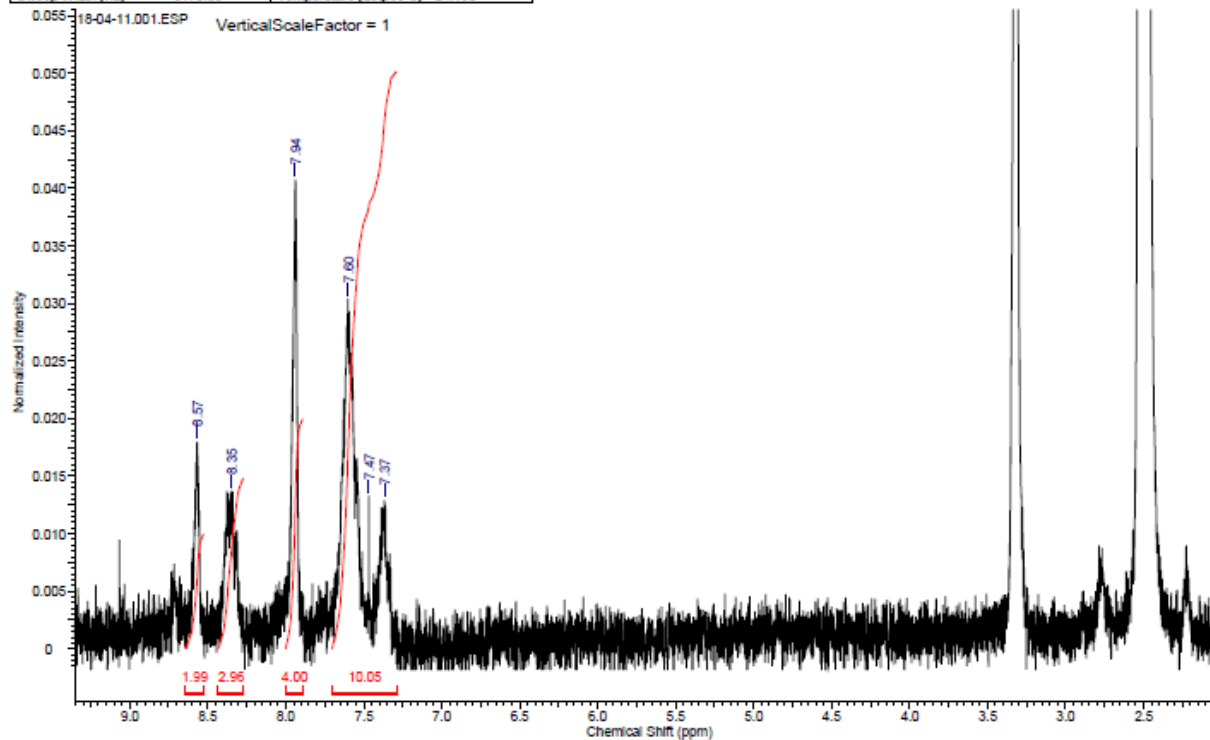


DM12

This report was created by ACD/NMR Processor Academic Edition. For more information go to www.acdlabs.com/nmrproc/

4/30/2019 4:03:52 PM

Acquisition Time (sec)	6.3308	Comment	BrCzPhCzBr	Date	11 Apr 2018 16:26:08
Date Stamp	11 Apr 2018 16:26:08				
File Name	C:\USERS\RENOV\DOCUMENTS\MEGA\DOCTORADO\SYNTHESIS\NMR\18-04-11\1\FID	Frequency (MHz)	250.13		
Nucleus	¹ H	Number of Transients	16	Origin	spect
Owner	root	Points Count	32768	Original Points Count	32768
SW (cycles) (Hz)	5175.98	Pulse Sequence	zg30	Receiver Gain	912.30
Solvent	DMSO-d ₆	Spectrum Offset (Hz)	1546.6217	Spectrum Type	STANDARD
Sweep Width (Hz)	5175.83	Temperature (degree C)	24.160		

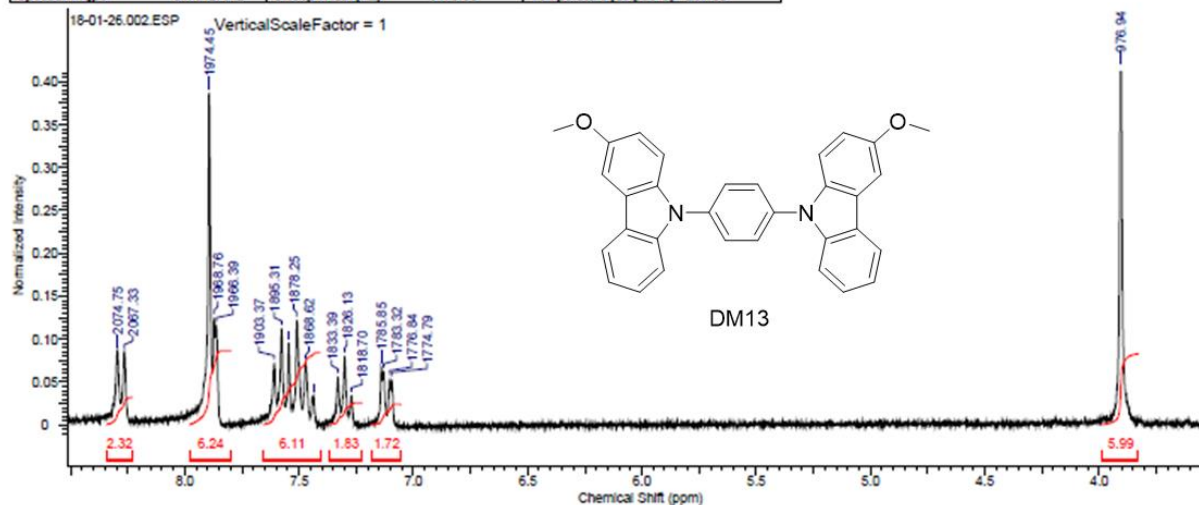


DM13

This report was created by ACD/NMR Processor Academic Edition. For more information go to www.acdlabs.com/nmrproc/

9/21/2018 1:34:54 PM

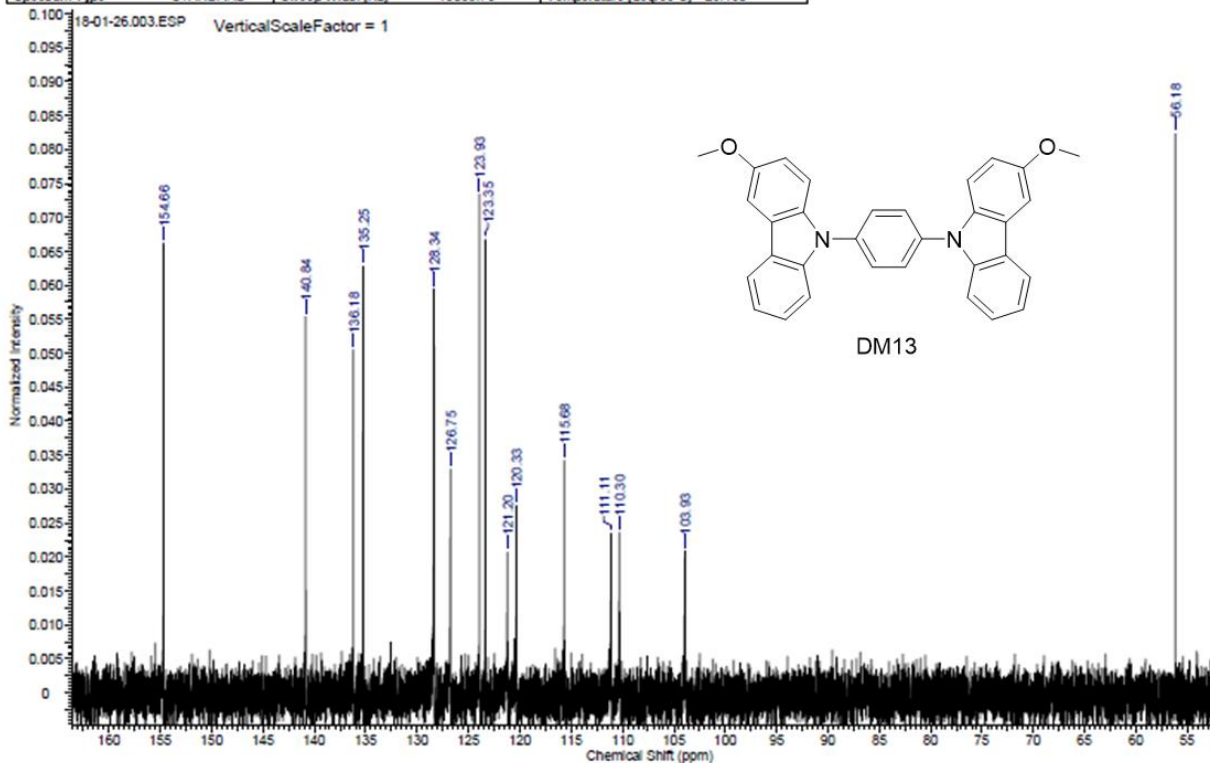
Acquisition Time (sec)	6.3308	Comment	-OC ₂ PhC ₂ O-	Date	26 Jan 2018 17:38:24
Date Stamp	26 Jan 2018 17:38:24			File Name	C:\USERS\LANOVA\DOCUMENTS\DOCTORADO\SYNTHESIS\NMR\18-01-26\2\FID
Frequency (MHz)	250.13	Nucleus	¹ H	Number of Transients	16
Original Points Count	32768	Owner	root	Points Count	32768
Receiver Gain	912.30	SW (cycles)	5175.98	Solvent	DMSO-d ₆
Spectrum Type	STANDARD	Sweep Width (Hz)	5175.83	Temperature (degree C)	23.160
				Pulse Sequence	zg30
				Spectrum Offset (Hz)	1547.5657

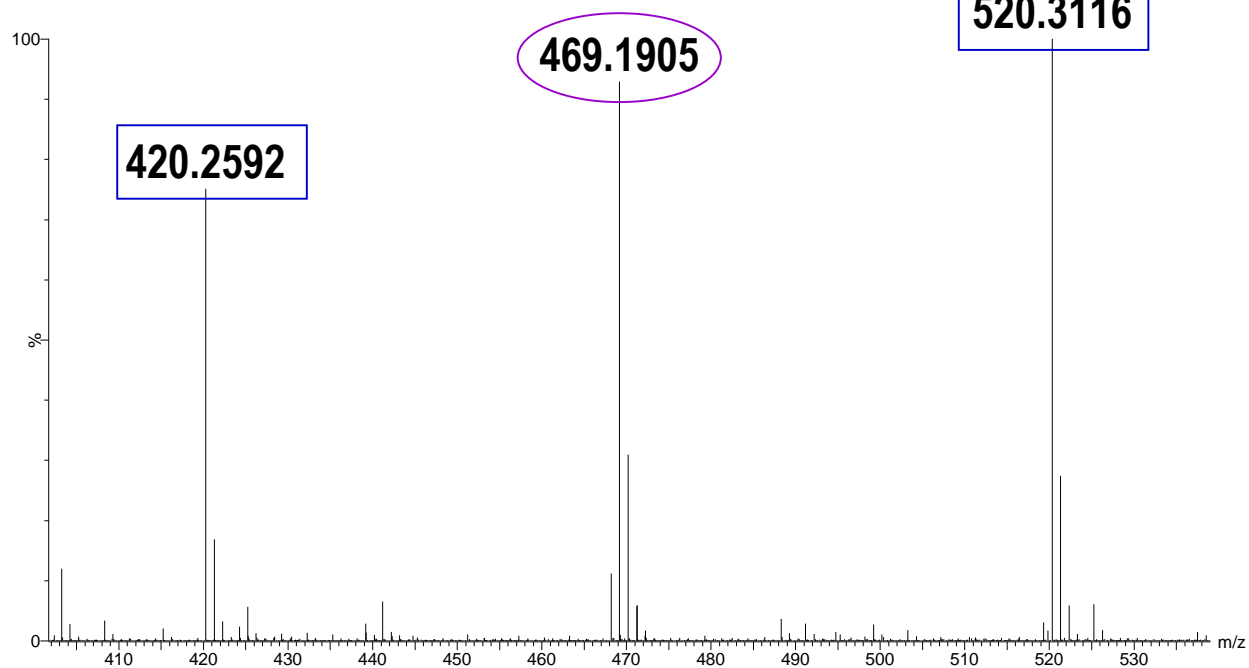


This report was created by ACD/NMR Processor Academic Edition. For more information go to www.acdlabs.com/nmrproc/

9/21/2018 1:40:23 PM

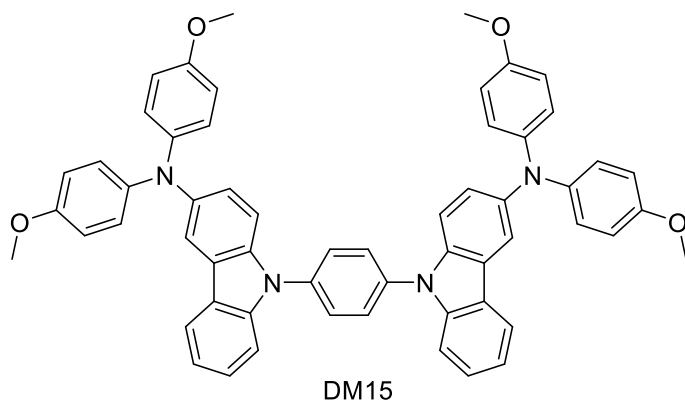
Acquisition Time (sec)	2.1758	Comment	-OC ₂ PhC ₂ O- carbon	Date	27 Jan 2018 11:27:12
Date Stamp	27 Jan 2018 11:27:12			File Name	C:\USERS\LANOVA\DOCUMENTS\DOCTORADO\SYNTHESIS\NMR\18-01-26\3\FID
Frequency (MHz)	62.90	Nucleus	¹³ C	Number of Transients	15054
Original Points Count	32768	Owner	root	Points Count	32768
Receiver Gain	6502.00	SW (cycles)	15060.24	Solvent	DMSO-d ₆
Spectrum Type	STANDARD	Sweep Width (Hz)	15059.78	Temperature (degree C)	23.160
				Pulse Sequence	zgpg30
				Spectrum Offset (Hz)	6289.0498



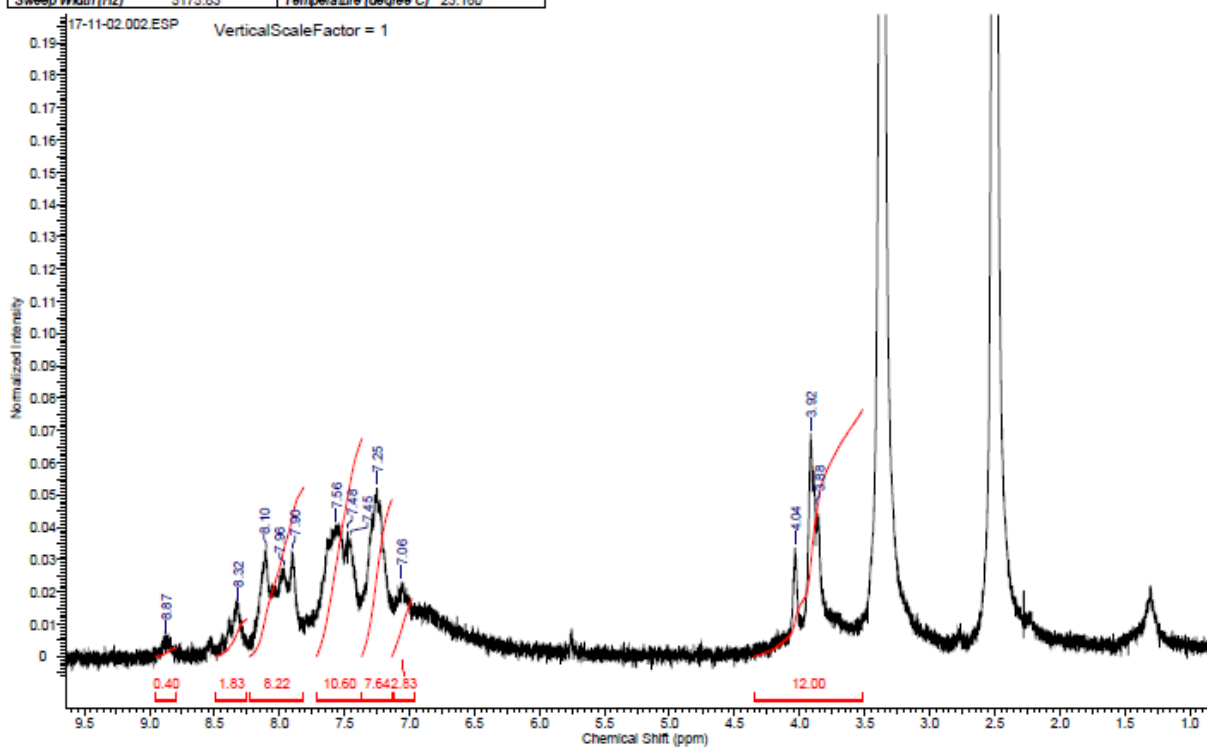


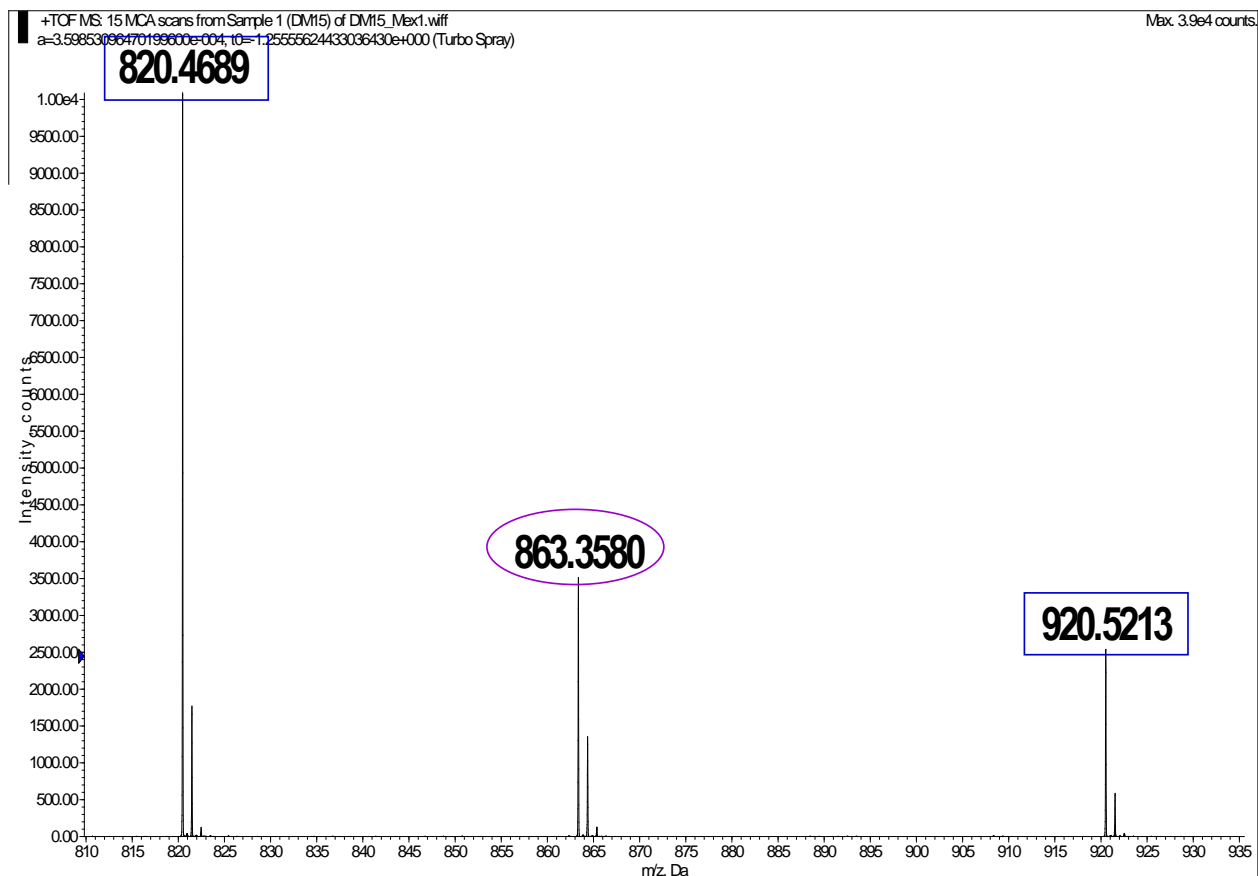
Spectre de masse haute résolution en mode electrospray positif de l'échantillon DM13 (exp. n° 1). L'ion ciblé est détecté à m/z 469.1905 et les pics retenus pour l'étalonnage interne sont observés respectivement à m/z 420.2592 et m/z 520.3116.

DM15



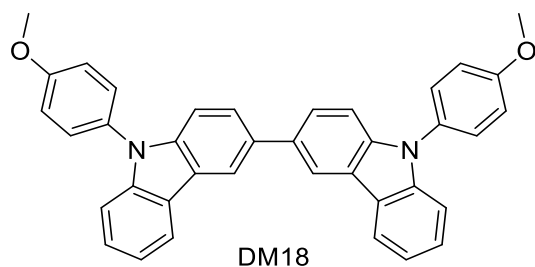
Acquisition Time (sec)	6.3308	Comment	DPACzPhCzDPA	Date	02 Nov 2017 15:58:08
Date Stamp	02 Nov 2017 15:58:08				
File Name	C:\USERS\RENOV\DOCUMENTS\MEGA\DOCTORADO\SYNTHESIS\NMR\17-11-02\2\FID			Frequency (MHz)	250.13
Nucleus	¹ H	Number of Transients	16	Origin	spect
Owner	root	Points Count	32768	Pulse Sequence	zg30
SW (cyclical) (Hz)	5175.98	Solvent	DMSO-d ₆	Receiver Gain	912.30
Sweep Width (Hz)	5175.83	Temperature (degree C)	23.160	Spectrum Offset (Hz)	1549.1451
				Spectrum Type	STANDARD



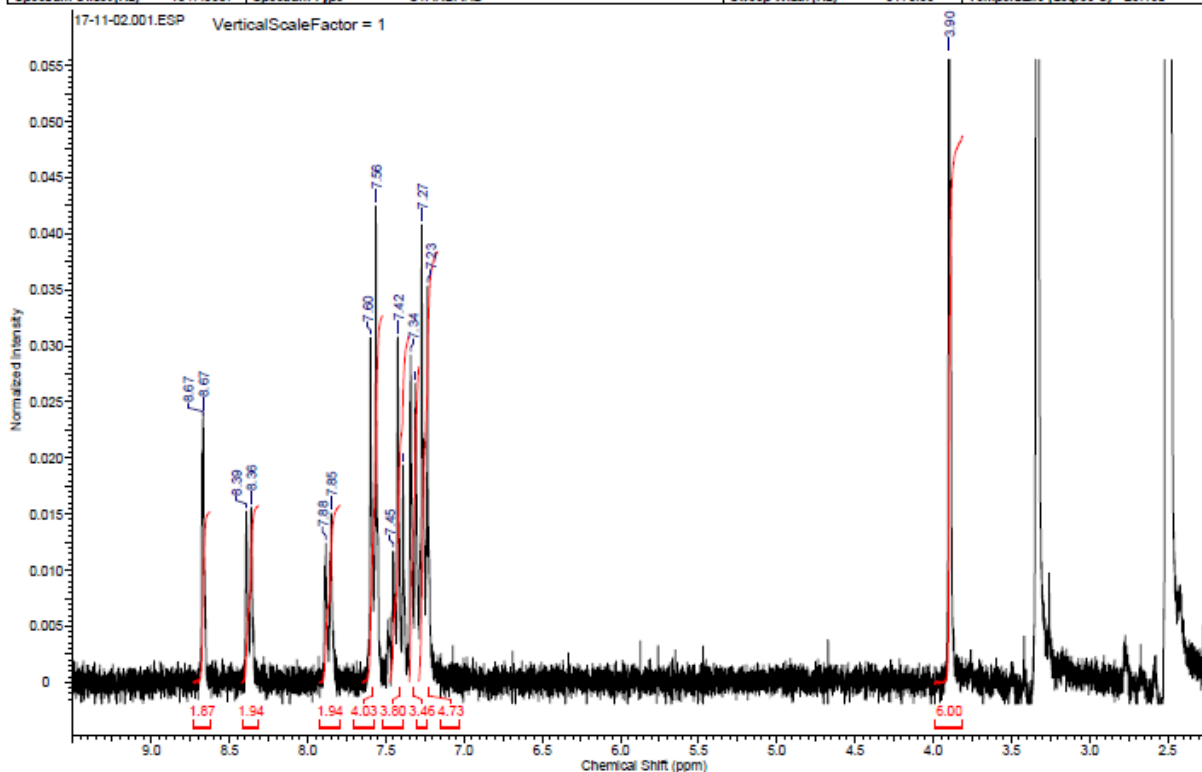


Spectre de masse haute résolution en mode electrospray positif de l'échantillon DM15 (exp. n° 1). L'ion ciblé est détecté à m/z 863.3580 et les pics retenus pour l'étalonnage interne sont observés respectivement à m/z 820.4689 et m/z 920.5213.

DM18

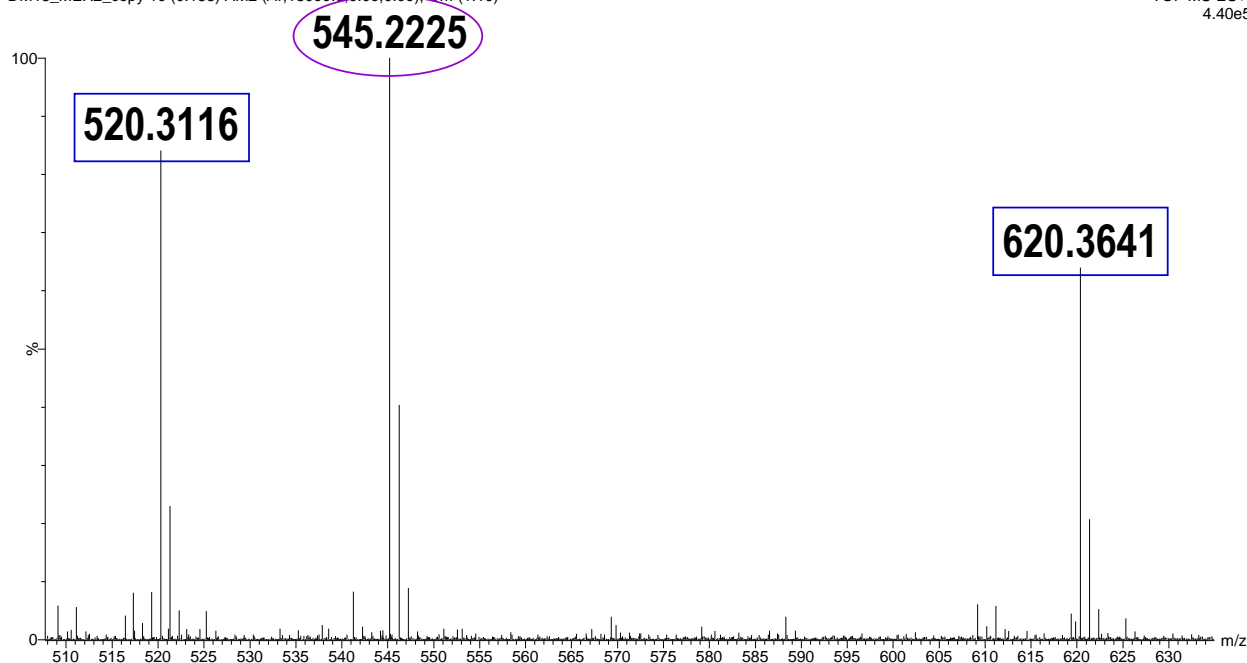


Acquisition Time (sec)	6.3308	Comment	CzPhOMe FeCl3 reaction	Date	02 Nov 2017 09:46:56
Date Stamp	02 Nov 2017 09:46:56	File Name	F:\17-11-02\1\FID	Frequency (MHz)	250.13
Nucleus	¹ H	Number of Transients	16	Origin	spect
Pulse Count	32768	Pulse Sequence	zg30	Original Points Count	32768
Spectrum Offset (Hz)	1547.5657	Receiver Gain	912.30	SW (cycles) (Hz)	5175.98
		Spectrum Type	STANDARD	Solvent	DMSO-d6
				Sweep Width (Hz)	5175.83
				Temperature (degree C)	23.160



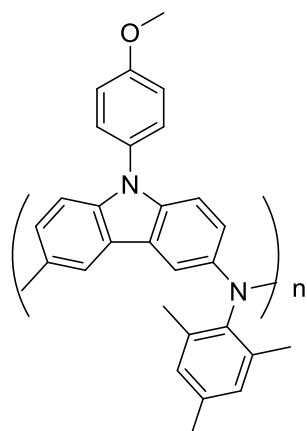
DM18_MEX2_copy 10 (0.188) AM2 (Ar,18000,0,0.00-0.00); Cm (1:10)

TOF MS ES+
4.40e5



Spectre de masse haute résolution en mode electrospray positif de l'échantillon DM18 (exp. n° 2). L'ion ciblé est détecté à m/z 545.2225 et les pics retenus pour l'étalonnage interne sont observés respectivement à m/z 520.3116 et m/z 620.3641

PCz1

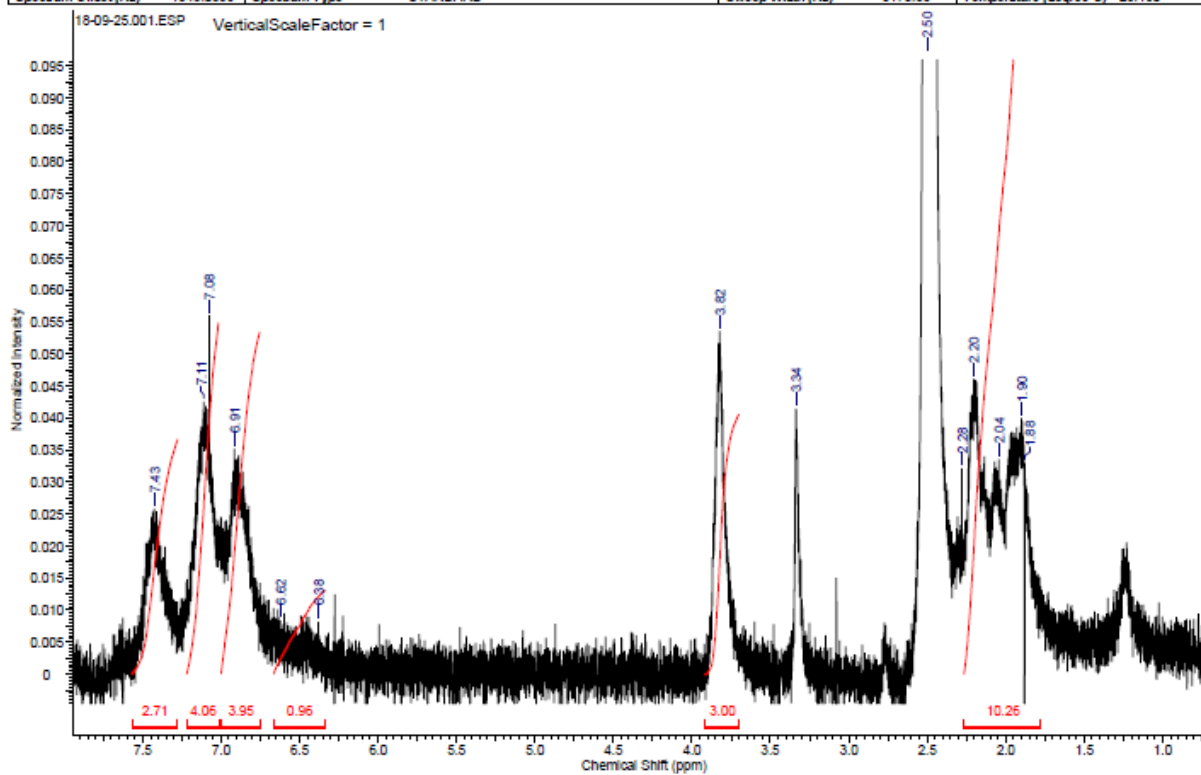


PCz1

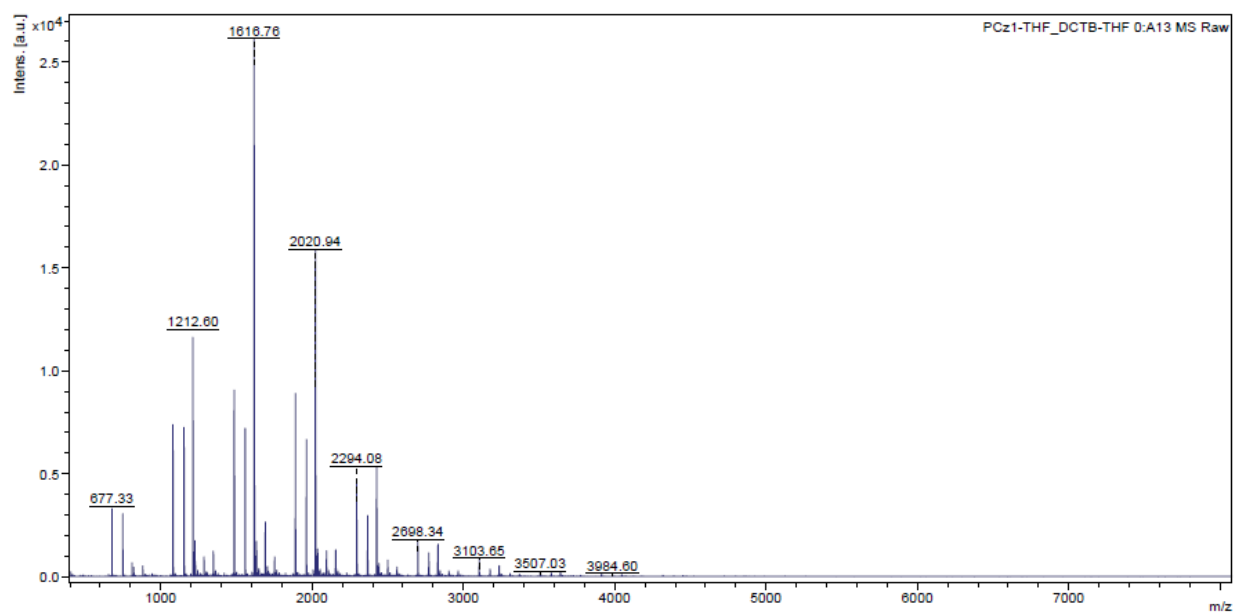
This report was created by ACD/NMR Processor Academic Edition. For more information go to www.acdlabs.com/nmrproc/

4/17/2019 8:22:14 PM

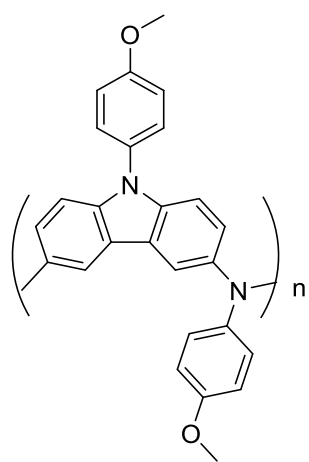
Acquisition Time (sec)	6.3308	Comment	PCz1 -OPhCz AnMe3	Date	25 Sep 2018 17:06:40
Date Stamp	25 Sep 2018 17:06:40	File Name	H:\18-09-25\1\FID	Frequency (MHz)	250.13
Nucleus	¹ H	Number of Transients	16	Origin	spect
Points Count	32768	Pulse Sequence	zg30	Original Points Count	32768
Spectrum Offset (Hz)	1548.0396	Receiver Gain	912.30	SW (cyclical) (Hz)	5175.98
		Spectrum Type	STANDARD	Solvent	DMSO-d6
				Sweep Width (Hz)	5175.83
				Temperature (degree C)	23.160



MALDI-TOF

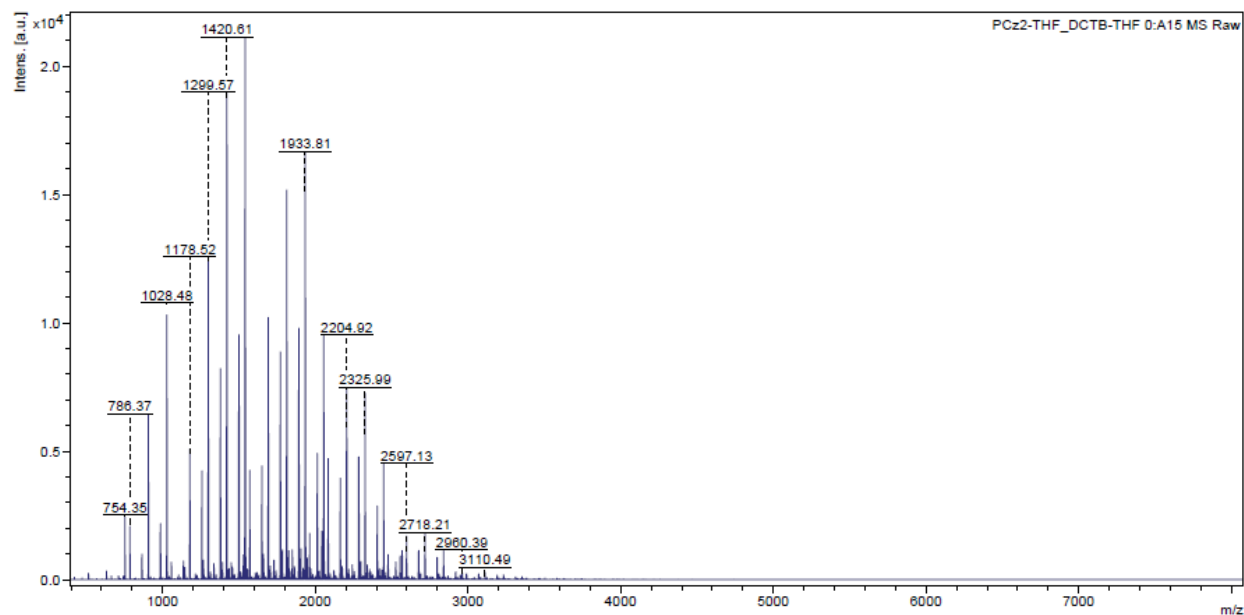
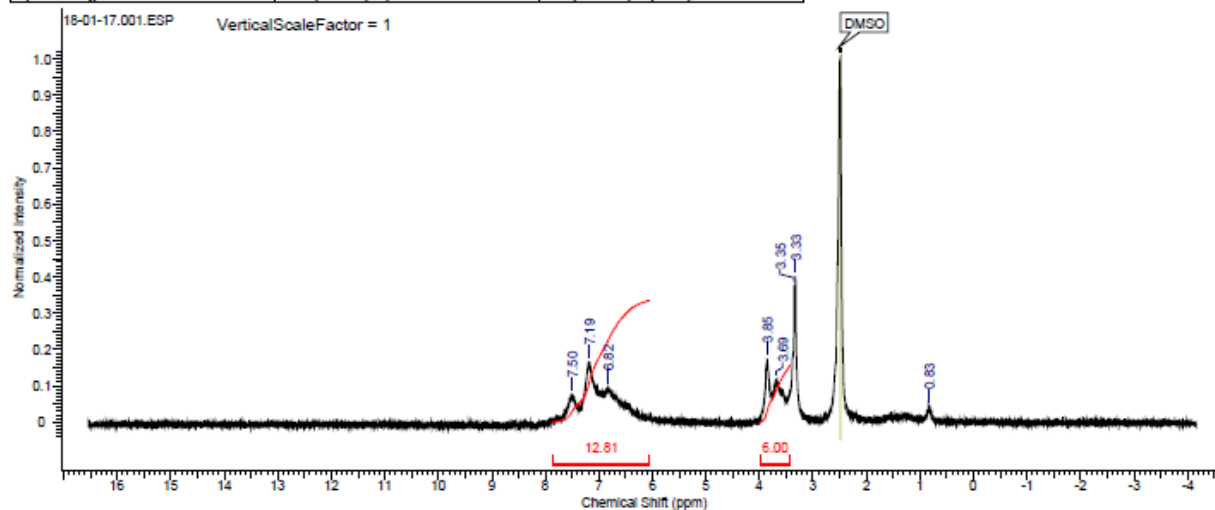


PCz2

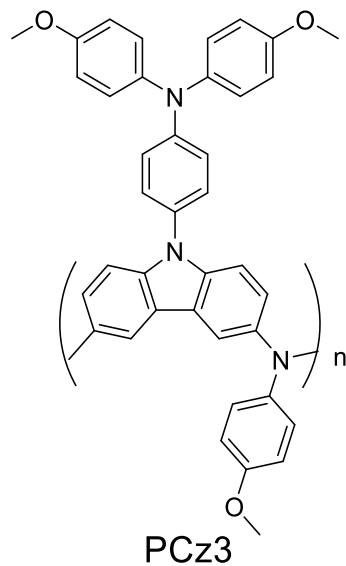


PCz2

Acquisition Time (sec)	6.3308	Comment	CzPhOMe AnOMe polymer	Date	17 Jan 2018 11:40:00
Date Stamp	17 Jan 2018 11:40:00	File Name	C:\USERS\LANOVA\DOCUMENTS\DOCTORADO\SYNTHESIS\NMR\18-01-17\11\FID	Origin	spect
Frequency (MHz)	250.13	Nucleus	¹ H	Number of Transients	15
Original Points Count	32768	Owner	root	Points Count	32768
Receiver Gain	912.30	SW (cycles) (Hz)	5175.98	Pulse Sequence	zg30
Spectrum Type	STANDARD	Solvent	DMSO-d ₆	Spectrum Offset (Hz)	1548.0396
		Sweep Width (Hz)	5175.83	Temperature (degree C)	23.160



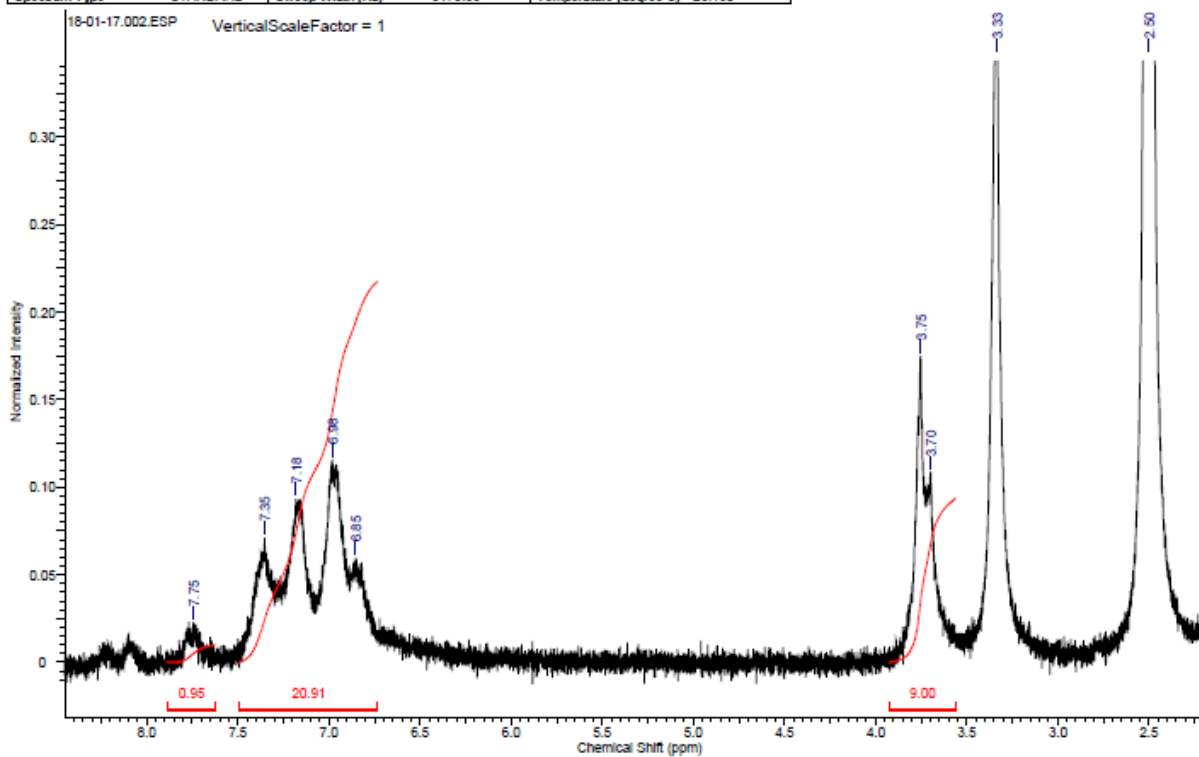
PCz3

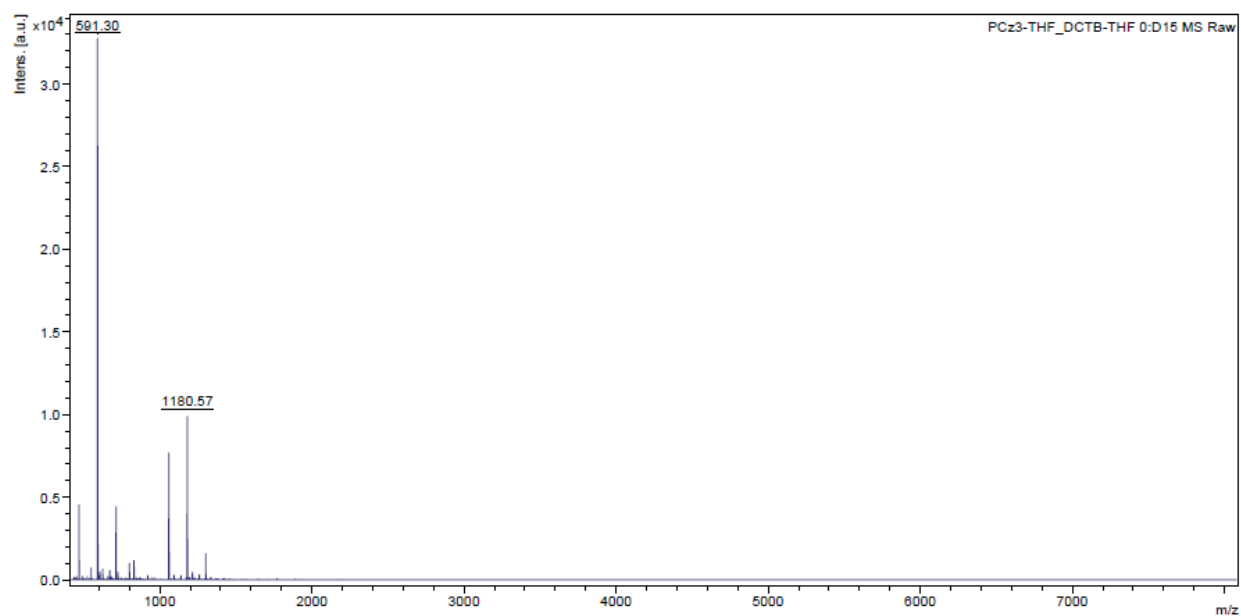


This report was created by ACD/NMR Processor Academic Edition. For more information go to www.acdlabs.com/nmrproc/

4/30/2019 4:37:56 PM

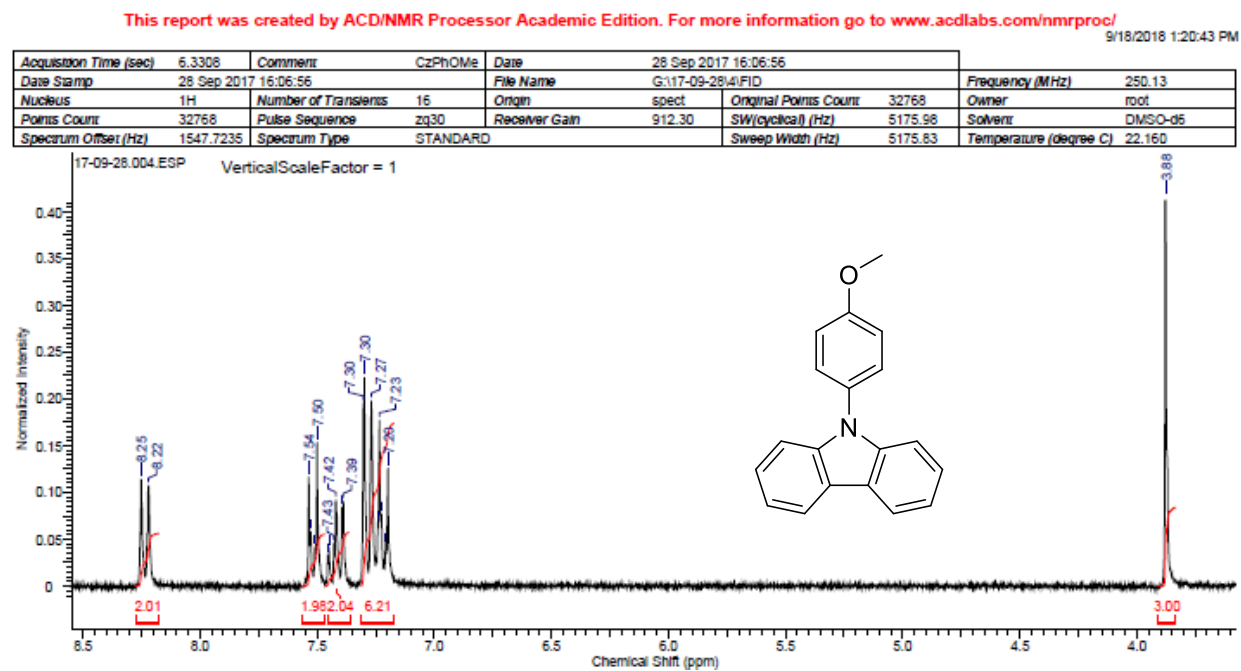
Acquisition Time (sec)	6.3308	Comment	CzTPA AnOMe polymer	Date	17 Jan 2018 11:48:32
Date Stamp	17 Jan 2018 11:48:32	File Name	C:\USERS\LANOVA\DOCUMENTS\DOCTORADO\SYNTHESIS\NMR\18-01-17\2\FID	Origin	spect
Frequency (MHz)	250.13	Nucleus	¹ H	Number of Transients	15
Original Points Count	32768	Owner	root	Points Count	32768
Receiver Gain	912.30	SW (cyclical) (Hz)	5175.98	Solvent	DMSO-d6
Spectrum Type	STANDARD	Sweep Width (Hz)	5175.83	Temperature (degree C)	23.160
				Pulse Sequence	zg30
				Spectrum Offset (Hz)	1547.5657





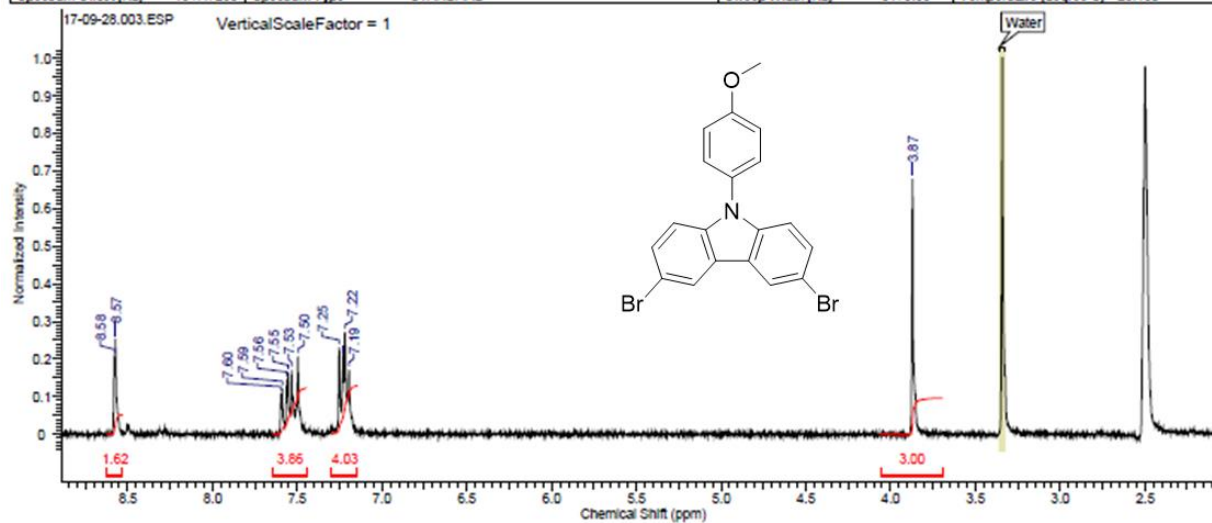
PCzX precursors

N-(4-methoxybenzene)-carbazole

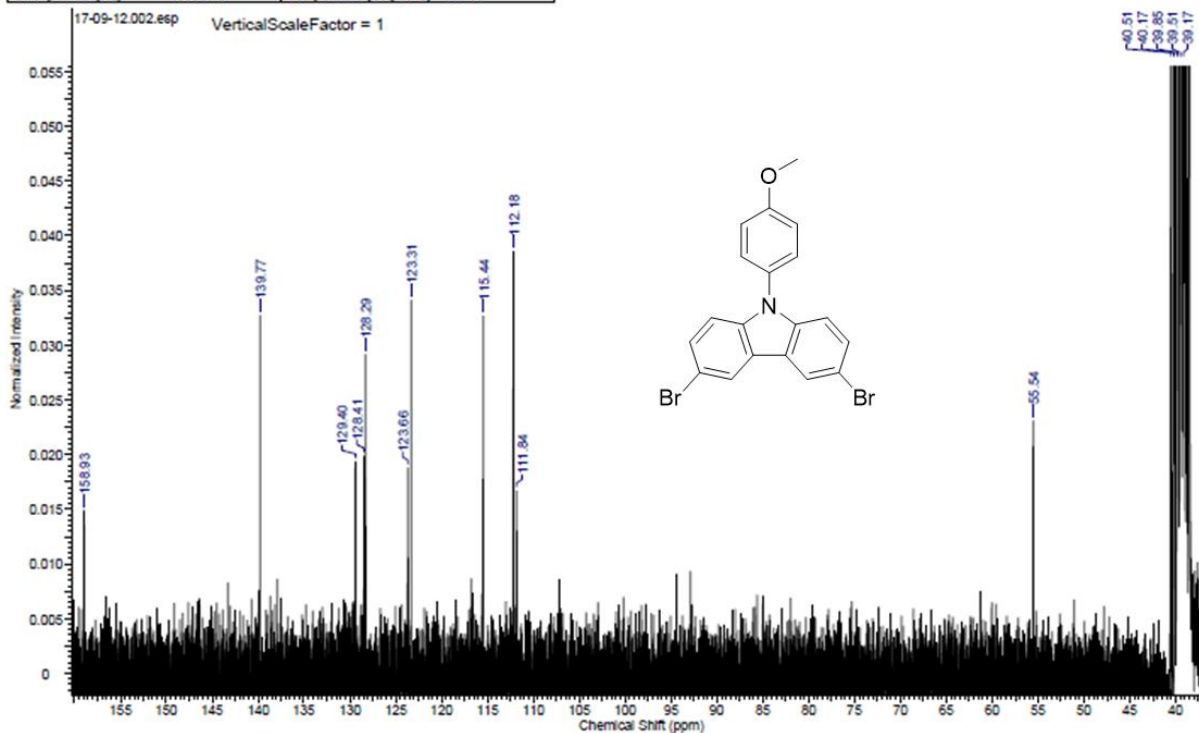


N-(4-methoxybenzene)-3,6-dibromo-carbazole

Acquisition Time (sec)	6.3308	Comment	Br2CzPhOMe	Date	28 Sep 2017 16:00:32
Date Stamp	28 Sep 2017 16:00:32	File Name	G:\17-09-28\3\FID	Frequency (MHz)	250.13
Nucleus	¹ H	Number of Transients	16	Origin	spect
Points Count	32768	Pulse Sequence	zg30	Original Points Count	32768
Spectrum Offset (Hz)	1547.7235	Spectrum Type	STANDARD	Receiver Gain	912.30
				SW (cyclical) (Hz)	5175.98
				Solvent	DMSO-d ₆
				Sweep Width (Hz)	5175.83
				Temperature (degree C)	23.160



Acquisition Time (sec)	2.1758	Comment	diBrCzPhOMe coupling diBrCz and iPhOMe	Date	13 Sep 2017 06:54:24
Date Stamp	13 Sep 2017 06:54:24	File Name	C:\USER\RENOV\DOCUMENTS\MEGA\DOCTORADO\SYNTHESIS\NMR\17-09-12\2\FID	Frequency (MHz)	62.90
Nucleus	¹³ C	Number of Transients	11024	Origin	spect
Owner	root	Points Count	32768	Original Points Count	32768
SW (cyclical) (Hz)	15050.24	Pulse Sequence	zgpg30	Receiver Gain	6502.00
Spectrum Offset (Hz)	15059.78	Solvent	DMSO-d ₆	Spectrum Offset (Hz)	6262.0190
Sweep Width (Hz)		Temperature (degree C)	23.160	Spectrum Type	STANDARD

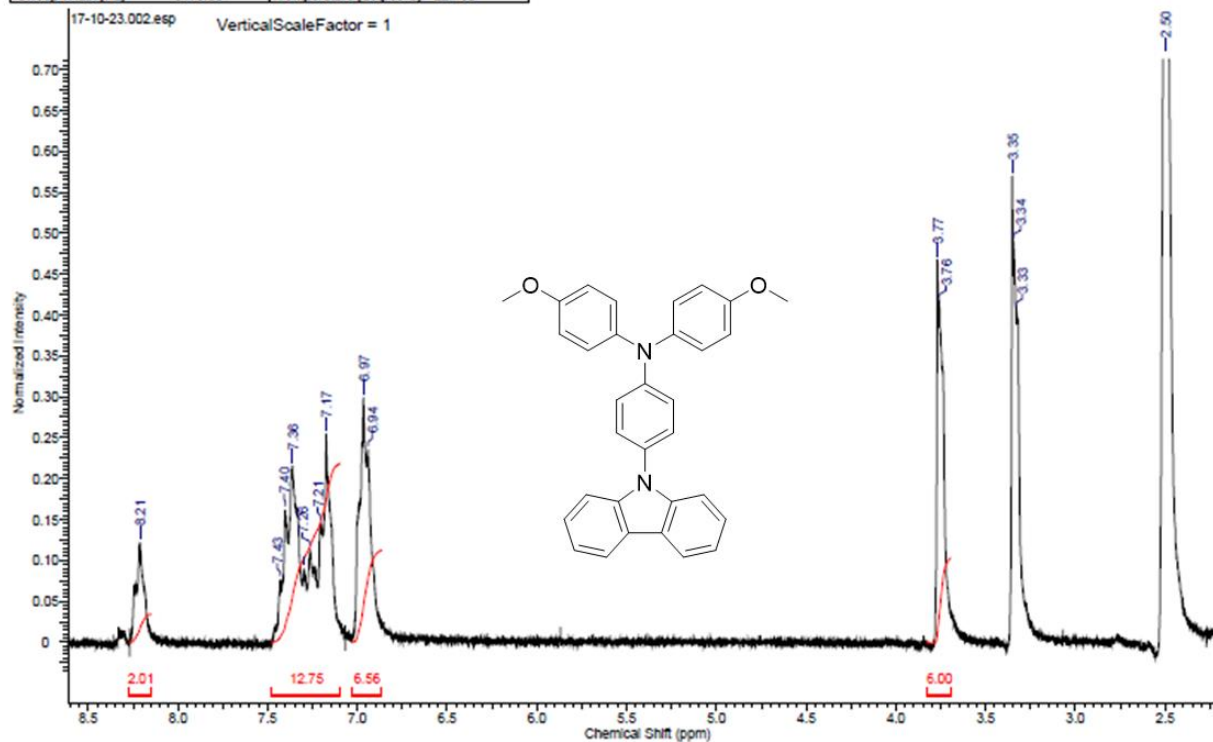


N-(4-(N,N-bis(4-methoxyphenyl)aniline)carbazole (CzTPA).

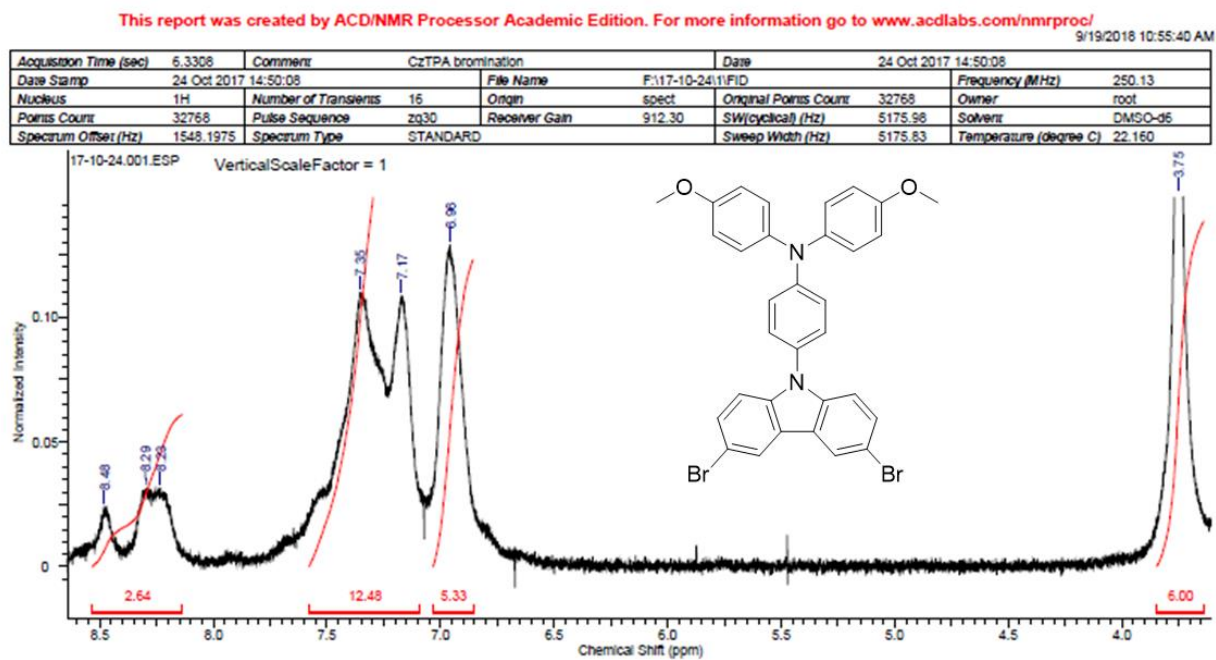
This report was created by ACD/NMR Processor Academic Edition. For more information go to www.acdlabs.com/nmrproc/

4/30/2019 4:53:06 PM

Acquisition Time (sec)	6.3308	Comment	CzTPA	Date	23 Oct 2017 11:40:16
Date Stamp	23 Oct 2017 11:40:16				
File Name	C:\USERS\RENOV\DOCUMENTS\MEGA\DOCTORADO\SYNTHESIS\NMR\17-10-23\2\FID			Frequency (MHz)	250.13
Nucleus	¹ H	Number of Transients	16	Origin	spect
Owner	root	Points Count	32768	Original Points Count	32768
SW (cyclical) (Hz)	5175.98	Solvent	DMSO-d ₆	Pulse Sequence	zg30
Sweep Width (Hz)	5175.83	Temperature (degree C)	22.160	Receiver Gain	912.30
				Spectrum Offset (Hz)	1547.0917
				Spectrum Type	STANDARD



N-(4-(N,N-bis(4-methoxyphenyl)aniline)-3,6-dibromocarbazole (Br₂CzTPA).



Abstract

During the last ten years, research around hybrid perovskite solar cells has achieved high photovoltaic efficiency conversion. Add to this, its solution processability and low-cost manufacture materials like ammonium lead (II) iodide, make of PSC one of the best on developing solutions to attain solar power. Organic hole transport materials (HTM) like Spiro-OMeTAD are an integral part of its architecture. The presented thesis aims to develop alternative solutions for the HTM layer, synthesizing new molecules that can match suitable carrier properties for its use on Perovskite solar cells (PSC). For this matter, the heterocycle carbazole (Cz), which is a well-known molecule used in organic electronics, is selected as a base molecule for our study. Due to its low cost production, ease modification of its structure over fixed positions and versatility over different reaction paths. For the later reasons Cz makes an ideal option to explore its use as HTM. Chapter 1 is a brief resume on photovoltaics and state of the art of PSC. The introduction describes the most common composition and function of the different layers that constitute the photovoltaic device's layers. Followed by a review of carbazole molecules use as HTM until now, which are described and compared to lay the foundation of the present work.

Chapter 2 reports the synthesis of two a two series of new hole transporting materials (HTMs). The presented molecules are composed by two diphenylamine(DPA) fragments linked to carbazole unit. From dibromo-carbazole as a starting material, synthesis is performed by a simple two-step synthetic procedure providing the target products in high yield. Two series of molecules designated as DMx and iDMx are obtained, differentiated between each other by their substitution position 3,6-Cz (DMx) vs 2,7-Cz (iDMx) on the carbazole (Cz) core by the DPA groups. The molecules are examined along with thermal and optoelectronic characterization, film formation ability and further test on perovskite photovoltaic devices as well.

Chapter 3 is detailed description of anionic and radical polymerization essays over molecule called DM1, which bears an alkene polymerizable function. The resulted polymer DM1P, is fully characterized and tested over PSC modules and compared with its origin monomer. The second part of Chapter 3, consist on the synthesis of a series of 3,6-carbazole linked conjugated copolymers, designated as PCzX series. With the present PCzX molecules, we explore the possibility of the use of conjugated polymers on PSC devices as an alternative to the actual small

molecules. The synthesized polymers are fully characterized and preliminary photovoltaic results are presented.

Chapter 4 describes a series of bicarbazolyl (two carbazole heterocycles connected by N- atom to a benzene ring in para position) molecules (DM1X), conceived to test its subsequent oligomerization/polymerization by further oxidative coupling reactions. This kind of polymerization can be potentially achievable with carbazole molecule under the right conditions. The present study pretends to compare the optoelectronic and thermal differences between a monomer and the derived oligomer/polymer.

Keywords: Carbazole, conjugated-polymer, non-conjugated polymer, oxidative polymerization, Hole transport material, Perovskite solar cell, photovoltaics.

Résumé

Au cours des dix dernières années, les recherches sur les cellules solaires hybrides à pérovskite (PSC) ont permis d'atteindre des rendement photovoltaïques élevés. De plus, la facilité de mise en œuvre et l'utilisation de matériaux à faible coût comme notamment l'iodure de plomb d'ammonium (II), font des dispositifs PSC l'une des meilleures solutions de développement pour capter l'énergie solaire. Les matériaux de transport de charges organiques (HTM) tels que Spiro-OMeTAD font partie intégrante de la structure du dispositif. Le travail de thèse présenté vise à développer des solutions alternatives dans la conception de molécules pour la couche HTM, en élaborant de nouveaux matériaux répondants aux propriétés physiques recherchées pour l'application PSC. Dans ce cadre, des molécules à base de carbazole (Cz), unité bien connue utilisée largement en électronique organique, a été choisi comme unité de base pour notre étude. Son faible coût, ses multiples et larges possibilités de structures organiques synthétisables en fait un bon candidat pour explorer son utilisation en tant que HTM.

Le chapitre 1 résume brièvement l'état de l'art du photovoltaïque et l'état de la technique des cellules PSC. L'introduction décrit la composition et la fonction des différentes couches constituant un dispositif photovoltaïque. Puis, sont présentée et décrite l'état de l'art des molécules à base de carbazole utilisées comme HTM pour l'application photovoltaïque permettant d'apporter les bases de la discussion du présent travail.

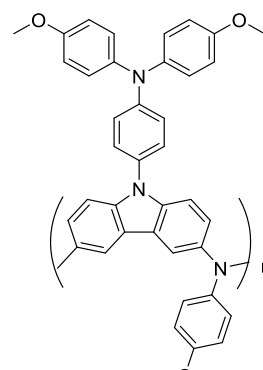
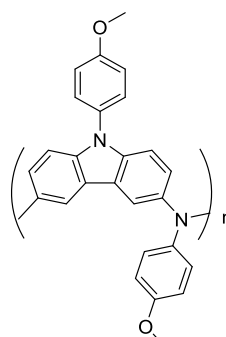
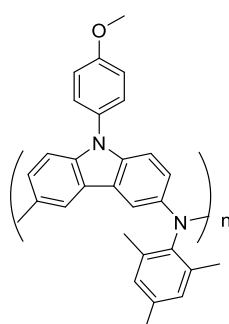
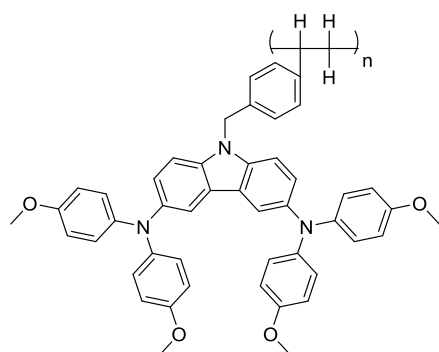
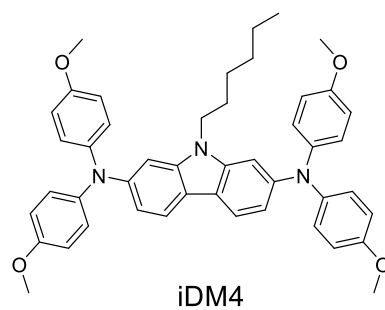
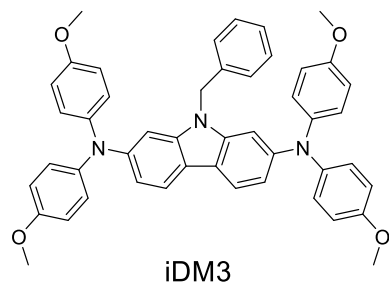
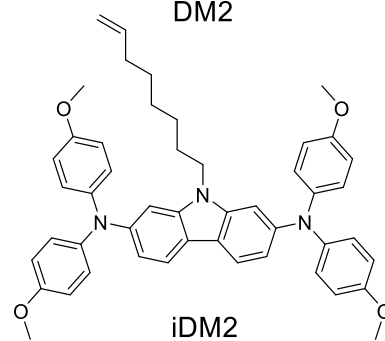
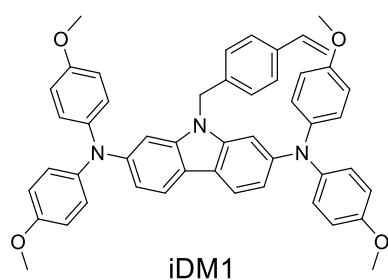
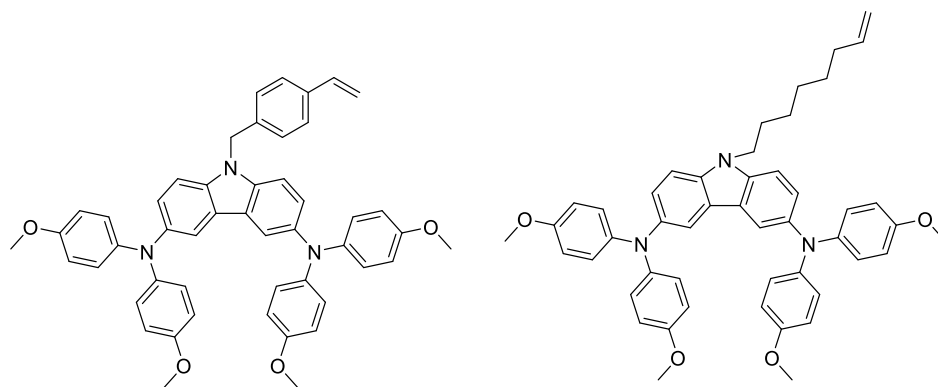
Le chapitre 2 présente la synthèse de deux familles de nouvelles molécules de transport de trous (HTM). Les molécules présentées sont composées de deux fragments de diphenylamine (DPA) liés à l'unité carbazole. À partir du dibromo-carbazole en tant que produit de départ, la synthèse est réalisée par une procédure de synthèse simple en deux étapes, fournissant les produits cibles avec un rendement élevé. On obtient deux séries de molécules désignées DMx et iDMx, différenciées entre elles par leur position de substitution 3,6-Cz (DMx) vs 2,7-Cz (iDMx) sur le noyau carbazole (Cz) des groupes DPA. Les propriétés thermiques et optoélectroniques de ces matériaux sont pleinement identifiées ainsi que leur mise en œuvre sur film. Des premiers tests photovoltaïques sont présentés.

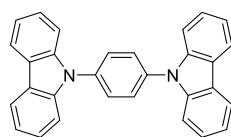
Le chapitre 3 décrit en détail des essais de polymérisation anionique et radicalaire sur la molécule phare (DM1) de ce travail, qui porte une fonction alcène polymérisable. Le polymère résultant

DM1P est entièrement caractérisé et testé sur des modules PSC et comparé à son monomère d'origine. La deuxième partie du chapitre 3 présente la synthèse d'une série de oligomères conjugués à base de 3,6-carbazole, appelée série PCzX. Avec les molécules PCzX actuelles, nous explorons la possibilité d'utiliser des oligomères conjugués sur des dispositifs PSC comme alternative aux petites molécules réelles. Les oligomères synthétisés sont entièrement caractérisés et des résultats photovoltaïques préliminaires sont présentés.

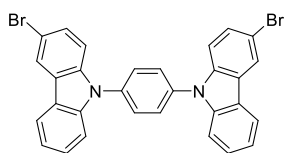
Le chapitre 4 décrit une série de molécules (DM1X) bicarbazolyle (constituées de deux unités carbazole reliés par un atome d'azote à un noyau benzénique en position para), élaboré afin de tester ses capacités à se coupler par moyens oxydantes. La présente étude prétend comparer les différences optoélectroniques et thermiques entre les différentes molécules.

Synthesized molecules

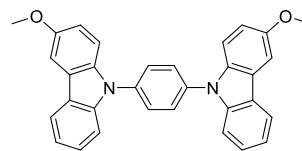




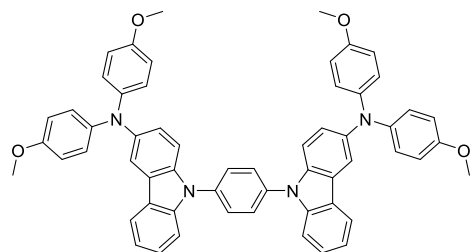
DM11



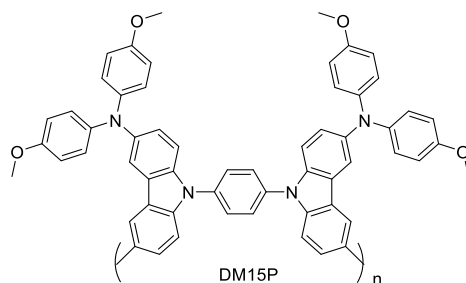
DM12



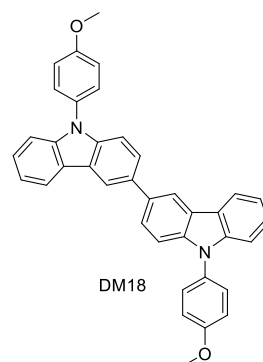
DM13



DM15



DM15P



DM18